Towards Clean Combustion and Decarbonisation

Proceedings of Australian Combustion Symposium 2023

Charles Darwin University
26 – 29 November 2023
Darwin, Northern Territory, Australia

Editors
Bogdan Z. Dlugogorski
and
Assaad R. Masri

Gold sponsor
NORTHERN TERRITORY GOVERNMENT

Silver sponsors
TERRITORY GENERATION
LAVISION FOCUS ON IMAGING
Lastek Photonics Technology Solutions

Bronze sponsor
Ansys | leap

Australian Combustion Symposium - Welcome to Country

Good morning, Ladies, Gentlemen and distinguished guests

My name is Rochelle Fejo, and I am a Larrakia woman from my mother, my grandfather, and my great grandfather in what Aboriginal culture calls grandfather law.

Firstly, I would like to acknowledge and thank the Australian and New Zealand Section of the Combustion Institute and Charles Darwin University for asking me here today to welcome you to Larrakia land.

The Larrakia people are the traditional owners and custodians of the greater Darwin region and although we are known as Saltwater People, our land boundaries extend approximately fifty kilometres inland.

Saltwater People means that we believe that our ancestors come from the land and sea. There is a story of the first Larrakia man, we call, Old Man Rock which is a reef that is seen on the low tide near here at the back of the Casuarina campus of the University.

Old Man Rock is the first Larrakia Man who created the Larrakia people and gave us a system of governance that we call the kinship system, he also gave us language so we could communicate, and he taught us how to live off and maintain our land and seas.

We are the first people to live on this land and as hosts of Larrakia country, it is my honour to welcome you all here today. As part of the Australian Combustion Symposium, you are here today to build a better world and a decarbonised economy through the combustion of clean fuels. By doing this you are protecting our lands and protecting our people.

Larrakia people say that the land is our mother and when we take care of our mother, our mother provides for us. Our lifestyle and identity stems from who we are and where we come from so when you care for our mother, you are caring for us. For this I thank you.

This is the connection in what you are doing with the connection we share together across our lands as First Nations people, as Territorians, as Australian and New Zealand colleagues and as people who care for our Earth.

You have come by way of Larrakia Land, you will hear the voices of our ancestors, when you leave, you will take the Larrakia message with you. Reverend W. Fejo

Ladies and gentlemen, it is my honour to welcome each and every one of you to Larrakia Land. May our ancestor guide and protect you always.

Thank you

Bogdan Z. Dlugogorski and Assaad R. Masri, Eds
Towards Clean Combustion and Decarbonisation: Proceedings of Australian Combustion Symposium 2023, Charles Darwin University, 26 – 29 November 2023

Except for Invited Contributions, each article included in Proceedings has been subject to a peer-review process by three independent expert referees. The reviewers provided written feedback on the papers. Authors were given the option of publishing only the abstract of their submission. Authors who opted to have their full-length papers included in Proceedings revised their manuscripts to address the comments. The revised manuscript of each paper was then considered by Editors before acceptance for inclusion into Proceedings.

Proceedings of the Australian Combustion Symposium: ISSN 1839-8162 (Online)

Charles Darwin University 2023

Message from the Chairman

The Australian Combustion Symposium returns to in-person attendance after the interruption imposed by Covid. The combustion community in Australia is eager to reconvene as it positions itself to contribute to the global process of decarbonisation. Many of our researchers are already leading the efforts of investigating the utilisation of “green” fuels and relevant blends for current and future power conversion systems.

Against this background, it is fitting that the Australian Combustion Symposium 2023 has adopted the theme of “Towards Clean Combustion and Decarbonisation”. Professor Michael Brear sets the scene in the Bilger Lecture confirming the continued importance of combustion in achieving net zero carbon and in greenhouse gas abatement. The remaining invited and contributed paper reinforce the numerous facets of this message hence testifying to the depth of this research in Australia.

As Chairman of the ANZ-Section and on behalf of all our membership and delegates, I would like to thank the local Organising Committee in Charles Darwin University for their tireless work and dedication in making the 2023 Australian Combustion Symposium an outstanding success. In particular, our thanks go to Organising Committee which included Professor Bogdan Dlugogorski and his PhD candidates at CDU - Mr Caleb Ojo, Mr Angel Aguilar-Morones, Ms Ramya Khandika and Mrs Azeb Bekele; Mrs Gopika Prema from Energy and Resources Institute at CDU who navigated all administrative hurdles and led operational arrangements; and Associate Professor Shaun Chan from the University of New South Wales for his massive efforts in setting up and maintaining the Symposium website. I also extend my words of appreciation to the members of the Technical Committee for reviewing thrice each contribution submitted for consideration to the Symposium, especially, for their time and excellence of the review comments.

Assaad R. Masri
23 November 2023

Preface

In 2023, the Australian Combustion Symposium (ACS) was held in Darwin, Northern Territory. This is perhaps the first time for this gathering to come to the Top End. The Symposium was jointly organised by the Charles Darwin University and the Australian and New Zealand Section of the Combustion Institute. The attendance was only in person as the Covid restrictions had been removed allowing everyone once again to meet face-to-face. Around 60 participants joined the meeting, mainly from Australian Universities, with small contingents from New Zealand and from industry.

As it is in the Australian tradition, the Symposium started from a Welcome to Country, delivered by Rochelle Fejo, a Larrakia woman, as Darwin sits on the ancestral lands of Larrakia Nation. As Larrakia are Saltwater People, Rochelle spoke about their progenitor emerging from the sea to give Larrakia their language and the system of governance to maintain Larrakia's land and sea. Rochelle stressed the connections among protecting the lands and protecting the people and decarbonising the economy.

Professor Scott Bowman AO, Vice-Chancellor of the Charles Darwin University, welcomed the delegates to Charles Darwin University and Professor Suresh Thennadil to the CDU's Energy and Resources Institute. The University is undergoing rapid growth under the leadership of Professor Bowman, especially in science and technology disciplines, including ever increasing contingents of international students. Professor Assaad Masri greeted the delegates on behalf of the Australian and New Zealand Section of the Combustion Institute.

Australia and New Zealand progress assiduously to decarbonise their economies and the technical program of the Symposium reflected this effort, with 16 out of 41 accepted contributions in this area. These contributions dealt with hydrogen and ammonia-based fuels and decarbonised liquid fuels, within the contexts of burners and internal combustion engines. Consistent with these new directions in combustion research, *Towards Clean Combustion and Decarbonisation* became the theme of the Symposium and the title of these Proceedings.

Evidently, biomass combustion stirs less interest as a means to decarbonise the economy, in comparison to hydrogen and ammonia fuels. In a germane field of circularity of hydrocarbon materials, three presentations concentrated on treating end-of-life tyres and waste electronic and electrical equipment. In comparison with the past Symposia, only one contribution covered the combustion of coal, signifying a truly dramatic change in the combustion scene in Australia and New Zealand.

Wildland and wildland-urban interface fires in hot, drying climates of Australia, and new threats due the battery, building and warehouses fires represented the second largest source of contributions for the Symposium, of about 25 %. Finally, nine manuscripts addressed advance concepts in particle combustion, propulsion, mixing, machine learning and energy storage, some of them stemming from research on decarbonisation.

The Bilger and Plenary Lecturers established the setting of the conference discussing abatement of greenhouse gases (Professor Brear), operation of internal combustion engines on clean fuels (Professor Bae), catalytic pyrolysis of polymers (Professor Uddin), and hydrogen safety (Associate Professor Salehi). The Committee of the ANZ Section of the Combustion Institute selected three outstanding mid-career Australian researchers to deliver Invited Thematic Reviews in building fire safety (Associate Professor Chan), turbulent flames of green fuels (Dr Dunn) and reciprocating engines operating on ammonia (Associate Professor Yang).

Editors are enormously grateful to the members of the Technical Committee for insightful reviews of the papers submitted to the Symposium. Their work had greatly improved the quality of the papers. Each member of the Committee reviewed between 3 and 6 contributions. We also thank senior associates in research groups operated by the members of the Technical Committee, as we realise

that the reviews often represented joint efforts. The Technical Committee comprised the following colleagues:

Associate Professor Yasir Al-Abdeli, Edith Cowan University
Professor Michael Brear, The University of Melbourne
Professor Richard Brown, Queensland University of Technology
Associate Professor Shaun Chan, UNSW Sydney
Professor Matthew Cleary, The University of Sydney
Dr Matthew Dunn, The University of Sydney
Dr Alexander Filkov, The University of Melbourne
Dr Maryam Ghodrat, UNSW Canberra
Dr Vinny Gupta, The University of Sydney
Professor Evatt Hawkes, UNSW Sydney
Professor Eric Kennedy, University of Newcastle
Professor Shawn Kook, UNSW Sydney
Professor Alexander Klimenko, The University of Queensland
Professor John Mackie, University of Newcastle
Professor Paul Medwell, The University of Adelaide
Professor Behdad Moghtaderi, University of Newcastle
Dr Vinuthaa Murthy, Charles Darwin University
Professor Gus Nathan, The University of Adelaide
Professor Vasily Novozhilov, Victoria University
Associate Professor Fatemeh Salehi, Macquarie University
Dr Zhiwei Sun, The University of Adelaide
Associate Professor Mohsen Talei, The University of Melbourne
Professor Vincent Wheatley, The University of Queensland
Associate Professor, Yi Yang, The University of Melbourne
Professor Dongke Zhang, The University of Western Australia
Professor Dan Zhao, University of Canterbury

with the Committee Chaired and Co-Chaired by two Editors. Each regular submission (but one!) received three sets of review comments. Authors could select to include their full papers in the Proceeding (so-called Mode 1 contributions) or only their abstracts (called Mode 2 contributions). The reader will notice that Proceedings contain 23 Mode 1 papers and 18 Mode 2.

We took an advantage of empty space below each abstract of Mode 2 contributions, to include colour images generated by Mr Angel A. Aguilar Morones, using Midjourney – a generative artificial intelligence program that creates images based on the textual information provided in the abstracts of Mode 2 papers. The authors and the readers can judge by themselves on how well AI converts the vernacular used in our field to images. AI now pervades all facets of our society and the field of combustion in not an exception.

Australian English is forgiving. While its traditional spoken variants derive from British and Irish English, it allows American spelling to enter the language of engineering and science. We followed the traditional spelling conventions of Australian English in the front matter to these Proceedings but resolved to leave the spelling conventions of individual articles to their authors. Thus, the reader will notice, for example, “modeling” and “modelling”, used in different articles. While we provided a template to all authors for typesetting the papers, many authors modified the fonts and outlines of their written contributions. Again, we concluded not to interfere with these individual preferences. Finally, we did not insist on the authors following the traditional SI conventions for writing units and symbols, especially for typesetting the symbols in italics and leaving single spaces between numbers and their units.

Among many people who assisted us in preparing these Proceedings, we would like to distinguish Mr Angel A. Aguilar-Morones and Ms Ramya Narayan Khandika, both PhD candidates at the Charles Darwin University. Angel prepared the front page of the Proceedings and spotted several typographical errors in the text, while Ramya organised the author index.

Bogdan Z. Dlugogorski and Assaad R. Masri
25 November 2023

Contents

Fires and Process Safety (FPS)

Circularity and Hydrocarbon Fuels (CHF)

Fundamentals and New Concepts (FNC)

Invited Contributions: Bilger Lecture
B. Z. Dlugogorski and A. R. Masri, Eds
Towards Clean Combustion and Decarbonisation
Proceedings of the Australian Combustion Symposium
26 – 29 November 2023, Darwin, Northern Territory, Australia

What does deep greenhouse gas abatement mean for combustion research?

M. J. Brear*
Director, Melbourne Energy Institute and Department of Mechanical Engineering, The University of Melbourne, Victoria 3010 Australia, mjbrear@unimelb.edu.au

Abstract

Our need to achieve deep greenhouse gas abatement is often assumed to mean that combustion will be largely or completely displaced by alternatives. However, climate change is addressed by reducing greenhouse gas emissions to the atmosphere, not by 'stopping combustion', and abatement can be achieved in many ways. Using the Net Zero Australia Project (NZAu) as a case study, as well as several other sources, this paper will first discuss what energy sources, energy vectors and end-use appliances could have significant roles in deeply decarbonised energy systems. I will then discuss which of these energy supply chains could plausibly use combustion and how. Finally, I will consider several low emission devices that could use combustion in future, with those devices potentially superior in utility, economics and environmental impact relative to alternatives. This survey of options will conclude that combustion should continue to play an important role in deeply decarbonised energy systems. However, the fuels that we burn, the conditions at which we burn them, and the services that we will require from combustion devices may be quite different to current practice. Similarly, we will face significant new challenges in fire safety. This means that the combustion community should view deep abatement as a major opportunity for research, innovation and teaching, rather than a threat.

Keywords: decarbonisation, energy system, combustion research

1. Introduction

My first encounter with Prof. Bilger was in late 2001 at the Australian Fluid Mechanics Conference in Adelaide, when I was a new Lecturer at the University of Melbourne. Since then, I met with Prof. Bilger during several Australian and International Combustion Symposia and visited the University of Sydney several times. Throughout all our exchanges, Prof. Bilger remained deeply engaged with more fundamental *and* applied aspects of combustion and energy-related research, with his interests ranging well beyond the areas of research for which he is most well-known. I think that Prof. Bilger's fascination with many questions of our discipline, and his appreciation of the deep relationship between the fundamental and the applied, are hallmarks of the best scholars.

These principles are also arguably no more important than when we consider how we might decarbonise. We cannot prescribe how the world needs to change without first having a good understanding of *how the world currently works*, e.g. [1]. Whilst this is, of course, an obvious statement, many still ignore or dismiss it when thinking about energy. But, just as a surgeon needs to understand the function of a part of the body on which she/he is about to operate, all of us need to first know how our part of the energy system works if we wish to improve it. And if we do not take this task of understanding seriously, we risk our work having no effect or even making things worse.

Energy researchers therefore need to engage with the applied deeply and sincerely. Why do we use coal so much, let alone crude oil and natural gas? Is this just because of these fossil fuels' physical properties coupled with the technical characteristics of the devices that extract, transport and use them? Or might other things, including social, economic and even environmental factors, be significant determinants of how our energy system came into existence, is configured and functions? And how does the functioning of our societies depend on how we use energy? Would we have cities as we currently know them without the internal combustion engine driving passenger vehicles, heavy industry providing steel and cement, and electricity transmission enabling power generation remotely from its use [1]? And if this is not the case, how will decarbonisation change how we live? Will it be a 'business as usual' existence as we 'get off' fossil fuels, or will our lives be more disrupted? And why are the Japanese and Koreans so interested in hydrogen, and how will India's demand for energy evolve over the 21st Century?

None of us can understand all these matters, even though they are very important. As such, we also need to be humble in acknowledging the vast scale and complexity of the decarbonisation task, the many things that we don't know, and therefore expect that we may be wrong! There is no place for the over-simplified narratives that we have all heard *and sometimes profess!* These might broadly be classified as 'combustion = bad' and 'renewables = good', or any permutation that includes electrification, nuclear or your technology of choice. Another is 'we know what to do, we just have to do it'. This is a particularly unhelpful view that, I think, marginalises the centrality of technological disruption and thus research to the challenges ahead. I *don't* think that we really know how to deeply decarbonise, although we do know quite a lot. Renewables are making remarkable strides, and *maybe* the combustion of fossil fuels will cease by mid-century. But if it does, that doesn't necessarily mean that combustion will cease. *And maybe* many combustion and non-combustion technologies will play a role, just as they do today.

* Corresponding author:
Email: mjbrear@unimelb.edu.au

On the eve of the 28th United Nations Climate Change Conference (COP28), let us therefore not view the decarbonisation task as a case for or against combustion. That is simply missing the point. The reduction of greenhouse gas emissions is the objective, and these are caused by many inter-related and complex systems.

Let us therefore view the need to deeply decarbonise as a vast challenge and opportunity to learn how the world currently works and an equally vast challenge and opportunity to envisage how we might improve it *and then do so.* These challenges are as fascinating as they are evidently important. We should therefore approach them with vitality and safe in the knowledge that those who rise to these challenges – and thus commit to a life of learning about and 'doing' energy - will be needed by our communities, industry and governments, whilst those with over-simplified narratives inevitably come and go.

2. The Net Zero Australia (NZAu) Project

The Net Zero Australia (NZAu) Project [2] is a partnership between the University of Melbourne, the University of Queensland, Princeton University and management consultancy Nous Group. In keeping with my own sentiments in the Introduction, and given the immense complexity, large degree of uncertainty and the contested nature of the decarbonisation challenge, this Project considers what its authors call the 'boundaries of the Australian debate' by intentionally varying important parameters across the scenarios examined. These include wide ranges in the rate of electrification, renewable build rates, and limits on fossil fuels and carbon capture, utilisation and storage (CCUS), amongst many. The NZAu Project does not state that any of these scenarios is more desirable or achievable. Rather, the intent of the NZAu Project is to illustrate

- the scale, complexity and cost of the net zero challenge, irrespective of which specific pathway is preferred or taken,
- the implications of key choices, and
- the potential impacts for society and the environment.

Irrespective of the scenario, the NZAu Project shows that reaching net zero emissions is an immense challenge. It potentially involves

- growing renewables by mid-century to 400-500 GW capacity for the domestic energy system and potentially even several thousand GW for energy exports around the Nation (Figures 1 and 2),
- establishing a fleet of batteries, pumped hydro energy storage and gas-fired firming that is larger in capacity than our domestic energy system today (Figure 2),
- greatly increasing electrification and energy efficiency across all sectors, ranging from the uptake of electric vehicles to the displacement of gas-fired heating with electrically driven equivalents in our homes and some businesses,
- developing a large carbon capture, utilisation and storage industry that can sequester of order 50-100 Mt pa of CO_{2e} as an important part of reaching net zero,

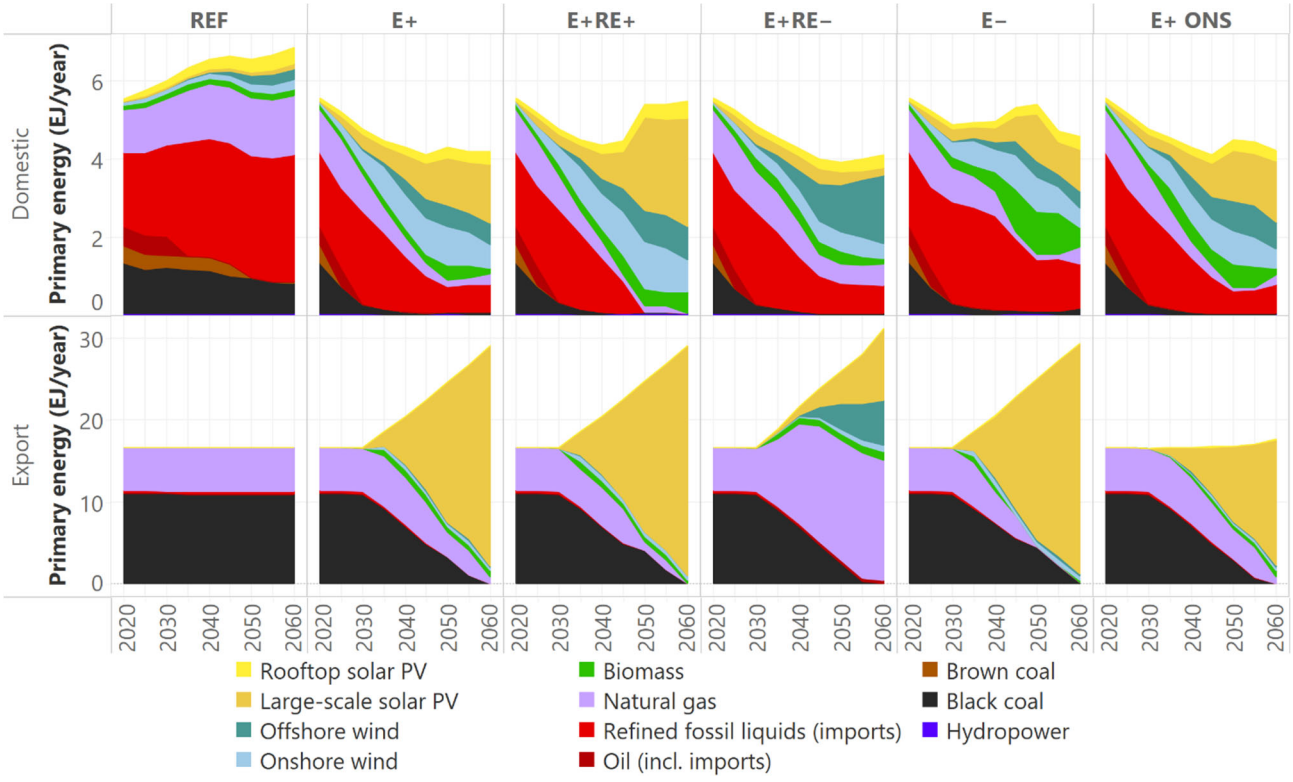

Figure 1: The NZAU Project's domestic (top row) and export (bottom) primary energy production across its 6 Core Scenarios (REF has no GHG constraint; the other 5 are different net zero scenarios all defined in [2])

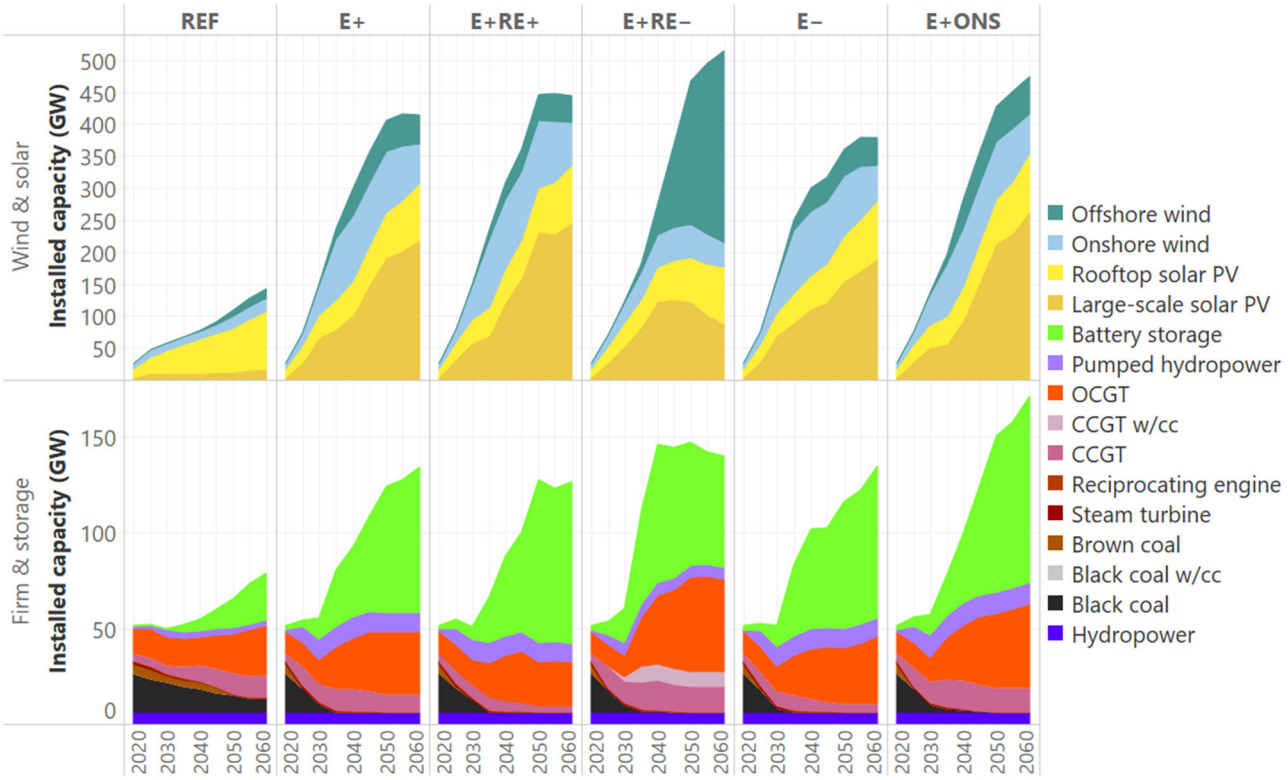

Figure 2: The NZAu Project's [2] domestic energy system capacities for renewable generation (top row) and energy storage and firm generation (bottom row) across its 6 Core Scenarios

- greatly expanding our energy networks, not only by electrification but also the transmission of several new network delivered commodities such as hydrogen and carbon dioxide, and
- attracting and deploying $7-9 trillion of capital by mid-century for domestic and export-related investments.

The export of clean processed minerals, such as clean iron rather than iron ore or clean aluminium rather than bauxite or alumina, could also play a major role in this transformation. This is because the offshore processing of these minerals releases large amounts of GHG, and we may be able to produce clean processed minerals more cheaply locally. This is due to our very significant renewable resource potential that is often, but not necessarily, co-located with these ores.

Also, achieving net zero will require us to invest a great deal in our people and our land (Figure 3). This includes the energy sector's workforce potentially growing several times from about 100,000 today in different communities around the Nation. We must also dramatically reduce land sector GHG emissions from order 100 Mt_{CO2e} to about zero and, preferably, net negative emissions whilst also protecting and potentially enhancing the Indigenous Estate, natural ecosystems and agriculture.

Clearly, these are all immense, extraordinarily complex and very uncertain challenges.

2.1 Limitations of the NZAu Project

Of course, there are many limitations to any project. I will now discuss my own views on some of these limitations to the NZAu Project that are potentially most relevant to the combustion community.

End-use appliances in homes and businesses

The NZAu Project has not (yet) performed an economic optimisation on any end use appliance. Rather, we have imposed demand for services (not the energy demanded) and the technological choices over the entire demand side, e.g. lighting, heating and cooling, etc. However, appliance use in homes and businesses is arguably the most 'community-facing' part of the energy system, and the associated, mainly private investments are a significant fraction of the total costs of the transition. They are also a very significant portion of private citizens' capital. For example, Australia currently has roughly 10M homes which currently have a total capital value of roughly 10 $Tr [3]. Thus, the current value of all Australian homes is comparable to the total required capital investment that the NZAu Project found is required to decarbonise our domestic energy and our exports.

Further, many Australian buildings are relatively old and energy-inefficient, particularly in Victoria. What we choose to demolish and replace, let alone retrofit and upgrade with new appliances, is therefore an immense planning and investment task that is comparable to that of the energy system itself. A great deal of research needs to be done in working out this task, considering many things such as

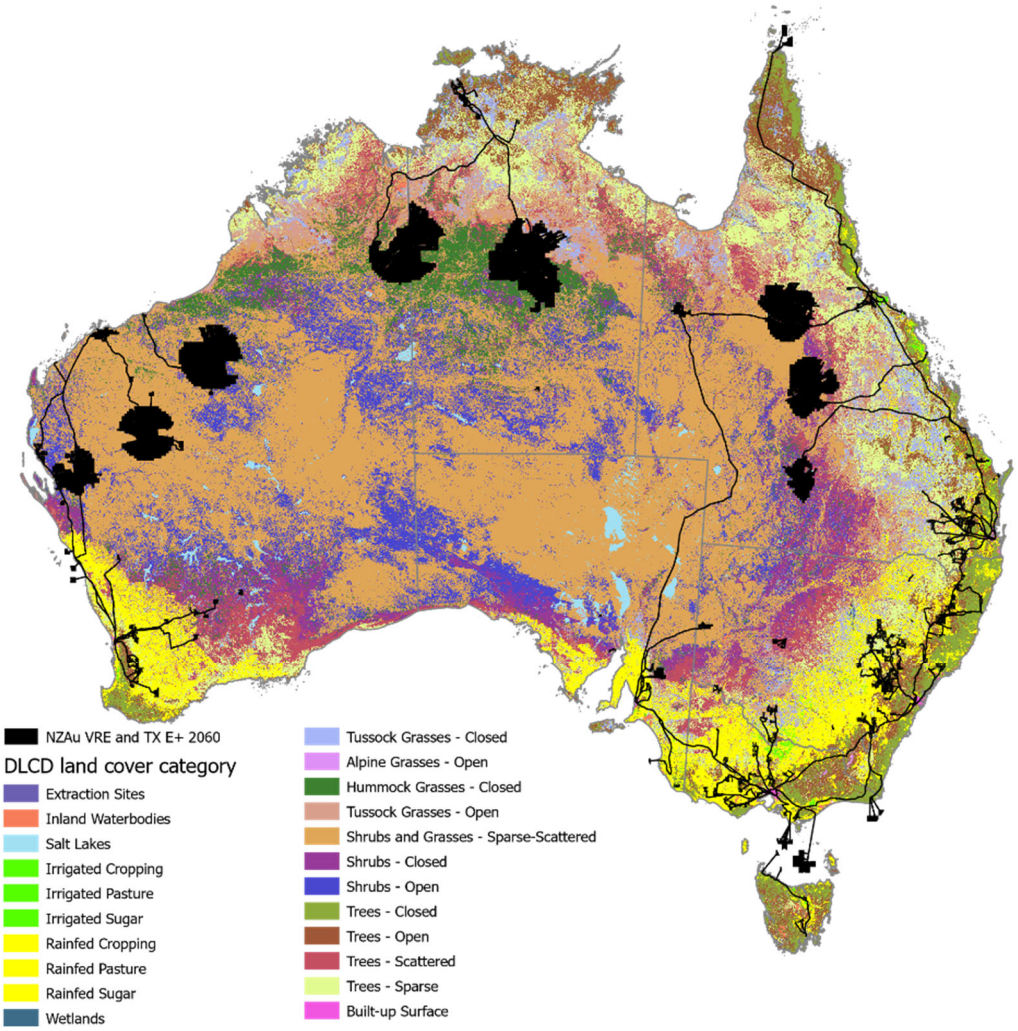

Figure 3: An *indicative* map of the Australian domestic and export energy systems superimposed onto land cover for the E+ Scenario in 2060 from the NZAu Project [2]

- the current and projected energy productivity of the current range of Australian residential and commercial building stock;
- the relative merits of new build vs retrofit, both of which include any potential combination of insulation, electrification, distributed energy resources (i.e. solar PV and battery), dynamic thermal management, EV integration, natural gas appliance performance and potentially even hydrogen-to-the-home or bio-methane / synthetic-methane injection into gas networks; and
- the consumer's ability-to-pay and willingness-to-pay for different options, considering the wide range of Australian homes and businesses and the wide range of individual wealth and engagement in energy-related matters.

The transport system

The NZAu Project has imposed demand for all road vehicles and their motive energy sources, and imposed demand for air, sea, road and rail freight as a function of population growth. These are again major simplifications. Just Australia's spend on new cars and light commercial vehicles (LCVs) is 50-70 $B pa. Much more research needs to be done on transport as well, including

- assessment of the technological options for passenger and commercial road transport, rail, sea and aviation, including ideal and expected consumer choice - this will include assessment of full electrification, hybridisation, lower carbon fuels and more vehicle types required to meet the demanded services;
- integration of technical, social and environmental factors, e.g. energy/transport coupling (particularly electricity networks), modal switching, socioeconomic distributions of ability-to-pay and willingness-to-pay and health costs;
- examination of the conditions under which different potential regulations could be close-to-optimal whilst not forcing the uptake of low emission vehicles in a non-regressive way, e.g. avoiding subsidising the rich to buy EVs that they don't drive much (and therefore

don't abate much) whilst not helping the poor who continue to drive older and less efficient, conventional vehicles.

As part of this work, it is very likely that at least air and sea transport will remain mostly or even entirely based on combustion engines of some form.

Heavy industry

Whilst the NZAu Project has identified some pathways for the decarbonisation of heavy industry through electrification and fuel switching, this is arguably the area in which we the study is least complete. This is because 'heavy industry' is not an easily definable set of well-characterised industrial processes. Rather, heavy industry features many different and usually complex processes that require detailed, individual treatment in order to assess their abatement potential [4]. As a result, the NZAu Project has only studied the steel, aluminium, cement and synthetic liquid fuels sub-sectors in any detail to date. And again, in these cases, we imposed demand for their products rather than allowed the model to develop an economically optimal response. Clearly, much more work is required to examine heavy industry decarbonisation.

Energy Exports

The NZAu Project only considered the export of clean ammonia as an alternative to the continued export of Australian coal and natural gas. This is despite there being other options for clean energy export, such as methanol [5] and liquid hydrogen [6,7], to name only two. Indeed, the choice of clean energy carriers for international energy trade is a complex and uncertain matter that is also subject to a great deal of research [8].

New and potentially disruptive technologies

No study can consider all potential options, and thus the NZAu Project – like any system-level study of deep decarbonisation – had to limit the number of technological options that it considered. The NZAu Project therefore only included what its authors thought were the most commonly considered technologies and energy carriers. The excluded technologies range from the more conventional, such as the use of reciprocating internal combustion engines in stationary power generation, to the less conventional, such as fusion for stationary power generation.

Of course, the 'unknown unknowns' of energy technologies that have not yet been thought of, let alone demonstrated, may also prove to be disruptive, and it is not prudent to exclude such possibilities over the next 30 or so years even if they can't be modelled. For example, a similar study undertaken in the mid-1990s or even the early 2000s could not have foreseen the dramatic impact of unconventional oil and natural gas on North American, Australian and global energy trade, let alone the *current* impact of LED lighting, the internet, wireless communications, smart phones and lithium-ion batteries. These new technologies continue to impact the energy system very significantly, and we had little or no anticipation of these impacts 20 or so years ago.

3. Some combustion technologies and related research for decarbonising systems

Figure 4 shows estimates of the total costs of Australia's domestic energy transition for the NZAu Project's 6 Core Scenarios [2]. Whilst the total levelized (i.e. annualised) costs of achieving net-zero emissions are not projected to rise significantly as a fraction of GDP, these costs are still 2-3% of GDP higher than not pursuing net-zero emissions. As a result, the cost of abatement for these net-zero scenarios ranges up to roughly 100-200 $/t$_{CO2e}$.

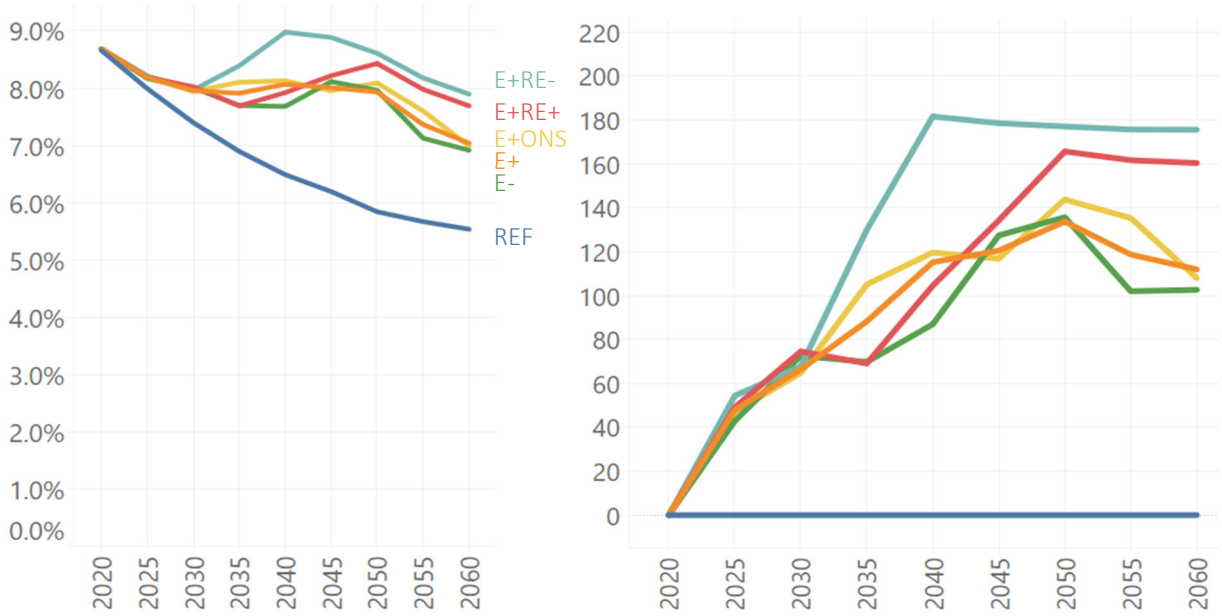

Figure 4: The NZAu project's [2] levelised domestic energy total costs as share of Australian GDP (left) and average domestic cost of abatement (2020 AUD/t$_{CO2e}$, right) across its 6 Core Scenarios

We can now immediately identify a major challenge for innovators and researchers: *make deep abatement more affordable.* Whilst many can pay significantly more for energy, several billion people still consume as much energy on a per capita basis as was consumed in all of Europe, the United States and Australia *in the mid-19th century* [9]! These people will want – and should receive – more energy over the coming decades. Further, many who can afford to pay significantly more for energy will not want to do so for different reasons. Reducing the cost of clean energy therefore mitigates very significant social problems whilst improving the lives of lower-income communities globally. It is not an over-statement to consider this as 'promoting world peace and prosperity'!

3.1 Potential clean energy supply chains

It is helpful to think about how we should go about the challenge of making clean energy more affordable by considering prospective clean energy supply chains, from the primary energy source to end use. For example, the NZAu Project models both 'blue' ammonia (i.e. from natural gas with CCS) and 'green' ammonia (i.e. from renewables) supply chains from Australia to a potential Asian customer, and finds that net-zero emissions by mid-century delivers green ammonia to this customer at roughly 35 $AUD/GJ [2]. This is roughly 2-3 times more expensive than (pre-COVID and pre-Ukrainian War) delivered natural gas [10], and thus we might consider how we can make the cost of this clean energy approach this important fossil equivalent.

This green ammonia supply chain features:

1. the generation of renewable electricity from solar and wind in favourable areas, e.g. the large dark circular regions in Figure 3;
2. the conversion of electricity to hydrogen within these regions via electrolysis;
3. the transmission of hydrogen to ports;
4. the conversion to hydrogen to ammonia at ports;
5. the shipping of ammonia to the customer; and
6. the reconversion of ammonia to hydrogen and then use, or the direct use of ammonia at the customer.

The cost of renewable electricity ($/J) is dominated by its capital costs ($/W), and the total (capital and operating) costs ($/J) of each of the subsequent processes is mainly the cost of its respective feedstock/s. As such, innovations in renewable energy that reduces its capital cost and innovations in the efficiencies of all the subsequent processes drive down the total cost of the delivered energy significantly. Indeed, using plausible estimates of improved performance in each of these processes, including only 2 that are already being demonstrated but not yet deployed [11,12], at least a 30% reduction in the delivered cost of green ammonia may be prospective, with a 50% reduction conceivable:

- highly efficient electrolysis, promising 90%+ efficiencies relative to the NZAu Project's assumed 50-60% efficiencies, e.g. [11]; and
- highly efficient, hydrogen fuelled reciprocating engines, promising 50-60% thermal efficiency compared to 35-45% typically today, e.g. [12].

Such performance could make delivered green ammonia (or reconverted to hydrogen) comparable in cost to current natural gas *without subsidy.*

Of course, whilst such levels of clean energy supply chain performance may not be achieved, we should also not dismiss the challenges of the competition. For example, only a small proportion of Australians – let alone the 'other 99.7%' of the global population - can currently afford to fully electrify our homes and replace their cars with electric vehicles (EVs) [2]. It is also unclear as to whether our electricity networks will have the capacity to accommodate widespread EVs and fully electric buildings, particularly in colder climates *where most of Australia's fossil fuels are currently exported and used.* It is certainly *not* the case that 'we know what to do, we just have to do it'. Rather, we need to attack this challenge on many fronts simultaneously and *learn by doing.*

3.2 Potential combustion research

Combustion can play an important role in several of these steps along the green ammonia supply chain. Most obviously, step 6 may involve the combustion of either ammonia or hydrogen in a wide variety of end-use appliances ranging from heavy industrial processes, transport, power generation as well as residential and commercial heating. However, this is not a complete summary of the potential use of combustion in this supply chain. All the processes after the generation of the renewable electricity require clean energy to drive them, e.g. for drying green hydrogen, for gas compression in hydrogen transmission and ammonia production, or to propel a ship. This *firm* energy requirement is likely to use combustion engines of some form, often along with energy storage and renewables, just as power generation at the customer may also likely require. Thus, determining how we can burn several different clean energy carriers in many different devices is a very important challenge.

These challenges are also very significant since we need to achieve very high performance to reduce costs, when we have relatively little experience with these fuels, e.g. [5,13-20]. This, in turn, requires us to continue to push the limits of combustion science in advanced forms of current devices or even new devices. For example, just considering green ammonia again, our fundamental understanding is lacking in key respects that limit our ability to design high performance and/or safe combustion devices that will use this fuel [19,20], including the

- sub-, trans- and super-critical injection of ammonia;
- autoignition and combustion of gaseous ammonia/hydrogen/oxygen mixtures or equivalent mixtures with air or device-representative gases; and
- pollutant formation and aftertreatment to meet contemporary and future emission regulations.

These phenomena need to be understood at extreme conditions since advanced devices are tending to higher pressures, higher levels of dilution or more exotic mixtures and, in some cases, higher temperatures. Similarly, dispersion problems need to consider highly dilute mixtures at a wide range of temperatures. This research is required if we are to properly characterise ammonia injection, dispersion, ignition and combustion for a very wide range of devices whilst also enabling new design tools and improving safety standards. Of course, similar arguments also hold for other clean energy supply chains, so our thinking should be expansive.

3.3 Lithium-ion battery safety

I close this paper with a brief discussion of arguably the ideologue's 'greatest enemy' of combustion – the lithium-ion battery! By now, we have all read stories about and watched YouTube videos of lithium-ion battery fires. These are scientifically fascinating phenomena [21] caused by *thermal runaway,* which it itself complex and dependent on the battery chemistry, structure and history of abuse. Remarkably, thermal runaway can include several reactions occurring *between the materials inside the battery* that produce *oxygen and combustible species.* Thus, starving the battery of atmospheric oxygen doesn't necessarily extinguish a lithium-ion battery fire, and the products of combustion can include gases that are very dangerous to human health [21].

Given the massive potential uptake of lithium-ion batteries (e.g. Figure 2), understanding how to avoid thermal runaway and suppress lithium-ion battery fires, particularly whilst enabling higher power densities, appear to be rich opportunities for innovation and research. Indeed, lithium-ion battery safety appears to be in the relatively early stages of its evolution and therefore deserves serious research. In at least this regard, perhaps combustion and electrification can be friends!

4. Closing remarks

I first restate the sentiments put forward in the Introduction, and I hope that the subsequent arguments are compelling justifications of these sentiments and show why combustion innovation and research remain very important to achieving deep decarbonisation. I will now only add one more thing. Most of us will only make small contributions to the sum of knowledge of combustion research and practice. However, collectively, we will teach very many students, and those students will go out into the world and hopefully play a role in the immense decarbonisation challenge that we all face. Indeed, the employment task is vast and we will need a lot more people who *'understand and do energy',* including combustion [2]. In addition to our own, lifelong learning in our fields of specialisation, let us therefore work hard to embed a love of understanding of *how the world works* whilst also teaching our students the many different options for *how we might improve it.*

5. Acknowledgments

I first acknowledge the many colleagues who worked on the Net Zero Australia (NZAu) Project [2]. This was a deeply collaborative effort between many people from whom I have learnt a great deal. Nonetheless, this paper is sole authored and is not a publication on behalf of the NZAu Project. I also acknowledge the many other people with whom I have worked over the decades. Many of these people are members of the Australian combustion community and, globally, the Combustion Institute.

6. References

[1] Smil, 2022, "How the World Really Works", Penguin, ISBN 987-0-241-98967-8
[2] The Net Zero Australia Project, https://www.netzeroaustralia.net.au/, accessed 02/11/2023
[3] Australian Bureau of Statistics, https://www.abs.gov.au/statistics/economy/price-indexes-and-inflation/total-value-dwellings/jun-quarter-2023, accessed 02/11/2023
[4] Heavy Industry Low-carbon Transition Cooperative Research Centre (HILT CRC), https://hiltcrc.com.au/, accessed 02/11/2023
[5] Olah, G. A., 2005, Angewandte Chemie International Edition, vol. 44, no. 18, pg. 2636-2639
[6] Hong et al., 2021, International Journal of Hydrogen Energy, vol. 46, no. 65, pg. 32914-32928
[7] Okonkwo et al., 2021, International Journal of Hydrogen Energy, vol. 46, no. 72, pg. 35525-35549
[8] Future Energy Exports Cooperative Research Centre (FENEX CRC), https://www.fenex.org.au/, accessed 02/11/2023
[9] Malanima, 2020, "World Energy Consumption: A Database, 1820-2018", https://histecon.fas.harvard.edu/energyhistory/DATABASE%20World%20Energy%20Consumption.pdf, accessed 02/11/2023
[10] https://www-statista-com.eu1.proxy.openathens.net/statistics/1238190/japan-lng-import-price/, accessed 02/11/2023
[11] https://hysata.com/, accessed 02/11/2023
[12] Mumford et al., 2023, "Application of Westport's H2 HPDITM Fuel System to a Demonstration Truck", 44th International Vienna Motor Symposium, accessed 02/11/2023
[13] Verhelst and Wallner, 2009, Progress in Energy and Combustion Science, vol. 35, pg. 490–527
[14] Dryer et al., 2007, Combustion science and technology, vol. 179, pg. 663-694
[15] Candel et al., 2006, Combustion Science and Technology, vol. 178, pg. 161-192
[16] Ng and Lee, 2008, Journal of Loss Prevention in the Process Industries, vol. 21, no. 2, pg. 136-146
[17] Peterson et al., 2019, Cryogenic Safety: A Guide to Best Practice in the Lab and Workplace, Springer
[18] Schildberg, 2021, Plenary, 38th Int. Symp. on Comb., https://www.youtube.com/watch?v=dSl5jDHljuU
[19] Kobayashi et al., 2019, "Science and technology of ammonia combustion", Proceedings of the Combustion Institute, vol. 37, pg. 109–133
[20] Valera-Medina et al., 2018, "Ammonia for power", Progress in Energy and Combustion Science, vol. 69, pg. 63–102
[21] Wang et al., 2019, "A review of lithium ion battery failure mechanisms and fire prevention strategies", Progress in Energy and Combustion Science, vol. 73, pg. 95–131

The future of internal combustion engines using clean fuels

C. Bae*, Y. Ki
Department of Mechanical Engineering, Korea Advanced Institute of Science and Technology, Daejeon, South Korea

Abstract

Many countries are currently revising their energy technology perspectives with the objective of achieving NZE (Net Zero Emission) and carbon-neutrality by 2050 as recommended by IEA (International Energy Agency) in 2021. The internal combustion engine will continue to contribute to the carbon neutral future of transportation albeit with clean fuel or carbon-neutral fuel. Fuel options are analyzed among the variety of energy resources for future transport powertrain systems: battery, synthetic hydrogen-based fuel, bio-fuel and oil. Synthetic hydrogen-based fuel, so-called e-fuel, is introduced from its value by showing its carbon-neutral performance via LCA (Life Cycle Assessment). E-fuel is made by combining clean hydrogen and captured carbon or bio-driven carbon, and at first needed to propel high-energy-density powerplants for aviation, shipping and heavy-duty or construction application. E-fuel has the advantages of its compatibility in its use in conventional powertrain and fuel supply system. E-fuel is also valuable as an energy carrier in that it could re-distribute renewable energy resources from concentrated resource locations to all over the world. Hurdles in realizing the feasible e-fuel production and utilization will be tackled. Efficient and economical production will lead to the establishment of sustainable e-fuel supply chain

Keywords: net zero emission, internal combustion engine, e-fuel

Energy technologies for carbon neutrality and internal combustion engines

The global landscape of energy policy is currently undergoing a significant transformation [1]. The urgency to mitigate the impacts of climate change has never been more profound, leading to worldwide efforts towards achieving net-zero emissions and carbon neutrality. Carbon neutrality refers to a state where the quantity of greenhouse gases emitted into the atmosphere is balanced by an equivalent amount removed from it. This balance can be achieved through a combination of reducing emissions and increasing the removal of atmospheric CO_2. The concept is gaining traction globally as nations grapple with ways to combat climate change and reduce their carbon footprint [2]. The Paris Agreement on climate change, which came into force in 2016, underscored this urgency [3]. Its member countries pledged to limit global warming to well below 2 degrees Celsius above pre-industrial levels while pursuing efforts to limit it further to 1.5 degrees Celsius. According to data from the International Energy Agency (IEA), global transportation accounts for around 20% of total CO_2 emissions in 2022 [1]. Figure 1 illustrates how worldwide CO_2 emissions from transportation and industry will decrease by about 20% by 2050. The pace of reduction will pick up speed in the 2030s as low-emission fuels and other emission reduction strategies are implemented [1]. However, there are a number of areas in transportation and industry where it will be impossible to completely eliminate emissions, such as aviation and heavy industry, and both sectors will have a low level of residual emissions in 2050.

Addressing these challenges related to transportation sector emissions is therefore crucial for achieving our carbon neutrality goals [4]. However, transition towards

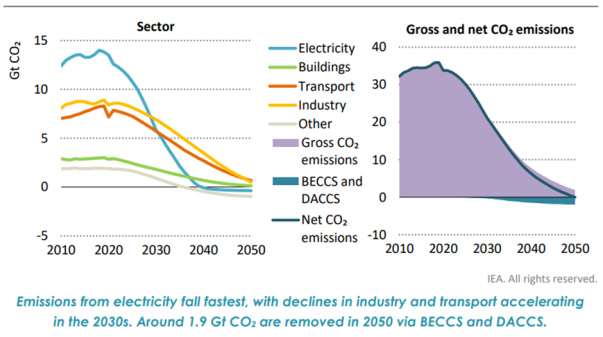

Figure 1: Global net-CO_2 emissions by sector, and gross and net CO_2 emissions in the NZE [1]

sustainable modes of transport involve overcoming several technological and infrastructural hurdles. Electric vehicles (EVs) powered by renewable energy sources present one viable solution for reducing carbon emissions from passenger cars [5-7]. However, while EVs have seen impressive advancements over recent years - thanks largely due improvements in battery technology - they are not without limitations [8, 9]. High upfront costs compared with conventional internal combustion engine (ICE) vehicles; limited driving range; undistinguishable fire; long charging times; lack of charging infrastructure; instability in battery-material supply are some barriers that affect EV adoption rates globally [10]. Furthermore, there are areas within the transport sector where electrification might not be practical or sufficient with given current technology constraints - such as aviation, shipping and heavy-duty transportation - making it clear that alternative solutions need serious consideration if we want a comprehensive approach towards carbon-neutral transport.

One such promising alternative lies in clean or carbon-neutral fuels for internal combustion engines - particularly synthetic hydrogen-based fuel or e-fuel [11].

* Corresponding author:
Phone: (+82) 10 90955044
Email: csbae@kaist.ac.kr

E-fuels offer an exciting prospect: they can be produced using surplus electricity from renewable sources like wind or solar power via power-to-x processes; this involves producing hydrogen through electrolysis which is then combined with captured CO_2 from industrial processes or direct air capture (DAC) technologies resulting in synthetic hydrocarbon fuels [12]. The use of carbon-neutral fuels like e-fuels in internal combustion engines is a promising strategy to reduce greenhouse gas emissions from the transport sector. E-fuels offer several advantages: they can be used with existing internal combustion engines with minor modifications; they don't require new infrastructure unlike electric vehicles; their energy density makes them suitable for applications where battery-electric solutions fall short like aviation, shipping and heavy-duty transportation as depicted in Fig 2 [13]; additionally, their production process allows harnessing of surplus renewable energy effectively, reducing waste [14]. Based on its favorable attributes, the IEA has projected that hydrogen-based e-fuel will represent 28% of the worldwide energy consumption by 2050, as depicted in Fig 3 [1].

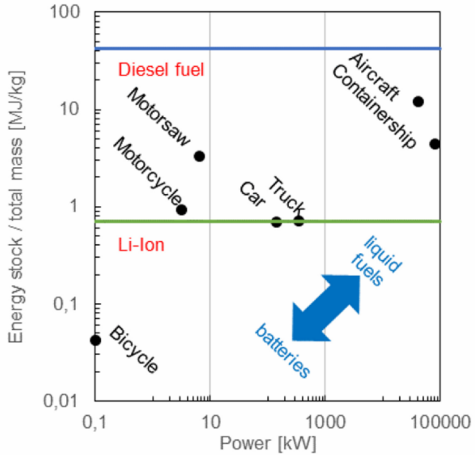

Figure 2: Energy storage capacity of some systems compared to the energy density of storage forms [13]

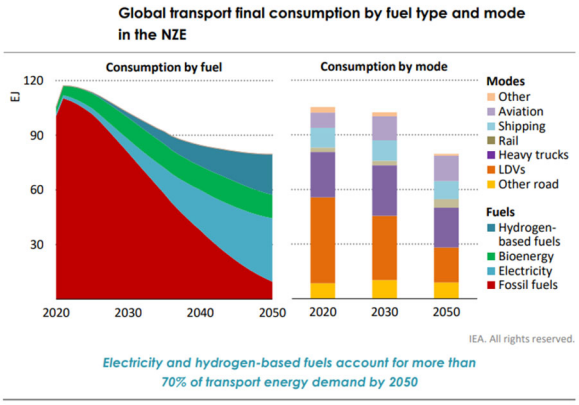

Figure 3: Global transport final consumption by fuel type and mode in the NZE [1]

However, the development and adoption of e-fuels cope with challenges including high production costs, low energy efficiency in the power-to-x process, and the need for large amounts of renewable electricity and CO_2 capture capacity [15]. Furthermore, a transition to these fuels requires addressing several technical challenges related to fuel production, distribution, and utilization [16]. Policies that encourage the development and use of carbon-neutral fuels are necessary to drive this transition [17]. Despite these challenges, e-fuels represent an exciting opportunity for decarbonizing the transport sector. They have potential applications in various modes of transport including cars, trucks, ships and airplanes, making them a versatile solution for reducing greenhouse gas emissions.

This paper aims at providing an overview of these alternative solutions with specific focus on e-fuel: its production process; its potential role in helping achieve carbon neutrality especially within hard-to-decarbonize areas within transport sector; its advantages over traditional fossil fuels as well as current hurdles that need to be overcome for its widespread adoption.

E-fuel Production Methods: Carbon Capture, Electrolysis and Biomass Conversion

Carbon capture technologies offer an innovative approach for addressing climate change by turning harmful emissions into valuable resources. One promising application of carbon capture technologies is the production of e-fuel, also known as renewable synthetic fuel. E-fuels are synthesized by combining hydrogen with carbon dioxide (CO_2) or nitrogen (N_2), offering the potential to replace conventional fossil fuels in existing internal combustion engines. E-fuel production processes include electrolysis and biomass conversion, both benefiting from the integration of carbon capture technologies.

Electrolysis involves using electricity to split water into its constituents : hydrogen and oxygen. The process begins by passing an electric current through water which results in the separation of hydrogen and oxygen atoms [18]. This process is typically powered by renewable energy sources such as wind or solar power, making it a sustainable method for producing hydrogen, which is so-called green hydrogen or low-emission hydrogen. Once the green hydrogen has been produced through electrolysis, it is then combined with captured CO_2 to create synthetic hydrocarbons - these are what we refer to e-fuels. Conceptual diagram of e-fuel for transportation is depicted in Fig 4. The combination of hydrogen and CO_2 occurs under specific conditions in a reactor vessel where they react together under heat and pressure [13]. The resulting e-fuels can then be refined further depending on their intended application. The use of renewable energy sources during this process ensures that the resulting e-fuels are carbon-neutral. Moreover, this method offers several advantages including compatibility with existing fuel infrastructure; suitability for applications where battery-electric solutions fall short like aviation, shipping or heavy-duty trucking; ability to harness surplus renewable energy effectively reducing waste [14, 19].

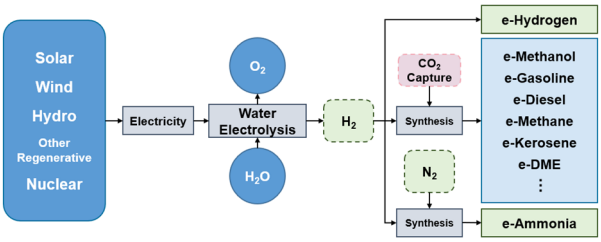

Figure 4: Conceptual diagram of e-fuels for transportation

Biomass conversion is another method for producing e-fuels. Biomass includes organic materials such as plant matter (like crops or algae) and agricultural waste products which can be converted into biofuels through thermochemical processes like gasification or biochemical processes like fermentation [20, 21]. Gasification involves heating biomass at high temperatures without combustion which results in syngas - a mixture primarily composed of carbon monoxide and hydrogen. This syngas can then be processed further to produce liquid biofuels [20]. On the other hand, fermentation involves breaking down carbohydrates present in biomass using microorganisms such as yeast or bacteria to produce ethanol – an alcohol-based biofuel [21]. During the production of these biofuels, the extra carbon in the biomass is often emitted as biogenic CO_2 since the fuels produced do not completely utilize all of the carbon content. However, it is feasible to introduce additional hydrogen into the manufacturing process (to the syngas or biogas) to utilize this surplus biogenic carbon. Figure 5 shows that this approach can yield extra fuel without necessitating carbon capture and thus produces what are referred to as bio-e-fuels [22].

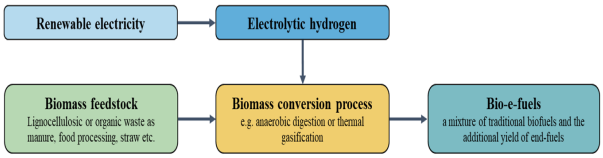

Figure 5: The pathway of producing bio-e-fuels [22]

Carbon capture, electrolysis and biomass conversion offer promising pathways towards achieving reduction of greenhouse gas emissions within hard-to-decarbonize sectors such as transportation but require significant technical advancements along with strong policy support for wider adoption.

Advantages of e-fuels

E-fuels hold significant promise in the quest for carbon-neutral energy solutions. Striving to reduce greenhouse gas emissions, particularly within the transport sector, e-fuels offer several advantages that make them an attractive option. One of the most notable benefits of e-fuels is their compatibility with existing internal combustion engines. The physical and chemical properties of e-fuels are such that they can be used in conventional powertrains without necessitating significant modifications. This makes e-fuels a potentially straightforward and cost-effective solution for decarbonizing existing vehicles and infrastructure. The ability to use e-fuels in current engines can lead to substantial reductions in CO_2 emissions without requiring a complete overhaul of the world's vehicle fleet or major investments into new technologies [23]. Furthermore, leveraging the existing fuel supply system is another crucial advantage offered by e-fuels. The infrastructure currently used for distributing and storing liquid fuels such as gasoline and diesel can be employed for e-fuels without major alterations [19]. This feature significantly reduces the costs associated with transitioning to a carbon-neutral transportation system compared to other options like electric vehicles which necessitate substantial investments in new infrastructure like charging stations [24]. E-fuels also serve as an efficient energy carrier due to their high energy density. They store considerably more energy per unit volume compared to batteries, making them particularly suitable for applications where weight and space are critical factors such as aviation or long-haul trucking. In these sectors where electrification is challenging due to technical constraints or economic reasons, e-fuels present an effective alternative solution. The ability of e-fuel production processes to harness surplus renewable energy effectively reducing waste is another key advantage [19]. During times when renewable power generation exceeds demand, such as on windy days or during peak sunlight hours. This excess power can be used efficiently by converting it into e-fuel rather than wasting it or overloading power grids. Moreover, unlike electricity stored in batteries which degrades over time if not used promptly, e-fuel does not suffer from this limitation [14]. This means that they can be stored over long periods without significant losses allowing seasonal storage of renewable energies providing flexibility when and where renewable energy is produced and consumed.

In conclusion, while there are challenges related to scaling up production processes for large-scale deployment and making them cost-competitive with fossil fuels; however considering various advantages they offer including compatibility with existing infrastructures & engines; suitability for sectors hard-to-electrify; high-energy density; capacity to store surplus renewable energies effectively reducing waste - it's evident that e-fuel holds considerable potential towards achieving our goals related climate change mitigation within hard-to-decarbonize sectors.

Hurdles in Realizing Feasible E-fuel Production and Utilization

While e-fuels offer numerous advantages, there are several hurdles that need to be addressed to realize their full potential in terms of production and utilization. Overcoming these challenges is crucial for the widespread adoption of e-fuels as a viable carbon-neutral energy solution. One significant hurdle lies in the economic feasibility of large-scale e-fuel production. Currently, the cost of producing e-fuels is relatively high

compared to conventional fossil fuels [23]. The high cost can be attributed to various factors such as the energy-intensive processes involved in their production, the need for substantial renewable electricity capacity, and the availability and cost-effective capture of CO_2 [25]. To make e-fuels economically competitive, advancements in technology and economies of scale are required.

Another hurdle is related to feedstock availability. Biomass-based e-fuel production relies on organic materials such as plant matter or agricultural waste [20]. However, ensuring a sustainable supply chain for biomass feedstock without causing negative environmental impacts like deforestation or competition with food crops presents a challenge [26]. Developing efficient and sustainable biomass sourcing strategies will be crucial for long-term viability.

Additionally, policy support plays a vital role in overcoming hurdles associated with market adoption. Implementing supportive policies such as carbon pricing mechanisms or incentives can help bridge the gap between the higher costs of producing e-fuels compared to conventional fuels [27]. Policy frameworks that promote research and development investments while encouraging private sector engagement can accelerate technological advancements necessary for cost reduction.

Lastly, public acceptance and awareness are essential factors influencing the successful implementation of e-fuel technologies. Educating consumers about the benefits of using carbon-neutral transportation fuels is crucial for driving demand. Public perception surrounding issues like sustainability concerns or misconceptions about biofuel feedstocks needs addressing through effective communication strategies.

While there are hurdles associated with realizing feasible large-scale production and utilization of e-fuels – including economic viability; feedstock availability; policy support; public acceptance - addressing these challenges through technological advancements, supportive policies frameworks along effective communication strategies will pave the way towards wider adoption.

E-fuels application in engines

E-fuels offer several unique advantages that position them as an attractive alternative to fossil fuels. Notably, they are compatible with existing internal combustion engines, which means that they can be used without significant modifications to current vehicle technologies or fueling infrastructure [24]. Moreover, e-fuels have high energy density compared to batteries making them suitable for applications where weight and space are critical factors such as aviation or long-haul trucking [15]. The performance of e-fuels in internal combustion engines has been a major focus of research. Studies have shown that e-fuels can deliver comparable or even superior performance to conventional fossil fuels [23]. Their high octane-number allows higher compression ratios and increased engine efficiency [12]. Moreover, due to their clean burning properties, they can reduce engine wear and extend engine life [24]. Efficiency is another critical aspect when considering e-fuels for engine applications. Due to their high energy density compared to other alternative fuels like hydrogen or electricity stored in batteries, they offer better range and payload capacity for vehicles [15].

E-fuels can be used in aviation to reduce emissions, especially in long flights where electrification is challenging. The present aviation business model favors larger planes with heavier payloads. The majority of aviation emissions are ascribed to long-distance flying, with approximately 27% assigned to medium haul (1500-4000 km) passenger flights, 27% attributed to long haul (>4000 km) passenger flights, and 19% allocated to freight flights [28]. Hydrogen-powered planes face comparable issues, requiring nearly four times the amount of fuel volume to power a plane than kerosene when stored optimally [29].

Porsche is in the forefront of global research on the implementation of e-fuels, specifically focusing on the development of renewable e-fuels using Methanol-to-Gasoline (MtG) technologies. Extensive study has been dedicated to incorporating these e-fuels into engine applications [30-32]. These studies indicate that e-fuels can achieve a significant decrease in particulate matter (PM) by up to 90%, hydrocarbons (HC) by 30%, and nitrogen oxides (NOx) by 20% compared to current European market fuels. Figure 6 illustrates the total concentration of particulate matter when utilizing Porsche's newly developed electronic fuel (POSYN) [33]. Evidently, POSYN demonstrates a substantial decrease in PM levels in comparison to RON98, a fuel extensively utilized in the European market. The findings underscore the possibility of achieving significant reductions in emissions through the use of synthetic fuels.

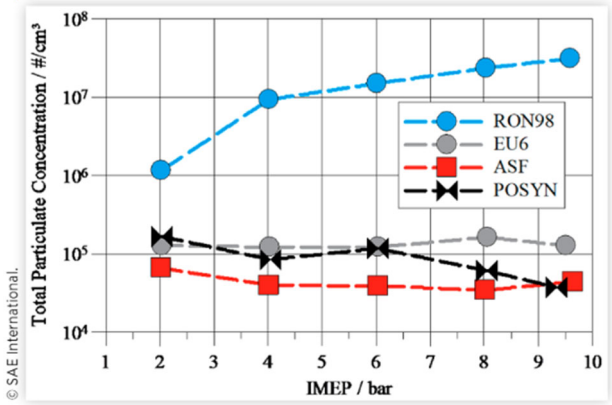

Figure 6: Total particulate concentration of the investigated fuels RON98, EU6, ASF and POSYN [33]

Multiple investigations were actively performed to harness the potential of e-fuels. We conducted a comparative analysis to examine the spray characteristics of e-methanol and diesel. The investigation showed that e-methanol has high evaporation characteristics, leading to increased penetration, as shown in Fig 7. Furthermore, we conducted experiments on dual fuel combustion,

utilizing diesel with e-methanol and e-ethanol, to investigate flame properties such as flame propagation speed and flame surface area. Figure 8 illustrates the visualization of combustion behavior during combustion.

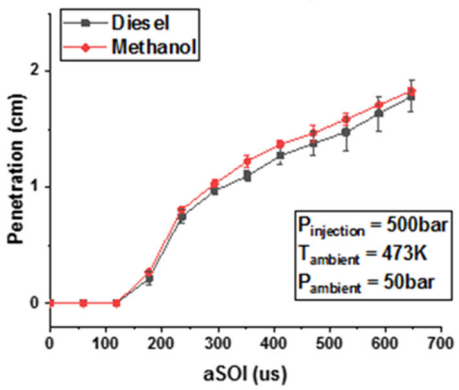

Figure 7: Penetration of e-methanol and diesel over time after start of injection

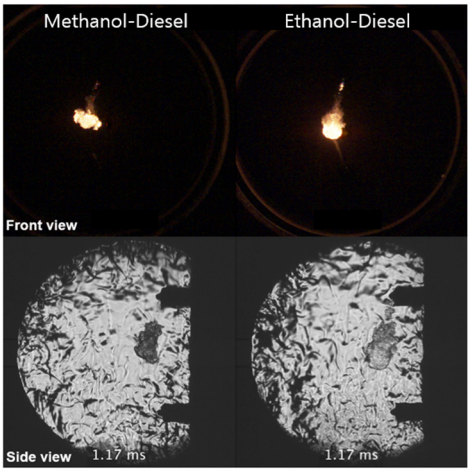

Figure 8: Visualization of combustion behavior in dual fuel combustion

In addition, a parametric analysis has been undertaken to optimize hydrogen internal combustion engines [34, 35]. Figure 9 illustrates the diagram of these engines. This study aimed to expand the lean limit of hydrogen, which is a crucial step in improving stratified hydrogen combustion. This method has resulted in significant enhancements in both efficiency and emission characteristics.

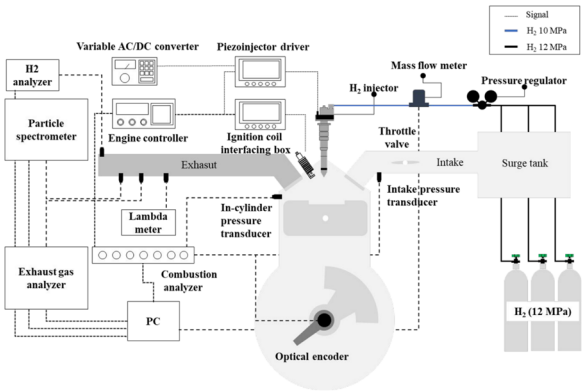

Figure 9: Experimental setup of a single cylinder hydrogen engine [34]

The application of e-fuels in engines presents a viable pathway towards reducing carbon emissions from transportation while maintaining high-performance standards. A few researches have been conducted in optimizing e-fuels engines, showcasing the adaptability and promise of these alternative fuels. The future of engine applications appears bright with the integration of e-fuels, and our ongoing work continues to support their adoption and further exploration in pursuit of a cleaner and more sustainable transportation future.

Summary

The urgency of mitigating climate change impacts has necessitated a global shift towards carbon-neutral energy solutions, with transportation being a sector of significant focus. Electric vehicles, while promising, have limitations that impede their applicability in certain areas such as aviation and heavy-duty trucking. E-fuels, synthetic hydrogen-based fuels produced using surplus renewable electricity, emerge as a viable alternative.

E-fuels are compatible with existing internal combustion engines and infrastructure, possess high energy density suitable for weight and space-sensitive applications, and provide an avenue to harness surplus renewable energy effectively reducing waste. However, challenges such as high production costs, technical hurdles related to fuel production and utilization, feedstock availability for biomass-based e-fuel production methods, policy support needs for market adoption facilitation and public acceptance exist.

This paper provided an overview of e-fuel's potential role in achieving carbon neutrality within the transport sector hard-to-decarbonize areas; its advantages over traditional fossil fuels; current hurdles that need overcoming for its widespread adoption; along with insights into research, focusing on optimizing e-fuel use in engines.

As we progress towards sustainable transport solutions under the shadow of climate change imperatives, continued research into optimizing these promising fuels within existing technologies is very important alongside supportive policy frameworks facilitating their wider adoption.

Acknowledgments

This research was supported by the Ministry of Science and ICT (MSIT) and the National Research Foundation of Korea (NRF) under Grant 2021R1A2C200871113.

References

[1] IEA, Net Zero by 2050 - A Roadmap for the Global Energy Sector, 2021
[2] IPCC, In Global Warming of 1.5°C, 2022, ISBN 978-1-00-915794-0
[3] United Nations Framework Convention on Climate Change (UNFCCC), THE PARIS AGREEMENT, 2016

[4] F. Creutzig, Transport Reviews, 36(3) (2016)341-360
[5] World Economic Forum, Industry Agenda Electric Vehicles for Smarter Cities: The Future of Energy and Mobility, 2018
[6] IEA, Global EV Outlook 2020 Entering the decade of electric drive, 2020
[7] B. Nykvist, M. Nilsson, Nature Climate Change, 5 (4) (2015) 329-332
[8] J. Neubauer, A. Pesaran, Journal of Power Sources, 196 (23) (2011) 10351-10358
[9] B.K.Sovacool, J.Axsen, Transportation Research Part A, 118 (2018) 730-746
[10] K.Lebeau, J.Van Mierlo, P.Lebeau, O.Mairesse, C.Macharis, Transportation Research Part D, 17 (8) (2012) 592-597
[11] C.Graves, S.D. Ebbesen, M.Mogensen, K.S. Lackner, Renewable and Sustainable Energy Reviews, 15 (2011) 1-23
[12] M. J. Palys, P.Daoutidis, Computers and Chemical Engineering165 (2022)
[13] D.B. Hartl, C.K. MSc, M. Jaensch, Proc. Vienna Motor Sym. 43 2022-39
[14] B.J. Alqahtani, D. Patiño-Echeverri, Appl. Energy 169 (2016) 927–936.
[15] A.W. Schäfer, S.R.H. Barrett, K. Doyme, L.M. Dray, A.R. Gnadt, R. Self, A. O'Sullivan, A.P. Synodinos, A.J. Torija, Nature Energy4 (2) (2019) 160-166
[16] Quéré et al., Earth System Science Data10, (4) (2141–2194) (20018).
[17] F. Creutzig, P. Agoston, J.C. Goldschmidt, G. Luderer, G. Nemet, R.C. Pietzcker, Nature Energy Vol2 (9) (2017)
[18] S. Szima, C.C. Cormos, Energies, 14 (5) (2021)
[19] M. Götz, J. Lefebvre, F. Mörs, A. McDaniel, Koch, F. Graf, S. Bajohr, R. Reimert, T. Kolb, Renewable Energy Vol85 (2016) 1371-1390
[20] A.V. Bridgwater, Biomass Bioenergy 38 (2012) 68–94.
[21] R.E.H. Sims, W. Mabee, J.N. Saddler, M. Taylor, Bioresource Technology Vol 101 (Issue6) (2010), p1570-1580
[22] M. Grahn, E. Malmgren, A.D. Korberg, M. Taljegard, J.E. Anderson, S. Brynolf, J. Hansson, I.R. Skov, T.J. Wallington, Progress in Energy 4 (3) (2022)
[23] Agora, The Future Cost of Electricity-Based Synthetic Fuels, 2018
[24] ICCT, Electric vehicle capitals: Accelerating the global transition to electric drive, 2017
[25] Global Alliance POWERFUELS, Powerfuels: Missing link to a successful global energy transition, 2021
[26] T. Searchinger, R. Heimlich, Science319 (5867) (2008) 1235-1238
[27] IRENA, Reaching zero with renewables: Eliminating CO2 emissions from industry and transport
[28] J. Peacock, R. Cooper, N. Waller, G. Richardson, International Journal of Hydrogen Energy (2023) 0360-3199
[29] Transport&Environment, Roadmap to decarbonizing European aviation, 2018
[30] M. Albrecht, H. Deeg, D. Schwarzenthal, P. Eilts, SAE Technical Paper 2020-37–0025
[31] J. Villforth, A. Kulzer, A. Weißhaar, H. Deeg, M. Bargende, SAE Technical Paper 2021-01–0632
[32] A. Kulzer., H. Deeg, J. Villforth., D. Schwarzenthal, M. Schilling, E. Barrientos, B. Kanach, M. Lindner, SAE Int. J. Adv. & Curr. Prac. in Mobility 2(4):1870–1892, 2020
[33] M. Albrecht, H. Deeg, D. Schwarzenthal, P. Eilts, SAE Technical Paper 2020-01–0285
[34] S. Lee, G. Kim, C. Bae, International Journal of Engine Research, 23 (5) (2022) 816-829
[35] S. Lee, G. Kim, C. Bae, Applied Thermal Engineering 209:118276, 2022

Catalytic pyrolysis of plastic polymer waste into fuel

Md. Azhar Uddin*
Graduate School of the Environmental, Life, Natural Science and Technology, Okayama University, Japan

Abstract

Pyrolysis of waste plastics into fuel represents a sustainable way for the recovery of the organic content of the polymeric waste and also preserves valuable petroleum resources in addition to protecting the environment. We studied the catalytic pyrolysis of polypropylene (PP)/polyethylene (PE)/polystyrene (PS)/poly(vinyl chloride) (PVC)/high impact polystyrene with brominated flame retardant (HIPS-Br) plastics mixed with poly(ethylene terephthalate) (PET) was performed at 430 ºC under atmospheric pressure using a semi-batch operation. The presence of PET in the pyrolysis mixture of PP/PE/PS/PVC/HIPS-Br affected significantly the formation of decomposition products and the decomposition behavior of the plastic mixture: (i) the yield of liquid product decreased and the formation of gaseous products increased; (ii) a waxy residue was formed in addition to the solid carbon residue; (iii) the formation of SbBr3 was not detected in liquid products; (iv) the yield of chlorinated branched alkanes increased as well as vinyl bromide and ethyl bromide were formed. The use of carbon composite (Ca-C) completely removed the chlorine and bromine content from the liquid products the Ca-C increased the yield of liquid products about 3–6 wt.%, as well as enhanced the gaseous product evolution and decreased the yield of residue. The halogen free liquid hydrocarbons can be used as a feedstock in a refinery or as a fuel.

We also studied effect of iron oxide carbon composite catalyst (Fe-C) for catalytic debromination process during pyrolysis of heating impact polystyrene (HIPS-Br) with various brominated flame retardants at 430ºC into fuel oil. Particularly, the effect of antimony oxide (Sb_2O_3: synergist) in HIPS-Br containing decabromo diphenyl oxide (DDO) and decabromo diphenyl ethane (DDE) as flame retardant was investigated. The thermal degradation of HIPS-Br produced various brominated hydrocarbons and also hydrobromic acid (HBr) in addition to various hydrocarbons. The presence of Sb_2O_3 (5 wt.%) decreased both the hydrogen bromide and brominated hydrocarbons by forming SbBr3 and produced high quantity of lower hydrocarbons (C_7–C_{11}).

Keywords: waste plastics, catalytic pyrolysis, fuel oil

1. Introduction

The feedstock recycling (conversion waste polymer into valuable products) was found to be a promising technique for the halogenated mixed plastics, among the various recycling methods for the waste plastics. The waste from electric and electronic equipment mostly consists of high impact polystyrene (HIPS), acrylonitrile – butadiene–styrene additives, e.g., flame retardants. The inherent flammability of plastic materials constitutes a fire hazard to users and in many cases, it is necessary to improve their resistance to ignition in order to comply with fire safety regulations or even to surpass them in the event they are inadequate. This is usually achieved by adding suitable flame retardants to the plastic matrix. Antimony oxide produces vapor-phase radical scavengers while used as a flame retardant. Antimony halides appear to form an important link in the radical scavenging cycle during flame retardancy. Antimony trioxide(Sb_2O_3) and pentoxide(Sb_2O_5) are used along with halogen flame retardant additives or halogenated polymers due to their synergistic interaction arising from the formation of antimony trihalide

A study has demonstrated the compatibility of brominated flame retardant plastics with feedstock recycling and energy recovery processes [1]. Uddin et al. [2] reported the thermal and catalytic decomposition of high impact polystyrene containing brominated flame retardant (HIPS-Br), which involved simultaneous debromination to produce halogen free liquid products, i.e., a potential fuel oil.

There is abundant literature on the fundamental investigation on the pyrolysis and chemical recycling of waste plastics [3–7]. The recent report [8] shows that the wide variety of polymers such as acrylonitrile–butadiene–styrene, polyethylene (PE), poly(ethylene terephthalate) (PET), poly(vinyl chloride) (PVC), polypropylene (PP), polystyrene (PS) including high impact polystyrene (HIPS), etc. have been found in the waste plastics from residential electronics recycling. The process concept and profitability study of halogen containing plastics has been reported by Kaufer and von Quast [9]. We have reported on the pyrolysis of HIPS-Br mixed with PP/PE/PS/PVC and the debromination by carbon composite of calcium carbonate (Ca-C) [10]. The effects of the presence of organic flame retardants such as decabromodiphenyl ether (DDO) or decabromo-diphenyl ethane (DDE) along with Sb2O3 on the pyrolysis of HIPS-Br are not well known

The present report discusses the pyrolysis studies of PET mixed with PP/PE/PS/ PVC/HIPS-Br plastics and the dehalogenation of liquid products with calcium carbonate carbon composite (Ca-C).

The effect of Sb_2O_3 on the thermal degradation of HIPS-Br containing DDO with Sb_2O_3, DDO without Sb_2O_3, DDE with Sb2O3, DDE without Sb_2O_3 and also the effect of iron oxide carbon composite (Fe-C) catalyst for the debromination process are reported.

* Corresponding author:
Phone: (+81) 86 2518897
Email: alazhar@cc.okayama-u.ac.jp

2. Results and Discussion

2.1 Catalytic Pyrosis of PP/PE/PS/PVC/HIPS-Br plastics mixed with PET on Calcium Carbonate Carbon Composite (Ca-C)

The pyrolysis of 3P/PVC/HIPS-Br plastics mixed with PET was carried out at 430 ºC under atmospheric pressure ia a semi-batch operation; the decomposition products and the yields are given in Table 1. The results of 3P/PVC/HIPS-Br decomposition in the absence of PET are also presented for comparison. The decomposition products were classified as oil, gas, and decomposition residue. As Table 1 shows, the thermal decomposition of 3P/PVC/HIPS-Br produced higher liquid yield than the thermal and catalytic decomposition of 3P/PVC/HIPS-Br/PET. The presence of PET in the plastic mixture has decreased the formation of gaseous products (17–13 wt.%) and increased the carbon residue (12–25 wt.%). It also produced a wax residue (2 wt.%), which was not observed during the thermal and catalytic decomposition of 3P/PVC/HIPS-Br [11].

Table 1

Yields and properties of liquid products of the thermal and catalytic (Ca-C) decomposition of PP/PE/PS/PVC/HIPS-Br mixed with PET at 430 °C

Sample	Ca-C (g)	Yield of degradation products (wt.%)				Liquid products	
		Liquid (L)	Gas[a] (G)	Residue (R)		Cnp[b]	Density (g cm^{-3})
				Carbon	Wax		
3P/PVC/HIPS-Br	–	71	17	12	0	13.7	0.82
3P/PVC/HIPS-Br and PET	–	60	13	25	2	11.4	0.80
3P/PVC/HIPS-Br and PET	4	63	20	17	0	11.2	0.80
3P/PVC/HIPS-Br and PET	8	66	21	13	0	11.7	0.80

Sample weight: PP: 3 g; PE: 3 g; PS: 2 g; PVC: 1 g; HIPS-Br: 0.5 g; PET: 0.5 g [3P = PE(3 g) + PP(3 g) + PS(2 g)].
[a] G = 100 − (L + R).
[b] Cnp: average carbon number of liquid products based on C-NP gram.

The Ca-C catalyst has been applied for the dehalogenation of liquid products during the pyrolysis of 3P/PVC/HIPS-Br mixed with PET. It was observed that the catalytic decomposition produced higher liquid yields than the thermal decomposition and it also increased the yield of gaseous products (Table 1). Fig. 1.1 shows the dehalogenation efficiency of Ca-C catalyst. The thermal and catalytic decomposition of 3P/PVC/HIPS-Br clearly shows that the use of Ca-C (4 g) completely removed the halogen content and produced halogen free liquid products [11].

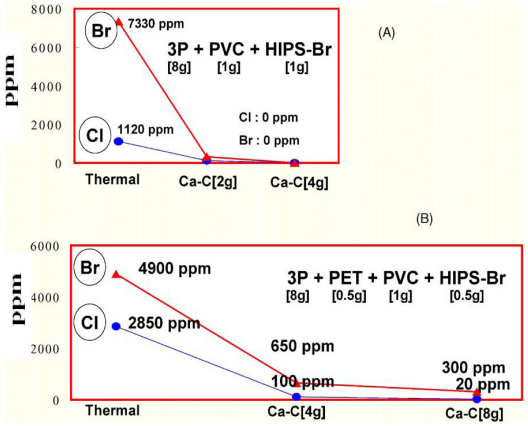

Fig.1.1 Effect of Ca-C on the dehalogenation of 3P/PVC/HIPS-Br (A) and 3P/PVC/HIPS-Br with the addition of PET (B) [3P = PE(3 g) +PP(3 g) + PS(2 g)].

However, the addition of PET to 3P/PVC/HIPS-Br reduced the dehalogenation efficiency of the catalyst and the same amount of Ca-C could not remove completely the halogen content (Cl, Br) from the liquid products (Fig. 2B). The use of 4 g Ca-C decreased the bromine content from 4900 to 650 ppm and the chlorine content from 2850 to 100 ppm. To remove the total halogen content from the liquid products, 8 g Ca-C was used during the decomposition; still the liquid products contained 300 ppm of bromine and 20 ppm of chlorine. It is evident from Fig. 2B that Ca-C could not completely remove the halogen content of 3P/PVC/HIPS-Br in the presence of PET.

Fig. 1.2 shows the chlorine and bromine compounds formed during the pyrolysis of 3P/PVC/HIPS-Br plastics with and without the addition of PET. It is evident from Fig. 1.2 that there are distinct halogenated organic compounds produced in the presence PET.

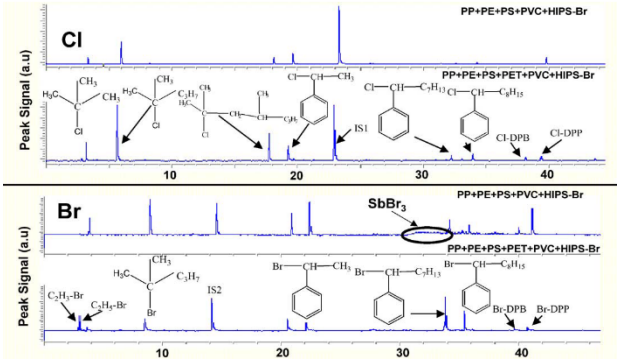

Fig. 1.2. GC–AED selective analysis of bromine and chlorine compounds of the pyrolysis liquid of 3P/PVC/HIPS-Br with and without the addition of PET
[3P = PE(3 g) + PP(3 g) + PS(2 g)] IS1 and IS2: internal standards 1,2,4-trichlorobenzene and 1-bromohexane. Cl-DPB: 2-chloro-2,4-diphenylbutane;
Cl-DPP: 2-chloro-2,4-diphenylpentane; Br-DPB: 2-bromo-2,4-diphenylbutane; Br-DPP: 2-bromo-2,4-diphenylpentane.

The main chlorine-containing products are monochlorinated branched alkanes (2-chloro-2-methylpropane, 2-chloro-2- methylpentane, and 2-chloro-2,4-dimethylheptane). These compounds are derived from PP decomposition products by the addition of HCl released during PVC pyrolysis. It is noted that the tertiary carbon atoms of PP products are more prone to Cl addition than the secondary C-atoms of *n*-alkenes and *n*-alkadienes, which are the main unsaturated products of PE pyrolysis. Thus, chlorinated *n*-alkanes are not formed in discernible amount. HCl also reacts with styrene monomer and dimer resulting in significant amount of 1-chloro-ethylbenzene and a smaller amount of chlorinated diphenyl butane and pentane.

Fig. 1.3 shows the carbon number distribution of the liquid hydrocarbon products (C-NP gram) obtained during the thermal decomposition and the thermal decomposition followed by catalytic dehalogenation of 3P/PVC/HIPS-Br plastics mixed with PET. These values were obtained by plotting the weight % of hydrocarbon compounds [g(C_n) × 100/g(oil) wt.% from GC–FID] in the product oil against the carbon number of normal paraffins. As Fig. 1.3 illustrates, the hydrocarbon distribution has a big peak at C9 which includes the major

polystyrene decomposition products (styrene and ethyl benzene) as well as 2,4-dimethyl-1-heptene representing the main polypropylene product (trimer).

Fig. 1.3. C-NP gram of liquid products obtained during the pyrolysis of 3P/PVC/HIPS-Br mixed with PET at 430 ◦C [3P = PE*(*3 g*)* + PP*(*3 g*)* + PS*(*2 g*)*].

The Ca-C catalyst does not have marked effect on the hydrocarbon distribution. The small decrease in the formation of liquid products with *n*-C7to *n*-C10 was observed with the use of Ca-C, while the average carbon number and the density of the liquid did not change significantly (Table 1).

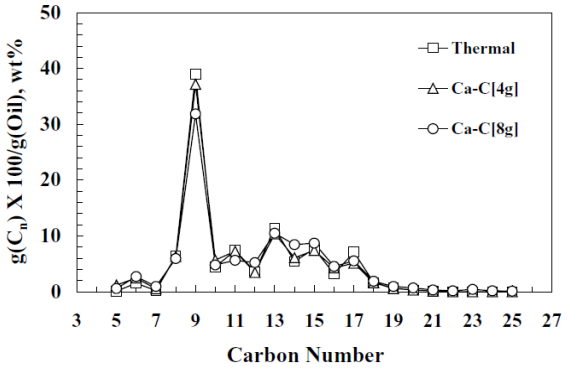

Fig. 1.3. C-NP gram of liquid products obtained during the pyrolysis of 3P/PVC/HIPS-Br mixed with PET at 430 ◦C [3P = PE*(*3 g*)* +PP*(*3 g*)* + PS*(*2 g*)*].

In comparison with the experiment on 3P/PVC/ HIPS-Br, it can be established that the addition of PET to 3P/PVC/HIPS-Br altered the properties of liquid products, i.e., the average carbon number (Cnp) and the density of liquid products have decreased (Table 1).

Analogous to a C-NP gram approach, Br-NP gram (Fig. 4) and Cl-NP gram (Fig. 1.4) showed the volatility distribution of bromine and chlorine compounds in the liquid products.

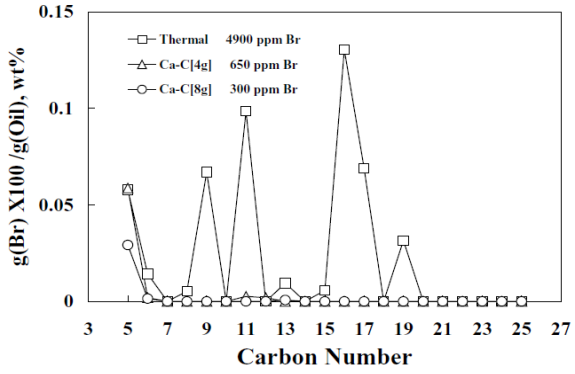

Fig. 1.4. Br-NP gram of liquid products obtained during the pyrolysis of 3P/PVC/HIPS-Br mixed with PET at 430 ◦C [3P = PE*(*3 g*)* +PP*(*3 g*)* + PS*(*2 g*)*].

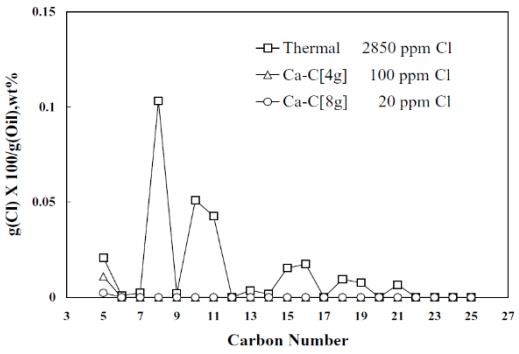

Fig. 1.5. Cl-NP gram of liquid products obtained during the pyrolysis of 3P/PVC/HIPS-Br mixed with PET at 430 ◦C [3P = PE*(*3 g*)*+PP*(*3 g*)*+PS*(*2 g*)*].

2.1 Effect of Sb_2O_3 on DDO and DDE(Flame Retardants) Containing Brominated Heating Impact polystyrene (HIPS-Br) and Debromination of the Pyrolysis Liquid Products by Iron Oxide Carbon Composite Catalyst (Fe-C)

Pyrolysis of heating impact polystyrene (HIPS) containing various brominated flame retardant plastics were performed in thermal and also in the presence of Fe-C catalyst with vapor phase contact. The pyrolysis of plastic was performed in a glass reactor (length: 35 cm; i.d.: 3 cm) under atmospheric pressure by batch operation under identical experimental conditions and temperature program shown in Fig. 2.1.

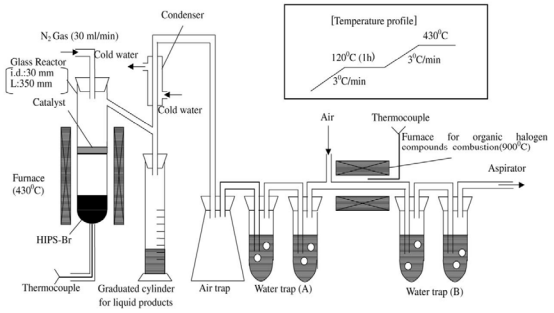

Fig. 2.1. Schematic experimental setup for heating impact polystyrene (HIPS) containing DDO and DDE flame retardants at 430 ºC

The heating impact polystyrene (HIPS) containing DDO and DDE flame retardants was used for the degradation process. The structure of the flame retardants (DDO and DDE) is shown in Fig. 2.2. The details of the samples and their symbols used in the present study are given in Table 1.

The thermogravimetric analysis (TGA) of DDO-Sb(5), DDO-Sb(0), DDE-Sb(5) and DDE-Sb(0) was performed and the thermograms are presented in Fig. 2.3. As can be seen from Fig. 2.3 that the degradation temperature of plastic sample depends on the type of flame retardant present and synergist in it. The residue amount is less than 5 wt.% for all four plastic samples examined.

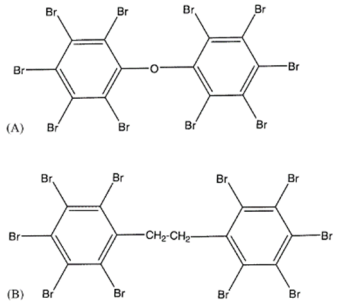

Fig. 2.2. The structure of flame retardants added to the heating impact polystyrene.

Table 2.1

Bromine content and Sb_2O_3 content in heating impact polystyrene (HIPS-Br) with various brominated flame retardant samples and their codes

Sample code	Flame retardant	Sb_2O_3 content (wt.%)
DDO-Sb(5)	Decabromo diphenyl oxide with Br content 10.8 wt.%	5
DDO-Sb(0)	Decabromo diphenyl oxide with Br content 10.8 wt.%	0
DDE-Sb(5)	Decabromo diphenyl ethane with Br content 10.7 wt.%	5
DDE-Sb(0)	Decabromo diphenyl ethane with Br content 10.7 wt.%	0

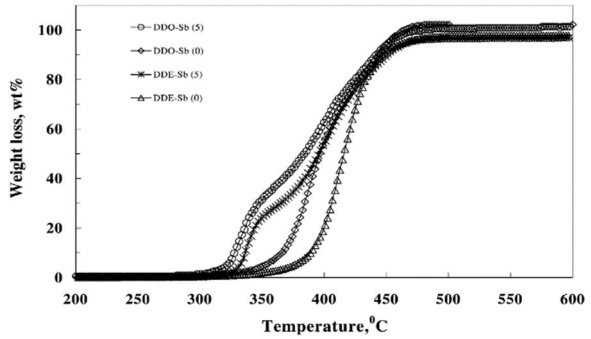

Fig. 2.3. Thermogravimetric analysis of DDO-Sb(5), DDO-Sb(0), DDE-Sb(5), and DDE-Sb(0).

The yield of degradation products and the properties of liquid products were tabulated in Table 2. Table 2 shows the yield of liquid products during thermal degradation of above four samples were in the range of 68 wt.% (DDE-Sb(5)) to 72 wt.% (DDO-Sb(0)). The yield of gaseous products was comparatively less with DDO-Sb(5), DDE-Sb(5) pyrolysis than DDO-Sb(0), DDE-Sb(0) pyrolysis. However, there is no appreciable change in the residue during the pyrolysis of above four samples.

It is interesting to note that the presence of Sb in the plastic sample decreased the average carbon number (Cnp) and increased the density due to the presence of $SbBr_3$ compound in the liquid products (Table 2.2). The total bromine content about 11.5 wt.% was found in liquid products during the degradation of DDO-Sb(5) and 3.80, 11.3 and 1.63 wt.% during DDO-Sb(0), DDE-Sb(5) and DDE-Sb(0), respectively. It is clear from Table 2 that the presence of Sb in plastic sample produced more bromine content in liquid products.

Table 2.2

Products yield and properties of liquid products during thermal degradation of various HIPS samples at 430 °C; weight of sample: 10 g

Sample code	Yield of degradation products (wt.%)			Liquid products		Total Br in liquid (organic:inorganic) (wt.%)
	Liquid, L	Gas, G[a]	Residue, R	Cnp[b]	Density (g/cm^3)	
DDO-Sb(5)	72	4	23	12.5	1.03	11.5 (8:92)
DDO-Sb(0)	67	10	23	13.9	0.93	3.80 (100:0)
DDF-Sb(5)	69	5	26	12.4	1.02	11.3 (12:88)
DDE-Sb(0)	68	12	20	13.8	0.93	1.63 (100:0)

[a] G = 100 − (L + R).
[b] Cnp: average carbon number of liquid products based on C-NP gram.

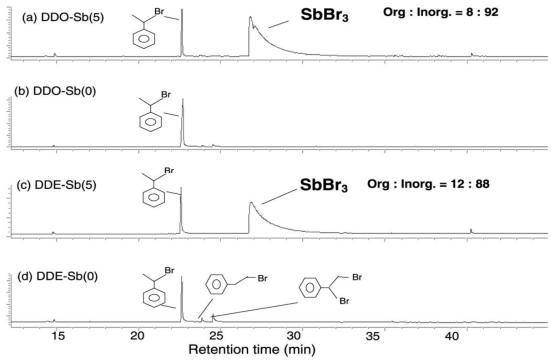

Fig. 2.4. GC-AED chromatograms of selective bromine compounds during the pyrolysis of DDO-Sb(5), DDO-Sb(0), DDE-Sb(5), andDDE-Sb(0).

Figure 2.4 shows the identification of various brominated hydrocarbons in liquid products. The presence of $SbBr_3$ in the liquid products during the pyrolysis of Sb containing samples such as DDO-Sb(5) and DDE-Sb(5) is due to the reaction of hydrogen bromide with the antimony oxide. The formation of SbBr3 in our present study is in well agreement with the earlier studies on thermal degradation of polyester flame-retarded with antimony oxide/brominated polycarbonate [10].

The hydrocarbons are distributed only in the two regions such as C_7–C_{11} and C_{16}–C_{20} and very few hydrocarbons were observed during C25 carbon number as shown in Fig. 2.5. The polystyrene is the main polymer in DDO-Sb(5), DDO-Sb(0) DDE-Sb(5), and DDE-Sb(0) and it produced the styrene monomer in large proportion. As can be seen from Fig. 5 that the presence of Sb in plastic samples such as DDO-Sb(5) and DDE-Sb(5) facilitated the formation of higher liquid products in C_7–C_{11} range with higher proportion, the plastics samples without Sb such as DDO-Sb(0), DDE-Sb(0) produced higher liquid products in C_{16}–C_{20} range.

Fig.2. 5. C-NP gram of liquid products obtained during the pyrolysis of DDO-Sb(5), DDO-Sb(0), DDE-Sb(5), and DDE-Sb(0).

The weight percent of brominated hydrocarbons are presented in a Br-NP gram in Fig. 2.6. The majority of hydrocarbons containing the bromine were distributed in the range of C11–C13. The major bromine compound

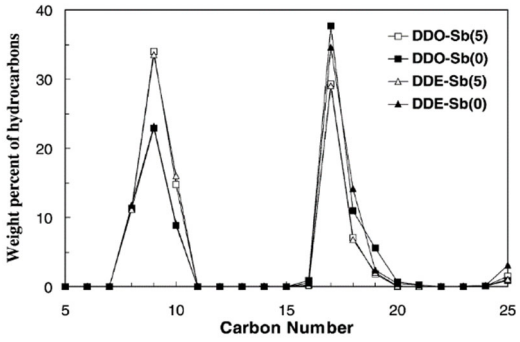

observed in the liquid products was the 1-bromo-1-benzyl ethane and very small quantities of 1-bromo-2-benzyl ethane and 1,2-dibromo-1-benzyl ethane were identified.

The distribution of bromine in other degradation products such as residue, inorganic gas such as HBr (water trap A in Fig. 2.1), organic gas (water trap B in Fig. 2.1), was determined and the results were presented in Fig. 2.7.

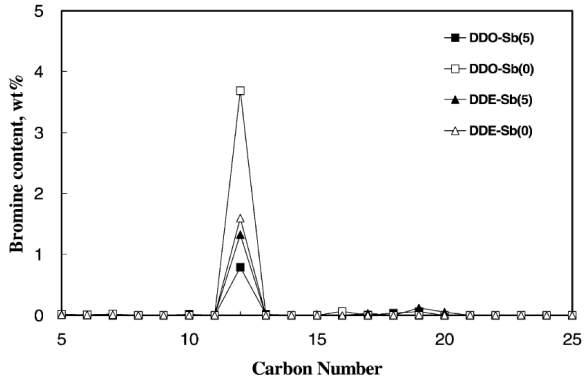

Fig. 2.6. Br-NP gram of liquid products obtained during the pyrolysis of DDO-Sb(5), DDO-Sb(0), DDE-Sb(5), and DDE-Sb(0

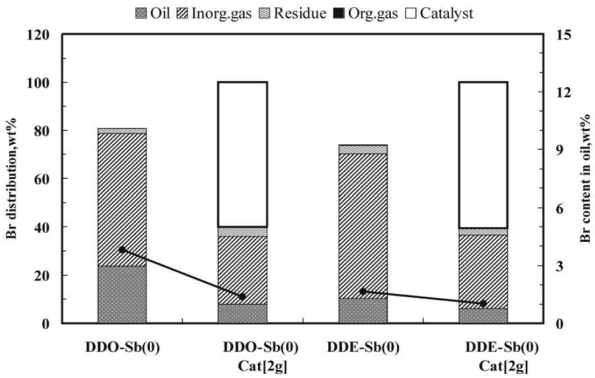

Fig. 2.7. The distribution of Br content in various degradation products obtained during the thermal degradation of DDO-Sb(5), DDO-Sb(0), DDE-Sb(5), and DDE-Sb(0).

The liquid products produced during the pyrolysis of DDO-Sb(5) contained about 76 wt.% of total bromine and DDO-Sb(0), DDE-Sb(5) and DDE-Sb(0) liquid products contained 24, 72, 10 wt.% of total bromine, respectively. The DDO-Sb(5), and DDE-Sb(5) produced the more halogen content in liquid products in the form of SbBr3 (Table 2.2 and Fig. 2.4) and DDO-Sb(0), and DDE-Sb(0) produced the more hydrogen bromide (HBr) in the ion-exchanged water trap about 55 and 60 wt.%, respectively. The gaseous products, which are not condensed as liquid products, were passed through the high temperature furnace (900 ◦C) with the aspirator. During this, the gaseous halogenated organic compounds (if any) were converted into halogenated inorganic compounds, which were then passed through the ion-exchanged water trap to capture as HBr (Fig. 2. 1) and this was considered as organic gas. Very small amount (ca. 0.2 wt.%) of bromine compound in organic gas was observed in all the four samples examined during the present study. In addition, the bromine content in the residue of DDO-Sb(5), DDE-Sb(5) was 5.5 and 5 wt.%, respectively and DDO-Sb(0), and DDE-Sb(0) residues contain 2.2 and 3.5 wt.%, respectively (Fig. 2.7).

It clearly shows the presence of more halogen content in the residue of Sb containing samples. The presence of organic and inorganic bromine in the liquid products cannot permit to use for further applications such as fuel oil or feedstock in refinery. The debromination of liquid products is an essential step to produce the halogen free liquid products to use as a fuel.

The pyrolysis of DDO-Sb(5), DDO-Sb(0), DDESb(5) and DDE-Sb(0) was performed using iron oxide carbon composite catalyst (Fe-C) for the debromination process to produce the halogen free liquid products. The debromination effect by Fe-C catalyst for DDO-Sb(0), and DDE-Sb(0) was performed and the distribution of bromine in various pyrolysis products are presented in Fig. 2.8 and compared with the thermal degradation. Fig. 2.8 shows the decrease of bromine content in liquid products from 24 to 8 wt.% during the pyrolysis of DDO-Sb(0) with Fe-C (2 g) catalyst. In a similar way the bromine content decreased in liquid products from 10 to 6 wt.% during DDE-Sb(0) pyrolysis.

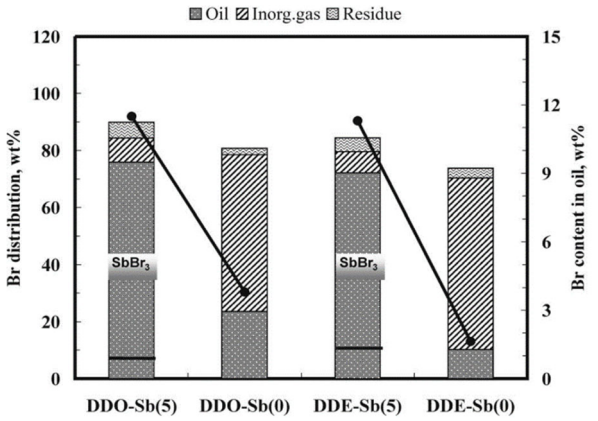

Fig. 8. The distribution of Br content in degradation products of DDO-Sb(0), and DDE-Sb(0) with Fe-C catalyst.

The use of Fe-C (2 g) catalyst also decreased the HBr formation from 55 to 28 wt.% during DDO-Sb(0) pyrolysis and from 60 to 30 wt.% during DDE-Sb(0) pyrolysis. The debromination effect by Fe-C catalyst for DDO-Sb(5), and DDE-Sb(5) was performed and the distribution of bromine content in various degradation products were presented in Fig. 2.9 and compared with the thermal degradation. Fig.2.9 shows the decrease of bromine content in liquid products from 72 to 2 wt.% during DDE-Sb(5) pyrolysis.

The C-NP gram of liquid products obtained during the DDO-Sb(5) degradation with 2 and 8 g of Fe-C catalyst were presented in Fig. 10.2. It is clear from Fig. 10that the use of Fe-C catalyst during the degradation process facilitated the formation of high quantity of lower

hydrocarbons (C_7–C_{11}) by cracking the higher hydrocarbons (C_{16}–C_{20}).

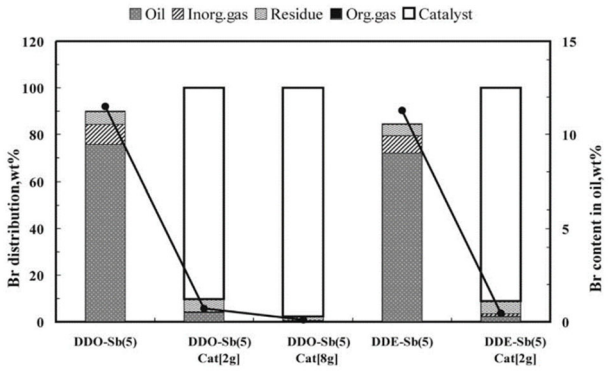

Fig.2. 9. The distribution of Br content in degradation products of DDO-Sb(5), and DDE-Sb(5) with Fe-C catalyst.

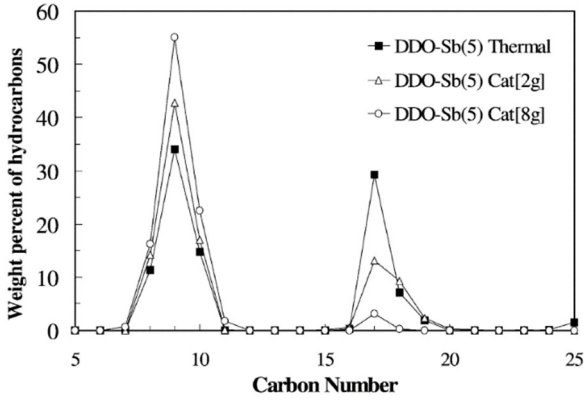

Fig. 10. C-NP gram of liquid products obtained during the thermal degradation of DDO-Sb(5) and also in the presence of Fe-C catalyst.

3. Conclusions

In the catalytic pyrolysis of 3P(PE, PP,PS)/PVC/ HIPS-Br and PET with Calcium carbonate carbon composite catalyst The yield of chlorinated branched alkanes increased significantly, which were formed apparently from the pyrolysis products of PP via HCl addition. The formation of brominated alkenyl benzenes was enhanced, which are obviously brominated mixed products of PS and PP decomposition. Furthermore, vinyl bromide and ethyl bromide were evolved, which appear to be formed from the ethylene segments of PET via bromination reactions. The formation of $SbBr_3$ was hindered and the yield of liquid products was decreased from 3P/PVC/HIPS-Br in the presence of PET. The use of Ca-C removed more than 94% of the bromine and more than 99% of the chlorine content of the liquid during the pyrolysis of 3P/PVC/HIPS-Br mixed with PET.

In the pyrolysis of heating impact polystyrene (HIPS-Br) with various brominated flame retardants and Sb2O3 at 430 ◦C into fuel oil: various brominated hydrocarbons were produced in liquid products in addition to hydrogen bromide. The presence of antimony decreased the formation of various brominated hydrocarbons with the formation $SbBr_3$ in liquid products. The use of Fe-C catalyst drastically decreased the bromine content in liquid products. The presence of Sb in the plastic samples facilitated the formation high quantity of lower hydrocarbons than the plastic samples without Sb.

4. Acknowledgments

The author gratefully acknowledges the direct contribution of the following authors and his colleagues in this research:

·Emeritus Professor Yusaku Sakata of Okayama University, Japan.

·Dr. Thallda Bhaskar, Catalytic Conversion Process Division (CCPD), Indian Institute of Petroleum (IIP), Dehradun, India.

·Dr. Emma Jakab, Research Laboratory of Materials and Environmental Chemistry, Chemical Research Center, Hungarian Academy of Sciences, Hungary·

·Dr. Mihai Brebu, Petru Poni Institute of Macromolecular Chemistry, Iasi, Romania.

5. References

[1] T. Imai, S. Hamm, K.P. Rothenbacher, Environ. Sci. Technol. 37 (2003) 652.
[2] M.A. Uddin, T. Bhaskar, J. Kaneko, A. Muto, Y. Sakata, T. Matsui, Fuel 81 (2002) 1819.
[3] H. Bockhorn, A. Hornung, U. Hornung, P. Jakobstroer, M. Kraus, J. Anal. Appl. Pyrol. 49 (1999) 97.
[4] M.A. Uddin, K. Koizumi, K. Murata, Y. Sakata, Polym. Degrad. Stab. 56 (1997) 37.
[5] Y. Sakata, M.A. Uddin, A. Muto, M. Narazaki, K. Koizumi, K. Murata, K. Mitsuo, Ind. Eng. Chem. Res. 37 (1998) 2889.
[6] M. Blazso, E. Jakab, J. Anal. Appl. Pyrol. 49 (1999) 125.
[7] A. Pifer, A. Sen, Angew. Chem. Int. Ed. 37 (1998) 3306.
[8] Report of American Plastics Council Inc., April 2000.
[9] H. Kaufer, O. von Quast, Kunstsoffe 87 (1997) 190.
[10] T. Bhaskar, T. Matsui, J. Kaneko, M.A. Uddin, A. Muto, Y. Sakata, Green. Chem. 4 (2002) 372.
[11] K.S. Betts, Env. Sci. Tech. (2001) 274A.

Invited Contributions: Plenary Lecture 3
B. Z. Dlugogorski and A. R. Masri, Eds

Towards Clean Combustion and Decarbonisation
Proceedings of the Australian Combustion Symposium
26 – 29 November 2023, Darwin, Northern Territory, Australia

Models for hydrogen safety and reliability

F. Salehi[1, *]
[1]School of Engineering, Macquarie University, NSW 2109 Australia

Abstract

This paper aims to provide an overview of hydrogen safety aspects and risk assessment methods including computational fluid dynamics methods and quantitative risk assessment techniques. Hydrogen and hydrogen vectors have great potential to assist with the decarbonisation of different sectors, particularly those sectors which are difficult for direct electrification. It is an effective solution to store and export renewable energies. It can be also used to generate heat and electricity with zero greenhouse gas emissions. The widespread adoption of hydrogen technologies faces safety and reliability challenges such as hydrogen dispersion, fire, and explosion. To meet the requirements for scaling clean hydrogen a holistic approach is required (i) to enhance the physical understanding of hydrogen dispersion, fire, and explosion, (ii) to develop predictive fast computational fluid dynamics models, and (iii) to create engineering tools for risk assessment. The integration of the generated knowledge and developed tools accelerates the development of codes and standards, improving safety measures for future hydrogen infrastructure. It also helps with developing more reliable and cost-effective tools for smart asset integrity management of hydrogen facilities, reducing the operation and maintenance costs.

Keywords: hydrogen safety, hydrogen fire and explosion, hydrogen storage and delivery, computational fluid dynamics (CFD)

1. Introduction

The global energy landscape is still heavily reliant on fossil fuels which account for 83% of the world's energy demand. The production and use of fossil fuels are associated with particulate and greenhouse gas emissions, which contribute to global warming and cause serious health issues. With the growing population and increasing energy demand, reliance on fossil fuels has become a significant challenge from not only an environmental perspective but also energy and fuel security point of view. Hence, there has been an increasing demand for scaling renewable energies such as clean hydrogen which has emerged as a promising solution for facilitating the expansion of renewable energy sources [1].

Expanding the production and utilisation of clean hydrogen in different sectors necessitates thorough strategic planning to tackle various issues that directly impact the cost of hydrogen. Among these crucial issues, safety concerns stand out as a key barrier, hindering the widespread adoption of hydrogen in industries [2]. To enhance the safety and reliability of hydrogen systems and infrastructure, it is required to understand what may go wrong, how often it may happen, and what the consequences are if something goes wrong. A thorough analysis of these steps provides a reliable risk assessment, helping to minimise the likelihood of an accident and/or to reduce the impact of an accident (see Fig. 1). Currently, there is a lack of undegrading about the primary causes and factors that contribute to hydrogen incidents and accidents. This is due to the lack of data and uncertainties about the suitability of the existing dynamic risk models for hydrogen systems. Another key challenge is the lack of reliable tools for consequence modelling which are critical to develop strategies that minimise the impact of an accident within hydrogen facilities. The former necessitates improvement in data collection and probabilistic dynamic risk models while the latter demands enhancing the fundamental understanding of hydrogen dispersion, fire, and explosion. While various aspects of these critical phenomena have been studied by the combustion research community, there is still a lack of tools to transfer the developed knowledge for the safety and reliability analysis of hydrogen facilities. Hence, this paper aims to provide an overview of hydrogen risk components and the developed models to address the safety concerns in the production, transportation, and application of hydrogen, enabling scaling clean hydrogen.

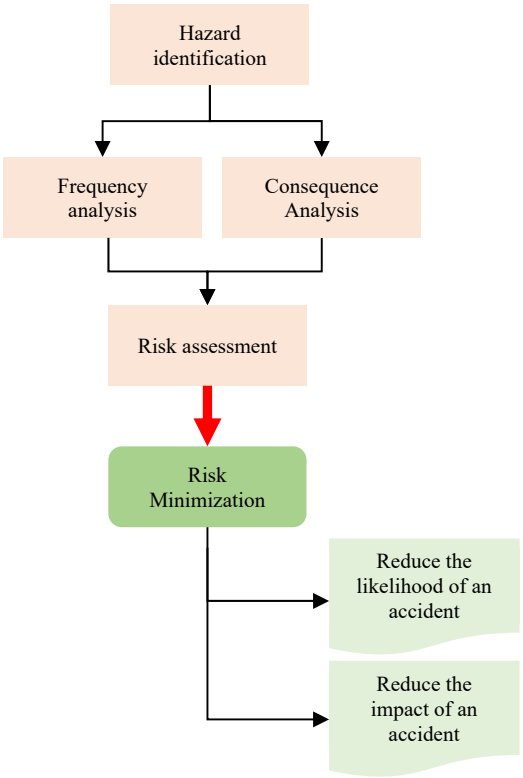

Fig. 1. Schematic view of risk assessment.

* Corresponding author:
Phone: (+61) 2 98507303
Email: fatemeh.salehi@mq.edu.au

2. An overview of hydrogen economy

The concept of hydrogen economy explores the pathways that hydrogen is the primary energy carrier. It includes four main interrelated phases: production, storage, utilisation, and safety [3]. This section provides a brief overview of production, storage, and utilisation phases while hydrogen safety is discussed in more detail in Sections 3 and 4.

Clean hydrogen can be produced either via thermochemical or electrochemical processes. The thermochemical methods employ carbon-based fuels such as fossil fuel feedstock which is a traditional way to produce hydrogen (e.g. steam methane reforming and coal pyrolysis). Once the process is combined with carbon capture and storage techniques, it yields clean hydrogen production (known as blue hydrogen). In contrast, the electrochemical process entails the separation of water into hydrogen and oxygen by utilising an electrical current which is produced using renewable energies such as solar and wind resources (it is known as green hydrogen). In some countries, the production of hydrogen using nuclear power is also considered clean since it does not produce CO_2 emissions. There is also interest in other clean hydrogen methods including methane pyrolysis to produce hydrogen and solid carbon from methane as well as biohydrogen using fermentation technologies. However, the technologies for these methods are still developing and they are not suitable for scaling hydrogen production.

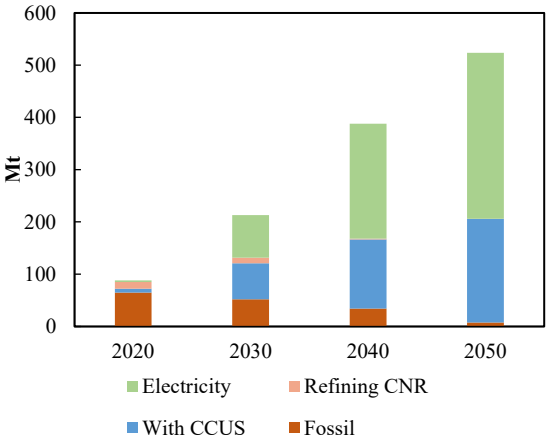

Fig. 2. Hydrogen production [4]. Refining CNR refers to hydrogen by-products from catalytic naphtha reforming at refineries.

The current worldwide annual hydrogen production is approximately 90 million metric tonnes (Mt), with the vast majority, around 79%, originating from natural gas or coal that is predominantly utilised in activities such as oil refining and fertiliser production (see Fig. 2). Around 3.9% of the worldwide demand for hydrogen is met through water electrolysis [5]. The remaining is a byproduct of processes initially designed for other purposes within refineries. Shifting to electrolysis-based hydrogen production would necessitate a capacity of more than 1,000 gigawatts of electrolysers, which surpasses the entire electricity generation capacity of the European Union at present. Hence, it may be concluded that scaling different methods of clean hydrogen production should be promoted to achieve global targets for hydrogen and its vectors by 2050 [4].

The storage of hydrogen could be in the forms of compressed gas, liquid hydrogen, slush, as well as solid or metallic hydrogen. The diversity of storage options is a key advantage of hydrogen, offering a practical pathway to store excess renewable energies such as solar and wind. The available hydrogen storage technologies can be classified into physical storage technologies and material-based storage systems. Within the physical storage methods, hydrogen is typically stored as either a liquid, in a cold/cryo-compressed form, or as a compressed gas.

As shown in Fig 3, while hydrogen has a high energy density, its volumetric energy density is very low and hence it is required to be stored in the form of either liquid or compressed gas. Compressed hydrogen is the most commonly used storage method, particularly for onboard storage systems such as hydrogen fuel cell vehicles. It offers a great release ratio and rapid filling. However, currently, there is a lack of infrastructure and refuelling stations which are hindered due to safety concerns, unclear codes and regulations, and public acceptance. On the other hand, liquid and cryogenic hydrogen offer a better storage capacity at a rate of 0.07 kg per litre which is approximately 2.33 times more than compressed hydrogen [6]. However, hydrogen liquefication is carried out at extremely low temperatures (less than - 253◦C), and it is challenging to maintain such a low temperature. The process is expensive with 40% energy loss which is much higher than the energy loss rate of 10% reported for compressed hydrogen [7].

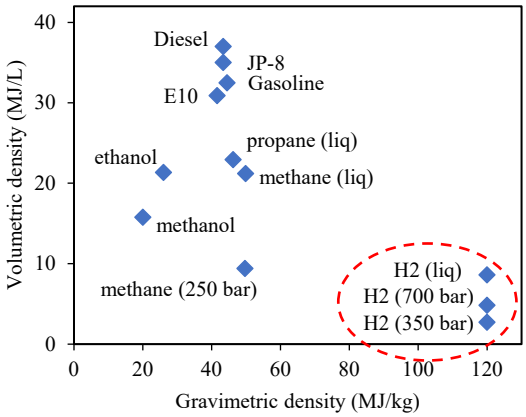

Fig. 3. Hydrogen properties compared to other fuels.

Material-based storage technologies can be divided into two primary subgroups: physical sorption/ physisorption and chemical sorption/ chemisorption [6]. Some of these methods could offer higher storage capacities and they are operating under moderate temperature and pressure conditions, providing a safer option compared to physical storage technologies. However, they are currently expensive and further research is still required.

Hydrogen can be used for a wide range of applications. Conventional applications of hydrogen are as raw materials in different industrial processes such as oil refining, chemical processes, and producing fertilisers. In recent years, there has been a significant interest in using hydrogen in the mobility sector and for electricity

generation and grid stability. Through thermodynamic means, hydrogen can be used in internal combustion devices using different strategies. The combustion of pure hydrogen or a mixture of hydrogen and natural gas in gas turbines has been widely studied which could be a suitable backup option to support green electricity generation. Hydrogen and hydrogen mixture can be also used in spark ignition and compression ignition engines to reduce the consumption of fossil fuels and consequently assist with the energy transition. There are also electromechanical/ electrochemical means to utilise hydrogen in different applications using hydrogen fuel cells. These processes generate water, heat, and electricity. Compared with hydrogen combustion, fuel cell systems exhibit superior efficiency, reduced emissions, and operate without producing vibrations while they are still expensive.

Finally, clean hydrogen can change the current dynamic of fuel markets. It enables exporting of renewable energies such as solar and wind. It will provide significant trading opportunities, particularly for Australia due to its strategic geographical location which is in close proximity to key Asian markets such as Japan, South Korea, and China. These countries are committed to net-zero targets by 2050 while they do not have the same hydrogen production capacity as Australia. The estimation shows Australia's hydrogen export by 2040 would be between 0.62 and 3.2 Mt. The growth of the clean hydrogen market will also increase demands for minerals such as nickel which is used in electrolysis. This will provide significant indirect economic benefits for Australia which is currently the fourth largest producer of nickel.

3. Hydrogen safety concerns

Despite relatively the small number of hydrogen projects, numerous accidents and incidents have occurred within hydrogen infrastructures. Historical data is critical to enhance the safety and reliability of the hydrogen facilities. H2Tools is an online portal which is managed by the Center for Hydrogen Safety in the US to collect data relevant to hydrogen accidents and incidents around the world. 221 accidents and incidents recorded up to July 2023. The reported data confirms that 68.33% of accidents occurred in storage, followed by 19.46% in production and 12.22% during delivery [8]. The majority of the reported accidents occurred during operations, followed by maintenance and inspection. Focusing on the cases where the hydrogen leakage was confirmed, it is found that 32% of them resulted in fire incidents, followed by explosions (30%), while only hydrogen leakages account for 28% of the incidents (Figure 4).

The reported data further confirms that ensuring safety is a crucial requirement in the planning, functioning, and operating of hydrogen facilities systems to safeguard assets, and preserve the well-being of employees and the safety of the surrounding community [9]. While the community has established a wealth of knowledge and best practices to handle gaseous and liquid fuels such as methane and propane, due to the unique characteristics of hydrogen, existing models, standards and code required to be reviewed and then accordingly revised.

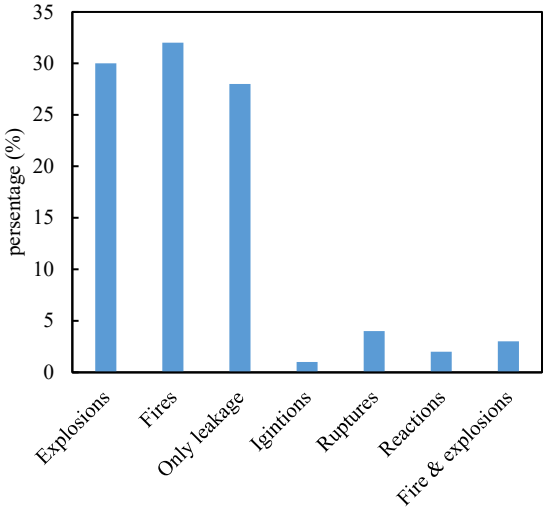

Fig. 4. Percentage of different accidents followed by hydrogen leakage.

Gaseous hydrogen has a very low density and hence its dispersion behaviour is different compared to other gases such as methane. It presents a wide range of flammability (4%-75%) with high heat of combustion (2.6 times more than methane). Similarly, liquid hydrogen differs from established liquefied fuels like liquid natural gas (LNG). Notably, liquid hydrogen has a considerably lower normal boiling point of 20 K, in contrast to LNG, which boils at 111 K. Hence, leakage of liquid hydrogen can cause the condensation of oxygen and nitrogen from the air while this does not necessarily occur for LNG spills. Furthermore, the density of liquid hydrogen and its enthalpy of vaporisation are much lower compared to LNG [10]. As a result, the surrounding surfaces experience much cooler temperatures in the event of liquid hydrogen spills, which is a critical consideration, particularly for structural components that may become brittle and susceptible to fracture.

Hydrogen risks can be classified as material properties issues and handling issues [11]. The material-related safety concerns primarily stem from the storage properties and the characteristics of hydrogen. Purity and impurities of hydrogen, environmental conditions, and the condition of the metal surface contribute to the risk of embrittlement, which can lead to mechanical failures and hydrogen leaks. Permeability is another safety concern, stemming from the hydrogen's low molecular weight. This hydrogen characteristic affects its storage and its utilisation in pipelines. Other materials such as metals, plastic liners, and composites have been used for compressed hydrogen vessels however other safety issues should be addressed. They include blistering, damage to carbon fibres, and reduced resistance to high temperatures [12]. On the other hand, materials used for the storage of liquid hydrogen are subjected to extremely low temperatures, which can result in changes in their properties, transitioning from ductile to brittle characteristics.

Figure 5 schematically shows the handling-related safety aspects. The release and accumulation of hydrogen can lead to a range of hazardous scenarios, notably jet

fires and explosions. If high-pressure releases of hydrogen experience instantaneous ignition, either in unenclosed or enclosed environments, hydrogen jet fires are formed. The immediate ignition of a sufficiently concentrated hydrogen-air mixture can lead to hydrogen flash fire that may result in deflagrations characterised by subsonic flame propagation. Consequently, damage to equipment and structures is expected when they are exposed to thermal radiation and direct hydrogen flames which could be extremely destructive [13].

In cases where hydrogen accumulates in confined and/or semi-confined spaces, flammable clouds are formed. The combination of this scenario with delayed ignition increases the potential for hydrogen explosions. Continuous or immediate leaks may also result in hydrogen explosions as long as a flammable cloud forms, and these explosions may progress into detonations if shock waves generate a supersonic flame, often due to obstacles in the vicinity.

There is a possibility of spontaneous ignition in confined or partially enclosed spaces with high-pressure hydrogen discharges, even in the absence of obvious ignition sources. Such ignition can occur due to the cumulative effects of factors such as the Joule-Thomson inversion temperature, static electricity, and principles related to diffusion theory.

In addition, electrical components, lack of understanding of the hazardous areas and human errors play important roles in incidents and accidents in hydrogen systems and facilities. Recent accidents in Santa Clara, the Gangwon, and the Kjørbo explosion confirmed hydrogen systems are vulnerable to fatal, destructive, and even costly catastrophic events which are caused by technical and human interaction.

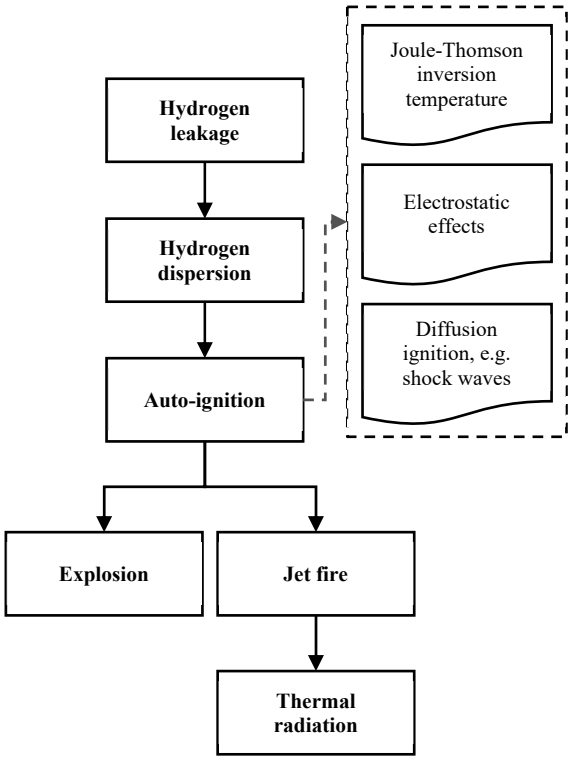

Fig. 5. Hydrogen safety aspects.

4. Hydrogen risk assessment

The models to assess hydrogen risk and safety include probabilistic and deterministic methods. The utilisation of quantitative risk analysis (QRA), through probabilistic methodologies has proven effective in examining the risks inherent in hydrogen systems, contributing significantly to the formulation of regulatory frameworks and safety standards [14]–[16]. A key barrier to developing accurate QRA models is the lack of real-time data for hydrogen-related accidents and detailed information about hydrogen facilities; hence, most risk assessment studies mainly used generic parameters. Different studies focused on hydrogen refuelling stations and adopted Semi-QRA, grid-based risk mapping method, and Bayesian network. While they provided some assessment tools, further real-time data is required to ensure the reliability of the developed models for hydrogen facilities.

Deterministic methods include experimental measurements and computational fluid dynamic (CFD) methods which have been mainly employed for consequence modelling and impact analysis. Experimental tests have studied complex phenomena such as hydrogen blowdown, unburned jet plumes, ignited jet fires, cryogenic hydrogen, and hydrogen accumulation [11], [17]. There are limited experimental studies such as [18] that provided measurements for temperature and concentration fields, enhancing the physical understating of complex phenomena presented in cryogenic hydrogen. Such datasets are valuable for the validation of CFD models; however, they are limited to the lab scale cases due to safety considerations. There are also some point measurements for both lab-scale cases and real-world scenarios. The key challenges with these types of measurements are that they provide limited information about the physical behaviour, and they are associated with high uncertainties, particularly for real-world scenarios since they were conducted in uncontrolled open-space environments [19], [20]. Despite, their importance in validating numerical models, there are some concerns about their suitability and accuracy.

Numerical CFD simulations have yielded valuable insights into the behaviour of hydrogen dispersion, fires, and explosions in various scenarios, encompassing both open and confined spaces, as well as phenomena such as jet fires and autoignition [21], [22]. Tolias et al. [17] provided some guidelines on numerical simulations and CFD benchmarking for hydrogen safety applications. The CFD simulations of hydrogen leakage, fire, and explosion, require models for high compressibility effects, turbulence and combustion interactions, radiation, and complex heat transfer for cryogenic gases. For modelling liquid hydrogen leakage and fire, the complexity of phase change including evaporation and condensation should be also addressed. Various studies, particularly for large-scale modelling, adopted RANS while some studies use direct numerical simulations (DNS) and large eddy simulations (DNS) to model different accident scenarios [23], [24].

The leakage of hydrogen from high-pressure tanks generates complex jet flows whose behaviour depends on the ratio of the stagnation pressure to the ambient

pressure, which is known as the nozzle pressure ratio (NPR). The nozzle pressure ratio of unity represents subsonic jets. A moderately under-expanded jet is expected at 1<NPR≤2; while a highly under-expanded jet occurs when NPR>2 [24]. In these flows, rapid jet expansion and the formation of shock waves may occur, making the modelling very challenging. While some DNS and LES studies adopted real gas models to enhance the understanding of under-expanded, it is common to use the notional nozzle technique provides a simplified approach for modelling under-expanded jets by replacing the actual nozzle with a hypothetical nozzle with the same mass flow rate. While maintaining a satisfactory accuracy, this model allows for more computationally efficient CFD simulations, particularly when the focus is further downstream and the development of flammable could which is the case in many hydrogen safety studies.

Hydrogen release may result in a jet fire due to the formation of a flammable mixture with air, resulting in rapid ignition and a jet-like flame upon encountering an ignition source. The eddy dissipation concept is commonly used for the combustion model. The unsteady characteristics of a high-pressure hydrogen jet leaking into the atmosphere show that when the energy supplied by the ignition source occurs within a time frame that is shorter than the characteristic time of the jet flow the energy is effectively delivered to a region with a high concentration of hydrogen, promoting ignition [25].

Hydrogen explosions result from high-pressure hydrogen release and accumulation, triggered when potential ignition sources are present in a flammable cloud [26]. These explosions pose significant risks to personnel safety and infrastructure integrity. Few numerical studies focused on the factors that influence the overpressure caused after an explosion. It has been found that hydrogen-air clouds exhibit higher explosion pressure, particularly at their edges, with turbulence intensity significantly influencing overpressure magnitude. Higher turbulence intensities lead to more intense combustion and greater explosion intensity [27], [28]. The timing of ignition and its delay also affect explosion intensity, with increasing ignition delay resulting in higher overpressure.

CFD models also offer solutions for risk management for safety components linked with the engineering aspects. They include hydrogen leakage detection, effective sensor arrangements, and optimised ventilation systems for hydrogen facilities and storage systems [29].

5. Conclusion

Hydrogen is a promising energy source and carrier with high energy capacities. Hydrogen and its vectors such as ammonia have a clear role in decarbonising different sectors, particularly, heavy-duty vehicles, maritime, aviation, and high-temperature processes. It is also an attractive choice for grid stabilisation, supporting renewable green electricity. While there is a significant investment in hydrogen production particularly in Australia, a clear pathway of hydrogen utilisation and end uses is still missing. The lack of demand hinders the growth of hydrogen production and consequently the reduction of its cost.

In addition to the high costs associated with hydrogen production, storage, operation, and maintenance, there are concerns about the safety, reliability, and regulatory approvals of hydrogen systems. The progress of safety and regulatory advancements has been integrated into several pilot and expansion initiatives due to their significant impact on the cost of hydrogen systems, the development of hydrogen technologies, and their scalability objectives. The improvement of safety protocols and training requires (i) addressing fundamental knowledge gaps in hydrogen dispersion, fire, and explosion, (ii) establishing detailed measurement datasets, (iii) developing accurate fast CFD and engineering tools, and (iv) enhancing risk assessment analysis. Ensuring hydrogen safety and reliability is also crucial for establishing public confidence, which plays a critical role in various aspects of the hydrogen economy, including the implementation of hydrogen-powered vehicles, pipelines, and infrastructure.

6. References

[1] S. Kumar, T. Baalisampang, E. Arzaghi, V. Garaniya, R. Abbassi, and F. Salehi, “Synergy of green hydrogen sector with offshore industries: Opportunities and challenges for a safe and sustainable hydrogen economy,” *J. Clean. Prod.*, p. 135545, 2022.

[2] J. O. Abe, A. Popoola, E. Ajenifuja, and O. M. Popoola, “Hydrogen energy, economy and storage: Review and recommendation,” *Int. J. Hydrog. Energy*, vol. 44, no. 29, pp. 15072–15086, 2019.

[3] T. Amirthan and M. Perera, “The role of storage systems in hydrogen economy: A review,” *J. Nat. Gas Sci. Eng.*, p. 104843, 2022.

[4] S. Bouckaert *et al.*, “Net zero by 2050: A roadmap for the global energy sector,” 2021.

[5] M. Minutillo, A. Forcina, N. Jannelli, and A. L. Lavadera, “Assessment of a sustainable energy chain designed for promoting the hydrogen mobility by means of fuel-cell powered bicycles,” *Energy*, vol. 153, pp. 200–210, 2018.

[6] S. Niaz, T. Manzoor, and A. H. Pandith, “Hydrogen storage: Materials, methods and perspectives,” *Renew. Sustain. Energy Rev.*, vol. 50, pp. 457–469, 2015.

[7] H. Barthélémy, M. Weber, and F. Barbier, “Hydrogen storage: Recent improvements and industrial perspectives,” *Int. J. Hydrog. Energy*, vol. 42, no. 11, pp. 7254–7262, 2017.

[8] “Hydrogen Tools.” [Online]. Available: https://h2tools.org/

[9] U. Mukherjee *et al.*, “Techno-economic, environmental, and safety assessment of hydrogen powered community microgrids; case study in Canada,” *Int. J. Hydrog. Energy*, vol. 42, no. 20, pp. 14333–14349, May 2017, doi: 10.1016/j.ijhydene.2017.03.083.

[10] B. Bowman and L. Klebanoff, “Historical perspectives on hydrogen, its storage, and its applications,” *Hydrog. Storage Technol. Mater. Appl.*, p. 65, 2012.

[11] E. Abohamzeh, F. Salehi, M. Sheikholeslami, R. Abbassi, and F. Khan, “Review of hydrogen safety during storage, transmission, and applications processes,” *J. Loss Prev. Process Ind.*, vol. 72, p. 104569, Sep. 2021, doi: 10.1016/j.jlp.2021.104569.

[12] R. Moradi and K. M. Groth, “Hydrogen storage and delivery: Review of the state of the art technologies and risk and reliability analysis,” *Int. J. Hydrog. Energy*, vol. 44, no. 23, pp. 12254–12269, 2019.

[13] K. Groth, J. LaChance, and A. Harris, “Early-stage quantitative risk assessment to support development of codes and standard requirements for indoor fueling of hydrogen vehicles.,” SAND2012-10150, 1057251, Nov. 2012. doi: 10.2172/1057251.

[14] N. Ade, A. Alsuhaibani, M. M. El-Halwagi, H. Goyette, and B. Wilhite, “Integrating safety and economics in designing a steam methane reforming process,” *Int. J. Hydrog. Energy*, vol. 47, no. 9, pp. 6404–6414, 2022.

[15] M. Dadashzadeh, S. Kashkarov, D. Makarov, and V. Molkov, “Risk assessment methodology for onboard hydrogen storage,” *Int. J. Hydrog. Energy*, vol. 43, no. 12, pp. 6462–6475, 2018.

[16] J. Nakayama *et al.*, “Qualitative risk analysis of the overhead hydrogen piping at the conceptual process design stage,” *Int. J. Hydrog. Energy*, vol. 47, no. 22, pp. 11725–11738, 2022.

[17] I. C. Tolias *et al.*, “Best practice guidelines in numerical simulations and CFD benchmarking for hydrogen safety applications,” *Int. J. Hydrog. Energy*, vol. 44, no. 17, pp. 9050–9062, 2019.

[18] P. P. Panda and E. S. Hecht, “Ignition and flame characteristics of cryogenic hydrogen releases,” *Int. J. Hydrog. Energy*, vol. 42, no. 1, pp. 775–785, 2017.

[19] P. Hooker, D. Willoughby, and M. Royle, “Experimental releases of liquid hydrogen,” 2011.

[20] R. D. Witcofski and J. E. Chirivella, “Experimental and analytical analyses of the mechanisms governing the dispersion of flammable clouds formed by liquid hydrogen spills,” *Int. J. Hydrog. Energy*, vol. 9, no. 5, pp. 425–435, 1984.

[21] P. Patel, T. Baalisampang, E. Arzaghi, V. Garaniya, R. Abbassi, and F. Salehi, “Computational analysis of the hydrogen dispersion in semi-confined spaces,” *Process Saf. Environ. Prot.*, 2023.

[22] T. T. Aung, A. Terada, H. Ryutaro, R. Nagaishi, and S. Kadowaki, “Simulation of the self-propagating hydrogen-air premixed flame in a closed-vessel by an open-source CFD code,” *J. Nucl. Sci. Technol.*, vol. 59, no. 5, pp. 573–579, 2022.

[23] Q. Ba, Q. He, B. Zhou, M. Chen, X. Li, and L. Cheng, “Modeling of cryogenic hydrogen releases,” *Int. J. Hydrog. Energy*, vol. 45, no. 55, pp. 31315–31326, 2020.

[24] Z. Ren and J. X. Wen, “Numerical characterization of under-expanded cryogenic hydrogen gas jets,” *AIP Adv.*, vol. 10, no. 9, 2020.

[25] M. Asahara, T. Iwasa, N. Tsuboi, and A. K. Hayashi, “Numerical study on unsteady characteristics of high-pressure hydrogen jet ejected from a pinhole,” *Int. J. Hydrog. Energy*, vol. 47, no. 74, pp. 31709–31728, 2022.

[26] H. Hussein, S. Brennan, and V. Molkov, “Dispersion of hydrogen release in a naturally ventilated covered car park,” *Int. J. Hydrog. Energy*, vol. 45, no. 43, pp. 23882–23897, 2020.

[27] I. Ahmed and N. Swaminathan, “Simulation of turbulent explosion of hydrogen–air mixtures,” *Int. J. Hydrog. Energy*, vol. 39, no. 17, pp. 9562–9572, 2014.

[28] X. Chang, C. Bai, and B. Zhang, “The effect of gas jets on the explosion dynamics of hydrogen-air mixtures,” *Process Saf. Environ. Prot.*, vol. 162, pp. 384–394, 2022.

[29] P. Patel *et al.*, “Machine Learning Regression-CFD Models for Predicting Hydrogen Dispersion in a Naturally Ventilated Area,” in *International Conference on Offshore Mechanics and Arctic Engineering*, American Society of Mechanical Engineers, 2023, p. V008T09A019.

Recent advances in building fire safety

Q. N. Chan[1, *], S. Xing[1], D. Gao[1,2], C. Wang[1], W. M. Lee[2] and G. H. Yeoh[1]
[1] School of Mechanical and Manufacturing Engineering, UNSW Sydney, NSW 2052 Australia
[2] Department of Architecture and Civil Engineering, City University of Hong Kong, Hong Kong, SAR

Abstract

This paper explores the demographic and living pattern shifts in Australia, and their potential implications on fire safety designs. It evaluates the opportunities presented by the performance-based approach in fire safety design in addressing these changes, and highlights some of the challenges encountered during implementation. The paper concludes by detailing recent innovations, including the use of advanced sensors and virtual reality surveys, as potential solutions to the challenges outlined.

Keywords: building fire, fire safety design, performance-based design

1. Introduction

Australia faces increasing fire risks associated with high-density dwellings, which can lead to significant economic and social costs. Over the past decade, Australia has experienced a population growth of 15%, with a notable trend toward uneven population distribution, as approximately 67% of the total population now resides in urban regions [1]. To address these challenges, major Australian cities have witnessed a surge in the construction of high-density dwellings, as evidenced by the growing proportion of apartments within the housing landscape. For instance, Sydney saw an increase in the fraction of apartments from 25.8% to 28.1% between 2011 and 2016 [2]. However, this shift towards high-density living brings with it an elevated potential for fire-related fatalities and losses.

Another noteworthy demographic trend is the rising proportion of older Australians, aged 65 and above. In 2020, this age group constituted 16% of the population [1, 3], up from 12% in 1996 [2], and this trend is projected to continue. Older adults are particularly vulnerable to fire-related injuries and fatalities due to age-related cognitive and sensory impairments, limited mobility, and other factors. This vulnerability is highlighted by the fact that, over a similar period, victims over the age of 65 accounted for 56% of reported fire fatalities, despite representing only a small fraction of the total population [4]. The convergence of increasing high-density living and an aging population raises concerns about a potential rise in fire-related injuries and fatalities.

Amidst these demographic shifts and evolving living patterns, a central question arises: How can we ensure buildings with lifespans typically spanning from 30 to hundreds of years, and fire safety measures designed based on today's demographics, continue to serve effectively as the demographic shifts and and living pattern changes?

1.1 Current fire safety requirements in Australia

Fire safety regulations in Australia are comprehensive and are enforced at both the national and state levels. They cover a wide range of aspects related to fire safety, which can be broadly classified into three main categories:

- Equipment: This involves the selection, design, installation, and commissioning of fire safety systems. For example, standards as AS 1841 for portable fire extinguishers, AS 1851 for routine service of fire protection systems and equipment, AS 2293 for emergency escape lighting and exit signs, and AS 2444 for portable fire extinguishers and fire blankets are applicable.
- Environment and Building Design: This addresses architectural and environmental aspects of building design to enhance fire safety. The Building Code of Australia lays out regulations regarding the fire safety systems and elements of commercial buildings. This includes Sections C, D and E that addresses issues pertaining to Fire Resistance, Access and Egress and Services and Equipment, respectively.
- Response and Fire Prevention: This outlines provisions for fire detection, prevention, and response measures. The fire safety regulations such as fire doors and other fire protection equipment

Table 1. Example of codes/standards in Australia relating to fire safety requirements.

Code/Standard		Categorization		
		Equip-ment	Envir o-nment	Respo -nse
Building Code of Australia (BCA)	Section C Fire Resistance		√	
	Section D Access and Egress		√	
	Section E Services and Equipment	√		√
AS 1841 Portable Fire Extinguishers General Requirements		√		
AS1851 Maintenance of Fire Protection Systems		√		
AS 2293 Emergency Escape Lighting and Exit Signs for Buildings		√		
AS2444 Portable Fire Extinguishers and Fire Blankets		√		

* Corresponding author:
Phone: (+61) 2 93854116
Email: qing.chan@unsw.edu.au

should be checked during and after construction to ensure they meet relevant standards. The AS1670 standard also plays a role here as it covers the design, installation, commissioning, and maintenance of automatic fire detection, warning, control, and intercom systems.

Fire safety regulations and fire safety design are closely intertwined. Regulations dictate the types of equipment, such as fire extinguishers, alarms, sprinkler systems, and emergency lighting, that must be installed in a building. The building design is also influenced by regulations, which may specify construction materials to prevent fire spread, corridor width for evacuation, and the number and placement of exits. Furthermore, fire safety design considers how occupants will respond in a fire event. This includes clear signage for evacuation routes and occupant training on using fire safety equipment. In essence, fire safety regulations set the standards that fire safety design must meet. The design process is a way to creatively solve the problem of how to meet these standards while still achieving other design goals.

2. Building fire safety design

2.1 Evolution of fire safety design

Fire safety design has seen a significant evolution since the 1900s, transitioning from traditional pescriptive methods to performance-based approaches, and now to the modern realm of smart design. This evolution has been propelled by advancements in building fire safety research and changes in insurance policies (see Fig. 1). Traditionally, fire engineering design was primarily based on prescriptive codes and strict requirements. These codes provided a set of regulations that dictated how buildings should be constructed to meet established safety standards. However, as buildings became more complex, diverse design goals emerged.

In response to these challenges, performance-based design (PBD) was introduced and has since gained global acceptance. PBD goes beyond prescriptive code requirements by offering cost-effective and innovative solutions to fire safety challenges. It is characterized as an outcome-based approach that introduces design flexibility through acceptable methodologies, analytical tools, and performance criteria. This approach allows the built environment to align with specific fire and life safety objectives. The PBD concept for fire safety emerged between the 1970s and early 1990s. Over time, building codes and regulatory bodies have gradually integrated performance-based design as a complement to prescriptive code-driven designs. Numerous design handbooks, guides, and codes pertaining to PBD are available today, and many countries permit and endorse performance-based solutions to design challenges. For instance, Australia embraced PBD in its Building Code of Australia (BCA) in 1996 and enhanced PBD guidelines in the National Construction Code (NCC) of 2019. In the context of addressing demographic shifts and evolving living patterns, PBD offers a more adaptable approach to addressing fire safety design, allowing fire safety measures to be modified as demographics and living

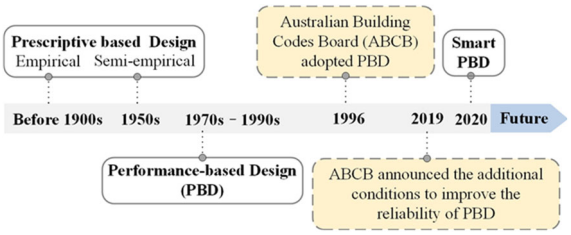

Fig. 1 Evolution of fire safety design [5, 6].

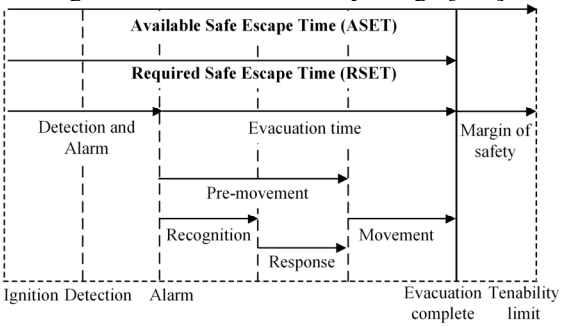

Fig. 2 Timeline for fire engineering analytical process.

patterns change, which could include upgrading or modifying fire safety systems as new technologies emerge or building usage changes. While PBD is not a fix-all solution, it offers a flexible and adaptable approach that can help ensure buildings and their fire safety measures continue to effectively serve their intended purposes amidst demographic shifts and evolving living patterns.

2.2 Assessment of fire safety design

At its core, PBD for life safety fundamentally ensures that occupants have sufficient time to exit the building before being overcome by fire [5, 7]. This fire engineering analytical process, as shown in Fig. 2, typically involves fire ignition, fire detection and alarm systems, and pre-movement and movement of occupants. The outcome of this process is evaluated by comparing the Available Safe Egress Time (ASET) and Required Safe Egress Time (RSET) [8]. The ASET refers to the duration of time from the ignition of a fire until conditions become untenable due to smoke, heat, or other hazards. It represents the time available for occupants to safely evacuate. On the other hand, RSET represents the time required for all occupants to safely evacuate from the building. Therefore, the assessment of a building's fire safety is based on ensuring that occupants can escape safely without being exposed to untenable fire-related conditions, i.e., ASET should be greater than RSET.

3. Optimization of fire safety design

Accurate estimation of ASET and RSET, coupled with the provision of a suitable safety margin, is vital for ensuring the safe evacuation.

3.1 Assessing ASET

ASET estimations employ empirical correlations from real fire scenarios or advanced fire modelling techniques. There are research concentrating on enhancing ASET in buildings, with the goal of prolonging the safe evacuation time during a fire [9]. This involves several innovative

strategies: incorporating fire safety considerations into modern architectural design, such as using fire-resistant materials and strategically placing exits and fire doors; developing and implementing advanced fire detection and suppression systems, including incorporating Internet-of-Thing (IoT) devices to monitor environmental changes, for early fire detection, warning and control.

3.2 Assessing RSET

The RSET assessment employs a multifaceted approach, incorporating computer-based fire modeling, evacuation simulations, and mathematical calculations. This comprehensive process takes into consideration various factors, including the building's layout, occupancy, and fire characteristics, to estimate the time required for safe evacuation under a range of scenarios. Evacuation simulations play a pivotal role in RSET assessment by simulating the behavior of individuals or groups during evacuations. These simulations provide insights that can significantly improve safety measures and procedures. Key factors considered within these simulations encompass the number of exits, escape route dimensions, as well as signage and lighting systems. In parallel, computer-based fire modeling is another key tool. It involves creating a virtual representation of the building and possible fire scenarios, considering factors such as the types of combustibles present, their associated product yields, ceiling height, space geometry where the fire initiated, physical barriers, and smoke ventilation systems. Mathematical calculations underpin the entire assessment process. These calculations incorporate empirical relations for walking speed and occupant flow rates through egress elements like doors, stairs, and corridors. Moreover, they account for variables such as alarm time, pre-movement time, and movement time. This multifaceted approach to RSET assessment allows for periodic re-evaluation and potential modifications to safety measures, ensuring they remain effective and adaptable in the face of dynamic transformations.

3.2.1 Evacuation model

Manual evacuation modelling, a traditional non-digital technique, has been used for decades to estimate evacuation time and the safety of structures during emergencies. This method typically employs equations from the Society of Fire Protection Engineers (SFPE) handbook to calculate mass flow evacuation from any building structure [10]. With the advent of performance-based design, there has been a surge in the use of computer-based simulations for more realistic evacuation calculations. Currently, over 70 models tailored for Fire Safety Engineering (FSE) applications are available in the pedestrian evacuation modelling market, with Pathfinder, STEPS, MassMotion, VISSIM and Pedestrian Dynamics being the most widely used models [11]. It is noteworthy that most of the key assumptions adopted by the evacuation models evacuation models were developed in the late 1980s and 1990s [12].

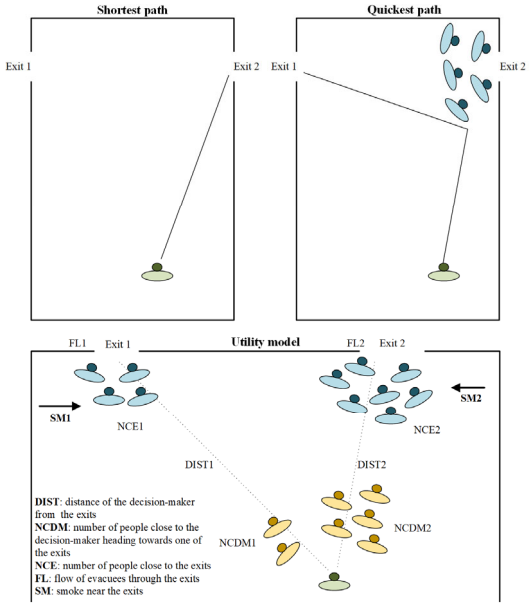

Fig. 3 Shortest path, quickest path, and utility exit choice models.

Table 2. The Route/exit choice mechanisms used in the evacuation models [15-19].

Evacuation model	Route/exit choice mechanism
Pathfinder	Quickest path
MassMotion	Quickest path
Vissim/Viswalk	Shortest path & Quickest path
Pedestrian Dynamics	Shortest path

These methods often overlook diverse personal and environmental factors people employ when choosing their evacuation route [13]. Recent studies have highlighted a mismatch between the most used evacuation models and the latest research developments [11]. An example is the exit choice model, which is the approach used in evacuation simulations to determine how simulated pedestrians choose their exit during an evacuation. Exit choice model such as the shortest path algorithm, which finds the shortest path between origin and destination, and the quickest path algorithm, which finds the path that takes the least time to traverse, are widely used in most popular evacuation simulation software (see Table 2). However, a portion of the evacuation modelling community has started to implement the utility-based model. This model allows for different personal and environmental factors to be taken into consideration (see Fig. 3), potentially providing a more refined simulation approach to better match the actual observations [14]. Despite the development of new modelling approaches over the past twenty years, they have not been widely adopted for mainstream FSE applications. This could be due to the time-consuming nature of developing and validating new models [12]. Instead of re-evaluating foundational assumptions, developers often prioritize refining existing models, adding features, or improving data visualization [12].

In the context of demographic and living pattern changes, the reliance on outdated assumptions can pose significant challenges. For example, the aging population, often marked by reduced physical capabilities and

mobility, demands more time for evacuation and has unique requirements that are often overlooked in conventional evacuation models. Older adults may necessitate assistance or specialized equipment to ensure their safe evacuation. Additionally, the progressively complex building structures required to accommodate the denser populations arising from urbanization can lead to extended evacuation distances and potentially increased interactions among evacuees. These interactions can manifest as bottlenecks or be influenced by evacuees with special needs, impacting the movements of those around them. In this context, PBD offers greater potential than traditional methods to address these complexities, as it can be adapted to account for the changing population and living patterns.

3.2.2 Recent innovations

The verification of evacuation models is a critical step in ensuring their reliability and applicability in real-world scenarios. Traditionally, this process has involved a comparison of model predictions with empirical data derived from actual evacuation situations or controlled experiments. However, the data collection process can be logistically challenging, time-consuming and costly. An example is the investigation of crowd motion synchronization, such as the study conducted by author's City University of Hong Kong (CityU) group [20], which exemplifies the extensive effort required even when examining a single facet of crowd behaviour. The initial stages involved recruiting 70 participants from various departments at Sichuan University and providing financial incentives. Detailed attention was crucial due to variations in the participants' movements. To precisely track their head, left foot, and right foot motions, distinct color-coded markers were employed. Additionally, a mean-shift clustering algorithm was used to extract the trajectories of these body parts. Overcoming technological challenges was a significant aspect. Instead of using multiple individual camcorders for tracking, an innovative video-recording system was introduced. This system utilized three strategically positioned camcorders, each responsible for monitoring one aspect: head, left foot, and right foot movements in the straight section. These camera feeds were seamlessly integrated into a unified video clip, allowing for simultaneous monitoring during each trial. This integration was essential, as synchronizing separate video clips was impractical. Nevertheless, it is important to note that even with these measures, the full spectrum of complexities inherent in real-world situations remains incompletely addressed. Due to these challenges, researchers have explored alternative methods for the verification and validation of evacuation models. One such method involves the analysis of historical data, where researchers examine past evacuation data to assess the performance of the model and derive insights for refining evacuation strategies. The integration of machine learning and artificial intelligence techniques, which are capable of efficiently analysing large datasets and identifying behavioural patterns, further enhances the effectiveness of this approach.

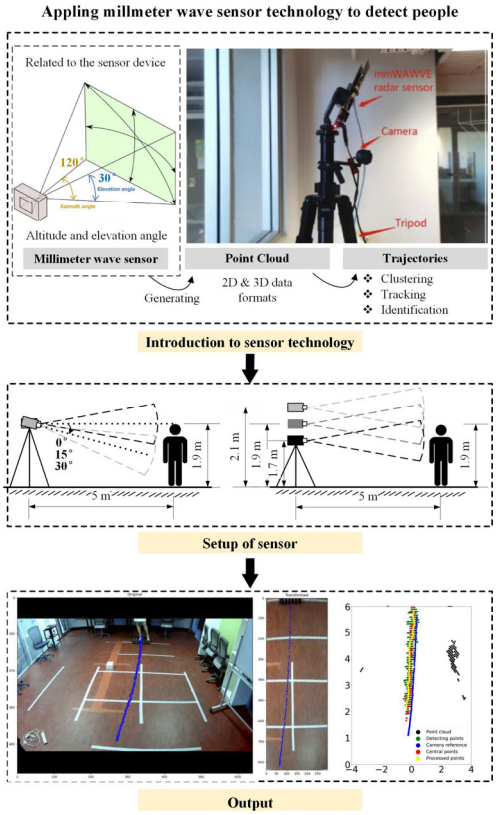

Fig. 4 Demonstration of millimetre wave sensor in capturing the movement of a mannequin' through comparison with ground truth videos.

Sensor data generated by technologies such as video cameras and tracking devices during evacuation drills and actual incidents can be useful for model development and validation. However, such approach has privacy concerns. Different innovative approaches have emerged to tackle this issue involves the use of non-imaging-based data collection methods. For example, the UNSW research group have recently explored the use of millimetre wave sensor technology, see Fig. 4. This indoor radar technology operates by transmitting short wavelength electromagnetic signals (30-300 GHz). The system emits electromagnetic waves that are reflected by objects in their path. The reflected signal is then captured and processed to infer the object's position, speed, and direction. This technology is particularly useful for human movement sensing applications, as it can provide precise information even in indoor conditions with poor visibility or high radiance. Unlike vision-based technologies, it does not raise privacy concerns as it does not capture visually identifiable information. The data gathered has the potential to be used as inputs to improve evacuation models or as a sensory input for to warn evacuees of potential hazards in evacuation pathways.

Crowdsourcing has emerged as another approach. In some instances, crowdsourcing platforms are utilized to collect data on simulated evacuation scenarios. Participants interact with virtual environments, and their actions and decisions provide essential information for model validation. For example, the co-authors from CityU have used virtual reality (VR) surveys [21, 22] to acquire data to assess the impact of cognitive psychology (i.e.,

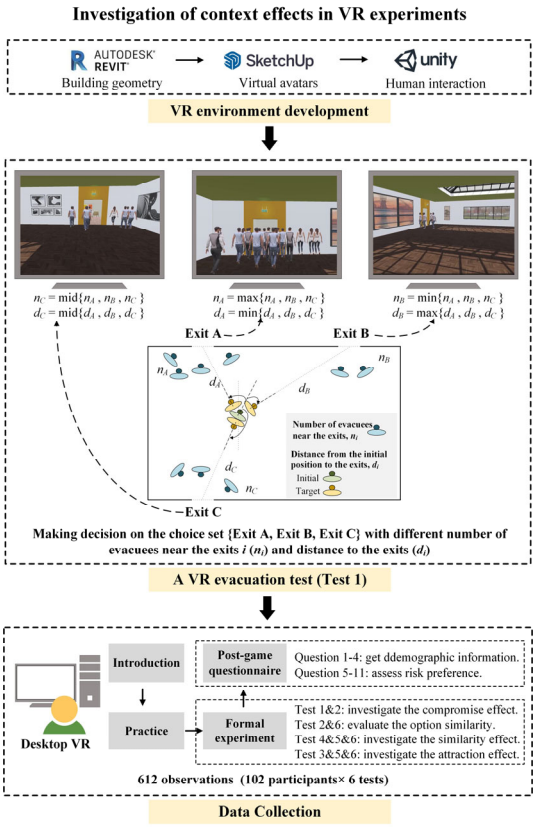

Fig. 5 A virtual reality-based approach to assess survey participant's exit choice [22].

exit preference changes based on option availability, see Fig. 5 [22]), an aspect not covered by existing commercial software. They created a virtual environment using Revit and imported it into Unity3D for further modelling and rendering to enhance realism. Virtual avatars, created with SketchUp and implemented in Unity3D, were used in these experiments. These avatars were either pre-programmed or controlled by survey participants, with their trajectories recorded for analysis.

4. Conclusion and Recommendations

Rapid changes in demographic and living patterns are presenting challenges to the design of fire safety in buildings. Traditionally, fire safety design has been largely prescriptive, following a set of predetermined rules or codes. However, there is a shift towards a more performance-based approach that relies heavily on science, engineering, calculations, and modeling rather than simply adhering to checklists. This shift presents a potential solution to the challenges posed by changing demographics and living patterns. At the heart of this performance-based approach are fire modelling, evacuation simulations, and mathematical calculations. When focusing on evacuation simulations, it is important to note that there are some inaccuracies in the commonly used models and challenges in implementing new changes. Despite these challenges, recent innovations show promise in overcoming them. These include the use of virtual reality platforms and less privacy-invasive sensing technologies. Virtual reality platforms can be used for crowdsourcing surveys to collect realistic model validation information. Non-imaging-based sensing technologies such as millimeter-wave sensors can be used for data acquisition during evacuation drills and actual incidents. These advancements could potentially provide pathways to improve fire safety design in response to changing demographics and living patterns.

5. Acknowledgement

The authors acknowledge the support of Australian Research Council via ARC Industrial Transformation Training Centre IC170100032 and ARC Research Hub for Fire Resilience Infrastructure, Assets and Safety Advancements (FRIASA) IH220100002.

6. References

[1] Australian Bureau of Statistics, Region population growth, Australia, 2016-2017, (2018)
[2] Australian Bureau of Statistics, Census of population and housing: General community Australia Revealed 2016, cat. No. 2024.0, (2016)
[3] Australian Institute of Health and Welfare, Older Australians, (28 Jun 2023)
[4] AIHW: Pointer S & Tovell A Hospitalised burn injuries Australia 2013–14, (2016)
[5] L.-c. Su, X. Wu, X. Zhang, and X. Huang, J. Build. Eng., 43 (2021).
[6] J. Greenwood, A. J. Constr. Econ. Build., 7 (2012) 37.
[7] C.M. Fleischmann, Fire Saf. Sci., 10 (2011) 77-94.
[8] S.L. Poon, Procedia Eng., 71 (2014) 173-181.
[9] A. Alvarez, B.J. Meacham, N.A. Dembsey, and J.R. Thomas, J. Fire Prot. Eng., 23 (4) (2013) 249-276.
[10] M.J. Hurley, D.T. Gottuk, J.R. Hall Jr, K. Harada, E.D. Kuligowski, M. Puchovsky, J.M. Watts Jr, and C.J. WIECZOREK, (2015).
[11] R. Lovreglio, E. Ronchi, and M.J. Kinsey, Fire Technol., 56 (3) (2020) 1133-1153.
[12] E. Ronchi, Fire Safety Journal, 120 (2021) 103020.
[13] M. Moussaïd, D. Helbing, and G. Theraulaz, Proceedings of the National Academy of Sciences, 108 (17) (2011) 6884-6888.
[14] R. Lovreglio, Politecnico of Bari, Milan and Turin, (2016).
[15] Pathfinder Technical Reference Manual. 2023.
[16] MassMotion Help Guide. 2019.
[17] PTV VISSIM 10 USER MANUAL. 2018.
[18] Pedestrian Dynamics Tutorial - INCONTROL Support. 2019.
[19] Fire Dynamics Simulator with Evacuation : FDS+Evac, TechnicalReferenceandUser'sGuide. 2018.
[20] Y. Ma, E.W.M. Lee, M. Shi, and R.K.K. Yuen, Nat. Hum. Behav., 5 (4) (2021) 447-457.
[21] D. Gao, W. Xie, and E.W. M. Lee, Physica A, 604 (2022).
[22] D. Gao, E.W. M. Lee, and Y.Y. Lee, Adv. Eng. Inform., 57 (2023).

Towards Clean Combustion and Decarbonisation
Proceedings of the Australian Combustion Symposium
26 – 29 November 2023, Darwin, Northern Territory, Australia

Challenges and insights using optical diagnostics in turbulent flames containing green fuels

M. J. Dunn[1, *], A. R. W. Macfarlane[1]
[1]School Aerospace, Mechanical, and Mechatronics Engineering, The University of Sydney, NSW 2006 Australia

Abstract

For many decades, the use of optical laser diagnostics has yielded tremendous insights into turbulent combustion and has propelled the field forward. With the recent goals of moving away from using fossil fuel-based fuels, green fuels are being investigated as potential replacements where electrification is not possible. The term green fuel umbrella covers many fuels, a particular emphasis in this paper is paid to ammonia and hydrogen.

Keywords: green fuels, turbulent combustion, ammonia, laser diagnostics

1. Introduction

The continued usage of fossil fuels and their corresponding carbon emissions are becoming increasingly under regulatory control in many countries through carbon emission and net zero target legislation. The need for green fuels is ever-increasing in applications that are either technically infeasible to be electrified or for the near-term reduction in carbon emissions utilising existing devices and infrastructure [1]. The term "green fuel" is a very broad term and is used here to represent a fuel that may or may not contain carbon, however, the fuel needs to be produced in a carbon-neutral fashion and if energy is required to produce the fuel, it is produced by a non-carbon emitting source such as a nuclear, hydro-electric, solar or wind source. Several other categories of fuels, such as e-fuels, electro-fuels, power to X fuels, biofuels and biodiesels could be generally considered to be green fuels if manufactured in a non-carbon emitting fashion.

Given that the cost of electrical energy has been rapidly increasing in most countries over the last decade and is expected to continue to increase in cost, this places a strong market pressure on the cost of producing green fuels which are often very energy-intensive to produce. Firstly, this places enormous emphasis on the development of new energy efficient ways to generate green fuels for chemists and chemical engineers. Secondly, for combustion researchers and engineers an even greater emphasis on efficiency is required due to the high er cost of fuel. Additional requirements such as different pollutants being problematic and being able to lend fuels are important considerations.

Generally, for most green-fuels, chemical kinetic mechanisms of sufficient predictive capability for first pass parametric engineering investigations using either zero-dimensional reactor networks or computational fluid dynamics are possible. These simulations are relevant to a wide array of engineering devices from furnaces to internal combustion engines through to gas turbines. Certainly, pollutant formation such as soot and NO_x, the kinetic mechanisms for the green fuels, particularly larger molecular weight fuels, require further development.

The further and development of chemical kinetic mechanisms for green fuels is an important goal, just as the computationally efficient implementation and accurate numerical modelling of the flame using green fuels CFD is important. Previous experience with simple hydrocarbon fuels such as methane has indicated that well posed experiments in canonical configurations has allowed rapid development the understanding of the use of simple fuels as well as accelerating the development of the numerical modelling tools. A key component to the success of this paradigm is the application of accurate, precise and multi-scalar measurements of key scalar quantities such as mixture fraction, scalar dissipation, scalar gradients, reaction rates, slow-forming pollutants such as nitric oxide and other key intermediates.

The two most highly cited books on laser diagnostics in combustion by Eckbreth in the 1980's and updated in second edition in 1996 [2] and the edited book by [3]. Both of these books indicate that the direction of the laser diagnostics community had been focused on laser diagnostics for ammonia systems in laminar flames for kinetics and NOx formation and reduction studies rather than for turbulent combustion systems. Equally, laser diagnostics for many of the green fuels that are considered promising future target fuels, such as methanol, ethanol, butanol, ethers and are not even mentioned. In part, this paper seeks to identify the key diagnostic techniques that will unlock the necessary insight into the turbulent combustion of green fuels in the future as well as outline some of the specific turbulent combustion experiments of green fuels executed at the University of Sydney in recent years.

2. Laser diagnostics for NH_3

While there are many laser diagnostic techniques that are capable of sensing fuels and intermediate molecules relevant to green fuels, in order for measurements in a turbulent combustion system of such fuels, measurements must be conducted in a temporally and spatially resolved

* Corresponding author:
Phone: (+61) 2 93517150
Email: matthew.dunn@sydney.edu.au

manner. These requirements rule out techniques such as line of sight absorption, such as techniques that require wavelength scanning such as degenerate four-wave mixing (DFWM) [4], techniques that require significant averaging such as differential LIght Detection And Ranging (LIDAR) [5], and Fourier Transform Infrared (FTIR) spectroscopy [6]. However, such techniques may be applied to turbulent combustion systems to provide indicative and relative global concentration levels [7]. Such techniques are a line-of-sight integration along the light or laser beam, however due to the scanning and time integration nature of the technique, they are not time-resolved or "single-shot".

The combustion of ammonia permits a rich range of new molecules to be explored in turbulent combustion systems. Unlike hydrocarbon and hydrogen-fuelled systems, direct laser-induced fluorescence of the fuel molecule, NH_3 is possible. For single photon NH_3 LIF, transitions are accessible in the near VUV (200-220 nm) for the A←X v'_2 symmetric N-H bend system [8], however due to the near VUV excitation photofragmentation, strong beam absorption and weak emission [9], have limited this approach in turbulent combustion applications. Two-photon transitions to pump the B←X and C'←X electronic system of NH_3 at excitation wavelengths of 303 nm and 305 nm, respectively, followed by collection from A←C' (Schusters bands) and A←B near 565 nm and 720 nm respectively are relatively attractive options [10, 11]. These wavelengths are readily achievable at the required fluence levels with a frequency-doubled Nd:YAG put has helped dye lasers, and that flame absorption and photofragmentation at these wavelengths is small. Single shot planar measurements of NH_3 have been successfully reported over a range of turbulent flames, NH_3 fuelled flames using nanosecond excited PLIF [12] and femtosecond excitation for 1D line imaging [13]. A challenge with two-photon femtosecond excitation of NH_3 is to obtain sufficient signal without causing excessive photodissociation [13]. Multi-scalar measurements incorporating two-photon NH_3 are also possible. Utilising modern laser systems achieving 65 mJ near 305 nm, planar images ~32 mm high with good SNR of two-photon C'←X excited PLIF, combined simultaneously with NH $A^3\Pi$-$X\Sigma^-$ (1,0) excited PLIF with collection centred at 336 nm and elastic Rayleigh scattering at 305 nm, effectively a three scalar experiment from the one laser beam [14]. Rather than using a single beam, however still a single laser system, the frequency doubled output of an Nd:YAG pumped dye laser is tuned to a transition near 304 nm to excite NH_3 via two photon and NH for PLIF, yet the wavelength specifically selected such that once mixed with the Nd:YAG fundamental at 1064 nm an additional wave mixed beam at 237 nm for NO PLIF with NO LIF emission collected from 250 nm to 270 nm [15].

NH_3 has also been detected in a single shot basis using deep UV photofragmentation and subsequent fluorescence from the resultant NH* fluoresce centred at 336 nm [16, 17]. Utilising an ArF laser at 193 nm, a single shot detection limit of 50 ppm at 1170 K over a 25 mm high sheet using ~85 mJ of 193 nm UV light has been reported [18].

Although a point measurement technique, laser-induced breakdown spectroscopy (LIBS) can still be considered a viable measurement technique for turbulent combustion systems. LIBS has the distinction advantage of being readily applied to any fuel irrespective of the molecular complexity of the fuel. Strategies to enhance the LIBS signal in the NH_3 flame case using a vibrationally resonant deep IR beam show a significant increase in sensitivity [19]. A hybrid between LIBS and fragmentation fluorescence techniques is when a very high instantaneous power femtosecond laser is used, where here, a line measurement and the subsequent spectra dominated by NH* and N_2* emission are processed to determine species concentrations [20-22].

Coherent Anti-Stokes Raman Spectroscopy (CARS) has been applied in a limited capacity to ammonia flames, essentially only as the first proof of principle studies [23]. Also not applied to the NH_3 molecule, dual broadband rotational CARS has been applied to determine temperature to high precision in an ammonia flame [24].

Spontaneous Raman spectroscopy, particularly when paired with Rayleigh scattering and other minor species LIF measurements [25], is the gold standard for highly accurate multi-scalar measurement in turbulent combustion. However, only recently have high-resolution Raman measurements been made in NH_3 flames [26, 27]. In addition, only recently, in 2021 [28], has the fundamental high-resolution spectra for NH_3 been necessary for processing the Raman NH_3 data with the hybrid matrix inversion technique [29], been available. In hydrocarbon flames, soot, soot precursor, and C_2 interferences have historically limited the application of high-precision Raman measurements, thus requiring high levels of partial premixed or dilution in the fuel stream [30]. While NH_3 flames do not contain carbon, a new interfering intermediate species, NH_2 has been identified [31], requiring either extensive corrections or other advanced approaches such as polarisation subtraction.

Though certainly NO can occur in NH_3 flames at higher concentrations compared to conventional hydrocarbon flames the standard excitation and collection schemes for NO and OH still apply to NH_3 flames[24]. The cyano radical, CN has been explored using numerous excitation and detections schemes over many years [32]. For the CN radical to be measured it requires that the NH_3 flame be blended with a carbon-containing fuel. The two most common $A^3\Pi$-$X\Sigma^-$ excitation schemes for, NH are reviewed in [33], indicating that the R-branch (0,0) yields a larger LIF signal compared to (1,0) schemes. However, the (0,0) scheme is challenging close to boundaries and flows with strong scattering such as from particles or droplets, due to the near-resonant nature of the excitation beam wavelength being only a few nm from the collection wavelength. In these cases (1,0) excitation would be preferrable.

Over the past decade, initial progress has been made on experiments using planar multi-scalar measurements in turbulent NH_3 flames. Highly turbulent

NH_3 flames have been featured in several publications [34, 35]. Measurements in turbulent non-premixed flames have also been recently reported [15].

3. Experimental progress

At the University of Sydney, we have been focusing on the usage of two burners for the exploration of turbulent flame structure relating to green fuels. The first burner, the Sydney inhomogeneous burner [36], as shown in Fig. 1, and its various derivatives [37] permits the exploration of turbulent flames of gaseous flames operating in diffusion, inhomogeneous, partially premixed and premixed regimes. When operating in inhomogeneous mode, the recess distance, as shown in Fig. 2 for a hydrogen flame, the blow-off conditions for the flame can be varied by essentially varying the level of fuel inhomogeneity at the exit plane. Detailed Raman measurements exploring the impact of hydrogen differential diffusion as shown in Fig. 3. To investigate the turbulent autoignition properties of green fuels, we have utilised the Sydney hot coflow burner. A schematic of this is shown in Fig. 4 as well as some sample lift-off conditions for different NH_3 concentrations.

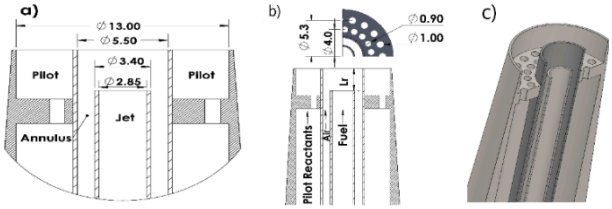

Fig. 1. Schematic and dimensions of the Sydney inhomogeneous burner, b) flow configuration c) 3-D cut-away.

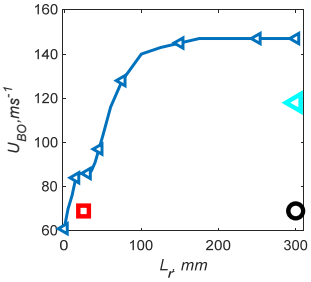

Fig. 2. Stability plot of H_2/N_2=40/60 at φ = 4.76 showing the blow-off velocity U_{BO} versus L_r. The square and circle indicate the experimental cases studied at Lr = 25 and 300 with the same velocity (U_{BO}, 80% @ L_r =25). The Triangle indicates L_r = 300 for (U_{BO}, 80% @ L_r=300).

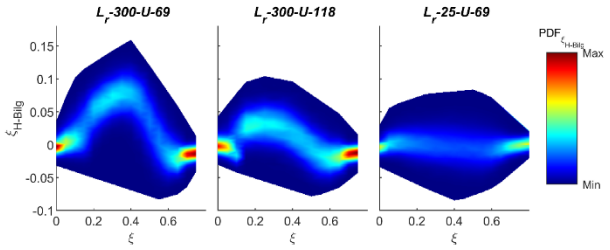

Fig. 3. Joint PDF plots of diffusion ($\xi_{H\text{-}Bilg}$) verse Mixture fraction (ξ) at x/D=1 for the three flames identified in Fig. 2.

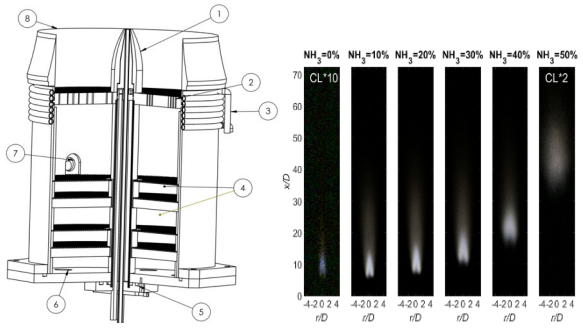

Fig. 4. Cross-sectional view of the hot coflow burner (Left). Mean flame chemiluminescence images for a hot coflow temperature of 1150 K (Right).

4. Conclusions

The turbulent combustion of green fuels presents many new challenges for combustion researchers. For hydrogen, we need to build on existing knowledge and progress whilst addressing open questions such as the challenge of differential diffusion. Whilst research into combustion involving NH_3 has been active for many decades, it is only in the past decade that very strong combustion community-wide investigation into the usage of NH_3 as a fuel has been intensive and diagnostic techniques developed and refined to explore the NH_3 major and minor species system in turbulent flames. The development and application of advanced laser diagnostics will play an important role in the development in the application of present and future green fuels in turbulent combustion system.

5. Acknowledgments

This work was supported by the Australian Research Council (ARC) and AFOSR (USA). The authors would like to acknowledge Prof. Assaad Masri from the University of Sydney and Prof. Gaetano Magnotti and Dr. Hao Tang from King Abdullah University of Science for their contributions to the presented work in this paper.

6. References

[1] Masri, A.R., Proceedings of the Combustion Institute. **38**(1): p. 121–155.

[2] Eckbreth, A.C., *Laser Diagnostics for Combustion Temperature and Species*. 1996, Amsterdam: Gordon & Breach.

[3] K. Kohse-Hoinghaus, J.B.J., *Applied Combustion Diagnostics*. 2002: Taylor&Francis.

[4] Georgiev, N., and M. Aldén., Applied Physics B, 1993. **56**(1): p. 281–286.

[5] Kaldvee, B., Christian Brackmann, Marcus Aldén, and Joakim Bood., Optics Express, 2012. **20**(18): p. 20688–20697.

[6] Barton, E.J., Sergei N. Yurchenko, Jonathan Tennyson, Sønnik Clausen, and Alexander Fateev, Journal of Quantitative Spectroscopy and Radiative Transfer, 2015. **167**: p. 126-134.

[7] W. Meienburg, J.W., H. Neckel, Twenty-Third Symposium (International) on Combustion, 1990. **23**: p. 231-236.

[8] Kaldvee, B., Christian Brackmann, Marcus Aldén, and Joakim Bood, Optics Express, 2012. **20**(18): p. 20688-20697.

[9] Cheng, B.-M., Hsiao-Chi Lu, Hong-Kai Chen, Mohammed Bahou, Yuan-Pern Lee, Alexander M. Mebel, L. C. Lee, Mao-Chang Liang, and Yuk L. Yung, The Astrophysical Journal, 2006. **642**(2): p. 1535.

[10] Westblom, U., and Marcus Aldén, Applied Spectroscopy, 1990. **44**(5): p. 881–886.

[11] Georgiev, N., and Marcus Alden., Applied Spectroscopy, 1997. **51**(8): p. 1229–1237.

[12] Brackmann, C., Odd Hole, Bo Zhou, Zhongshan S. Li, and Marcus Aldén, Applied Physics B, 2014. **115**(1): p. 25-33.

[13] Liu, J., Qiang Gao, Bo Li, Dayuan Zhang, Yifu Tian, and Zhongshan Li, Energy & Fuels, 2020. **34**(2): p. 1177-1183.

[14] Wang Ze, X.L., Lunang Li, Zhixin Zhao, Bo Zhou, and Xiaohua Gan, Combustion and Flame. **242**: p. 112185.

[15] Wang, G., Shixing Wang, and Thibault F. Guiberti, Combustion and Flame, 2023. **256**: p. 112981.

[16] Schendel, J.S., Robert E. Stickel, Cornelis A. van Dijk, Scott T. Sandholm, Douglas D. Davis, and John D. Bradshaw., Applied Optics. **29**(33): p. 4924–4937.

[17] Chadwick, B.L., Denise Charlston-Goch, Anthony Campisi, and Richard J. S. Morrison., Applied Spectroscopy, 1999. **53**(10): p. 1222-1225.

[18] Weng, W., Christian Brackmann, Marcus Aldén, and Zhongshan Li, Combustion and Flame, 2022. **235**: p. 111687.

[19] Yang, G., Guang Yang, Lei Liu, Lei Liu, Tao Wang, Lisha Fan, Xi Huang, DI Tian, Lan Jiang, Jean-Francois Silvan, and and Y. Lu, Optics Express, 2020. **28**(2): p. 1197–1205.

[20] Zhang, D., Qiang Gao, Bo Li, Jixu Liu, and Zhongshan Li, Applied Optics, 2019. **58**(5): p. 1210-1214.

[21] Zhang, D., Qiang Gao, Bo Li, Jixu Liu, and Zhongshan Li, International Journal of Hydrogen Energy, 2019. **44**(47): p. 25740–25745.

[22] Zhang, D., Qiang Gao, Bo Li, Jixu Liu, Yifu Tian, and Zhongshan Li, Applied Optics, 2019. **58**(28): p. 7810–7816.

[23] England, W.A., and Ansar Ali., Applied Spectroscopy. **42**(8): p. 1412–1421.

[24] Brackmann, C., Vladimir A. Alekseev, Bo Zhou, Emil Nordström, Per-Erik Bengtsson, Zhongshan Li, Marcus Aldén, and Alexander A. Konnov., Combustion and Flame, 2016. **163**: p. 370-381.

[25] Carter, C.D. and R.S. Barlow, Opt. Lett., 1994. **19**(4): p. 299-301.

[26] Zubairova, A., Haisol Kim, Marcus Aldén, and Christian Brackmann., Proceedings of the Combustion Institute, 2022. **39**(1): p. 1317-1324.

[27] Tang, H., Chaobo Yang, Yedhu Krishna, Guoqing Wang, William L. Roberts, Thibault F. Guiberti, and Gaetano Magnotti., Experimental Thermal and Fluid Science, 2023. **149**: p. 111020.

[28] Yang, C., Diana Ezendeeva, Tao Yu, and Gaetano Magnotti, Optics Express, 2021. **29**(21): p. 33234.

[29] Fuest, F., et al., Proceedings of the Combustion Institute, 2011. **33**(1): p. 815-822.

[30] Magnotti, G., D. Geyer, and R. S. Barlow., Proceedings of the Combustion Institute, 2015. **35**(3): p. 3765–3772.

[31] Tang, H., Diana Ezendeeva, and Gaetano Magnotti., Combustion and Flame, 2023. **250**: p. 112639.

[32] Zhou, B., Christian Brackmann, Zhongshan Li, and Marcus Aldén, Combustion and Flame, 2015. **162**(2): p. 368–374.

[33] Brackmann, C., B. Zhou, Z. S. Li, and M. Aldén., Combustion Science and Technology. **148**(4-5): p. 529-541.

[34] Xu, L., Qingshuang Fan, Xin Liu, Xiao Cai, Arman Ahamed Subash, Christian Brackmann, Zhongshan Li, Marcus Aldén, and Xue-Song Bai, Proceedings of the Combustion Institute, 2023. **39**(2): p. 2289-2298.

[35] Fan, Q., Xin Liu, Leilei Xu, Arman Ahamed Subash, Christian Brackmann, Marcus Aldén, Xue-Song Bai, and Zhongshan Li., Combustion and Flame 2022. **238**: p. 111943.

[36] Meares, S. and A.R. Masri, Combustion and Flame, 2014. **161**(2): p. 484-495.

[37] Macfarlane, A.R.W., M.J. Dunn, and A.R. Masri., Combustion Science and Technology, 2023. **195**(14): p. 3399-3413.

Towards Clean Combustion and Decarbonisation
Proceedings of the Australian Combustion Symposium
26 – 29 November 2023, Darwin, Northern Territory, Australia

Enhancing ammonia combustion in reciprocating engines: Strategies learned from fundamental experiments

Yi Yang*
Department of Mechanical Engineering, The University of Melbourne, VIC 3010 Australia

Abstract

Ammonia features a low reactivity in combustion and is commonly blended with a more reactive fuel to promote its flame propagation and autoignition. This work reviews ammonia combustion enhancers for their effectiveness on promoting fundamental combustion behaviors and the potential to power heavy-duty engines with ammonia as the primary fuel. Fundamental experiments reveal that enhancers are unlikely to resolve ammonia's slow flame propagation, with hydrogen being an exception. Autoignition, on the other hand, offers more promise due to the high sensitivity to small additions of enhancers. State-of-the-art ammonia engines are reviewed with enhanced spark-ignition and compression-ignition methods. Further research for combustion fundamentals and engine development is recommended.

Keywords: ammonia, internal combustion engines, dual-fuel, hydrogen, diesel

1. Introduction

Ammonia attracts major interests as a carbon neutral fuel for long-haul transport and heavy industry. Various energy agencies have predicted ammonia's major role in decarbonizing the shipping industry [1,2]. Ammonia combustion in large engines is therefore of particular importance.

As a combustion fuel, ammonia has considerably lower oxidation reactivity than conventional fuels. The properties in Table 1 indicates that ammonia is difficult to ignite and slow to burn. These properties are generally at odds with combustion requirements in reciprocating engines where combustion must start and complete within a short time window. Combustion of the nitrogen-containing fuel is also bound to produce NOx despite the lower flame temperature limiting thermal NOx formation.

Table 1 Fuel Combustion Properties

Properties	Hydrogen (H_2)	Ammonia (NH_3)	DME (CH_3OCH_3)	Gasoline	Diesel
State at STP	gas	gas	gas	Liquid	Liquid
LHV (MJ/kg)	120	18.6	28.4	42.5	45
T_{ad} (°C)	2110	1800	1994	-	-
$S_{L,max}$ at STP (m/s)	3.25	0.07	0.49	~0.5	-
Min. ignition energy (mJ)	0.018	8.0	-	~0.14	-
Flammability limit (%vol)	4-76	15.8-28	3.4-27	1.4-7.6	1-6
Autoignition temp. (°C)	572	650	350	~440	~233
RON	*vary*	>130	0	91-98	≤0

A primary method to address the slow burn issue is blending ammonia with a more reactive fuel, which is reviewed here. Alternatively, additives (e.g., ozone, hydrogen peroxide) and external energy (e.g. plasma) have also been investigated. The effectiveness of this approach depends on the enhancer and the mode of combustion, i.e., whether in a flame or via autoignition. Many publications have appeared in the recent literature, ranging from theoretical calculations of elementary reaction rates [3] to experimental investigation of marine-sized engine combustion [4]. This work will first discuss why neat ammonia is unfit for reciprocating engine applications. Enhancement of ammonia combustion in fundamental experiments will then be reviewed, particularly the promotion on laminar flame speeds and ignition delays. Enhanced ammonia combustion in spark ignition (SI) and compression ignition (CI) engines will be reviewed at last. The focus is on combustion enhancers that can be readily produced and can promote ammonia burn rate disproportionally at low blending levels.

This review will not cover ammonia combustion in gas turbines and industrial furnaces, or co-burning ammonia with low reactivity fuels such as natural gas and coal. In these applications, the slow burn issue is either not as critical (e.g., continuous combustion) or can be managed without an enhancer (e.g., by enhancing flow turbulence). Also not covered are pollutant formation and emissions, given that the NO_x-NH_3 trade-off is inherent to ammonia combustion and can't be resolved via combustion optimization. Aftertreatment therefore must be used, which is worth a separate review.

2. Combustion Enhancement Required for Ammonia-Fuelled Engines

Unlike gas turbines, combustion in reciprocating engines accounts for only a fraction of the thermodynamic cycle. Therefore, it must start and end within a suitable time window relative to the piston movement. Combustion in reciprocating engines proceeds in two forms, spark-initiated flame and compression-driven autoignition. In either case, sufficient burn rate is required for the engine to function properly.

Combustion in SI engine takes place as a turbulent premixed flame. Although the burn rate is largely driven

* Corresponding author:
Phone: (+61) 3 83448104
Email: yi.yang@unimelb.edu.au

by in-cylinder turbulence (which is a function of engine speed), ammonia's low flame speed, approximately 1/5 of that of hydrocarbon fuels (Table 1), will slow the heat release locally and overall. The high ignition energy and narrow flammability limits also make the combustion more susceptible to quenching and misfire. Combustion enhancer is therefore required to promote the flame propagation. At the same time, autoignition of the unburned gas could also be promoted by the enhancer, increasing the probability of engine knock.

Combustion in compression ignition engines is driven by autoignition, either as the initiating step (conventional diesel engine) or as the main combustion mode (advanced low-temperature combustion engine). Ammonia's low autoignition reactivity, as evidenced by its high autoignition temperature and unmeasurably octane number, indicates that neat ammonia is clearly not suitable for compression ignition. Ignition enhancer is therefore required, which can be introduced via pilot injection near the end of the compression stroke to trigger the combustion, which has been successfully used in natural gas-diesel dual fuel engines [5]. The other approach is to introduce the enhancer and ammonia together into the cylinder, as a premixed liquid or vapor, and ignite the mixture with compression. The process is similar to the homogeneous charge compression ignition (HCCI) combustion where stratification is required to control the combustion timing and heat release rate.

Enhancement of flame speed and autoignition, therefore, has been both pursued for solving ammonia's slow burn problem.

3. Enhancing Ammonia Combustion in Fundamental Experiments

3.1 Enhancers for Ammonia Flame Propagation

A wide range of fuels have been investigated for ammonia flame propagation, including different hydrocarbons, oxygenated hydrocarbons, and hydrogen. Lavadera et al. systematically investigated the laminar flame speed of ammonia/hydrocarbon mixtures using a heat flux burner at 338 K and atmospheric pressure [6,7]. A linear blending was reported on the mass basis, which led to the argument that cross reactions between different fuels are negligible.

Given the flame speeds of these neat hydrocarbons (and oxygenates reported elsewhere [8]) being similar to that of gasoline, these fuels will unlikely increase the flame speed on a par with gasoline in SI engines, unless with very high blending levels, which defeats the purpose of using ammonia as the primary fuel.

Hydrogen has a flame speed 5-6 time of hydrocarbon, thus of a much higher potential for promoting ammonia burn rate. Hydrogen can be produced on-board from ammonia cracking which potentially eliminates the need of carrying a second fuel. Many experiments have been conducted to measure the laminar flame speeds of ammonia/hydrogen mixtures, as reviewed by Kobayashi [9]. Two important features are noted from these results.

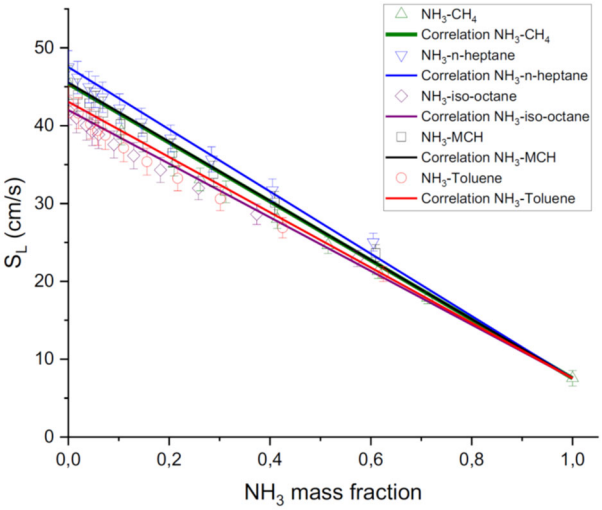

Fig. 1 Measured laminar flame speeds of ammonia mixtures with methane, n-heptane, iso-octane, methylcyclohexane, and toluene at 338 K and 1 atm with ϕ=1. Lines represent linear blending on mass basis [7].

One is the strong nonlinear blending, i.e., the most promoting effect occurring at hydrogen blending >50%. The second is the inhibition of pressure on flame propagation, which can be significant in boosted engines to offset the enhancement of hydrogen blending. Figure 2 shows the impact of temperature and pressure on laminar flame speeds under an example engine condition, calculated using latest kinetic models. It indicates that 50 vol% H_2 is required to promote the mixture flame speed to match that of iso-octane.

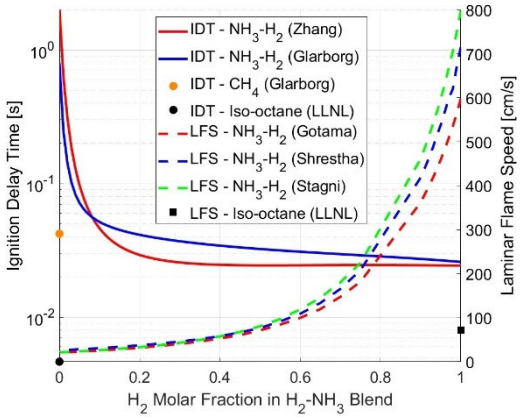

Fig. 2 Laminar flame speed (LFS) and ignition delay times (IDT) of stoichiometric ammonia/hydrogen mixtures in a CFR engine. LFS calculated using mechanisms from [10-12] at 661 K and 12 bar, corresponding to the spark timing condition (13 CAD bTDC) with CR of 7.9. IDT calculated using mechanisms from [13,14] at 920 K and 28 bar, the spark timing condition (13 CAD bTDC) with CR of 12. Reference LFS and IDT for iso-octane and methane are calculated at the same condition using mechanisms from [15] and [13].

3.2 Enhancer for Ammonia Autoignition

High autoignition reactivity fuels, including n-heptane, commercial diesel fuel, dimethyl ether (DME), and diethyl ether (DEE), have been blended with ammonia to promote combustion in dual-fuel compression-ignition engines. Hydrogen, which has a low autoignition reactivity, has also been found to be effective to promote ammonia autoignition.

Ammonia/diesel mixtures (incl. n-heptane) Yu et al. first investigated the ignition delay of ammonia/n-heptane mixtures with n-heptane energy content of 0-60% in a rapid compression machine (RCM) at 10-15 bar and 635-945 K and ϕ=1.0-2.0 [16]. They compiled a kinetic mechanism by merging a n-heptane mechanism [17] and an ammonia mechanism [13] and found that the mechanism could not reproduce the experiment, due to a lack of coupling reactions in the merged mechanism.

Thorsen et al. [18] developed a subset of cross reactions for amine and n-heptane, n-C_7H_{16} + NH_2 = n-C_7H_{15} isomers + NH_3, and updated the rate coefficient of NH_2+HO_2=NH_3+O_2. The updated mechanism largely improved the simulation of Yu et al.'s ignition delay and reproduced well the species profiles in their laminar flow reactor and jet stirred reactor at pressure up to 100 atm and 400-900 K. Dong et al. reported shock tube ignition delay at higher temperature (1000-1400 K) and 10 bar for NH_3/n-heptane mixtures (up to 50 mol% of NH_3) and reported similar results on simulation [19].

More recently Zhang et al. studied NH_3/diesel mixtures in a high-pressure RCM [20], extending their early work [21] from 20 bar to 50 bar and reducing the diesel blending from 50% to 10% (by energy). Increasing diesel content greatly reduced the ignition delay, although the neat ammonia case was not reported (Fig. 3). A subset of cross reactions was considered in the kinetic mechanism, including that between diesel surrogate compounds (n-cetane, iso-cetane, 1-methylnaphthalene) and NH_2, NO, NO_2, HN_2O, as well as their peroxyl radical ROO and these N-containing species, which largely improved the simulation.

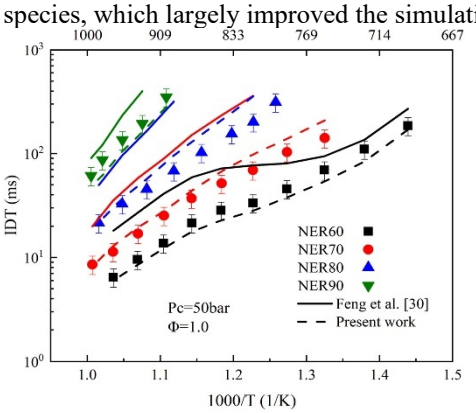

Fig. 3 IDT of ammonia/diesel mixtures in RCM [20]. NRE represents ammonia energy ratio. Incorporating cross reactions between fuels (dashed lines) improved the simulation with a previous mechanism [21] (solid line).

Ammonia/DME mixtures Dai et al. first studied NH3/DME mixtures in a RCM at 610 K to 1180 K and 10–70 bar with ϕ= 0.5, 1.0 and 2 [3]. They reported that a small amount of DME, at the mole fraction of 2% and 5% reduced the ignition delay of ammonia by more than an order of magnitude. A kinetic model including coupling reactions of nitrogen-containing species and DME was developed. Combined with the ab initio calculation for the rate coefficient of DME and NH_2 reaction, CH_3OCH_3+NH_2= CH_3OCH_2 +NH_3, the model well reproduced the measured ignition delay.

Issayev et al. investigated autoignition of ammonia/DME mixtures in a RCM at 649-950 K and 20 and 40 bar and confirmed the strong promotion effect with 5% DME in ammonia [22]. Jin et al. reported similarly strong promotion of DME on ammonia autoignition in a shock tube at 1150–1950 K and 1.4-10 bar [23].

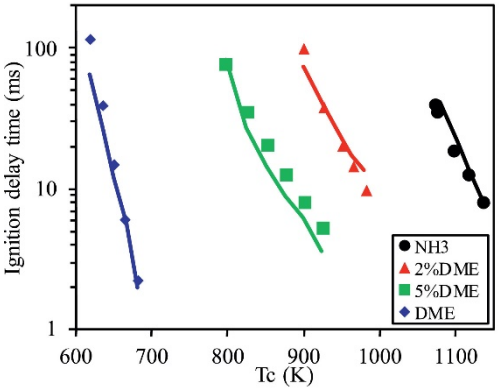

Fig. 4 IDT of ammonia/DME mixtures in RCM at 60 bar and ϕ=0.5 [3]. Lines represent simulation incorporating cross reactions between fuels.

Ammonia/Hydrogen mixtures Hydrogen's high autoignition temperature indicates a lower reactivity than most hydrocarbons. Nevertheless, studies have found that hydrogen strongly promotes ammonia autoignition.

He et al. reported the ignition delay of ammonia/hydrogen mixtures with 1-20 vol% hydrogen in a RCM at 20-60 bar, 950-1150 K and ϕ=0.5-2 [24]. They found strong promotion effect even at 1% hydrogen blending. However, the promotion effect was unable to be simulated by existing ammonia models. Dai et al. reported autoignition delays of NH_3/H_2 mixtures with 0-10 vol% H_2 in a RCM at 20–75 bar, 1040–1210 K and ϕ=0.5 -1.0 [25]. Similarly strong promotion was observed, which was reproduced well by a revised Glarborg model (unpublished). Chen et al. investigated the ignition delays of stoichiometric ammonia/hydrogen blends in a shock tube at higher temperatures (1020 to 1945 K) and lower pressures (1.2 and 10 atm) and 0-70 vol% hydrogen [26]. Existing mechanisms worked well at these conditions. They argued that hydrogen's promoting effect is not due to change of ammonia's oxidation pathways but enhancing the radical production, particularly via the reverse reaction of NH_2+H_2=NH_3+H.

An updated NH_3/H_2 mechanism is recently published by Zhang et al. [14] which was validated by shock tube ignition delays, JSR species profiles, and laminar flame

speeds. However, the high-pressure ignition delay in RCM were still not well reproduced.

Hydrogen's strong promotion on ammonia autoignition is demonstrated in Fig. 2 at engine relevant conditions, where 10% hydrogen reduces the ignition delay to be similar to methane. This makes hydrogen a promising ignition enhancer in ammonia engine, particularly considering the potential of on-board production from ammonia cracking. However, the chemistry at these pressure remains to be validated.

3.2 Learning from Fundamental Experiments

The review above demonstrates that autoignition of ammonia can be strongly promoted by a small amount of combustion enhancer. By contrast, laminar flame speed of ammonia cannot be promoted as effectively, except by hydrogen. Even for hydrogen, the promotion only becomes significant at blending level > 50 mol%, far less effective than the reduction in ignition delay. This suggests that compression ignition be the mode of combustion for overcoming ammonia's slow burn problem in engine application. In this case, not only the ignition delay is shortened by enhancers, the ensuing autoignition also enables volumetric heat release of which the rate is much higher than that of a flame. Furthermore, for heavy-duty applications, ammonia engines likely operate with significant boost of pressure, which inhibits flame propagation but promotes autoignition, thus enhancing the chance of knock in SI engines. The learning from fundamental experiments will be applied in reviewing ammonia engines in the following.

4. Enhancing Ammonia Combustion in IC Engines

4.1 Ammonia Fuelled SI Engines

Hydrogen as the only plausible enhancer for ammonia flame propagation has been investigated in several SI engine studies. In these studies, ammonia and hydrogen were fumigated into the engine, jointly or separately. Frigo and Gentili [27,28] investigated ammonia/hydrogen combustion in a 0.5 L single-cylinder, naturally aspirated engine with a compression ratio (CR) of 10.7. Hydrogen content of 6-12% fuel energy was investigated over 2500-5000 rpm. The combustion of the NH_3/H_2 blends showed acceptable performance, but due to the lower burn rate the power and thermal efficiency were consistently lower than that of gasoline (Fig. 5), which also led to higher cycle-to-cycle variations. The max load achieved was approximately 8 bar BMEP, which is ~ 20% lower than that of gasoline.

Lhuillier et al. [29,30] investigated NH_3/H_2 mixtures in a 0.4 L single-cylinder engine with a CR of 10.5. Mixtures containing 0-60 mol% of H_2 was studied at 1500 rpm. Stable combustion (COV<5%) was achieved with 5% H_2 blending at ϕ=0.8-1.2. The indicated thermal efficiency reached approximately 39% with 20% H_2 but dropped considerably with higher blends, which the authors speculated due to the increased heat losses. Intake pressure up to 1.2 bar was used and the maximum load reported is approximately 9 bar IMEP. Hydrogen blending was found to mostly affect the burn rate during early flame propagation (from spark timing to 10% heat release, CA10). Although comparison with gasoline was not reported, the maximum IMEP is less than 50% of the stock engine, indicating large room for improvement.

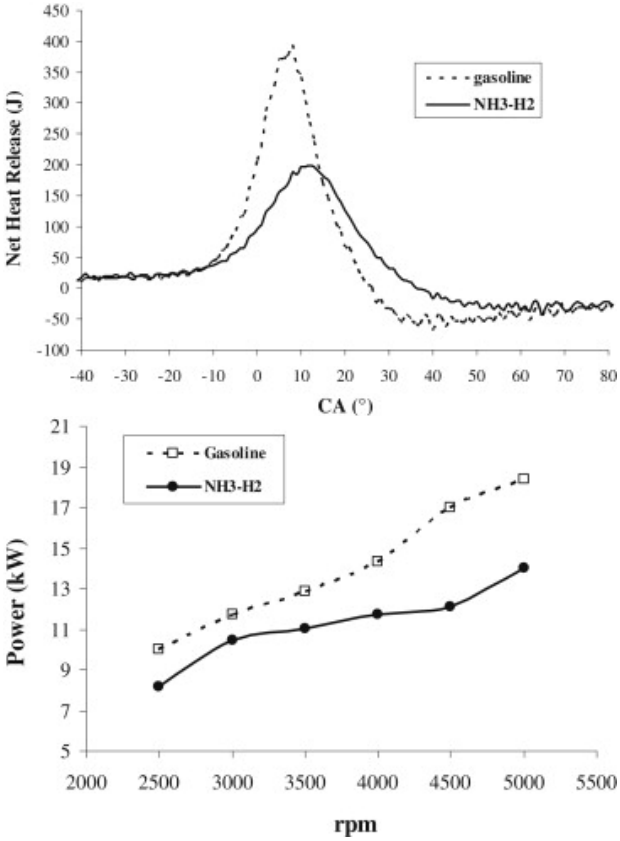

Fig. 5 Heat release rate (top) and brake power (bottom) of a NH3/H2 blend (6% H2 by energy) and gasoline in an SI engine at a fixed CR [27]. ϕ=1. Engine speed is 3000 rpm for the heat release plot.

To utilize the higher knock resistance of ammonia, SI engine with higher CRs has been used. Mørch et al. investigated NH_3/H_2 combustion in a CFR engine (single cylinder, 0.6 L) at a fixed engine speed of 1200 rpm and different compression ratios [31]. With 5-10 vol% H_2 in ammonia, the reduced autoignition reactivity allowed a higher knock-limited compression ratio (13.58) than gasoline (6.23), increasing the indicated thermal efficiency (from 30% to 35%) as well as IMEP which reached a maximum of approximately 7 bar.

Swift et al. investigated 0-10 vol% hydrogen in ammonia also in a CFR engine with CR of 14 and 17 at 900 rpm [32]. They reported stable combustion with 5% hydrogen and achieved 43% indicated thermal efficiency without knock. Interestingly, they noted that the ringing intensity, an indicator of autoignition induced combustion noise, increased rather gently with spark advance, suggesting a mild autoignition that is distinctively different from hydrocarbon fuels (Fig. 6).

They speculated that spark assisted compression ignition (SACI) occurred at these conditions.

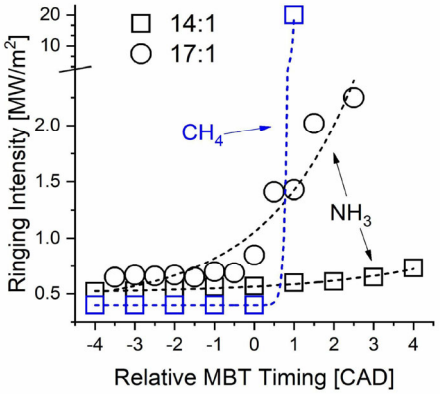

Fig. 6 Ringing intensity vs. spark advance for 5 vol% H_2 in ammonia and pure methane in a CFR engine [32].

These SI engine studies demonstrated that, despite the limited promotion of ammonia's laminar flame speed, a small fraction of hydrogen, e.g. 10 vol%, could enable sufficient burn rate to achieve stable combustion, likely from the help of in-cylinder turbulence [30]. However, the combustion is still slower than gasoline at the same compression ratio which reduces the thermal efficiency and work output. Higher compression ratio therefore should be used to utilize the stronger knock resistance of NH_3/H_2 mixtures. With the gaseous fuel fumigated into the engine, the engine load is constrained by the volumetric efficiency. Considerable intake boosting is therefore required to achieve comparable loads to gasoline combustion, which is yet to be demonstrated. One caveat is that increasing pressure could promote autoignition while reducing flame speed, therefore, knock could become an issue limiting this approach.

4.2 Ammonia Fuelled CI Engines

Ammonia-Diesel Dual Fuel Engine. Many studies have been published recently on dual fuel ammonia-diesel engine. Exclusively ammonia is fumigated or injected at the engine intake and diesel is direct injected before the end of the compression stroke to trigger the combustion. The combustion in these engines is fundamentally different from that in conventional diesel engine in that the diffusion burn barely occurs. Instead, both the pilot fuel and the fumigated charge primarily burn via autoignition. Here our review is limited to those using ammonia as the primary fuel, particularly those with no more than 20% diesel energy.

Hiraoka et al. conducted experiments and CFD simulation of ammonia-diesel dual-fuel combustion in a 0.76 L single-cylinder Yanmar engine (compression ratio unreported) [33]. Cases with 0-95% ammonia energy were investigated at 10 bar IMEP and 1200 rpm. Figure 9 shows the heat release rates of different cases. With 95% ammonia, the combustion shows a mild, single-peak heat release rate, whereas with 55% ammonia, the peak HRR is three time higher, suggesting considerable mixing of the pilot diesel and ammonia before autoigniting. On the other hand, the CFD results for the 95% ammonia case (which closely reproduced the experiment) shows that the pilot diesel autoignites rather locally at 7 CAD aTDC (near the peak of HRR) and the premixed ammonia/air mixture is barely affected by the heat and radicals from the pilot ignition. Therefore, the pilot ignition likely exerts its impact through the pressure rise generated which compress the premixed charge to autoignition.

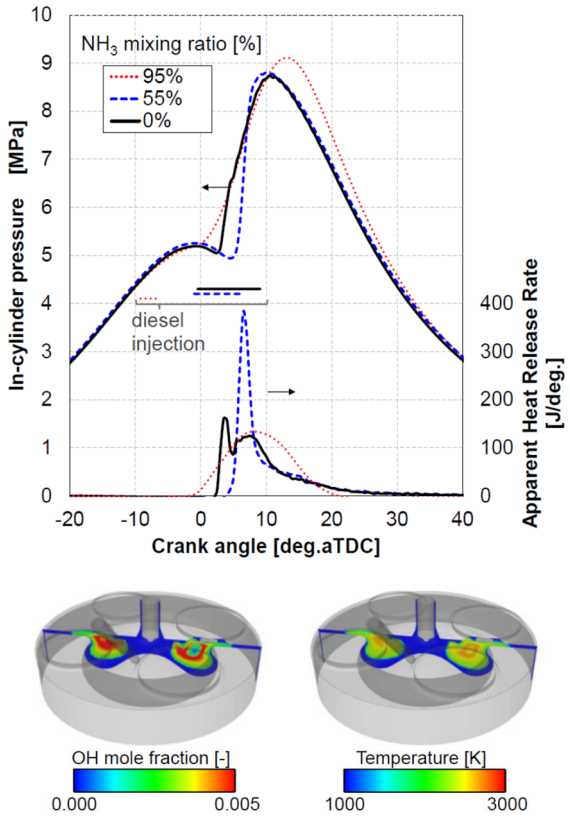

Fig. 7 Dual fuel CI engine combustion with 0, 55, and 95% ammonia by energy. Top: measured cylinder pressure and heat release rate. Bottom: calculated OH and temperature contour at 7 CAD aTDC with 95% ammonia blending [33].

Jin et al. investigated ammonia-diesel dual combustion in a 1.58 L single-cylinder engine (retrofitted from a six-cylinder engine) with a compression ratio of 18.5 [34]. Ammonia energy blending from 0-90% were investigated at 6 bar IMEP and 1000 rpm. The diesel injection timing was fixed at -14 CAD aTDC. Similar to the observation of Hiraoka et al., increasing ammonia content (0-50%) delayed the start of combustion, causing more rapid pressure rise and larger fraction burned in the premixed mode (Fig. 8). Above 50% of ammonia blending, the premixed burn fraction shrinked rapidly followed by a long tail of slow heat release, likely due to flame propagation through the rest ammonia charge. The combustion quality deteriorated with increasing ammonia blending, particularly for the 80% and 90% cases, indicating that the pilot fuel (injected at a fixed timing) became increasingly difficult to ignite the premixed charge. Split diesel injections have been attempted by the authors as

well as by Mi et al. [35] but the effectiveness was not evident.

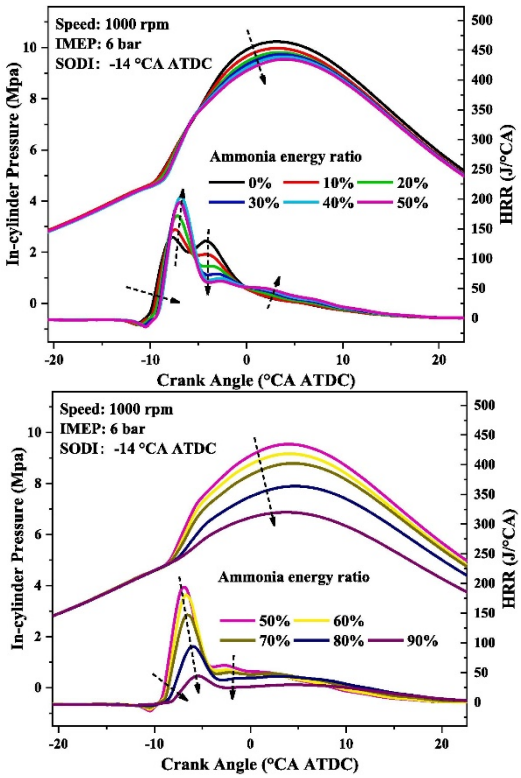

Fig. 8 Cylinder pressure and heat release rate of dual fuel CI engine combustion with 0-90% ammonia by energy at a fixed pilot injection timing [34].

Nadimi et al. investigated ammonia/diesel dual-fuel combustion in a 0.4 L single-cylinder engine with a CR of 16.5 at 1200 rpm [36]. Ammonia energy blending from 0-84% were studied at 7.5 bar IMEP. The pilot injection was fixed at 15.5 CAD bTDC. Similar impact of ammonia blending on heat release rates was reported. However, due to the base case having an overly advanced combustion timing (earlier than the MBT timing), the combustion retard caused by ammonia blending increased the thermal efficiency.

These studies indicated that injecting timing for the pilot fuel affects the combustion timing and engine performance. Mounaim Rousselle et al. investigated ammonia/n-dodecane dual-fuel combustion in a 0.5 L single-cylinder engine with a CR of 16.4 [37]. By varying the injection timing and applying split diesel injection (Fig. 9) they achieved 7.5 bar IMEP and 34% indicated thermal efficiency at 1000 rpm with as little as 1.5% n-dodecane by energy. Their results demonstrated the potential of optimizing injection strategy for controlling the combustion and minimizing the enhancer use for ammonia engine. However, injection optimization with practical diesel fuel under different engine operation conditions remain to be demonstrated.

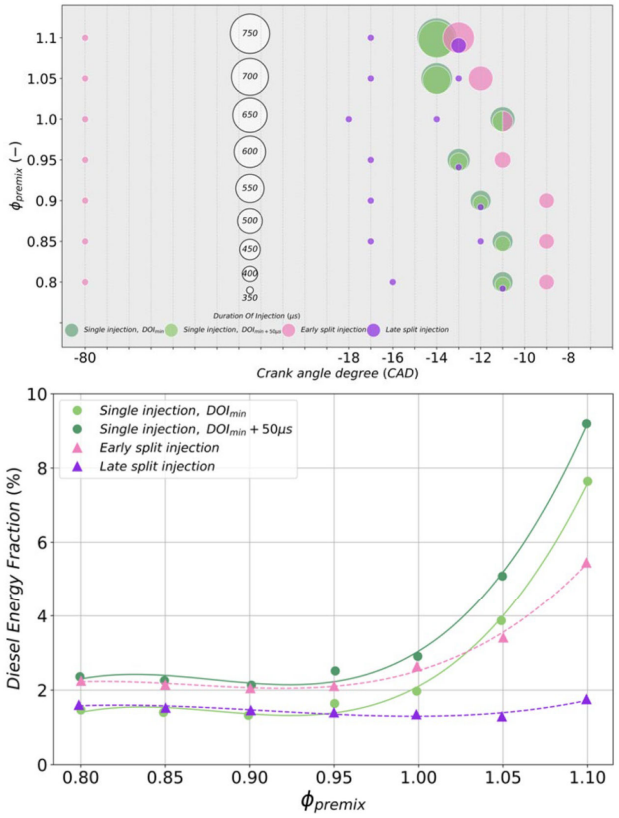

Fig. 9 Injection strategy (top) and diesel energy fraction required for achieving stable combustion (bottom) in a dual-fuel ammonia CI engine [37].

Ammonia-DME CI Engine The strong promotion of ammonia autoignition make DME a promising enhancer for CI engine. However, few studies have been conducted on this topic. Kong et al. [38,39] reported combustion of pre-blended ammonia-DME mixtures (with up to 60 wt% ammonia) in a 0.32 L single-cylinder engine with a compression ratio of 20:1. A GDI injector was used to deliver the blended fuel to the engine. The combustion occurred at low loads (up to 3.2 bar BMEP) and a range of injection timing was investigated over engine speed of 2200-3600 rpm. They reported that the engine operation became increasingly limited as more ammonia was blended due to the combustion becoming less stable and more HCCI like. An example result is shown in Fig. 10. Fumigating ammonia and direct injecting DME, as in the ammonia-diesel dual-fuel case, have not been reported.

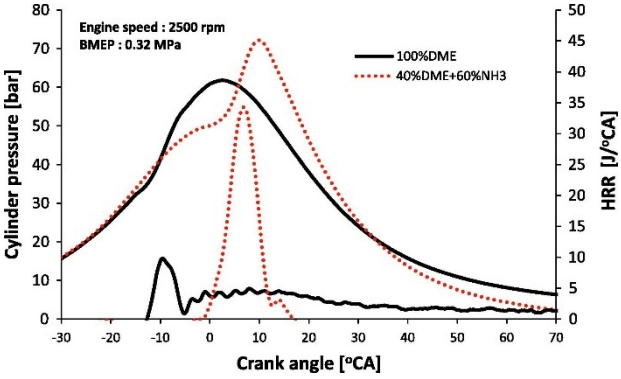

Fig. 10 Cylinder pressure and HRR of pure DME and 60 wt% ammonia in DME. SOI = 160 CAD bTDC [39].

Ammonia-Hydrogen CI Engine

Pochet et al. first investigated HCCI combustion with ammonia/hydrogen blends in a 0.5 L single-cylinder engine with a CR of 16:1 [40] and then in a 0.44 L single-cylinder engine with a CR of 22:1 [41], both at 1500 rpm. The experiment started with pure hydrogen, and ammonia was gradually introduced by increasing the intake temperature. For a given fuel energy input, increasing ammonia fraction reduced the heat release rate and the ringing intensity. As a result, for a given pressure rise rate, ammonia blends enabled higher engine load than pure hydrogen. HCCI combustion with up to 94 vol% ammonia was achieved. However, rather low load, ~ 5 bar IMEP, was reported [41].

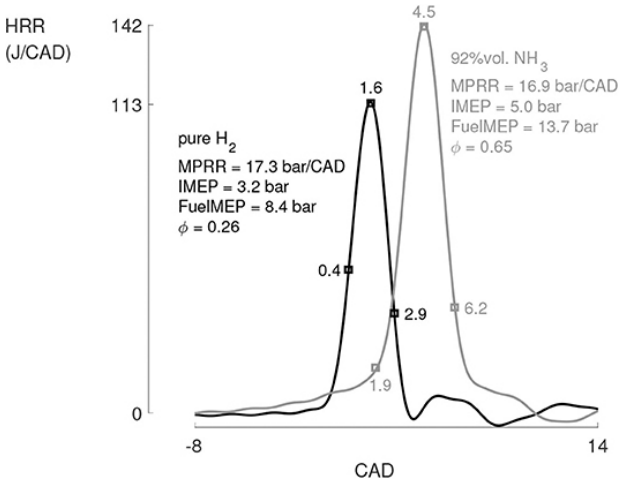

Fig. 11 Heat release rate of HCCI combustion with pure hydrogen and 8 vol% hydrogen in ammonia. At similar pressure rise rate, the ammonia/hydrogen mixture allows higher fuelling rate and engine load [41].

Given the lack of control for HCCI combustion, Reggeti et al. investigated spark-assisted compression ignition with ammonia/hydrogen mixtures in a CFR engine with a fixed CR of 18 at 900 and 1200 rpm [42]. The SACI approach has been demonstrated for neat ammonia by [43]. Stoichiometric mixtures were used with 0-5 vol% hydrogen in ammonia. Although the investigation was at rather low loads, ~3 bar IMEP, the spark assistance effectively promoted the combustion, and reduced the impact (requirement) of intake heating. Consequently, the combustion timing and duration are effectively controlled (Fig. 12). The energy release by the SI flame and autoignition is estimated, where the former accounted for ~ 25% of total energy release. In addition, the autoignition of ammonia/hydrogen mixtures show distinctively different response to spark advance compared with gasoline (Fig. 12). With ammonia blends, 1 CAD spark advance caused approximately ~ 1 CAD of autoignition advance, compared with ~ 0.2 CAD autoignition advance with gasoline. This is likely due to the slow heat release rate post autoignition. Additional investigation of engine speed, load, and cylinder charge motion/turbulence was recommended by the authors.

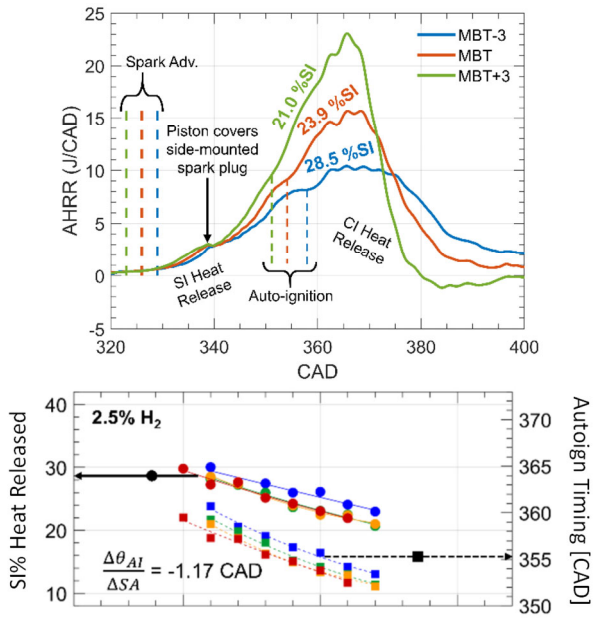

Fig. 12 Spark-assisted compression ignition of 2.5 vol% hydrogen in ammonia. Top: response of heat release rate to spark timing. Bottom: response of SI% of heat release and autoignition timing to spark timing [42].

4.3 Summary of Ammonia Engine Development

From the review in section, SI engines using hydrogen as the enhancer and dual fuel CI engine using diesel pilot are most advanced in term of development. CI engines using DME and hydrogen have been demonstrated but only at low loads. For all cases, further work is required to demonstrate engine load and thermal efficiency comparable to that using conventional fuels. This is a significant task, as modern turbocharged engines often achieve a BMEP of 20 bar, and 50% brake thermal efficiency is common for heavy duty engines. Out of the enhancer/engine combinations, SI engine with hydrogen as the enhancer might be limited by engine knock at high intake boost which is required for achieving high load. Dual-fuel diesel-ammonia engine might be limited by the diesel consumption which limits the GHG emission benefit. Advanced CI engines with DME and H2, although less developed at this stage, could offer more potentials given ammonia's high response to small additon of enhancers. Control of the combustion timing and heat release rate, the classic topic for low temperature combustion engines, are required for successful development of this technology. The slow oxidation kinetics of ammonia could offer some unique advantages in comparison with hydrocarbon fuels, as evidenced by the SACI combustion [42].

5. Concluding Remarks

Ammonia combustion, whether in a flame or via autoignition, is difficult to start and slow to complete. Fundamental experiments identified that enhancing ammonia's autoignition is much more effective than enhancing its flame propagation, suggesting CI engine as a more favourable venue for using ammonia fuels. Given the potential heavy-duty applications and the high cost of renewable fuels (both ammonia and enhancers), ammonia engine should be designed not only with reasonable burn rate but to deliver high performance combustion to utilize efficiently and effectively the carbon-free fuel. Major R&D efforts are required to achieve this target with the following fuel/engine combinations recommended from this review:

- SI engine with hydrogen as the enhancer. This needs to be combined with strong in-cylinder turbulence and to be further demonstrated for boosted combustion to achieve high load.
- Ammonia-diesel dual fuel CI engine with properly tuned injection strategy across engine operation map. Reducing diesel consumption is required to maximize the GHG emission benefit.
- Ammonia-DME CI engine with DME premixed with ammonia or injected as a pilot fuel. High load operation with robust combustion control is to be demonstrated. Minimizing DME consumption also required.
- Ammonia-Hydrogen premixed CI engine with ignition assistance. High load operation with robust combustion control is to be demonstrated with different ignition assistant methods.

Fundamental research is needed for 1) interaction chemistry between the nominated combustion enhancers and N-containing species from ammonia oxidation, and 2) thermo-kinetic-turbulence interactions related to hydrogen enhanced flame propagation and compression ignition with pilot fuel and spark assistance.

Although not reviewed in this work, direct injection of ammonia and enhancers could effectively increase the volumetric efficiency and enable high loads. The impact on charge preparation and combustion (flame or autoignition) should be investigated and understood.

6. References

[1] IEA, Energy consumption in international shipping by fuel in the Net Zero Scenario, 2010-2030, IEA, Paris.
[2] DNV GL, Maritime Forecast to 2050: Energy Transition Outlook 2023.
[3] L Dai, H Hashemi, P Glarborg et al. Combust Flame 227 (2021) 120–134.
[4] Z Zhang, W Long, P Dong et al. Fuel 332 (2023) 126086.
[5] L Wei, P Geng, Fuel Proc Tech 142 (2016) 264–278.
[6] ML Lavadera, X Han, AA Konnov, Energy Fuels 35 (2021), 7156−7168.
[7] ML Lavadera, M Pelucchi, AA Konnov, Combust Flame 237 (2022) 111839.
[8] C Tornatore, L Marchitto, P Sabia et al. Front Mech Eng 8 (2022) 944201
[9] H Kobayashi, A Hayakawa, K Somarathne et al. Proc Combust Inst 37 (2019) 109-133.
[10] GJ Gotama, A Hayakawa, EC Okafor et al. Combust Flame 236 (2022) 111753.
[11] KP Shrestha, C Lhuillier, AA Barbosa, et al. Proc Combust Inst 38 (2021) 2163–2174.
[12] A Stagni, C Cavallotti, S Arunthanayothin et al. React Chem Eng, 5 (2020) 696-711.
[13] P Glarborg, JA Miller, B Ruscic, et al. Prog Energy Combust Sci 67 (2018) 31–68.
[14] X Zhang, SP Moosakutty, RP Rajan, et al. Combust Flame 234 (2021) 111653.
[15] M Mehl, WJ Pitz, CK Westbrook et al. Proc Combust Inst, 33 (2011) 193-200.
[16] L Yu, W Zhou, Y Feng et al. Combust Flame 217 (2020) 4–11
[17] K Zhang, C Banyon, J Bugler et al. Combust. Flame 172 (2016) 116–135.
[18] LS Thorsen, MST Jensen, MS Pullich et al. Combust Flame 254 (2023) 112785.
[19] S Dong, B Wang, Z Jiang et al. Combust Flame 246 (2022) 112428.
[20] Y Zhang, W Zhou, Y Liang et al. Combust Flame 251 (2023) 112391
[21] Y Feng, J Zhu, Y Mao et al. Fuel 281 (2020) 118761.
[22] G Issayev, BR Giri, AM Elbaz et al. Renew Energy 181 (2022) 1353-1370.
[23] Y Jin , X Li , X Wang et al. Fuel 343 (2023) 127885.
[24] X He, B Shu, D Nascimento et al. Combust Flame 206 (2019) 189–200.
[25] L Dai, S Gersen, P Glarborg et al. Combust Flame 215 (2020) 134–144.
[26] J Chen, X Jiang, X Qin et al. Fuel 287 (2021) 119563.
[27] S Frigo, R Gentili. Int J Hydrogen Energy 38 (2013) 1607-1615
[28] M Comotti, S Frigo Int J Hydrogen Energy 40 (2015) 10673-10686.
[29] C Lhuillier, P Brequigny, F Contino et al. Fuel 269 (2020) 117448
[30] C Lhuillier, P Brequigny, F Contino et al. Proc Combust Inst 38 (2021) 5859-5868.
[31] CS Mørch, A Bjerre, MP Gøttrup et al. Fuel 90 (2011) 854–864.
[32] E Swift, S Kane, WF Northrop, Proc ASME ICEF2022-91825.
[33] K Hiraoka, D Matsunaga, T Kamino et al. SAE Tech Paper 2023-32-0102.
[34] S Jin , B Wu, Z Zi et al. Fuel 341 (2023) 127668.
[35] S Mi, H Wu, X Pei et al. Fuel 343, 127889.
[36] E Nadimi, G Przybyła, MT Lewandowski et al. J Energy Inst 107 (2023) 101158.
[37] C Mounaim Rousselle, P Brequigny, A Dupuy, SAE Tech Paper 2023-24-0076.
[38] CW Gross, SC Kong, Fuel 103 (2013) 1069–1079.
[39] K Ryu, GE Zacharakis-Jutz, SC Kong, Appl Energy 113 (2014) 488–499.
[40] M Pochet, I Truedsson, F Foucher et al SAE Tech Paper 2017-24-0087.
[41] M Pochet, H Jeanmart, F Contino, Front Mech Eng 6 (2020) 00043
[42] SA Reggeti, SP Kane, WF Northrop, J Ammonia Energy 1 (2023) 091–105.
[43] C Mounaïm-Rousselle, A Mercier, P Bréquigny et al. Int J Engine Res 23 (2021) 781-792.

Towards Clean Combustion and Decarbonisation
Proceedings of the Australian Combustion Symposium
26 – 29 November 2023, Darwin, Northern Territory, Australia

Characterisation of turbulent non-premixed hydrogen-blended flames in a scaled industrial low-swirl burner

A. J. Gee[1,*], N. Smith[2], A. Chinnici[1] and P. R. Medwell[1]
[1] School of Electrical and Mechanical Engineering, The University of Adelaide, Adelaide, SA 5005, Australia
[2]School of Chemical Engineering and Advanced Materials, The University of Adelaide, Adelaide, SA 5005, Australia

Abstract

The performance of a scaled industrial, non-premixed, low-swirl burner design was experimentally investigated for hydrogen addition to natural gas. Two strategies for introducing hydrogen are considered, namely, conserving (i) heat input and (ii) velocity/volumetric flow of the original fuel. This work characterises the effects on key performance metrics of the burner as hydrogen fraction is increased. Compared with natural gas, the results with hydrogen showed a 33% reduction in the radiant fraction and up to a 380% increase in NOx emissions. The lift-off height was reduced by a maximum of 23% and 51% for addition of 10 and 30 vol% hydrogen addition, respectively, with 100% cases becoming completely attached to the burner. The influence of hydrogen-addition strategy and air adjustment was shown to be significant with respect to NOx emissions but less significant than the resulting changes in fuel composition and heat input with respect to flame appearance, stability and radiant heat transfer.

Keywords: low-swirl, burner, non-premixed, turbulent, hydrogen

Artistic artificial intelligence images generated were based on the abstract content.

* Corresponding author:
Email: adam.gee@adelaide.edu.au

Clean Combustion and Decarbonisation Paper 2
B. Z. Dlugogorski and A. R. Masri, Eds

Towards Clean Combustion and Decarbonisation
Proceedings of the Australian Combustion Symposium
26 – 29 November 2023, Darwin, Northern Territory, Australia

Examining hydrogen premixed flames using a high-pressure burner

Abdulaziz Alahmadi *, Mohsen Talei and Yi Yang
Department of Mechanical Engineering,
The University of Melbourne, Parkville, Victoria, 3010, Australia

Abstract

This work introduces a burner aimed at studying combustion stability of turbulent hydrogen premixed flames at elevated pressures. The burner is designed to test a range of hydrogen mole fractions from 0-1. In this paper, the combustion stability of lean premixed hydrogen flames is investigated under a range of combustor pressures from 1.1 – 8.7 bar. The flow Reynolds number covered in the study varies between 6,000 and 29,700 while the equivalence ratio, flow velocity and the jet diameter are kept constant at 0.47, ~12 m/s, 5mm, respectively. The intensity of the flame heat release rate was estimated by capturing the OH^* chemiluminescence. The combustor pressure has an important impact on the flame shape and height. At elevated pressures, the flame shortens and the region with the maximum intensity of the heat release rate changes from the tip of the flame to the shoulder. There is also a non-monotonic relationship between the amplitude of the normalised pressure fluctuations and the combustor mean pressure, highlighting the complex interaction between the flame and chamber acoustics.

Keywords: hydrogen, combustion stability, canonical flame, flashback

Artistic artificial intelligence images were generated based on the abstract content.

* Corresponding author:
Phone: (+61) 468850333
Email: alahmadia@student.unimelb.edu.au

Clean Combustion and Decarbonisation Paper 3
B. Z. Dlugogorski and A. Masri, Eds

Towards Clean Combustion and Decarbonisation
Proceedings of the Australian Combustion Symposium
26 – 29 November 2023, Darwin, Northern Territory, Australia

Scalar mixing and flow dependence on seeding narrowband perturbation in reacting shear flows

M. N. Ali*, M. J. Cleary and B. Thornber
School of Aerospace, Mechanical and Mechatronic Engineering
The University of Sydney, Sydney, NSW 2006, Australia

Abstract

Direct numerical simulations of low Mach, transitional reacting syngas (CO/H2) counterflowing shear layers under three Kelvin-Helmholtz narrowband perturbations of different wavenumber ranges are performed. Transition to turbulence is induced by Kelvin-Helmholtz instabilities (KHIs) imposed on the initial velocity field through a vector potential approach to ensure a divergence-free velocity field in the initialisation. Integral mixing layer thickness measures were employed to track the growth of the reacting shear layer. The growth of the mixing layer is a function of the initial KHI perturbation wavelength and the streamwise velocity difference between the free streams, such that normalised plots of momentum and vorticity thicknesses showed evident collapse. Scalar dissipation thickness was compared between the different cases to characterise the onset of self-similar mixing, and it was determined that larger wavenumber initial perturbations achieve a more prominent mixing transition. This is supported by the mixture fraction variance where only the larger wavenumber cases homogenised their distinct scalar variance peaks. The enhanced mixing in larger wavenumber cases results in a more flamelet-like flame profile, as observed from pdfs of temperature and OH radicals.

Keywords: non-premixed, turbulent combustion, transitional regimes

1. Introduction

Turbulent mixing is a fundamental process that governs fluid flow behaviour in a wide range of natural and engineered systems. The challenge of studying turbulent mixing is due to the wide range of spatial and temporal scales involved and the coupling between the different fluid properties that affect the flow dynamics. With combustion, the complexity is exacerbated due to the interdependence of fluid dynamics, chemistry, and heat transfer. Therefore, understanding the primary turbulent-inducing instabilities and their mechanisms that lead to turbulent mixing is pivotal when optimising and designing for applications where turbulent mixing is critical.

Direct numerical simulations (DNS) of temporally evolving, reacting shear layers are performed here. Shear layer configurations have been extensively adopted [1,2]. Since the focus has normally been on the fully developed turbulent state rather than the transitional regime, the initial conditions in such studies usually consist of a broadband isotropic turbulent energy spectrum producing a rapid development of fully developed turbulence. Reacting shear-layer studies focusing on initialising the flow field with physically realistic initial perturbations are scarce. Some earlier work indicates that although the effects of initial conditions are diluted when the flow reaches fully developed turbulence, a degree of sensitivity remains. For example, there are discrepancies between experiments conducted to measure the normalised vorticity thickness and other turbulent statistics in fully developed high Reynolds number mixing layers [3]. This is particularly important to combustion applications, implying that initial flow conditions can influence species mixing and flame stability.

Non-reacting mixing layer research suggests that the fully developed turbulent state exhibits some sensitivity to the narrowband wavelength range of the primary KHI instabilities. Vreman et al. [4] thoroughly compared dynamic and non-dynamic subgrid models for the turbulent stress tensor employing incompressible large-eddy simulations. They built up on Rogers & Moser's [5] focus on vortex pairing events as the transition-inducing phenomena in mixing layers by realising that a state of self-similarity is only achieved in their LES if at least three pairing events took place. This finding has indirect implications on the wavelength of the seeding perturbation as it dictates, particularly for temporal simulations, that the most unstable mode of the perturbation should not have a wavelength greater than 1/8th of the streamwise domain dimension if fully developed turbulence is to be achieved. Baltzer [2] used this finding to investigate variable density effects in shear flows. The initial perturbation was seeded by 64 wavelengths of the most unstable mode in all their simulations, indicating six different vortex pairing events, i.e. double the number of pairing events suggested in [4]. This ensured a quick transition to turbulence and clear self-similarity. Almagro et al. [6] stressed the importance of running different realisations of the same initial conditions used by Pantano [1], finding that slight variations of the initial conditions (while still pertaining to the same overall spectral profile) affect the late time turbulent structures and statistics observed, where late time is defined as the time-period when the flow evolution is statistically characterized as self-similar [1-3,5-6].

The present work is part of ongoing research to understand transition to turbulence in reacting flows with particular interest in its application to high-speed propulsion where fuel and oxidiser may be initially laminar but rapid mixing is required for viable combustion. Specifically, we analyse the dependence of late-time mixing statistics on primary Kelvin-Helmholtz

* Corresponding author: Moustafa Ali
Email: mali5094@uni.sydney.edu.au

instabilities with different narrowband wavelength ranges.

2. Simulation Setup

The DNS is undertaken using the compressible solver called Flamenco. It is a Godunov-type finite volume solver run with a fifth-order MUSCL scheme for the spatial reconstruction of the inviscid terms [9]. To reduce dissipation and maintain adequate resolution of low Mach features, the pressure and density variations are scaled through a low Mach correction while still utilising the compressible governing equations [10]. The Harten, Lax and Leer Contact (HLLC) Riemann solver calculates the inviscid flux component [11], while the viscous and diffusive terms are computed using second-order central differences. Temporal integration is achieved via a second-order total variation diminishing (TVD) Runge–Kutta scheme[12]. The ideal-gas law is used for the thermodynamics with JANAF polynomials used to compute the specific heat capacities and hence the internal energies and enthalpies. Non-differential diffusion with unity Lewis number assumption is employed as the effect of differential diffusion on the present flow conditions is minimal [7,8]. Temperature-dependent viscosity is modelled by Sutherland's law, and Fourier heat conduction and Fickian molecular diffusion models are used. Since all species have equal diffusivities, the same Sutherland constants are employed throughout. The thermal conductivity is calculated from the kinetic theory. Hence, the resulting Schmidt (Sc) and Prandtl (Pr) numbers across the domain are equal (due to the unity Lewis number) but not explicitly defined. Inspection of the initial conditions shows a domain average Sc/Pr of ~0.7, which is common in studies for fuel-air mixtures [1].

The flow setup is based on the temporally evolving, non-premixed syngas shear layer DNS in [7]. The computational domain is 3D Cartesian, with x,y, and z

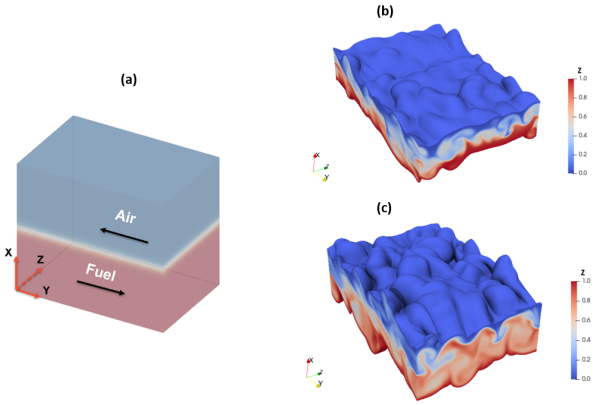

Figure 1 Domain setup and coordinate system (a) and surface contours of mixture fraction in Case A at $\frac{t\Delta U}{\lambda_{min,0}} = 10$*(b) and late time corresponding to Comparison Point marked in Figure 3.*

denoting the cross-stream, streamwise, and spanwise directions, respectively, as shown in Figure 1. The syngas fuel stream is diluted with nitrogen to allow for a computationally affordable, resolved reaction zone. The H2:CO:N2 volume ratio of 1:5:4 giving a stoichiometric mixture fraction of 0.42. The oxidiser stream is a 1:4 by-volume mixture of O2 and N2. Initially, the fuel and oxidiser free-streams flow in opposite directions with a velocity magnitude of $\frac{\Delta U}{2}$ and a differential of ΔU. Both free streams have an initial temperature of 500 K. The densities of the free-stream fuel and oxidiser streams are 0.5429 kg/m^3 and 0.7071 kg/m^3, respectively.

Table 1 provides an overview of the three DNS cases investigated here. The KHI is induced via a narrowband range of multimode velocity perturbations (derived from linear theory) at the fuel-oxidiser interface. Three different narrowband ranges are discussed here where $\overline{k_{min}}$ and $\overline{k_{max}}$ denote the smallest and largest wavenumber for each case and $\overline{k_0} = \frac{2\pi}{L_y}$. All three velocity perturbations have the same total energy in spectral space. The term narrow is used here to emphasize the narrow bandwidth of the perturbation length scale, where the ratio of the largest to smallest perturbation wavelength does not exceed 2 as shown in Table 1. The Mach number was increased with increasing wavenumber range to keep the initial Reynolds number constant. Although Case C has the same non-dimensional initial wavenumber range as A, it has a larger domain. This results in an effectively larger narrowband range, hence the lower initial Mach number.

Table 1 Case names and simulation parameters.

Case	Ma_c	$\frac{\overline{k_{min}}}{\overline{k_0}} \le n \le \frac{\overline{k_{max}}}{\overline{k_0}}$	$\frac{L_x}{\delta_{m,0}} \times \frac{L_y}{\delta_{m,0}} \times \frac{L_z}{\delta_{m,0}}$	$N_x \times N_y \times N_z$
A	0.16	$4 \le n \le 8$	$524.2 \times 600 \times 400$	$504 \times 576 \times 384$
B	0.32	$8 \le n \le 16$	$524.2 \times 600 \times 400$	$1344 \times 1152 \times 768$
C	0.08	$4 \le n \le 8$	$699 \times 1200 \times 800$	$336 \times 576 \times 384$

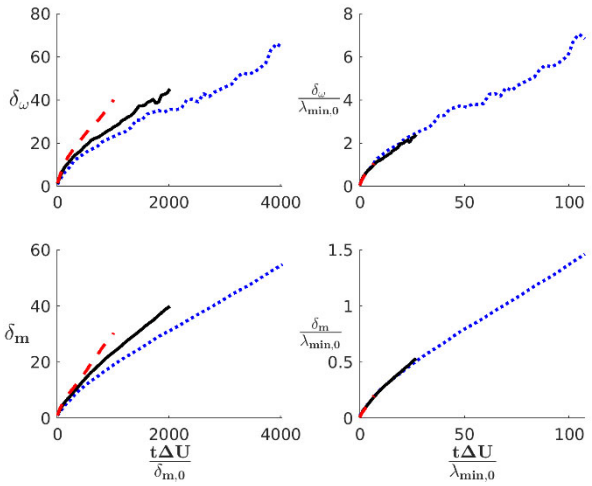

Figure 2 Integral mixing layer thicknesses for Case A (solid black), Case B (dotted blue), and Case C (dashed red). Simulations are stopped once domain boundary effects become important.

The grid resolutions are provided in Table 1. A thorough mesh convergence study was conducted for Case A, where three different mesh resolutions were considered, doubling the resolution between each case. The convergence study (not shown for brevity) showed grid convergence for key second-order fluctuation gradients including scalar dissipation, integral, Taylor, and Kolmogorov length scales, and integral scalar measures including total turbulent kinetic energy, enstrophy, and heat release rate. The grid resolutions for Cases B and C were obtained through scaling (from the converged resolution of A's mesh convergence study) with the initial narrowband KHI wavelength range.

3.Results

Figure 1 (b) shows isosurfaces of mixture fraction in the vicinity of the mixing layer around the start of the onset of turbulence where the initial perturbations have non-linearly grown to form non-coherent vortex structures that are beginning to exhibit three-dimensional variation. Figure 1(c) shows the mixture fraction isosurfaces at later time which is more representative of turbulent mixing behaviour.

Our focus is on the late time fields and their dependence on the initial narrowband wavelength range of the perturbations. Figure 2 shows the evolution of two integral measures of mixing layer thickness, namely the momentum thickness, δ_m, and the vorticity thickness, δ_ω. These are defined as:

$$\delta_m = \int_{-\infty}^{\infty} \left(\frac{1}{4} - \frac{\overline{U_2}^2}{\Delta U^2} \right) dx \quad (1)$$

$$\delta_\omega = \frac{1}{|\overline{\omega_3}_{,max}|} \int_{-\infty}^{\infty} |\overline{\omega_3}| \, dx \quad (2)$$

Quantities denoted by $\overline{(.)}$, are ensemble averages in the homogeneous plane at a given time instant. $\overline{U_2}$ is the streamwise velocity, and $\overline{\omega_3}$ is the spanwise vorticity. Both thicknesses show a similar trend where cases that are initialised with smaller wavenumbers have slower growth but can attain higher non-dimensional time before domain boundary effects become apparent. Figure 2 (right) shows that upon normalizing both the time and the thickness measures by the initial perturbation minimum wavelength, λ_{min}, there is a collapse to a single trend. At late times the trend is linear representing self-similar fully turbulent regime with constant growth rate. The results in Figure 2 indicate a direct dependence of mixing layer growth on the initial perturbation and that this dependence extends to late time, beyond the initial transition period regime.

To better observe the extent of the self-similar mixing regime attained by each of the cases, time evolution of the scalar dissipation thickness:

$$L_\chi = \int_{-\infty}^{\infty} (2D\widetilde{(\nabla Z'')^2}) \, dx \quad (3)$$

is shown in Figure 3, where L_χ is normalized by the product of the Favre averaged variance in the domain center plane and ΔU. After an initial rapid growth, the scalar dissipation thickness in Case B and to a lesser extent in Case A tend to stabilize to a constant value, indicating that larger wavenumber perturbations are better predisposed to sustaining self-similar evolution. With time evolution, the mixing layers are growing as shown in Figure 2, but scalar gradients are reducing due to enhanced mixing, so in self-similar growth, these two effects are expected to balance such that a total measure of the diminishing scalar gradients in the vicinity of the growing mixing layer should stabilise to a constant value. To compare these two cases at late time, the non-dimensional time corresponding to a similar L_χ value between the two cases is indicated by a cross on the right plot for Figure 3. The oscillations observed in the smaller wavenumber cases are indicative of mode saturation and statistical noise due to finite domain effects as the mixing layer significantly extends in the cross-stream direction as shown in Figure 4 (b) for Case A relative to (c) for Case B. The effect this has on mixing and flame development is observed through Favre plane averaged mixture fraction variance as outlined for the different cases at three different times in Figure 4 (a).

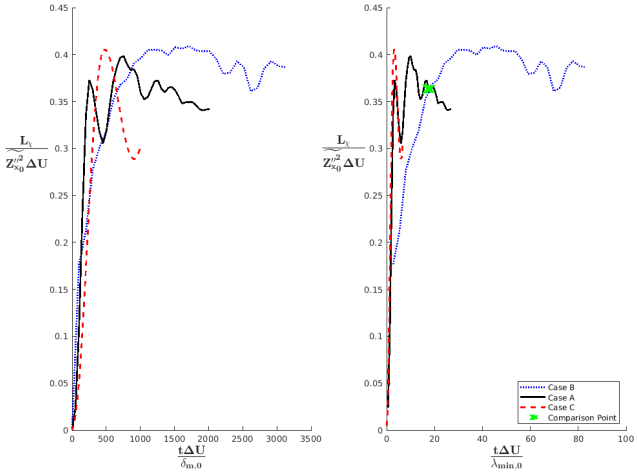

Figure 3 Scalar dissipation thickness measure with time normalised by initial momentum thickness (left) and initial perturbation wavelength (right). Same plot colour reference as Figure1.

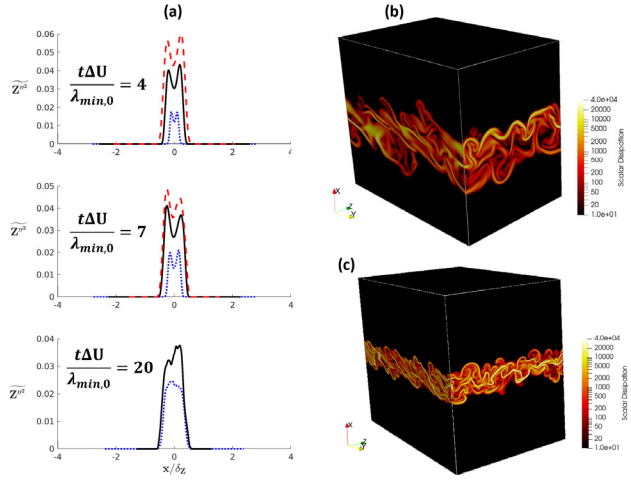

Figure 4 Favre averaged mixture fraction (a) with same plot colour reference as previous figures, and scalar dissipation contours for Case A (b) and Case B (c) at normalised time corresponding to the Comparison Point marked in Figure 3.

The last row of plots in Figure 4 (a) corresponds to the non-dimensional time marked in Figure 3, which is not attained by Case C. At early time, the mixture fraction variance forms two distinct peaks for all cases as expected

due to the entrainment of fuel and oxidizer streams to the center of the mixing layer leading to sharp differences in mixture fraction at the interface of the shear layer with the free streams. As the mixing layer grows and homogenizes, these two distinct peaks should merge into a single peak, which is a defining element of the mixing transition onset. This is clearly observed for B at the same normalized time where its scalar dissipation thickness begins its plateau, while A is still within the transitional mixing regime. The heat release rate plots indicate more burning with higher wavenumbers. Inspection of conditional pdfs in Figure 5 help explain the difference in flame behaviour between Cases B and A at the same normalized time.

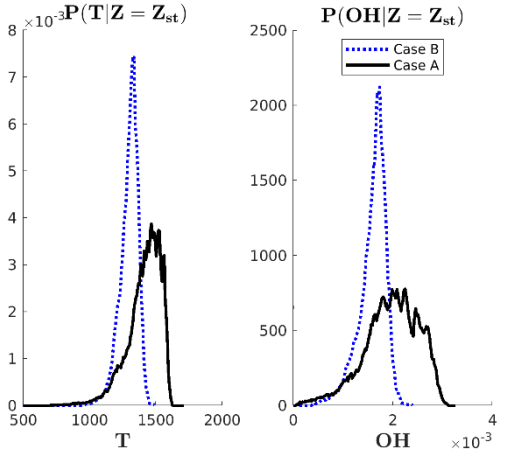

Figure 5 Conditional pdfs at stoichiometric mixture fraction are shown for both temperature and OH at normalised time corresponding to the Comparison Point marked in Figure 3 .

B sustains a more uniform flame with a thick reaction zone (not shown here) and a more flamelet-representative behavior. Whereas A's pdfs showcase a more distributed flame with isolated pockets that increasingly ignite over time and therefore produce higher absolute temperature and OH mass fraction values. This aligns with the mixing behavior of both cases, which explains the resulting flame attributes.

4.Conclusion

The effect of the initial perturbation wavelengths on the mixing layer development and chemistry in reacting shear layers is investigated. The growth of the mixing layer, even at late times, appears to be directly dependent on the initial narrowband wavelength range of the perturbation. Mixing layers induced by perturbations of larger narrowband wavenumbers grow less rapidly than ones induced by smaller wavenumbers. However, larger wavenumber cases can attain the mixing transition and self-similarly evolve, while smaller wavenumber cases are more resistant to transitioning into a fully turbulent regime. This could simply be due to smaller wavenumber cases requiring longer absolute time to reach the same normalized time $\left(\frac{t\Delta U}{\lambda_{min,0}}\right)$. However, discrepancies continue to manifest in the mixing statistics, at the same normalized time instance for the different cases, even when it is late enough in the flow evolution such that the rate of mixing appears to have stabilized. This potentially indicates that time is not the only factor to affect the onset of self-similar mixing with varying the initial perturbation wavenumber. The disparity in the mixing behavior between the cases results in clear distinction in the late-time flame profiles and combustion efficiency even at times when the different cases maintain similar scalar dissipation measures.

5. References

[1] J. R. Baltzer and D. Livescu, "Variable-density effects in incompressible non-buoyant shear-driven turbulent mixing layers," Journal of Fluid Mechanics, vol. 900, p. A16, 2020.

[2] C. Pantano and S. Sarkar, "A study of compressibility effects in the high-speed turbulent shear layer using direct simulation," Journal of fluid mechanics, vol. 451, pp. 329-371, 2002.

[3] I. Wygnanski and H. E. Fiedler, "The two-dimensional mixing region," Journal of Fluid Mechanics, vol. 41, no. 2, pp. 327-361, 1970.

[4] B. Vreman, B. Geurts, and H. Kuerten, "Large-eddy simulation of the turbulent mixing layer," Journal of fluid mechanics, vol. 339, pp. 357-390, 1997.

[5] M. M. Rogers and R. D. Moser, "Direct simulation of a self-similar turbulent mixing layer," Physics of Fluids, vol. 6, no. 2, pp. 903-923, 1994.

[6] A. Almagro, M. García-Villalba, and O. Flores, "A numerical study of a variable-density low-speed turbulent mixing layer," Journal of Fluid Mechanics, vol. 830, pp. 569-601, 2017.

[7] E. R. Hawkes, R. Sankaran, J. C. Sutherland, and J. H. Chen, "Scalar mixing in direct numerical simulations of temporally evolving plane jet flames with skeletal CO/H2 kinetics," Proceedings of the combustion institute, vol. 31, no. 1, pp. 1633-1640, 2007.

[8] S. Vo, O. Stein, A. Kronenburg, and M. Cleary, "Assessment of mixing time scales for a sparse particle method," Combustion and Flame, vol. 179, pp. 280-299, 2017.

[9] K. H. Kim and C. Kim, "Accurate, efficient and monotonic numerical methods for multi-dimensional compressible flows: Part II: Multi-dimensional limiting process," Journal of computational physics, vol. 208, no. 2, pp. 570-615, 2005.

[10] B. Thornber, A. Mosedale, D. Drikakis, D. Youngs, and R. J. Williams, "An improved reconstruction method for compressible flows with low Mach number features," Journal of computational Physics, vol. 227, no. 10, pp. 4873-4894, 2008.

[11] E. F. Toro, M. Spruce, and W. Speares, "Restoration of the contact surface in the HLL-Riemann solver," Shock waves, vol. 4, pp. 25-34, 1994.

[12] R. J. Spiteri and S. J. Ruuth, "A new class of optimal high-order strong-stability-preserving time discretisation methods," SIAM Journal on Numerical Analysis, vol. 40, no. 2, pp. 469-491, 200

Towards Clean Combustion and Decarbonisation
Proceedings of the Australian Combustion Symposium
26 – 29 November 2023, Darwin, Northern Territory, Australia

The effect of pressure on flame stability for CH_4 and H_2/NH_3 piloted jet flames

A. R. W. Macfarlane[1, *], C. D. Avila Jimenez[2], T. Guiberti[2], M. J. Dunn[1] and A. R. Masri[1]
[1]School of Aerospace, Mechanical, and Mechatronic Engineering, The University of Sydney, NSW, Australia
[2] Clean Combustion Research, King Abdullah University of Science and Technology (KAUST). Saudi Arabia

Abstract

This paper employs the Sydney inhomogeneous burner to report novel measurements of flame stability for CH_4 and blends of H_2 with NH_3 at a range of pressures. The CH_4 flames cover a range of pressures from 1-4 bar for two pilot power configurations. The NH_3 flames are blended with 40%, 30 % and 20 % H_2 for two pressures, 1 and 2 bar. All fuels show a decrease in blow-off velocity for an increase in pressure, although correspondingly, an increase in Reynolds number blow-off with pressure. High-speed 10 kHz OH-PLIF imaging was obtained to highlight how the OH layer becomes unstable and broken as the flames approach blow-off and further indicate the relative differences in break-up for different pressures. For the comparable CH_4 laminar flame speed, a blend of NH_3/H_2=60/40, the NH_3/H_2 flame had a significantly higher blow-off velocity, further emphasized by the lower powered pilot required. Laminar 1-D opposed flow calculations show the difference in stability between methane and NH_3/H_2, are more closely related to extinction strain rates, attributed to H_2 diffusion.

Keywords: turbulent jet flames, flame stability, high pressure

1 Introduction

As the energy sector progresses towards decarbonization, power fuels such as H_2 and NH_3 are becoming increasingly important [1]. Ammonia and H_2 have somewhat complementary properties. Gaseous H_2 has a very high flame speed, wide flammability limits and low volumetric energy density. Contrarily, liquid NH_3 has a low flame speed, narrow flammability limits and relatively high energy density [2]. The complementary properties mean that blending, and furthermore, partial cracking of NH_3 is a viable option. The large global energy demand entails that the process will be slow to switch to these fuels, since the infrastructure is currently unavailable. As such hydrocarbon-based fuels will be highly relevant for the foreseeable future, and partial blending with these green fuels will be a viable alternative in the near term.

The need to understand the combustion process of NH_3/H_2, and the varying the blends, is therefore the focus of the paper. The focus is to understand these blends in relation to CH_4, where a NH_3/H_2 blend, comparable to the flame speed of CH_4 is used. Furthermore, the fuels were characterised under turbulent and elevated pressure conditions, where flame speeds and diffusion change significantly, particularly relevant for H_2. A comparison between CH_4 and blends of $H_2/NH_3/N_2$ (cracked 40 %), in a turbulent bluff-body burner [3], highlighted that the blow-off velocity was an order of magnitude higher for the NH_3 blend. Furthermore, Raman-based measurements of $NH_3/H_2/N_2$ jet flames showed that significant H_2 diffusion occurred near the nozzle, ahead of the NH_3, providing additional stability [4].

The Sydney inhomogeneous burner [5] was used, in this study, in the KAUST high pressure (HPCD) duct operating at partially premixed/ homogeneous conditions. The flow through duct enables high-pressure conditions in a controlled experimental manner, with laser and optical access. This paper presents novel results to understand the sensitivity of NH_3 addition to H_2 piloted jet flames at atmospheric and high-pressure conditions. In addition, it extends the understanding of the well-studied inhomogeneous burner, to now include pressure effects and correlations.

2 Setup

The Sydney inhomogeneous burner was used throughout this experiment. The burner consists of three concentric tubes, an outer pilot, with an inner diameter ($Ø_{P,\ ID}$ = 13 mm), the middle annulus($Ø_{A,\ ID}$ = 5.5 mm) and the central jet($Ø_{J,\ ID}$ = 2.85 mm). The fuel enters through the central fuel jet and the air through the annulus. The mixing within this burner is controlled by recessing the central fuel jet within the annulus, providing inhomogeneous conditions. The equivalence ratio is the global equivalence ratio between the fuel and air and is kept constant at φ=4.76 throughout the study. Throughout this paper, the burner was operated in the homogeneous mode with a recess distance of L_r = 300 mm, such that the fuel and air are well mixed by the exit plane for this jet recess.

The experiment was conducted in the High-Pressure Combustion Duct (HPCD) at KAUST. The combustion duct consists of two high-flow rate air supplies, one for the annulus and one for the coflow, that shrouds the burner. The pressure is maintained using a diaphragm that is either closed or opened to increase or decrease the

* Corresponding author:
Phone: (+61) 2 93517150
Email: amac7548@uni.sydney.edu.au

pressure respectively. An additional bypass valve enables an increased amount of air to flow through the chamber to better regulate the temperature and acoustic stability of the duct.

A high-speed 10 kHz Edgewave Nd:YAG laser was used to pump ethanol and rhodamine 6G dye to excite the Q_1 OH branch at 283.9 nm. The system produced approximately 2.5 W at 283 nm, such that the laser beam could be expanded to produce a 100 mm beam at the probe volume. The beam was expanded using a F = -20 mm cylindrical lens in combination with a F = 1000 mm focal lens, to create a 100mm high by 200 µm sheet. The duct consists of six windows, one quartz window enables the UV, 283 nm, laser to enter whilst another quartz window is used to collect the ~310 nm UV emission. The planar laser induced fluorescence (PLIF) emission was collected using a Cerco UV 100 mm F/2.8 Sodern lens, coupled to a dual stage intensifier with a LaVision 10 kHz camera; ambient light and interference were removed using a 310nm ±10 nm band pass filter.

3 Experimental Description

The pilot composition was ethylene (C_2H_4) and air, for each fuel. However, it was stoichiometric for the CH_4 flames and lean (φ = 0.8) for the NH_3/ H_2 flames. The equivalence ratio was altered to ensure that the pilot cones always exited the tip of the pilot, for a chosen pilot power. The NH_3/H_2 flames, particularly NH_3/H_2 = 60/40, were highly reactive and difficult to achieve blow-off at a reasonable stoichiometric pilot of Q_{Pilot} = 1200 – 1800 W, which was used for CH_4. Therefore, a lowered pilot power of Q_{Pilot}= 300 – 600 W was used; the lean composition was required to produce elongated pilot cones. Scaling of blow-off velocity and pilot power has previously been studied [6] and showed to have a stronger dependance on pilot adiabatic flame temperature. As such, the difference between the powers for the CH_4 and H_2 flames are well understood and further highlighted the reactive nature of the H_2/NH_3 blends.

The pilot was increased from Q_{Pilot} = 1200 to 1800 W for pressures exceeding 3 bar for the CH_4 flames; this ensured that the pilot cones still exited the pilot tip. Similarly, the pilot was increased from Q_{Pilot} = 300 to 600 W for the NH_3/H_2=70/30 flames at 4 bar. A common pressure was taken at the lower and higher pilot powers, for each fuel, to obtain the relevant stability differences. The pilot, pressures and fuels used throughout the experiment are given in Table 1.

At high pressures, high flow rates up to 100 SLM of CH_4 and NH_3 were required. These high flow rates produce significant power of up to 80 kW in the duct, creating high temperatures in the exhaust. The high temperatures can cause damage to the diaphragm, as such, the burner is turned on for short periods; turned on long enough to establish steady-state conditions, identify blow-off and take OH measurements. This in turn meant that the OH-PLIF measurements needed to be taken at high speed, where 1000 images were taken here for each condition and location.

Table 1 Fuels used and their corresponding pressures and pilot conditions, the asterix (*) indicates the similar CH_4 and H_2/NH_3 flame speed case.

Fuel jet	Pressure (Bar)	Q_{Pilot} (W)	Φ_{Global}	S_L *(cm/s)*
CH_4	-1, 1.5, 2, 2.5, 3 -3, 3.5, 4	-1200 -1800	4.76	37*
NH_3/H_2=60/40	-1, 2	-300	4.76	30*
NH_3/H_2=70/30	-1, 2 -4	-300 -600	4.76	17
NH_3/H_2=80/20	- 1, 2	-300	4.76	12

It is noted, that if a pilot power is to be maintained across a range of pressures, the length of the pilot cones should be significant at the lower pressure. An increase in pressure correspondingly increases the density and reduces the velocity. Therefore, at higher pressure, the flash back propensity significantly increases due to both a lower velocity but also a reduction in the quenching distance.

Velocities for each fuel varied from 10 m/s until blow-off, at roughly 5- 10 m/s increments. At each velocity, 1000 OH-PLIF images were recorded. The OH-PLIF was used to identify how, with increasing velocity, the flame structure changed as it approached blow-off. The OH-PLIF methodology was particularly required for high pressures where significant flow rates couldn't be reached, or the acoustic feedback in the chamber was such that the blow-off velocity couldn't be achieved.

The camera was fixed at a height of~ 60 mm above the burner, the field of view (FOV) captured the location just above the pilot and included the known region of local extinction, around 10 – 15 *x/D*. For specific velocities, including low (stable), medium (partial extinction) and at 80 % blow-off, full flame images were taken.

4 Results

Single OH-PLIF images for CH_4 are presented in Figure 1 for 1 bar and a range of velocities approaching blow-off. The CH_4 flame images, of OH, are like those for NH_3/H_2 so for brevity they are not presented here. It is evident that at 10 – 40 m/s there is a continuous OH layer on either side of the central fuel jet. At 50 m/s, the OH layer is no longer continuous, where breaks in the OH layer are observed around 16 *x/D.* For increasing velocity, the OH layer further breaks, and by 70 m/s, the breaks have gotten larger and moved farther upstream, to about 9 *x/D*. Further increasing the velocity to 90 m/s, there are now larger portions without OH, and the only continuous OH layer is at 3 *x/D* to 8 *x/D*, and this is due to the pilot.

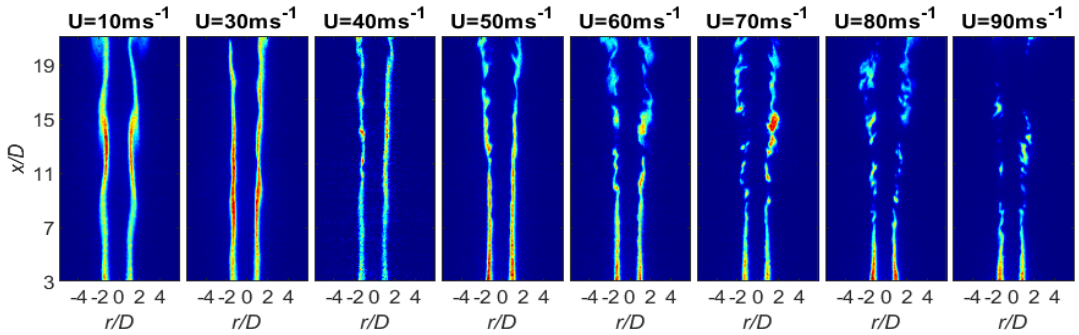

Figure 1: Instantaneous OH-PLIF images for CH_4 at 1 bar for a range of velocities approaching blow-off.

For this CH_4 case (1 bar), the blow-off velocity was determined to be 95 ms^{-1}. As such, the U = 90 ms^{-1} image is at 95 % blow-off. Similarly, U = 75 ms^{-1} is at 80 % of blow-off (shown in Figure 2). This velocity case exhibits a continuous flame front near the pilot and extinction events around 15 *x/D*.

The full flame OH-PLIF images are shown in Figure 2, for three velocities for the CH_4 flames, at 1 bar, given in Figure 1. The almost laminar flame, at 10 ms^{-1}, has a continuous OH structure upstream. The 40 ms^{-1} flame, equating to 42 % blow-off, is still momentum-driven downstream with two distinct OH layers. For the 75 ms^{-1} case (80 % of the blow-off velocity) there are distinct breaks in the OH layer, as seen in Figure 2Figure 1. It can now be seen that downstream, at around 30 *x/D*, the flame reignites where the velocity and local scalar gradients have decreased.

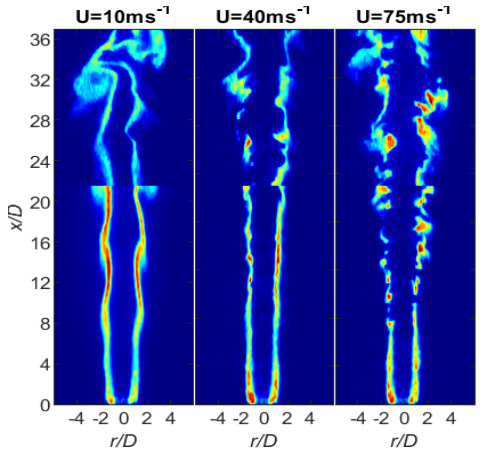

Figure 2 Full flame images for CH4, for three velocities

A comparison between the CH_4 flames at 1 bar and 3 bar are shown in Figure 3. It is evident that for the same velocities, U = 10, 20 and 50 ms^{-1} the higher-pressure flame has significantly more OH breaks. There are breaks in the OH layer for a jet velocity of U = 20 ms^{-1}, for a pressure of 3 bar. Conversely, the OH layer does not break until around 50 ms^{-1} for 1 bar. For this high-pressure (3 bar) flame the blow-off velocity is at 60 ms^{-1}. It is evident that the OH layer has thinned with increased pressure, however, this is not within the scope of this paper.

The difference in the blow-off velocity is consistent for all pressures. Whereby, an increase in pressure decreases the blow-off velocity. Whilst the blow-off velocity has reduced the blow-off Reynolds number has increased. The relationship between blow-off velocity and pressure is seen in Figure 4.

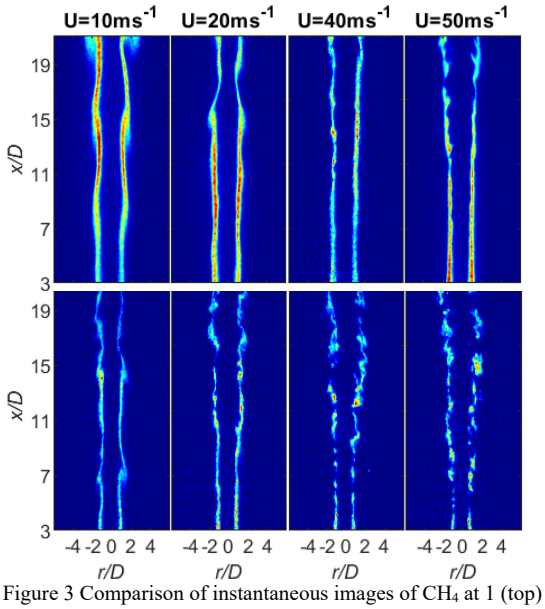

Figure 3 Comparison of instantaneous images of CH_4 at 1 (top) and 3 bar (bottom)

Figure 4 (CH_4) shows for an increase in pressure, with a constant pilot power (Q_{Pilot} = 1200 W), the blow-off velocity reduces from 95 ms^{-1} to 60 ms^{-1} for 1 and 3 bars respectively. For an increase in pilot power of 50%, Q_{Pilot} = 1800 W, the blow-off velocity has increased by 21 %. For this higher pilot power there is a similar correlation between pressure and blow-off velocity. The blow-off velocity is U = 76 and 60 ms^{-1} for P = 3 and 4 bar respectively.

The reduction in blow-off velocity, for CH_4, with increasing pressure is consistent for NH_3/H_2 flames, seen in Figure 4. The three different NH_3 blends of: 60, 70 and 80 % are given by the triangles, circles and squares, respectively. The dashed black line shows a common 70 % NH_3 case for a different pilot (Q_{Pilot} = 600 W).

It can be observed when comparing NH_3/H_2=60/40 with CH_4, the NH_3/H_2 flame has a higher blow-off velocity.

The 60/40 blend has a higher blow-off velocity of U = 110 ms^{-1}, whilst CH_4 has a velocity of U = 95 m.s^{-1}. This blend percentage has approximately the same flame speed as CH_4. It is further noted that the pilot power and adiabatic flame temperature are significantly lower, Q_{Pilot} = 300 W versus 1200 W, for NH_3/H_2=60/40. The significantly more stable flame is attributed to the diffusion of H_2 and discussed in the final section.

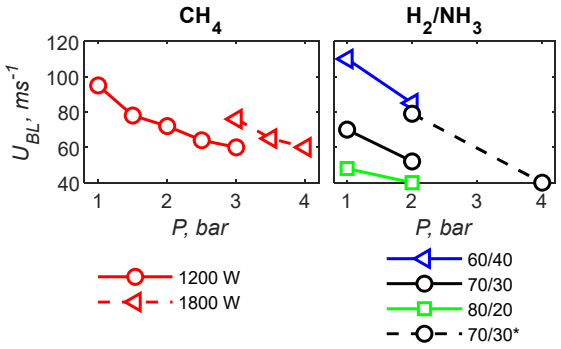

Figure 4: Blow-off velocity for CH_4 flames (left) and blends of NH_3/H_2 (right) vs pressure. Dashed lines indicate high pilot power.

Figure 5 compares the blow-off velocities for different NH_3 percentages for two pressures at the same pilot, Q_{Pilot} = 300 W. It is evident that for an increase in NH_3 content, there is a significant decrease in blow-off velocity. The decrease in blow-off velocity for the addition of H_2 is non-linear for the percentages studied. The decrease in blow-off velocity with NH_3 addition is also consistent at higher pressure.

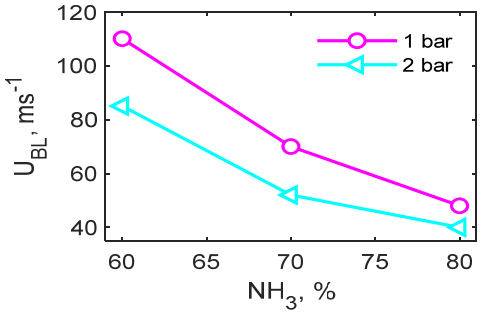

Figure 5: Blow-off velocities for three NH_3 blends with H_2: 60, 70 and 80 % at two pressures, 1 and 2 bar.

5 Discussion

The sensitivity of NH_3 addition to H_2 can be observed from laminar flame speeds, although extinction strain rates are more relevant. Furthermore, the similar laminar flame speed, between CH_4 and NH_3/H_2=60/40, doesn't account for the differences in blow-off velocity that were observed. Therefore, extinction strain rates were computed in Cantera, seen in Figure 6, for an opposed flow simulation of fuel and air.

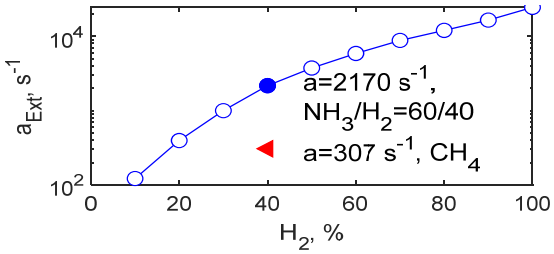

Figure 6 Log-y plot of extinction strain rates for a range of NH_3/H_2 blends and for a single pure CH_4 case (red triangle). The blue circle identifies the comparable CH_4 flame speed, NH_3/H_2= 60/40 case.

The simulations for CH_4 and the range of NH_3/H_2 blends used the GRI 3.0 and Han et al. [7] mechanisms respectively. The near order of magnitude difference in extinction strain rate for CH_4 and NH_3/H_2=60/40 of a = 307 s^{-1} and a = 2170 s^{-1} better represents the differences in the experimental blow-off velocities. Indicating that diffusion effects due to H_2,with NH_3 is significant, agreeing with Wiseman et al. [3]. It is noted the reactivity of the fuel is independent of pilot power and the pilot serves to increase or decrease the blow-off velocity similarly between fuels and fuel blends.

6 Conclusions

This paper presented blow-off velocities for CH_4 and blends of H_2/NH_3, at a range of pressures issuing from the piloted Sydney inhomogeneous jet burner. The OH-PLIF results highlighted that for increased pressures, the OH layer begins to break up for much lower velocities, consistent for both the CH_4 and NH_3/H_2 flames. The faster OH break-up for lower velocities indicates that the blow-off velocity decreases with increasing pressure, although blow-off occurs at higher Reynolds numbers.

Lower blow-off velocities were measured for increasing additions of NH_3 to H_2, consistent for all pressures. A higher blow-off velocity was observed for NH_3/H_2=60/40 compared to CH_4, despite similar flame speeds, this was well captured by the significantly higher extinction strain rate.

7 References

[1] A.R. Masri, Proceedings of the Combustion Institute, 38 (2021) 121-155.
[2] H. Kobayashi, A. Hayakawa, K.D.Kunkuma A. Somarathne, Ekenechukwu C. Okafor, Proceedings of the Combustion Institute, 37 (2019) 109-133.
[3] S. Wiseman, M. Rieth, A. Gruber, J.R. Dawson, J.H. Chen, Proceedings of the Combustion Institute, 38 (2021) 2869-2876.
[4] H. Tang, C. Yang, G. Wang, Y. Krishna, T.F. Guiberti, W.L. Roberts, G. Magnotti, Combustion and Flame, 244 (2022) 112292.
[5] A.R.W. Macfarlane, M.J. Dunn, A.R. Masri, Combustion Science and Technology, (2023) 1-15.
[6] T.F. Guiberti, H. Cutcher, W.L. Roberts, A.R. Masri, Energy & Fuels, 31 (2017) 2128-2137.
[7] X. Han, Z. Wang, Y. He, Y. Zhu, K. Cen, Combustion and Flame, 213 (2020) 1-13.

Clean Combustion and Decarbonisation Paper 5
B. Z. Dlugogorski and A. R. Masri, Eds

Towards Clean Combustion and Decarbonisation
Proceedings of the Australian Combustion Symposium
26 – 29 November 2023, Darwin, Northern Territory, Australia

Acoustic investigation of open, swirled, turbulent, premixed, hydrogen-enriched methane/air flames

J. Fleger[1, *], S. Mohammadnejad[2], S. Kheirkhah[2], J. Z. Ho[1], and M. Talei[1]
[1]Department of Mechanical Engineering, University of Melbourne, VIC 3010 Australia
[2]School of Engineering, The University of British Columbia, Kelowna, Canada, V1V 1V7

Abstract

This paper investigates the impact of hydrogen addition to methane on the acoustic spectrum of open, swirled, turbulent, premixed flames. Microphone measurements and optical OH* chemiluminescence imaging techniques are used for a pure methane flame and a methane/hydrogen mixture flame with 40% hydrogen by volume. Both flames feature stoichiometric conditions and a range of inflow velocities varying from 3 m/s to 23 m/s. It is shown that methane flames enriched with hydrogen produce more sound and exhibit a stronger correlation between the heat release rate fluctuations and pressure fluctuations compared with pure methane flames. Furthermore, hydrogen addition leads to significant differences in the spectrum for the time derivative of the OH* chemiluminescence, which is assumed to be correlated with the time derivative of the heat release rate. Notably, the slopes of the spectra at lower and higher frequencies are steeper, and the peak frequency is higher for hydrogen/methane flames.

Keywords: hydrogen, acoustics, premixed flames

Artistic artificial intelligence images were generated based on the abstract content.

* Corresponding author:
Phone: (+61) 402671328
Email: jfleger@student.unimelb.edu.au

Clean Combustion and Decarbonisation Paper 6
B. Z. Dlugogorski and A. R. Masri, Eds
Towards Clean Combustion and Decarbonisation
Proceedings of the Australian Combustion Symposium
26 – 29 November 2023, Darwin, Northern Territory, Australia

Experimental uncertainty and time-resolved process variability of biomass combustion during fouling tests

Akram Elsebaie[1, *], Mingming Zhu[2] and Yasir M. Al-Abdeli[1]
[1]School of Engineering, Edith Cowan University WA 6027, Australia
[2]School of Water, Energy and Environment, Cranfield University, Cranfield, Bedfordshire, MK 43 0AL, UK

Abstract

This study investigates experimental temperature data with particular attention to (i) uncertainty (between different test runs) and the (ii) time-resolved variability (in the transient start-up and steady state operation phase) in a fixed bed, laboratory-scale (biomass) combustors with secondary air staging at different. Temperatures measured from up to four zones are analysed: the packed fuel bed, freeboard (primary LI, secondary LII) and/or exhaust stack (fouling module). The study finds that peak bed temperatures have relatively low experimental uncertainty, while uncertainty in freeboard temperatures varies more widely. Additionally, experimental uncertainty (across all conditions) is notably low, does not exceed 5.00%, and does not appear to be zone specific (packed bed to exhaust stack). In comparison, time-resolved temperature variability can be zone specific at some conditions even within steady-state operation phase. The paper offers valuable insights for biomass combustion testing particularly when multiple runs are needed to collect fouling deposits over different air staging ratios.

Keywords: biomass, combustion, fouling, temperatures, steady state, transient sate, uncertainty

Nomenclature

Qp= Primary Air ($Lmin^{-1}$), Qs= Secondary Air ($Lmin^{-1}$), Qt= Total Air ($Lmin^{-1}$), LI= Primary Freeboard Length (mm), LII= Secondary Freeboard Length (mm)

1. Introduction

Increased uptake of biomass and other renewable energy sources helps achieve a carbon-neutral economy. Biomass combustion faces challenges in energy production because of high variability in the chemical composition of fuels [1, 2]. Additionally, solid fuel combustion generally leads to several operational issues [3] such as ash handling and incombustible solids buildup. In particular, biomass poses additional specific fouling challenges due to elevated levels of alkali and alkaline-earth elements [4-6]. Studies undertaken at the lab-scale into biomass fouling typically involve multiple runs over which fouling deposits are accumulated. This study highlights the need to better quantify the degree of variability, over the transient start-up and steady state operation phases during testing, all of which (cumulatively) contribute to fouling deposits formed. Fixed bed combustors are primarily used on a smaller scale, featuring a packed bed of biomass above an immobile grate. These systems are common in laboratories and household heating [7] and so an excellent platform for testing biomass fouling. Fixed bed combustors involve two zones where biomass reactions occur: a packed fuel bed over which the highest process temperatures occur and a freeboard zone in which additional reactions occur. The freeboard is further divided into primary and secondary freeboard lengths section when air staging (secondary air) is used.

Time-resolved process variations can arise from complex interactions in solid fuel combustion [8] and manifest themselves in temperature and other data. While fouling in most industrial systems arises during prolonged (steady state operation) due to the propensity of organic and inorganic matter to condense on surfaces within a (cooled) heat recovery section, during short duration but repeated lab-based runs (in fixed bed combustors having only a finite fuel charge), the start-up and shutdown phases become relatively appreciable. Thus, it is crucial to quantify any process variability in temperatures during both steady state and transient phases [9, 10]. Experimental uncertainty from experimental procedures further contribute to the complexities of the analysis across different runs. While existing studies provide detail the challenges associated with fouling in biomass combustion, there is a lack of data on process variability during lab testing. This paper makes the following contributions using temperature data derived from tests covering five air staging ratios Qs/Qt:

i. Quantifies the level of percent uncertainty in the steady-state phase data arising from multiple runs covering four zones, namely the packed bed, freeboard (primary, secondary) and fuel stack (fouling module)
ii. Compare the level of time-resolved variability in both steady state and transient operational phases over various zones of percent experimental uncertainty (from i).

The significance of these outcomes is to shed light on the testing regimes that straddle multiple repeated test runs as occurs in so as to accumulate appreciable deposits on fouling probes.

* Corresponding author:
Phone: +61 426 790 39654
Email: aelsebai@our.ecu.edu.au

2. Methodology

2.1 Combustor and fuel

Figure 1 illustrates the fixed-bed (counter-current) combustor made from SS310 with a 200mm inner diameter, 8.5mm wall thickness and a column height of 1,500mm. At its exhaust stack (top end) it includes fouling module with air cooled fouling probes. Fouling data is not presented in this paper. The combustor incorporates air-staged combustion whereby primary air is supplied beneath the fuel bed (from a plenum) while secondary air is distributed above the fuel bed (through a ring that can be vertically adjusted to vary LI and LII). The primary freeboard length LI is the space between the fuel bed top and secondary air ring, while the secondary freeboard length LII is the space from the secondary air ring to the end of the column (start of the exhaust stack). Two secondary air locations are used yielding LI= 200mm and 300mm. Airflow is governed by a compressor and regulated via flowmeters, dividing into primary and secondary streams. Table 1 shows that secondary air flowrates ranging from 70 to 420 $Lmin^{-1}$, while maintaining a constant primary flowrate of 140 $Lmin^{-1}$. Ratios of secondary to total flowrate are Qs/Qt= 0.33, 0.50, 0.66, 0.71, and 0.75. The fuel is commercially available hardwood pellets (make: Maxi heat) with an HHV of 19.1 $MJ.kg^{-1}$ and a bulk density of 713.4 $kg.m^{-3}$ are used throughout [11]. Each test batch uses 3.9 kg fuel. Data from unstable conditions are excluded [12].

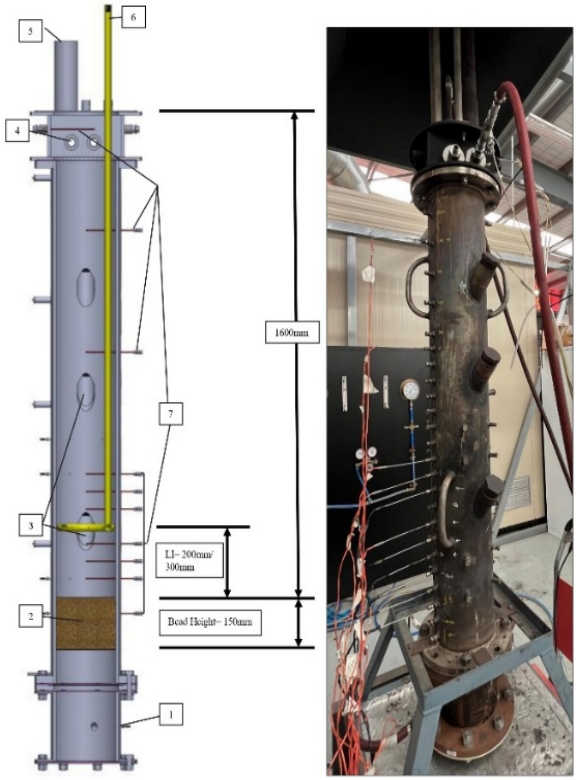

Figure 1 Combustor sectional view (left) and lab set-up (right): (1) primary air ports (x2)_, (2) packed fuel bed, (3) fuel charging ports, (4) fouling module and air cooled fouling deposition probes, (5) exhaust stack, (6) secondary air supply line and distribution ring (at lower end) and (7) thermocouples connected to data acquisition system.

LI (mm)	Qp ($Lmin^{-1}$)	Qs ($Lmin^{-1}$)	Qt ($Lmin^{-1}$)	Qs/Qt
200, 300	140	70	210	0.33
		140	280	0.50
		280	420	0.66
		350	490	0.71
		420	560	0.75

Table 1 Test conditions using raw biomass. Temperature data and experimental uncertainty is presented for all conditions. Process variability is presented for Qs/Qt=0.75.

2.2 Data acquisition

N-type and K-type thermocouples are used to capture axial temperature profiles within the combustor. N-type thermocouples, with an accuracy of ±0.75%, interfaced with a National Instruments (model: NI 9213) data acquisition system thermocouple module, measure temperatures at varying axial positions in the freeboard. In the fouling module, K-type thermocouples are employed in conjunction with a data acquisition system (make: OMEGA, model: DAQ -65). Fuel consumption is monitored using digital scale (±10 g resolution) carrying the combustor (make: RINSTRUM, model: R320), and used to determine steady-state conditions, using methods aligning with Rashidian et al. [13].

2.3 Data analysis

Temperature data is subject to two analyses: (i) experimental uncertainty (between runs) and (ii) time-resolved variability (transient phase, stead-state phase). Spatial locations based on thermocouple locations are resolved in both (i) and (ii) with each condition repeated thrice. Figure 2 shows a typical time-series of temperature data in the fuel bed, primary freeboard (L1), secondary freeboard (L2) and fouling module. The steady-state phase typically over 1,000-1,200 seconds (a) used normally to quantify (i) is identified. The 200sec time-window used to quantify (ii) is shown, in both the steady-state (b) and transient (c) phases. In the transient phase (c) the 200-sec time-window chosen spans either side of the bed thermocouple reaching 100°C. Given the rapid temperature escalation within such a brief timeframe, bed temperature time-resolved variability in this transient state is too short to characterize relevant to the steady state period. As such it is not reported. Time series of raw temperature data were post-processed to yield both the experimental uncertainty as well as the time-resolved variability. Each time series included a number of data points (N) over which the uncertainty and variability was expressed. These were expressed as percentile values over three runs (n=3). Equation (1) is first used to derive the mean temperature ($\bar{\phi}_i$), calculated over N points in each run. Because each test condition is repeated three times (i=1, 2, n). Equation (2) allows the average temperature over multiple runs to be derived (ϕ_{ave}). The standard deviation over these three runs (σ_s) is expressed by Eq. (3). The final step in Eq. (4) to established a percentile relative value (ε_r) of experimental uncertainty or time-resolved variability [14].

$$\bar{\phi}_i = \frac{1}{N}\sum_{i=1}^{N} \emptyset_i \quad (1)$$

$$\phi_{ave} = \frac{1}{N}\sum_{i=1}^{N} \emptyset_i \quad (2)$$

$$\sigma_s = \sqrt{\frac{\sum_{i=1}^{n}(\bar{\phi}_i - \phi_{ave})^2}{(n-1)}} \quad (3)$$

$$\varepsilon_r = (\frac{\sigma_s}{\sqrt{n}})(\frac{1}{\phi_{ave}}) \quad (4)$$

3. Results and Discussion

In Fig. 3-10 the packed bed, primary freeboard, secondary freeboard and fouling module zones are differentiated through background colors grey, green, yellow, and orange, respectively. The secondary air location is also represented by a dashed vertical line. Figure 3 and Fig. 4 show peak bed and freeboard temperature data over different air staging ratios (Qs/Qt) when averaged over three runs for each condition in Table 1. For Qs/Qt= 0.33 to 0.75, peak bed temperatures at LI= 200mm and LI= 300mm range from 775 to 990°C and from 823°C to 896°C, respectively. Freeboard temperatures in the fouling module vary from 128°C to 396°C (LI= 200mm) and 141°C to 319°C (LI= 300mm). These results show that steady state temperatures over the various air staging ratios (Qs/Qt) steadily decline over the length of the freeboard with those at 0.33 and 0.50 being the lowest.

(i) Experimental uncertainty over the steady state phase: To quantify the level of uncertainty in temperature data over the packed bed and freeboard regions, Figure 5 and Fig. 6 illustrate the percentage of uncertainty at LI=200mm and 300mm, respectively. Results show that across the three runs which designate each of the Qs/Qt conditions shown, the relative uncertainty does not exceed 5.00%. Experiments conducted at a primary freeboard LI= 200mm generally exhibit lower relative uncertainty at 3.00%. Conditions with Qs/Qt= 0.71 and 0.75 have the lowest relative uncertainty ranging between 0.23% and 2.06%. These results highlight that experimental uncertainty varies with the location and strength of secondary air staging.

(ii) Temperature variability (time resolved) over the stead state and transient phases: While the earlier data has confirmed the low experimental uncertainty of <5.00% over different runs (1, 2, 3), it does not shed light on the time-resolved variability which occurs within any single test run. It also does not compare between this variability over the transient start up and steady state operation phases. This variability over three runs also impacts periods over which fouling materials are deposited and is now quantified. Considering the earlier tests have shown that the relative uncertainty for Qs/Qt=0.75 is the lowest for both LI= 200mm and LI= 300mm, the ensuing analysis further sheds light on the time-resolved process (temperature) variability during the steady-state and transient phase.

For secondary air is at LI= 200mm, Fig. 7 shows variability that reaches up to 2.23% in the primary freeboard. While at LI=300mm, Fig. 8 shows the steady state temperature variability does not exceed 0.82% in the primary freeboard zone. Figure 9 and Fig. 10 again show that time-resolved process variability during transient phase for a secondary air located at LI= 200mm can be up to double that for LI= 300mm. Similar trends are observed during steady state combustion, especially in the region downstream of the secondary air location.

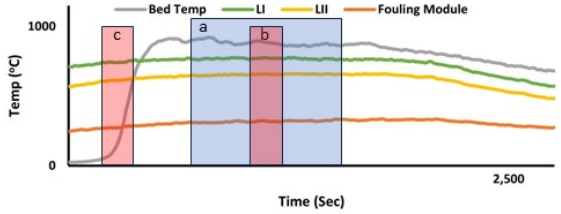

Figure 2 Typical time series in the fuel bed, primary freeboard, secondary freeboard, and fouling module. Analysis of time-resolved variability occurs over 200sec whether in the transient (c) or steady state phase (b). The time window used to analysis experimental variability over the steady state phase is also shown (a)

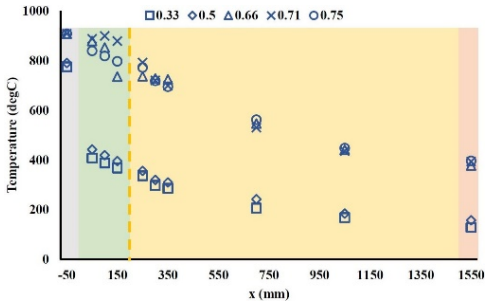

Figure 3 Temperatures in the packed bed (-50mm) and within the freeboard for LI=200mm.

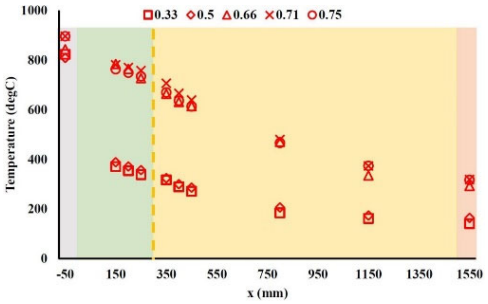

Figure 4 Temperatures in the packed bed (-50mm) and within the freeboard for LI=300mm.

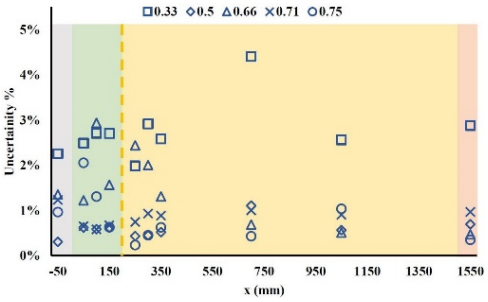

Figure 5 Temperature uncertainty for LI=200mm.

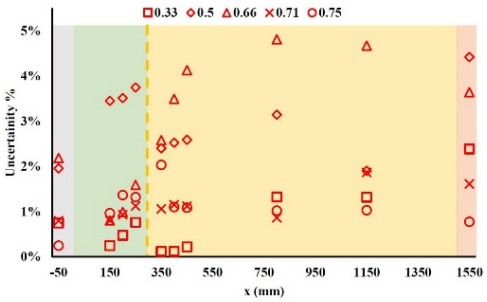

Figure 6 Temperature uncertainty for LI=300mm

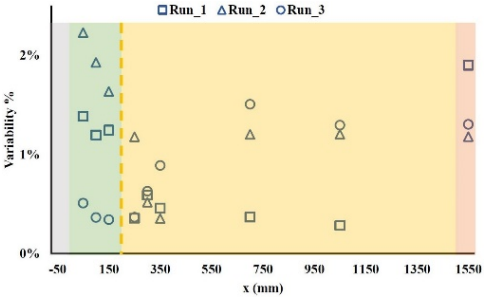

Figure 7 Steady state phase (time-resolved) temperature variability for Qs/Qt= 0.75 and LI= 200mm.

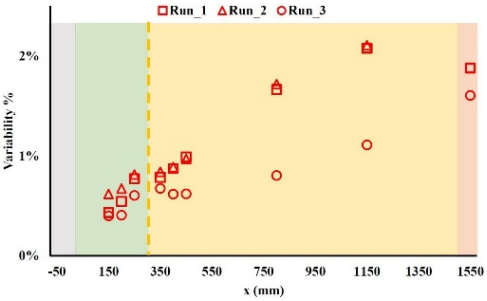

Figure 8 Steady state phase (time-resolved) temperature variability for Qs/Qt= 0.75 and LI= 300mm

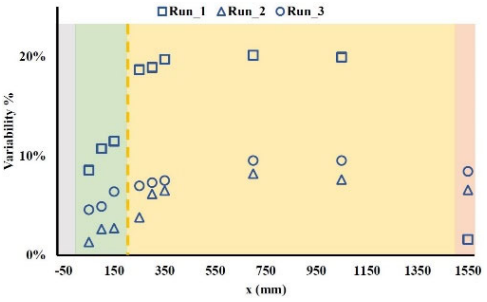

Figure 9 Transient phase (time-resolved) temperature variability for Qs/Qt= 0.75 and LI= 200mm

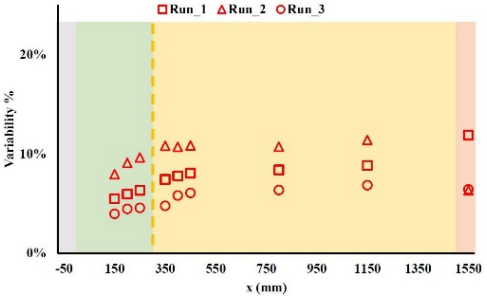

Figure 10 Transient phase (time-resolved) temperature variability for Qs/Qt= 0.75 and LI= 300mm.

4. Conclusions

This study provides a comprehensive analysis of temperature variability and experimental uncertainty in both the fuel bed and freeboard regions of a fixed bed combustor burning biomass. Results indicate that time-resolved process instability (reflected in temperature measurements) can be significantly large. Analyses reveal that although the relative uncertainty across all conditions is remarkably low and does not exceed 5.00%, thereby affirming the reliability of the experimental setup and measurements, time resolved process variability during both start-up a steady state are far more varied. Furthermore, the study identifies distinct trends in temperature variability during both transient and steady-state phases, which could have significant implications for combustor design and operation. In particular, the time-resolved temperature variability shown at some locations appears somewhat varied to others. As a future work recommendation, exploring data for blended fuels is proposed, using data processing techniques, aiming to investigate the impact of fuel composition on percentage variability and comparing it with raw fuel data, further enhancing our understanding of combustor performance and optimization.

5. References

1. Feoktistov, D.V., et al., Fuel Processing Technology, 2022. **236**: p. 107422.
2. Anand, A., S. Gautam, and L. Chand Ram, Fuel, 2023. **339**: p. 127483.
3. Shah, K.V., M.K. Cieplik, and H.B. Vuthaluru, P. Ravindra, Editor Springer International Publishing: Cham. 2015. p. 27-56.
4. Febrero, L., et al., Energies, 2015. **8**(9): p. 9794-9816.
5. Jagodzińska, K., et al., IOP Conference Series: Earth and Environmental Science, 2019. **214**: p. 012080.
6. Chapela, S., et al., Fuel, 2018. **234**: p. 1099-1122.
7. Obernberger, I., Biomass and Bioenergy, 1998. **14**(1): p. 33-56.
8. Mulvaney, J.J., et al., International Journal of Wildland Fire, 2016. **25**(4): p. 445-455.
9. Cai, Y., et al., Applied Energy, 2018. **230**: p. 1447-1544.
10. Koppejan, J. and S. van Loo, *The Handbook of Biomass Combustion and Co-firing*: Taylor & Francis 2012.
11. Riaz, S., et al., BioEnergy Research, 2022. **15**(1): p. 544-558.
12. Junejo, A., Y.M. Al-Abdeli, and J. Porteiro. in *Australian Combustion Symposium 2021*. 2021. Queensland: The Combustion Institute.
13. Rashidian, B., et al., Combustion Science and Technology, 2017. **189**(1): p. 79-102.
14. Moffat, R.J., Experimental Thermal and Fluid Science, 1988. **1**(1): p. 3-17.

Performance of biogas blended with hydrogen in a commercial self-aspirating burner

A. J. Gee[1,*], N. Smith[2], A. Chinnici[1] and P. R. Medwell[1]
[1] School of Electrical and Mechanical Engineering, The University of Adelaide, Adelaide, SA 5005, Australia
[2]School of Chemical Engineering and Advanced Materials, The University of Adelaide, Adelaide, SA 5005, Australia

Abstract

A hydrogen-enriched natural gas fuel mixture was diluted with carbon dioxide to simulate blending biogas with hydrogen (H_2). The performance of various biogas qualities and H_2 blend ratios was investigated for use in a commercial self-aspirating burner by quantifying the impact on primary air entrainment, blow-off and flashback limits, NOx emissions, radiant heat transfer and flame appearance. The results showed operating limits of a biogas or H_2 flame alone could be extended by blending one with the other and by increasing fuel injector size (lowering primary air entrainment), with the latter being more effective. The collateral impact of carbon dioxide and H_2 addition on radiant heat transfer could be mitigated by increasing injector size, with the carbon dioxide content in biogas maintaining NOx levels at or below the level of natural gas. Overall, there appears to be merit for H_2 and biogas to operate as a mutually beneficial fuel in a commercial self-aspirating burner design.

Keywords: hydrogen, biogas, commercial, self-aspirating, renewable

.

Artistic artificial intelligence images were generated based on the abstract content.

* Corresponding author:
Email: adam.gee@adelaide.edu.au

Clean Combustion and Decarbonisation Paper 8
B. Z. Dlugogorski and A. R. Masri, Eds

Towards Clean Combustion and Decarbonisation
Proceedings of the Australian Combustion Symposium
26 – 29 November 2023, Darwin, Northern Territory, Australia

Combustion performance and emission characteristics of a single-cylinder spark-ignition engine fuelled with partially dissociated ammonia

Xiaofei Yao[a,b], Jian Gao[b], Yang Liu[b], Juan Zhang[b,c], Jing Wang[a], Fangqin Cheng[a,c] and Dongke Zhang[a,c,*]

[a] State Key Laboratory of Technologies for Efficient Utilization of Coal Waste Resources, Shanxi University, Wucheng Road, Taiyuan, 030006, China

[b] Qingdao Institute of Bioenergy and Bioprocess Technology, Chinese Academy of Sciences, Qingdao, 266101, China

[c] Centre for Energy (M473), The University of Western Australia, 35 Stirling Highway, Crawley, WA 6009, Australia

Abstract

An engine test system was established to investigate the combustion characteristics of ammonia in a 402 ml single-cylinder spark-ignition engine with a compression ratio of 8.2. Ammonia (NH_3), considered as a promising carbon-free alternative fuel for transport, has been successfully tested in the spark-ignition internal combustion engine. To overcome the challenges posed by NH_3's high lower flammability limit, high ignition energy, and low burning velocity, NH_3 was partially dissociated on-board to produce a $NH_3/H_2/N_2$ mixture before being injected into the engine cylinder. This was simulated using $NH_3/H_2/N_2$ mixtures modelling by varying degree of NH_3 dissociation. Experiments were performed with varying dissociation degree (β) of 30%, 50%, and 70%, respectively. The performance of the engine was evaluated by measuring the engine powers (P) and brake thermal efficiencies (η) using a dynamometer. It was found that both P and η significantly increased with increasing β, implying the presence of H_2 can significantly improve the ignition characteristics and combustion performance of NH_3.

Keywords: ammonia, brake thermal efficiency, engine power, NH_3 dissociation; NOx emissions, spark-ignition engine

1. Introduction

One of the authors (Zhang) of this contribution has long advocated the use of ammonia (NH_3) and methanol (CH_3OH)[1,2] as hydrogen carriers as a potential means of surviving a hypothetical carbon-constrained world in the future and the use of NH_3 a carbon-free fuel for decarbonising transport[2]. NH_3 is considered a carbon-free fuel for the future[1-7]. However, due to the high latent heat of vaporisation and high autoignition temperature, compression ignition of NH_3 is quite difficult, and therefore spark-ignition engines should be more suitable for combusting NH_3[2,7]. Additional challenges to use NH_3 as a fuel in spark-ignition engines include its high lower flammability limit, high minimum ignition energy, and low burning velocity[1,2,7-11]. An effective strategy to combust NH_3 in a spark-ignition engine is to partially dissociate NH_3 on-board the vehicle to produce a $NH_3/H_2/N_2$ mixture before being injected into the engine cylinder[2,7,10]. The presence of H_2 can significantly improve the ignition and combustion properties of NH_3[8,9]. There have been limited literature reports on the combustion of partially dissociated NH_3 in spark-ignition engines. Ryu et al.[12] investigated the effect of NH_3 dissociation on the performance of a spark-ignition engine fuelling gasoline and NH_3 and found that partially dissociation of NH_3 increased the engine power, decreased the fuel consumption rate, and reduced the emissions of unburnt hydrocarbons and NH_3, CO, and NO_x. Comotti et al. [13] developed an NH_3 partial dissociation reactor and coupled it to a 505 ml twin-cylinder spark-ignition engine adopting only NH_3 as the fuel to investigate the effect of NH_3 dissociation on the performance of the spark-ignition engine. The dissociation degree was controlled at *ca.* 50%, and the experimental results indicated that NH_3 dissociation increased the engine brake thermal efficiency significantly.

The aforementioned studies validated that partial dissociation of NH_3 to release H_2 is an effective strategy to improve the performance of NH_3 spark-ignition engines. It follows that systematic investigation into the effect of NH_3 dissociation degree on the performance of engines is of practical significance. In the present work, an experimental test system was established to investigate combustion performance and emission characteristics of partially dissociated NH_3 gas in a 402 ml single-cylinder spark-ignition engine. Particular attention was given to the effect of the nominal total NH_3 flowrate, degree of NH_3 dissociation degree and engine speed on the engine torque, power output, efficiency, and NH_3 and nitrogen oxides (NOx and N_2O) emissions.

2. Experimental

Figure. 1 shows a schematic of the engine test setup, consisting of a 402 ml naturally aspirated single-cylinder four-stroke spark-ignition engine (Yamaha MX400, compression ratio 8.2), fuel supply system, exhaust gas analysis system, and dynamometer (Weige ACD-11kW). The Yamaha MX400 engine was chosen for its simplicity and popularity in light transport (motorbikes) and standalone power gen applications. It was intended to serve as a makeshift platform for preliminary and comparative studies of the feasibility of use of NH_3 as

* Corresponding author:
Phone: (+61) 8 6488 7600
Email: Dongke.Zhang@uwa.edu.au

zero-carbon transport fuel. The dynamometer is coupled to the output shaft of the engine to provide the load conditions. The engine revolution speed and torque are measured for the estimation of power and engine brake thermal efficiency. The partially dissociated NH_3 gas is simulated by mixing a NH_3 stream with an H_2/N_2 (V_{H2}:V_{N2}=3:1) mixture provided from high-pressure gas cylinders. The flow rates are controlled and monitored by using mass flow controllers. The engine performance tests were carried over a range of nominal NH3 flow rate (Q) of Q = 15 – 25 L/min, degree of NH_3 dissociation (β) of β = 20 – 70% and engine speed between 1,500 and 3,200 rpm.

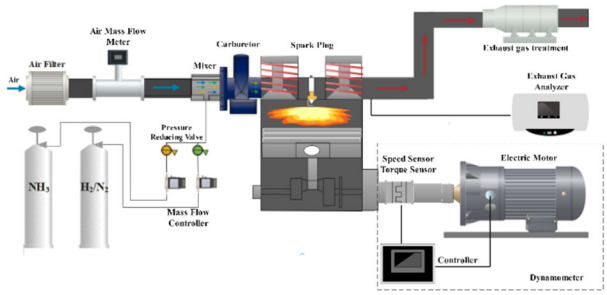

Figure 1 A schematic of the experimental setup

2. Results and Discussion

Figure 2 shows the effect of β and Q_{NH3} on the engine speed and torque under the tested conditions. The engine maximum speed significantly increased from *ca.* 2100 rpm to *ca.* 3000 rpm as β increased from 20% to 50%, then slightly increased from *ca.* 3000 rpm to *ca.* 3200 rpm as β further increased from 50% to 70% at a total Q_{NH3} of 25 L/min as shown in Figure 2a. The maximum engine speed increased with increasing β due to the flame propagation speed of the fuel mixture became higher with increasing the H_2 fraction in the engine chamber[7-10]. The torque firstly increased and then decreased at each constant β with increasing the engine speed at a total Q_{NH3} of 25 L/min (Figure 2a). The torque values reached the maximum at the speed of *ca.* 1200 rpm at the lower β of 20 – 40%, while, at the higher β of 50 – 70%, the maximum torque was achieved at the speed of ~ 1100 rpm. As β increased from 20% to 50%, the maximum torque increased from 5.7 to 11.2 Nm.

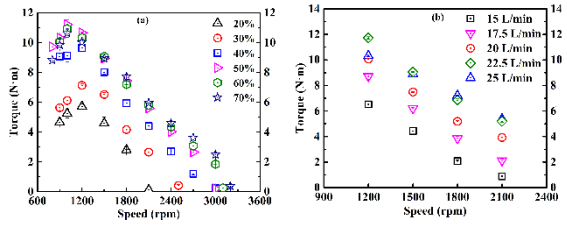

Figure 2 Effect of (a) β (Q_{NH3} 25 L/min) and (b) Q_{NH3} (at β 50%) on engine speed and torque

Because H_2 has much wider flammability limits and faster flame speed, as β increases, more H_2 is available to enhance the combustion performance, resulting in much greater combustion intensity[7-9]. In the meantime, the highest indicated pressure of the engine also increased[10], resulting a higher torque. However, as β increased from 50% to 70%, the measured maximum torque decreased from 11.2 to 10.6 Nm, which is thought to be that with a higher β, the more N_2 produced from NH_3 dissociation caused a higher heat loss during the combustion in the engine[9-15]. It was merely sufficient to maintain the engine speed and torque when β = 50%. Comotti[13] had designed a hydrogen generation system that can achieve 40 – 80% H_2 conversion at 400 – 500°C and successfully coupled to an engine. Figure 2b shows at β = 50% and 1200 – 2100 rpm, as Q increased from 15 to 22.5 L/min, the maximum torque increased from 6.5 to 11.7 Nm at 1200 rpm. As Q increased from 22.5 to 25 L/min, it was observed that the maximum torque decreased from 11.7 to 10.32 at 1200 rpm and basically invariant at 1500 – 2100 rpm.

Figure 3 shows the effect of β and Q on the measured engine power. As speed increased from 800 to 3200 rpm, the power increased first then decreased (Figure 3a). The power reached a maximum at ~1200 rpm for β = 20%, ~1500 rpm for β = 30 – 60% and ~1800 rpm for β = 70%. As β increased from 20% to 50%, the maximum power increased from 0.73 to 1.41 kW. Further increasing β from 50% to 70%, the maximum power increased from 1.41 to 1.45 kW. There is no significant difference in torque at β = 50 – 70%, especially at the speed <2400 rpm. This is because at low β, increasing β enhances the combustion of the gas mixture due to the presence of additional H_2 improving the burning rate, which leads to greater power output in fixed volume and residence tine. However, this beneficial effect of H_2 was dampened by the presence of excess N_2 as β further increases. Figure 3b shows at β = 50% and 1200 – 2100 rpm, as Q increased from 15 to 22.5 L/min, the power increased from 0.82 to 1.49 kW. But as Q increased from 22.5 to 25 L/min, the maximum power decreased from 1.49 kW to 1.31 kW at 1200 rpm and basically unchanged at 1500 – 2100 rpm. It is believed that increasing Q initially increases the thermal throughput and therefore the power output at low Q. However, at high Q the engine combustion becomes limited by the amount of naturally aspirated air, consequently, further increasing Q does not change the power output.

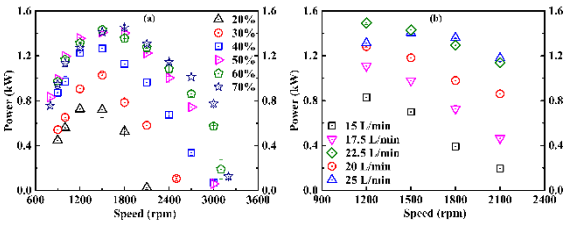

Figure 3 Effect of (a) β and (b) Q on the measured engine power output

Figure 4 shows the effect of β and Q on engine brake thermal efficiency. As speed increased from 800 to 3200 rpm, the efficiency increased first then decreased (Figure 4a). The efficiency reached a maximum at speed of 1200 rpm for β = 20 – 30%, 1500 rpm for β = 40 – 60% and ~1800 rpm at β = 70%. As β increased from 20% to 50%, the efficiency increased from 11.5% to 20.3%, in agreement with the literature[10,16]. However, as β further increased from 50% to 70%, the efficiency was invariant, especially for the engine speed <2400 rpm. Figure 4(b)

shows at β = 50% and 1200 – 2100 rpm, as Q increased from 15 to 22.5 L/min, the efficiency increased from 20.0% to 23.8% at 1200 rpm. However, as Q further increased from 22.5 to 25 L/min, the efficiency significantly decreased over 1200 – 2100 rpm. These consistent with the observed power output trend as discussed above.

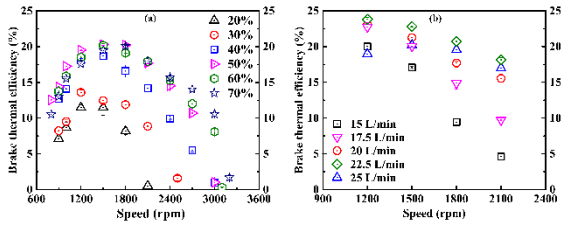

Figure 4 Effect of (a) β and (b) Q on the measured engine brake thermal efficiency

Engine emissions are always of concern and interest. Figure 5 shows the effect of β and Q on the NH_3 concentration in engine exhaust. Figure 5a shows that as engine speed increased from 800 to 3200 rpm the exhaust NH_3 concentration decreased first then remained constant. At <1200 rpm, the exhaust NH_3 concentration was too high. At >2100 rpm, although the exhaust NH_3 concentration remained constant, the brake thermal efficiency was too low (Figure 4). The low exhaust NH_3 concentration at >2100 rpm is a result of the increased air flow rate by naturally aspiration, causing a lower efficiency and fuel wastage. As β increased from 30% to 70 % the exhaust NH_3 concentration significantly decreased at speed 800 to 1200 rpm but then remained constant as speed further increased. The NH_3 emission was much higher at β = 30% than at β = 50%, resulting a low torque, power and efficiency. Figure 5b shows that increasing Q from 15 – 22.5 L/min increased the exhaust NH_3 concentration. Further increasing Q from 22.5 – 25 L/min more significantly increased the exhaust NH_3 concentration by ~1%, resulting in low torque, power and efficiency, due to large amounts of unburned NH_3. The NH_3 emission results are consistent with the engine power output and efficiency observations and are characteristic of naturally aspirated small engines.

Figure 6 shows the effect of β and Q on the exhaust NO concentration. It can be seen that the exhaust NO concentration increased with increasing engine speed from 1200 – 2100 rpm at Q = 25 L/min (Figure 6a). NO is primarily formed in the high temperature flame front in the cylinder[17]. Our tests also observed that as engine speed increased from 1200 to 2100 rpm the exhaust temperature also increased (not reported here), indicating that the engine cylinder temperature also increased, resulting a high NO emission. Increasing β from 30% to 70% saw an increase in the exhaust NO concentration, in agreement with literature report[13].

Figure 6b shows that at β = 50%, the engine speed increased from 1200 to 2100 rpm while the NO concentration decreased when Q increased from 15 to 17.5 L/min. Further increasing Q from 20 to 25 L/min saw the exhaust NO concentration first increased and then decreased, achieved a maximum at Q = 25 L/min and engine speed of ~4300 ppm, where the estimated equivalence ratio is 0.86. These observations are consistent with the literature report[18] where it is also shown that significant NO emissions were found for low equivalence ratios of 0.8 – 0.9, due to the presence of excess O_2.

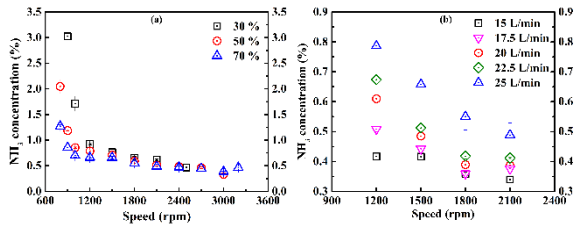

Figure 5 Effect of (a) β and (b) Q on the measured engine exhaust NH_3 concentration

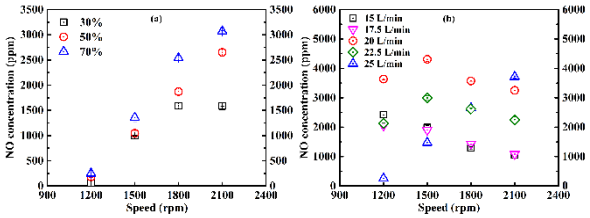

Figure 6 Effect of (a) β and (b) Q on the measured exhaust NO concentration

Figure 7 shows the effect of β and Q on the measured exhaust NO_2 concentration. Figure 7a shows that at Q = 25 L/min, increasing engine speed from 1200 to 2100 rpm resulted in an increase in the exhaust NO_2 concentration. Increasing β from 30% to 70% increased the exhaust NO_2 concentration. In Figure 7b, at β = 50%, as speed increased from 1200 to 2100 rpm the NO_2 concentration increased. As shown in Figure 7b, at β = 50% as engine speed increased from 1200 to 2100 rpm, the NO_2 concentration decreased for Q = 15 and 17.5 L/min but increased for Q = 20 and 22.5 L/min. The NO_2 concentration decreased with increasing engine speed when Q = 25 L/min. The variation in NO_2 was similar to NO, only differing in quantity. In general, NO_2 concentration is around 10% of that of NO.

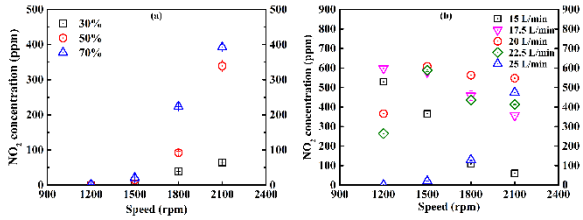

Figure 7 Effect of (a) β and (b) Q on the measured exhaust NO_2 concentration

Figure 8 shows the effect of β and Q on the measured exhaust N_2O concentration. It can be seen from Figure 8a that at Q = 25 L/min, as the engine speed increased from 1200 to 2100 rpm and as β increased from 30% to 70% the N_2O concentration increased, in agreement with the literature[20]. Figure 8b shows that at β = 50%, as Q increased from 15 to 25 L/min the exhaust N_2O concentration increased. Clearly, NO is overwhelmingly the dominant nitrogen oxides emissions from engine fuelled with NH_3, as with conventional hydrocarbon fuels.

Notably, the exhaust N_2O concentration was slightly higher than that of NO_2. It is known that during combustion processes, both NO_2 and N_2O are derived from NO, and the contribution of N_2O formation to total NO consumption rate was not more than 30% and the NO_2 formation was not more than 5%[21]. So the formation of both NO_2 and N_2O was closely related to NO.

While the present is work in progress, the clearly observed high levels of nitrogen oxides (NOx and N_2O) call for further scientific research and technological innovation to either reduce NOx formation or implement post-combustion NOx control using SCR. The existing Add-Blue can be readily applied[19].

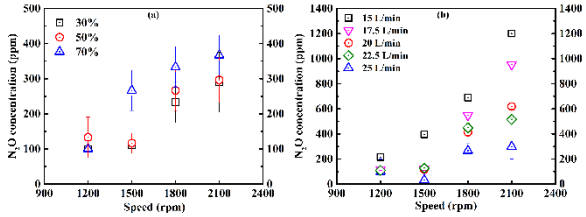

Figure 8 Effect of β and Q on the measured exhaust N_2O concentration.

3. Conclusions

The effect of the degree of NH_3 dissociation and NH_3 flowrate on the engine performance showed that increasing the degree of NH_3 dissociation increased the speed, torque, power output and brake thermal efficiency. As the flowrate increased from 15 to 22.5 L/min, the engine performance improved, however, further increasing the flowrate from 22.5 to 25 L/min did not change the engine performance.

The exhaust NH_3 concentration decreased with increasing the degree of NH_3 dissociation from 30% to 70%, especially at low speed. The NH_3 combustion efficiency was also increased as the degree of NH_3 dissociation increased. The higher the degree of NH_3 dissociation, the higher exhaust temperature, and the higher the engine brake thermal efficiency. As NH_3 flowrate increased from 15 to 25 L/min, the exhaust NH_3 concentration and exhausted temperature increased. However, the 25 L/min NH_3 flowrate and equivalence ratio of 0.9 saw the lowest NH_3 combustion efficiency under all conditions tested in the present work.

The NO, NO_2 and N_2O emissions showed an increasing trend with increasing the degree of NH_3 dissociation.

4. Acknowledgments

This work receives financial and other support from the Australian Research Council under the Discovery Projects Scheme (DP210103766 and DP220100116), Future Energy Export CRC (FEnEX CRC Project # 21.RP2.0059), Shanxi Keteng, and Qingdao Institute of Bioenergy and Bioprocess Technology (QIBEBT).

5. References

[1] Zhang, D., Options for Hydrogen Production: Transitional Path and Future Scenarios, an invited keynote at ***Hydrogen and Fuel Cell Futures Conference***, Perth, September 2004

[2] Zhang, D., et al., A spark-ignitor and a method for spark ignition of ammonia in internal combustion engines, ***China Patent*** 201810368115.4, 2018

[3] Valera-Medina, A., et al., ***Progress in Energy and Combustion Science***, 2018. **69**: p. 63-102

[4] De Vries, N., et al., in *Techno-Economic Challenges of Green Ammonia as an Energy Vector*. 2021. p. 105-154

[5] Mounaïm-Rousselle, C. and P. Brequigny, ***Frontiers in Mechanical Engineering***, 2020. **6**.

[6] MacFarlane, D.R., et al., ***Joule***, 2020. **4**(6): p. 1186-1205.

[7] Lesmana, H., Zhang, Z., Wan, Z., Wang, C., Li, X., Zhu, M., Xu, W., and **Zhang, D.**, ***Journal of Energy Resources Technology*** 141, 070703-1/070703-12, 2019

[8] Lesmana, H; Zhu, M; Zhang, Z., Jian G., Junzhi W., and Zhang, D., ***Fuel,*** 278, 118428, 2020

[9] Lesmana, H., Zhu, M., Zhang, Z., Gao, J., Wu, J., Zhang, D., ***Combustion and Flame***, 2022. **241**

[10] Yao, X., Liu, Y., Zhang, J., Gao, J., Wang, J., Cheng, F., Zhang, D., Preliminary observations of performance of ammonia combustion in a single-cylinder spark-ignition engine, Paper No. 48, The Proceedings of The 46th International Technical Conference on Clean Energy, Clearwater, The US, August 2022

[11] Nozari, H. and A. Karabeyoğlu, ***Fuel***, 2015. **159**: p. 223-233

[12] Ryu, K., G.E. Zacharakis-Jutz, and S.-C. Kong, ***International Journal of Hydrogen Energy***, 2014. **39**(5): p. 2390-2398

[13] Comotti, M. and S. Frigo, ***International Journal of Hydrogen Energy***, 2015. **40**(33): p. 10673-10686

[14] Xu, X., et al., ***Energies***, 2022. **15**(3)

[15] Frigo, S. and R. Gentili, ***International Journal of Hydrogen Energy***, 2013. **38**(3): p. 1607-1615

[16] Yang, W., et al., ***International Journal of Hydrogen Energy***, 2022. **47**(20): p. 11083-11100

[17] Zhang, H., et al., ***Fuel***, 2023. **332**

[18] Lhuillier, C., et al., ***Fuel***, 2020. **269**

[19] Schmidt, A., et al, ***Applied Sciences***, 2021, *11*(15), 6907

[20] Mounaïm-Rousselle, C., et al., ***Energies***, 2021. **14**(14)

[21] Osipova, K.N., et al., ***Combustion and Flame, 2022***, **246**

Towards Clean Combustion and Decarbonisation
Proceedings of the Australian Combustion Symposium
26 – 29 November 2023, Darwin, Northern Territory, Australia

Effect of ignition assistant plug protrusion depth on jet fuel flames in a compression ignition engine

J. Yang[1], D. Kim[1], S. Kook[1,*] , K. S. Kim[2] and C. B. Kweon[3]
[1]School of Mechanical and Manufacturing Engineering, The University of New South Wales
[2] DEVCOM Army Research Laboratory

Abstract

This study evaluates jet fuel flames in an optical compression ignition (CI) engine with an emphasis on the ignition assistant plug enhanced combustion of a low-reactivity alcohol-to-jet (ATJ) fuel. Three different ignition assistant plug protrusion depths are examined to understand the effect of plug location on the jet fuel flame development. For each condition with the ignition assistance plug operated continuously, a total of 100 individual cycle high-speed flame movies are recorded and post processed for flame image velocimetry (FIV). The FIV results show similar overall flow structure evolution and turbulence distribution for any ignition assistant plug protrusion. However, longer plug protrusion shows higher spatially averaged bulk flow magnitude and lower cyclic variations compared to the other two shorter protrusions, suggesting enhanced and more stable combustion due to improved heat distribution within the piston bowl.

Keywords: flame image velocimetry, ignition assistant plug, flow structure, turbulence, cyclic variation

Artistic artificial intelligence images were generated based on the abstract content.

* Corresponding author:
Phone: (+61) 2 9385 4091
Email: s.kook@unsw.edu.au

Towards Clean Combustion and Decarbonisation
Proceedings of the Australian Combustion Symposium
26 – 29 November 2023, Darwin, Northern Territory, Australia

Investigation NO emissions, entropy generation, and thermal performance in an ammonia/methane-fueled micro-combustor

He Zhao[1,*], Dan Zhao[1], Xinyu Zhao[1], Hui Rong[1]
[1] Department of Mechanical Engineering, Faculty of Engineering, University of Canterbury, Private Bag 4800, Christchurch 8140, New Zealand

Abstract

Ammonia stands out as a promising alternative fuel with the potential to combat climate change. To enhance the flammability of ammonia, blending it with methane is considered a viable strategy to improve its laminar burning velocity. In this study, we delve into the thermal performance, second law efficiency, and NO emissions of a micro-combustor fuelled by ammonia/methane, exploring the impact of varying the inlet volume rate (Q_{in}) and the inlet mole blended ratio of CH4 ($\xi_{\mathrm{CH_4}}$). Our findings reveal that increasing the inlet volume rate results in improved thermal performance, accompanied by a rise in wall temperature. Specifically, the mean wall temperature at Q_{in}=14.4 mL/s exceeds that at Q_{in}=7.2 mL/s by 156K. Similarly, the exergy, efficiency, and power output of the micro-thermal photovoltaic system associated with the micro-combustor also demonstrate positive trends with increasing Q_{in}. Specifically, the exergy, efficiency, and power at Q_{in}=14.4 mL/s are 100%, 36%, and 71.9% higher than those at Q_{in}=7.2 mL/s, respectively. However, it's essential to note that increasing Q_{in}also results in higher NO emissions, with NO emissions at Q_{in}=14.4 mL/s being 21.1% higher than those at Q_{in}=7.2 mL/s. Furthermore, while increasing the CH_4 mole blended ratio has limited impact on thermal performance, it proves beneficial in enhancing the exergy and second law efficiency of the micro-combustor and reducing NO emissions. Specifically, the mean wall temperature at $\xi_{\mathrm{CH_4}}$==0.6 is only 18 K higher than that at $\xi_{\mathrm{CH_4}}$==0.3, yet the second law efficiency and exergy show significant improvements of 22% and 23.7%, respectively.

Keywords: climate change, ammonia fuel, decarbonisation, micro-combustor

Artistic artificial intelligence images were generated based on the abstract content.

* Corresponding author:
Phone: (+64) 0224550340
Email: he.zhao@pg.canterbury.ac.nz

Towards Clean Combustion and Decarbonisation
Proceedings of the Australian Combustion Symposium
26 – 29 November 2023, Darwin, Northern Territory, Australia

LES/PDF modelling of piloted turbulent premixed flames using an MMC – shadow position mixing model in the high Karlovitz number regime

Y. Shoraka[1, *], S. Galindo-Lopez[1], M. J. Cleary[1], A. R. Masri[1] and A. Y. Klimenko[2]
[1]School of Aerospace, Mechanical and Mechatronic Engineering, The University of Sydney, Sydney, NSW 2006, Australia
[2]School of Mechanical and Mining Engineering, The University of Queensland, Brisbane, QLD 4072, Australia

Abstract

This paper presents the results obtained from the LES/PDF simulation of piloted premixed turbulent flames in the high Karlovitz regime using the premixed-MMC mixing model with a shadow position reference variable. The SDEs that govern how shadow positions evolve include a diffusion coefficient that depends on the model parameter λ, which denotes the ratio between a reference turbulent propagation speed and the laminar flame speed. The λ parameter is calculated based on the local flow conditions in this study. To investigate the performance of the premixed-MMC mixing model for flames in the high Karlovitz number regime, lean piloted premixed turbulent flames, PM1-100 and PM1-200, which were experimentally studied by Dunn et al. [18, 19] are numerically investigated. The results obtained from the study indicate that the premixed-MMC model is more effective in capturing the instantaneous flame structure of the PM1-100 flame, which is closer to the flamelet regime. However, when it comes to the PM1-200 flame, which has a higher Reynolds number, the simulations do not accurately capture the extinction-reignition events, leading to considerable overprediction of species production.

Keywords: high Karlovtiz number regime, premixed combustion, multiple mapping conditioning, shadow position

1. Introduction

Creating low-pollution mixed-mode combustors requires validated numerical models. Direct Numerical Simulation (DNS) is still not feasible for engineering applications, notwithstanding the improvements in the computational capacities of modern high-performance computing facilities. Large Eddy Simulation (LES) is a cost-effective alternative that captures turbulent combustion's unsteady physics while avoiding DNS's excessive computational costs by filtering small dissipative structures. In LES, however, a Turbulent-Chemistry Interaction (TCI) model is required to calculate the filtered chemical source term as the flame front is commonly unresolved [1, 2]. The TCI models proposed for LES of turbulent premixed combustion are commonly developed based on the flamelet assumption [3, 4], which theoretically limits their range of application. An alternative option is the Transported Probability Density Function (TPDF) approach, wherein the chemical source appears in the closed form; thus, it does not rely on any restricting assumptions [5-7]. Still, a mixing model is required in the TPDF approach to model the effects of molecular mixing at sub-filter scales [2, 8]. The development of mixing models for turbulent premixed combustion is still in progress. Commonly used mixing models, such as Modified Curl and Interaction by Exchange with the Mean (IEM), do not preserve the physical localness of mixing, which causes erroneous prediction of flame's propagation speed and structure [8].

Multiple Mapping Conditioning (MMC) is a promising paradigm for constructing mixing models that are not prone to this shortcoming. Therein, mixing locality is imposed within a mathematically independent reference space [9]. Robust and efficient mixing models are developed for LES of turbulent non-premixed flames using the MMC framework, which can provide accurate predictions using a sparse set of Lagrangian particles by incorporating a mixture fraction-like reference variable [10]. Still, it can't be extended to premixed flames as burned and unburned fluid parcels with similar mixture fractions can exist across the flame front [11]. Alternative options recommended for this purpose include a progress variable-like [6] and shadow-position reference variables [12].

Shadow-position reference variables suggested by Sundaram and Klimenko [15] temporally evolve according to the Stochastic Differential Equations (SDEs) that are similar to SDEs proposed for the Shadow Position Mixing Model (SPMM) by Pope [13]. Nonetheless, an effective diffusion coefficient proportional to the ratio between the turbulent and laminar flame propagation speeds, denoted as λ, is used therein instead of the turbulent diffusion coefficient used by Pope. This change of parameter, nonetheless, does not affect the linearity and independence of the original SPMM model. Shadow-position reference variables proposed by Sundaram and Klimenko [12] quantify the filtered position of the flame front in the shadow-position reference space, and the localness of mixing is ensured by enforcing localness in the shadow-position space.

* Corresponding author:
Email: yashar.shoraka@sydney.edu.au

The premixed-MMC mixing model utilising shadow-position reference variables was previously used for LES modelling of turbulent piloted premixed flames in the thin reaction zone using constant [14, 15] and flow-adapted λ values [16, 17]. The aim of this paper is to examine the performance of the premixed-MMC model in LES modelling of turbulent premixed flames at high Karlovitz number regimes by simulating PM1-100 and PM1-200 flames from the piloted premixed jet burner (PPJB) flames series, which were experimentally studied by Dunn et al. [18, 19].

2. Methodology

2.1 Premixed MMC mixing model

The governing SDEs for Lagrangian simulation of the PDF transport equations are:

$$d\boldsymbol{x}^P = \left[\widetilde{\boldsymbol{U}} + \frac{1}{\bar{\rho}}\nabla(\bar{\rho}\mathcal{D}_t)\right]dt + \left(\sqrt{2\mathcal{D}_t}\right)d\boldsymbol{w}_x^p, \quad (1)$$

$$d\phi_\alpha^P = [\omega_\alpha(\boldsymbol{\phi}^p) + \mathbb{S}(\phi_\alpha^P)]dt, \quad (2)$$

$$\left\langle \mathbb{S}\left(\phi_\alpha^p\right) | \boldsymbol{\xi}^p = \boldsymbol{\xi} \right\rangle = 0, \quad (3)$$

where bar $\overline{(\,)}$ and tilde $\widetilde{(\,)}$ indicate spatially filtered, and Favre filtered quantities. Superscript $(\,)^p$, ρ and $\boldsymbol{U}$ show notional particles' quantities, density, and velocity vector, respectively and $\mathcal{D}_t = \mathcal{D} + \mathcal{D}_{sgs}$ stands for the summation of the molecular and sub-grid scale diffusivities. The molecular mixing and the vector of independent Wiener processes are shown by $\mathbb{S}(\,)$ and $d\boldsymbol{w}$, respectively, and **c**hemical reactions are represented by $\omega(\,)$.

As shown by Eq. 3, the MMC mixing process locally conserves mean scalar values in the $\boldsymbol{\xi}$-space. The filtered position of the flame front is resolved in the $\boldsymbol{\xi}$-space; therefore, the evolution of $\boldsymbol{\xi}^P$ follows the evolution of the $\boldsymbol{x}^P$, and the local conservation of mean scalar values in the shadow-position space translates into the local conservation of mean scalar values in the physical space.

The SDE that governs the temporal evolution of the notional particles in the shadow-position space is:

$$d\boldsymbol{\xi}^P = \widetilde{\boldsymbol{U}}dt + \frac{\boldsymbol{x}^P - \boldsymbol{\xi}^P}{\tau_\xi} + \left(\sqrt{2\mathcal{D}_\xi}\right)d\boldsymbol{w}_\xi^p, \quad (4)$$

where τ_ξ denotes the turbulent flame front motion's characteristic time relative to its filtered position, and here is set equal to the sub-grid fluctuations' time scale. In the above equation, $\mathcal{D}_\xi$ is the effective diffusion coefficient in shadow-position space, which is obtained as [12]:

$$\mathcal{D}_\xi = \mathcal{D}\lambda^2, \quad (5)$$

where $\lambda = u_t/S_L$, and u_t and S_L denote the flame's turbulent and laminar propagation speeds, respectively.

The premixed MMC mixing model maintains the flamelet structure of flame in the shadow-position space by imposing localness in $\boldsymbol{\xi}$-space which minimises mixing across the filtered flame front. In case of a small dispersion between the location of notional particles in physical and shadow-position spaces, flamelet structures will also be maintained in the physical space. Otherwise, the structure of the flame will be distorted in the physical space due to substantial dispersion between $\boldsymbol{\xi^p}$ and $\boldsymbol{x^p}$. Thereby, the structure of the flame in physical space depends on the relative dispersion between the location of notional particles in shadow-position and physical spaces.

2.2 Model's implementation

The MMC-LES modelling of piloted premixed flames is performed using the mmcFoam package, which is developed as an OpenFOAM-compatible hybrid Lagrangian/Eulerian solver for MMC modelling of turbulent combustion [20]. A low-Mach, compressible LES solver with PISO pressure-velocity coupling and Smagorinsky [21] sub-grid scale model is used here to obtain the filtered velocity, pressure and turbulent diffusivity. The λ parameter is obtained using Charlette's model [22] for the flame wrinkling factor [16, 17]. Once the calculation of Eulerian fields is performed, Eulerian fields are interpolated at the particle locations. Afterwards, the simulation of the Lagrangian phase is carried out by integrating the SDEs (1), (2), and (4). Two-way coupling between the Eulerian and Lagrangian solution is performed using an equivalent enthalpy method [20]. For mixing, notional particle pairs are selected using a k-dimensional tree algorithm that finds the nearest particles in $\boldsymbol{\xi}$-space. Thereafter particle pairs are mixed as

$$\phi_\alpha^p(t + \Delta t) = \phi_\alpha^p(t) + \mu\left[\bar{\phi}_\alpha^{p,q}(t) - \phi_\alpha^p(t)\right], \quad (6)$$

$$\phi_\alpha^q(t + \Delta t) = \phi_\alpha^q(t) + \mu\left[\bar{\phi}_\alpha^{p,q}(t) - \phi_\alpha^q(t)\right], \quad (7)$$

In the above Eqs., $\bar{\phi}^{p,q}$ is the weighted mean, and μ indicates the mixing extent obtained as:

$$\mu = 1 - \exp\left(-\frac{\Delta t}{\tau_L^{p,q}}\right), \quad (8)$$

where the sub-filter mixing timescale, $\tau_L^{p,q}$, is obtained as:

$$\tau_L^{p,q} = \frac{C_f(\Delta_E)^2}{2\lambda\mathcal{D}_t}. \quad (9)$$

In Eq. (9), C_f is a constant value equal to 0.1 and Δ_E denotes the LES filter width. The sub-filter mixing timescale, which is commonly evaluated using the equilibrium assumption, underpredicts the scalar dissipation rate in LES of turbulent premixed flames when the flame front is unresolved. Therefore, the sub-filter mixing frequency is enhanced by dividing the sub-filter mixing timescale by the flame wrinkling factor to improve the accuracy of the estimation of the scalar dissipation rate [23].

2.3 Simulation setup

The PPJB burner issues a high-speed central lean premixed methane-air fuel jet with an equivalency ratio of 0.5 and a diameter of D=4mm. A low-speed pilot that

consists of burnt products of a stochiometric methane-air mixture with a bulk velocity of 5.2 m/s surrounds the central fuel jet. Jet and pilot streams are shrouded by a hot co-flow comprising the burned products of a lean premixed hydrogen-air mixture [18, 19]. As mentioned previously, PM1-100 and PM1-200 flames are studied here. The bulk velocity of the central jet is equal to 100 m/s for PM1-100 flame, corresponding to Reynolds and Karlovitz numbers of 25000 and 1600, respectively. For PM1-200 flame, the bulk central velocity of 200 m/s results in the Reynolds and Karlovitz numbers of 50000 and 3500, respectively. A cylindrical computational domain with a height of 75D and a diameter of 25D is used in current numerical simulations, which is discretised using a non-uniform computational grid that comprises ~650000 computational cells. The fuel jet boundary conditions are obtained using separate pipe simulations. The rest of the boundary conditions are set according to the recommendations of Rowinski and Pope [5].

3. Results and Discussion

Figures 1 and 2 illustrate the scatter plots and conditional means of CO and OH concentrations, respectively. Results are collected at six locations along the axial coordination in the X direction. Scatter plots are obtained from numerical results. Darker shades of grey in these pictures indicate more data points and are just a by-product of the post-processing step, not explicitly quantified. Results shown in Fig. 1 indicate that the CO production is overestimated for PM1-200. A similar trend can also be observed for the predictions obtained for the OH concentrations in Fig. 2.

Figure 3 illustrates the results obtained for the conditional mean values for the CO and OH concentrations product at $\psi = 1400K$, where ψ indicates the sample space variable for temperature. It can be observed that the results obtained for PM1-100 show a continuous decrease along the flame, which agrees with the trend observed in experimental results. The discrepancy between the experimental and numerical results is higher at upstream locations for PM1-100, and the accuracy of simulation improves downstream. The major reason for this discrepancy could be due to overprediction of the pilot entrainment observed in the simulations. For PM1-200, however, the numerical results show a substantial overprediction throughout the flame, which is consistent with the results depicted in Figs 1 and 2. The discrepancies observed for PM1-200 indicate that extinction–reignition events that occur in this flame are not accurately captured in numerical simulations.

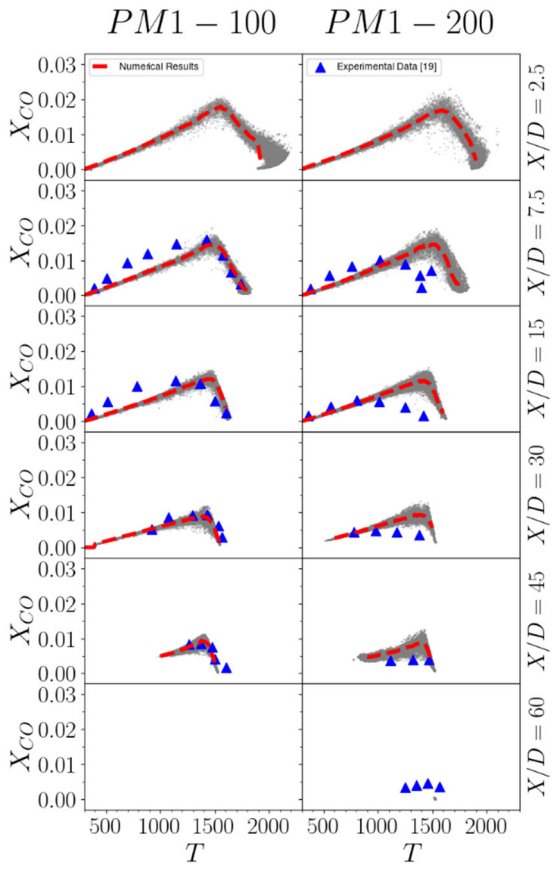

Figure 1: Scatter plots and conditional means of X_{CO} compared with experimental data [19]

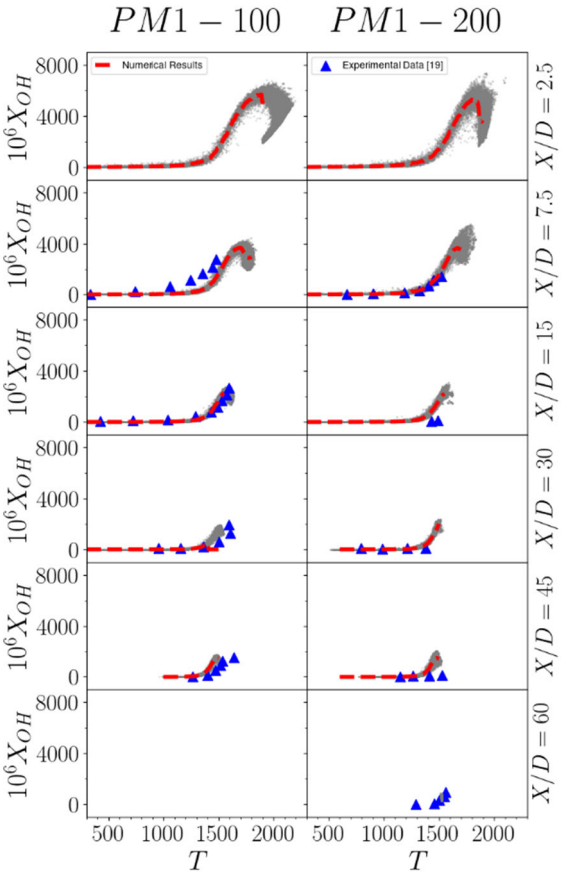

Figure 2: Scatter plots and conditional means of X_{OH} compared with experimental data [19]

It should be mentioned that previous studies have also found the PM1-200 challenging in this regard [3, 5, 7]. According to Rowinski and Pope [5], the mixing model's performance plays a crucial role in accurately predicting reaction progress. Hence, investigating the sensitivity of results to variations in λ and sub-filter mixing timescale calculations is essential to improve the model's performance for predicting reaction progress in PM1-200 flame.

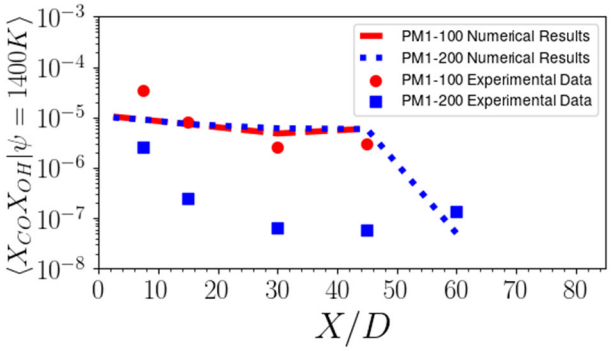

Figure 3: Conditional mean values for the product of CO and OH concentrations at $\psi = 1400K$, where ψ indicates the sample space variable for temperature, compared with experimental data [19]

4. Conclusions

LES/PDF simulations using a premixed-MMC mixing model with a shadow position reference variable were performed for piloted premixed turbulent flames, PM1-100 and PM1-200, in the high Karlovitz regime. The premixed-MMC model includes a flow-adapted model parameter λ that controls the turbulent propagation speed of the flame. The results obtained indicated that the premixed-MMC model could capture the instantaneous flame structure of the PM1-100 flame with reasonable accuracy. Still, it has not accurately captured the extinction-reignition events in PM1-200 flame and considerably overpredicted species production. Therefore, further investigation into the sensitivity of the results to variations in λ and sub-filter mixing time-scale calculations is necessary to improve the accuracy of numerical results for PM1-200 flame.

5. Acknowledgments

This research is supported by the Australian Research Council. The Artemis high-performance computing cluster at the University of Sydney is utilised for numerical simulations.

6. References

[1] A. Masri, Challenges for turbulent combustion, Proc. Combust. Inst. 38 (2021) 121-155.
[2] N. Swaminathan, X.-S. Bai, N.E.L. Haugen, C. Fureby, G. Brethouwer, Advanced turbulent combustion physics and applications, Cambridge University Press, 2022.
[3] Y. Chen, M. Ihme, Large-eddy simulation of a piloted premixed jet burner, Combust. Flame 160 (2013) 2896-2910.
[4] F.C.C. Galeazzo, B. Savard, H. Wang, E.R. Hawkes, J.H. Chen, G.C. Krieger Filho, Performance assessment of flamelet models in flame-resolved LES of a high Karlovitz methane/air stratified premixed jet flame, Proc. Combust. Inst. 37 (2019) 2545-2553.
[5] D.H. Rowinski, S.B. Pope, PDF calculations of piloted premixed jet flames, Combust. Theor. Model. 15 (2011) 245-266.
[6] C. Straub, A. Kronenburg, O.T. Stein, G. Kuenne, J. Janicka, R.S. Barlow, D. Geyer, Multiple mapping conditioning coupled with an artificially thickened flame model for turbulent premixed combustion, Combust. Flame 196 (2018) 325-336.
[7] H. Zhou, Z. Ren, D.H. Rowinski, S.B. Pope, Filtered density function simulations of a near-limit turbulent lean premixed flame, J. Propul. Power 36 (2020) 381-399.
[8] D.C. Haworth, Progress in probability density function methods for turbulent reacting flows, Prog. Energy Combust. Sci. 36 (2010) 168-259.
[9] A.Y. Klimenko, S.B. Pope, The modeling of turbulent reactive flows based on multiple mapping conditioning, Phys. Fluids 15 (2003) 1907-1925.
[10] G. Neuber, F. Fuest, J. Kirchmann, A. Kronenburg, O.T. Stein, S. Galindo-Lopez, M.J. Cleary, R.S. Barlow, B. Coriton, J.H. Frank, Sparse-Lagrangian MMC modelling of the Sandia DME flame series, Combust. Flame 208 (2019) 110-121.
[11] B. Sundaram, A.Y. Klimenko, M.J. Cleary, U. Maas, Prediction of NOx in premixed high-pressure lean methane flames with a MMC-partially stirred reactor, Proc. Combust. Inst. 35 (2015) 1517-1525.
[12] B. Sundaram, A.Y. Klimenko, A PDF approach to thin premixed flamelets using multiple mapping conditioning, Proc. Combust. Inst. 36 (2017) 1937-1945.
[13] S.B. Pope, A model for turbulent mixing based on shadow-position conditioning, Phys. Fluids 25 (2013) 110803.
[14] Y. Shoraka, S. Galindo-Lopez, M. Cleary, A. Masri, F. Salehi, A. Klimenko, Modelling of a turbulent premixed flame series using a new MMC-LES model with a shadow position reference variable, Proc. Combust. Inst. 38 (2021) 3057-3065.
[15] Y. Shoraka, S. Galindo-Lopez, M.J. Cleary, A.R. Masri, A.Y. Klimenko. LES/PDF Modelling of Turbulent Premixed Flames Using an MMC – Shadow Position Mixing Model Incorporating Detailed Chemistry. In: Australian Combustion Symposium; 2021.
[16] Y. Shoraka, S. Galindo-Lopez, M.J. Cleary, A.R. Masri, A.R. Klimenko. LES/PDF Modelling of Turbulent Premixed Flames Using an MMC – Shadow Position Mixing Model with Local Model Parameters. In: 23rd Australasian Fluid Mechanics Conference; 2022.
[17] Y. Shoraka, S. Galindo Lopez, M. Cleary, A. Masri, A. Klimenko. Modelling of a turbulent premixed flame series using an MMC-LES model with a shadow position reference variable with locally adjusted model parameters. In: 14th Asia-Pacific Conference on Combustion (ASPACC 2023); 2023.
[18] M.J. Dunn, A.R. Masri, R.W. Bilger, A new piloted premixed jet burner to study strong finite-rate chemistry effects, Combust. Flame 151 (2007) 46-60.
[19] M. Dunn, A. Masri, R. Bilger, R. Barlow, G.-H. Wang, The compositional structure of highly turbulent piloted premixed flames issuing into a hot coflow, Proc. Combust. Inst. 32 (2009) 1779-1786.
[20] S. Galindo-Lopez, F. Salehi, M.J. Cleary, A.R. Masri, G. Neuber, O.T. Stein, A. Kronenburg, A. Varna, E.R. Hawkes, B. Sundaram, A stochastic multiple mapping conditioning computational model in OpenFOAM for turbulent combustion, Comput. Fluids 172 (2018) 410-425.
[21] J. Smagorinsky, General circulation experiments with the primitive equations: I. The basic experiment, Mon. Weather Rev. 91 (1963) 99-164.
[22] F. Charlette, C. Meneveau, D. Veynante, A power-law flame wrinkling model for LES of premixed turbulent combustion Part I: non-dynamic formulation and initial tests, Combust. Flame 131 (2002) 159-180.
[23] H. Wang, T. Pant, P. Zhang, LES/PDF Modeling of Turbulent Premixed Flames with Locally Enhanced Mixing by Reaction, Flow Turbul. Combust. 100 (2018) 147-175.

Towards Clean Combustion and Decarbonisation
Proceedings of the Australian Combustion Symposium
26 – 29 November 2023, Darwin, Northern Territory, Australia

Emission analysis of an ammonia fueled micro-combustor with double-channel reverse flow structure

Hui Rong, Dan Zhao* and He Zhao
Department of Mechanical Engineering, Faculty of Engineering, University of Canterbury, Private Bag 4800, Christchurch 8041, New Zealand

Abstract

This study proposes a novel micro-combustor fueled by ammonia and oxygen, employing a double-channel inlet and double-channel outlet (DIDO) configuration with the reverse flow structure. The investigation delves into the parameters of volumetric flow rate of ammonia (Q_v), inlet pressure (P_{in}), equivalence ratio (Φ), on nitrogen oxide emissions of the micro-combustor. It is observed that, in comparison to conventional systems, the DIDO combustor is capable of generating a vortex at the outlet, thereby reducing NOx emissions. Specifically, at a Q_v of 900 mL/min, the NO concentration at the outlet can be curtailed by 29.23%. Furthermore, NO emissions exhibit a gradual decline with the increase of Φ and P_{in}. This study demonstrates the feasibility of reducing emissions by varying its structure for thermophotovoltaic applications.

Keywords: thermodynamics, micro-combustion, ammonia, NOx emissions

Artistic artificial intelligence images were generated based on the abstract content.

* Corresponding author:
Email: dan.zhao@canterbury.ac.nz

Clean Combustion and Decarbonisation Paper 13
B. Z. Dlugogorski and A. R. Masri, Eds

Towards Clean Combustion and Decarbonisation
Proceedings of the Australian Combustion Symposium
26 – 29 November 2023, Darwin, Northern Territory, Australia

Endoscopic high-speed imaging for hydrogen gas jet visualisation in a production spark ignition engine

C. Zhang[1], D. Kim[1] and S. Kook[1,*]
[1]School of Mechanical and Manufacturing Engineering, The University of New South Wales, NSW 2052 Australia

Abstract

Hydrogen plays a key role in reducing carbon dioxide emissions from combustion engines. In the spark ignition engine, its use is limited by backfiring, preignition and knocking issues. To tackle these, hydrogen direct injection technology has been developed in which complex jet-flow interactions occur during the fuel injection in the compression stroke. In this study, endoscopic high-speed gas jet visualisation (eHS-GV) is performed in a near-production engine for enhanced fundamental and practical knowledge about the jet development. The intake air is seeded with olive oil droplets and a high-speed laser inserted through an endoscope is used to illuminate them. Another endoscope connected to a high-speed camera captures darker signals caused by relatively cold gas jet injection. The acquired high-speed movies are post processed to analyse the gas jet penetration duration, and air entrainment and mixing duration. The engine is controlled to vary the injection timing and pressure while keeping the engine load and speed conditions constant at 160 Nm and 2000 revolutions per minute. The results show higher injection pressure leads to faster jet penetration and reduced mixing duration to reach more lean homogeneous mixture conditions required for nitrogen monoxide suppression. The retarded injection timing results in longer penetration duration due to the back pressure build-up; however, the mixing duration is reduced due to positive interactions with the tumble flow.

Keywords: SI engine, endoscopic imaging, hydrogen gas jet, direct injection

Artistic artificial intelligence images were generated based on the abstract content.

* Corresponding author:
Phone: (+61) 02 9663 1222
Email: s.kook@unsw.edu.au

Towards Clean Combustion and Decarbonisation
Proceedings of the Australian Combustion Symposium
26 – 29 November 2023, Darwin, Northern Territory, Australia

Ignition and combustion characterisation of hydrogen/methane blends in direct-injection engine conditions

Yijun Lin[1], Quancen Wan[1], Guanxiong Zhai[1], Cheng Wang[1], Paul R. Medwell[2], Sanghoon Kook[1], Guan Heng Yeoh[1] and Qing Nian Chan[1, *]

[1] School of Mechanical and Manufacturing Engineering, University of New South Wales, NSW 2052, Australia
[2] School of Mechanical Engineering, The University of Adelaide, SA 5005, Australia

Abstract

This work aims to assess the ignition and combustion characteristics of methane (CH_4), hydrogen-methane blend (H_2-CH_4) and hydrogen (H_2) jet in simulated direct-injection, compression-ignition conditions. The experimental parameters were set at a constant value, including ambient temperature (1060 K), ambient density (24 kg/m^3), ambient oxygen concentration (21 vol.%) and reservoir pressure (20 MPa). High-speed schlieren imaging, pressure trace measurement and heat release rate analysis were applied to the jet flames. The optical images reveal three distinct ignition patterns can be observed for the fuel blends, namely, single-kernel ignition, multi-kernel ignition and voluminous ignition, with proportions dependent on fuel compositions. The results also show that the ignition patterns can impact the associated apparent heat release rate profile and flame stabilisation.

Keywords: hydrogen compression ignition, methane compression ignition, constant-volume combustion chamber, direct injection, flame evolution patterns

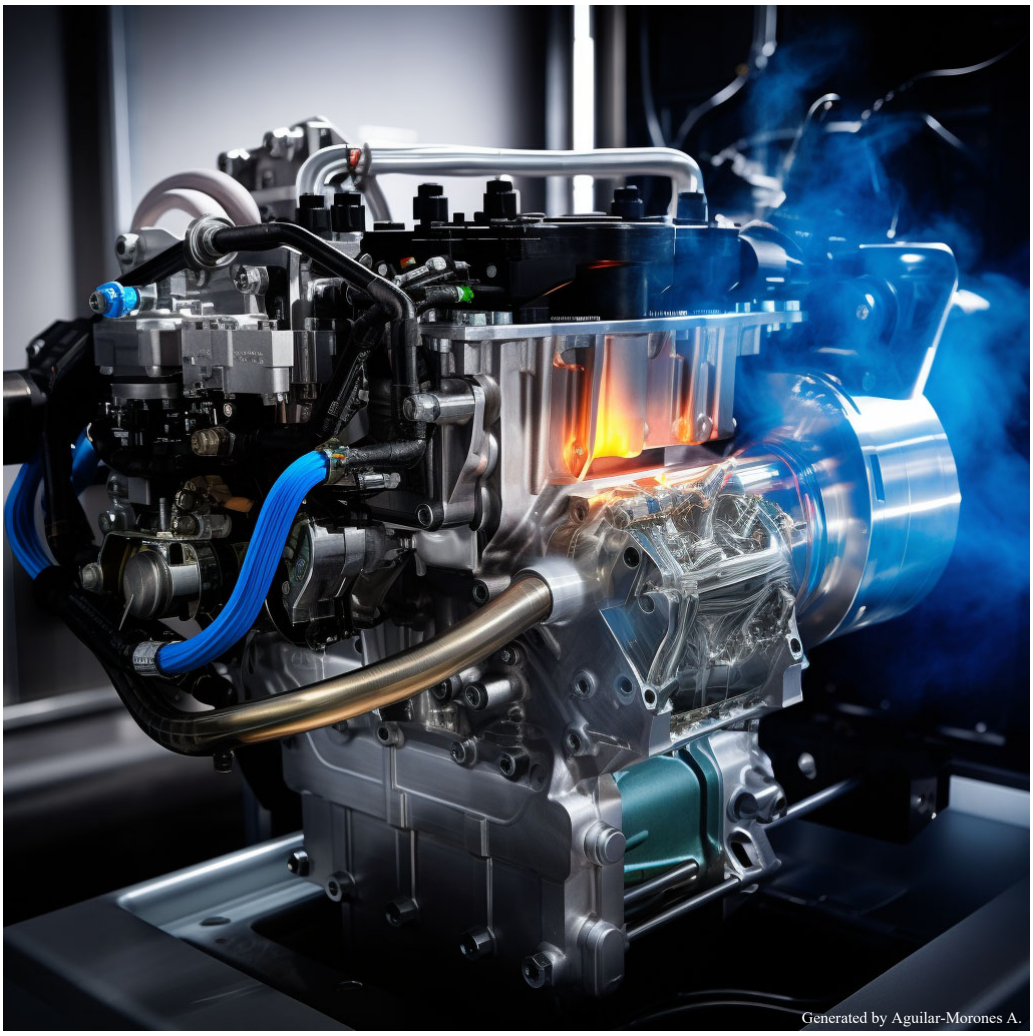

Artistic artificial intelligence images were generated based on the abstract content.

* Corresponding author:
Email: qing.chan@unsw.edu.au

Clean Combustion and Decarbonisation Paper 15
B. Z. Dlugogorski and A. R. Masri, Eds

Towards Clean Combustion and Decarbonisation
Proceedings of the Australian Combustion Symposium
26 – 29 November 2023, Darwin, Northern Territory, Australia

The impact of nitric oxide (NO) on hydrogen oxidation in a high-pressure turbulent flow reactor

Junqiu Jiang, Yi Yang* and Michael Brear
Department of Mechanical Engineering, The University of Melbourne, Parkville, Victoria 3010, Australia.

Abstract

Hydrogen (H_2) oxidation produces only water which makes hydrogen an attractive fuel to reduce green-house gas emissions. However, due to its high combustion temperature, H_2 produces high nitrogen oxide (NO_x) emissions when used in combustion engines which could significantly alter the end gas autoignition behaviour. This work investigates H_2 oxidation sensitised by 50-1000 ppm nitric oxide (NO) in a turbulent flow reactor at 1 to 44 bar, 750 to 900 K, and with an equivalence ratio of 0.02-0.05. A consistent promoting effect on H_2 oxidation is observed with increasing NO addition at a given temperature and pressure. By contrast, at a given NO level, higher pressure monotonically inhibits hydrogen oxidation, where more NO is required to maintain the oxidation rate. Literature models are found to reproduce H_2 profiles reasonably well but fail to predict NO and NO_2 profiles.

Keywords: hydrogen oxidation, NO_x, high-pressure flow reactor

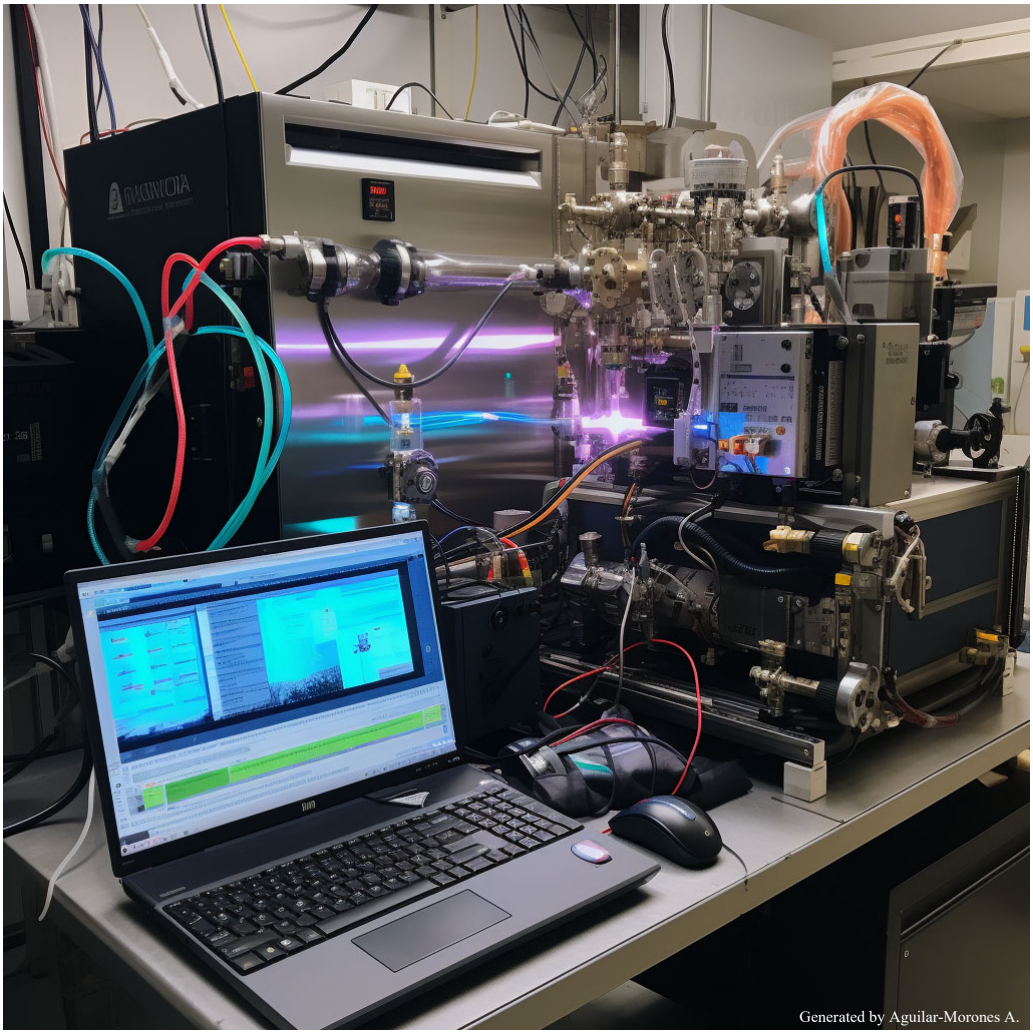

Artistic artificial intelligence images were generated based on the abstract content.

* Corresponding author:
Email: yi.yang@unimelb.edu.au

Clean Combustion and Decarbonisation Paper 16
B. Z. Dlugogorski and A. R. Masri, Eds

Towards Clean Combustion and Decarbonisation
Proceedings of the Australian Combustion Symposium
26 – 29 November 2023, Darwin, Northern Territory, Australia

Visibility of hydrogen flames: Spectral imaging and impact of sodium

Douglas Proud[1,*], Adam Gee[1], Neil Smith[1], Michael Evans[2] and Paul Medwell[1]
[1] School of Mechanical Engineering, The University of Adelaide, Adelaide, SA 5005, Australia
[2] UniSA STEM, University of South Australia, Mawson Lakes, SA 5095, Australia

Abstract

Despite the enormous decarbonisation potential of the direct replacement of natural gas with hydrogen, there are some operational constraints due to the different burning characteristics of hydrogen. One of the challenges is the low visible light emission from hydrogen flames. The change in visible radiation from the combustion of hydrogen compared with natural gas is a safety concern, whereby visual observation of a flame may be difficult. This paper aims to provide clarity on the visual appearance of hydrogen flames via a series of measurements of flame visibility and emission spectra, accompanied by the assessment of strategies to improve the safe use of hydrogen. Of particular note is the impact of sodium on the visual appearance of hydrogen flames, which was verified via spectroscopy and filtered flame photography.

Keywords: hydrogen, safety, flame visibility

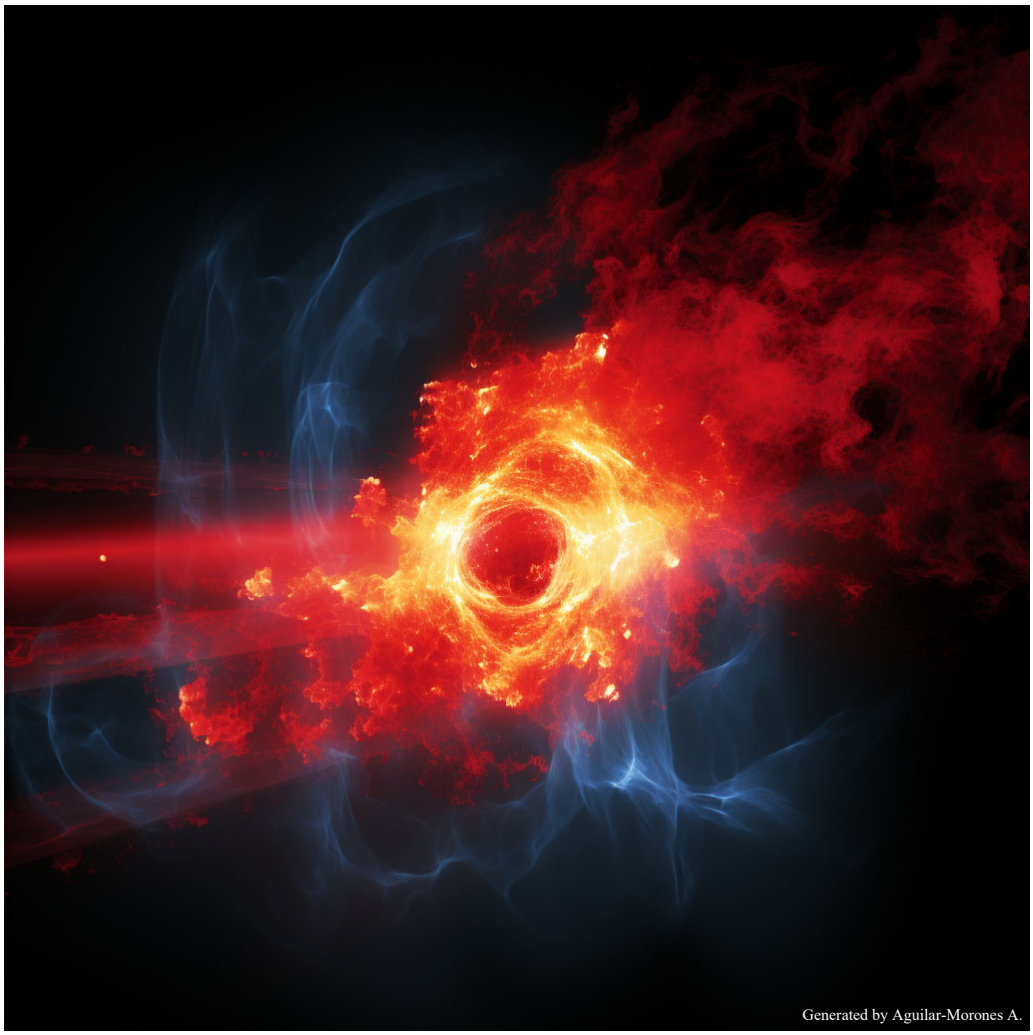

Artistic artificial intelligence images were generated based on the abstract content.

* Corresponding author:
Email: douglas.proud@adelaide.edu.au

Fires and Process Safety Paper 1
B. Z. Dlugogorski and A. R. Masri, Eds

Towards Clean Combustion and Decarbonisation
Proceedings of the Australian Combustion Symposium
26 – 29 November 2023, Darwin, Northern Territory, Australia

Probabilities of burn-through and back surface flaming of pressure treated wood exposed to firebrand pile at large scale

M. Mohamed*, T. D. Penman, and A. I. Filkov
School of Agriculture, Food and Ecosystem Sciences, Faculty of Science, The University of Melbourne, 4 Water St., Creswick, Victoria 3363, Australia

Abstract

Firebrands are responsible for a large fraction of structural losses in the Wildland-Urban Interface by increasing the rate of fire propagation by either direct ignition of structures or contributing for structure-to-structure fire spread. The current study aims to explore the effect of firebrand pile exposure on ignition likelihood of pressure treated wood decking specimens in the presence of wind. Three parameters are varied through the tests, namely, wind speed (1.4 m/sec and 2.7 m/sec), moisture content (7 % and 26 %), and firebrand pile orientation with respect to airflow (0° and 90°). Probability of burn-through along the depth of the specimen, flaming ignition at the back surface of the specimen and re-flaming ignition at the back surface were investigated. Thermal behaviour was captured by using DSLR cameras at the top and back surface of the tested samples. For the current experimental conditions, it is determined that 2.7 m/sec wind speed is accompanied by high propensity of burn-through and is necessary for the occurrence of back flaming. The firebrand pile orientation affects the airflow dynamics within the burning zone and consequently, the occurrence of burn-through and back surface flaming. The 7 % MC is found to raise the propensity of burn-through and back surface flaming. The highest probability of burn-through and back surface flaming was associated with 2.7 m/sec wind speed, 7 % MC and pile orientation of 90° or 0°, respectively.

Keywords: wildland urban interface fires, firebrands, firebrand piles, ignition

1. Introduction

Wildfires are uncontrolled fires that occur in areas dominated by vegetation [1]. Particularly, wildfires become dangerous when propagate into the Wildland-Urban Interface (WUI). Nowadays, WUI fires are becoming a significant concern in areas where wildland vegetation is adjacent or in close proximity to areas of human development [2]. The potential threat of WUI fires is also elevated due to the increased expansion of urbanization into the wildland [3]. Strong convective updrafts in WUI fires can propel small pieces of burning vegetation and solid materials, also called firebrands, into the atmosphere [4] and result in new ignitions several kilometres from the main fire front [5]. The process of spotting is a stochastic form of fire spread and a common mechanism of WUI fire propagation, posing a significant threat to humans' life and environmental settings in WUI [6]. Generally, the role of firebrands in spotting fires is accompanied by the following mechanisms: generation, transport, and ignition of recipient fuel after landing [7]. Typically, the accumulation of firebrands upon landing in the form of piles has been found to be responsible for a large fraction of structure losses by increasing the rate of fire spread by direct ignition and acting as a source of structural fire propagation. However, existing research is mostly focused on the small-scale ignition of fuel beds or structural elements by single firebrand or group of individual firebrands [8-12]. In fact, the influence of firebrand piles exposure on the ignition propensity of building materials has been significantly limited and further investigation is needed by performing large-scale laboratory experiments to replicate real scenarios and to identify the parameters dominating the ignition, combustion, and burning rate of various structural elements and assemblies when exposed to firebrand piles. Thus, the aim of the present study is to carry out large-scale firebrand piles exposure experiments to investigate ignition propensity and thermal behaviour of a representative building materials by varying the applied wind speed, moisture content of tested samples, and firebrand pile orientation.

2. Experimental set-up

The current study employs a particular set-up to conduct large-scale firebrand exposure experiments. The set-up includes a decking specimen, a system of fans to replicate the effect of the wind and firebrand piles of different orientation (Fig. 1). During the tests, the mass loss (ML), mass loss rate (MLR) and temperature of the specimen surface were measured using a balance (PGL 20001) and a FLIR T1040 thermal camera, respectively. These results are not included here and will be presented in future work. Firebrand pile of 8±0.5 grams was deposited on a specimen. It was prepared by burning approximately 100 grams of birch dowels on a burner for around 25 seconds and left till no flames are observed. Firebrand piles of 5 cm x 10 cm x 2.5 cm (LxWxD) with the 2 orientations were tested in the study: parallel (5 cm facing air flow, 0° hereafter) and perpendicular (10 cm facing air flow, 90° hereafter). The tested firebrand pile mass and shape are consistent with observed in experiments of decking assemblies ignition when exposed to firebrand showers [13] and have also been

* Corresponding author:
Phone: (+61) 447398638
Email: memohamed@student.unimelb.edu.au

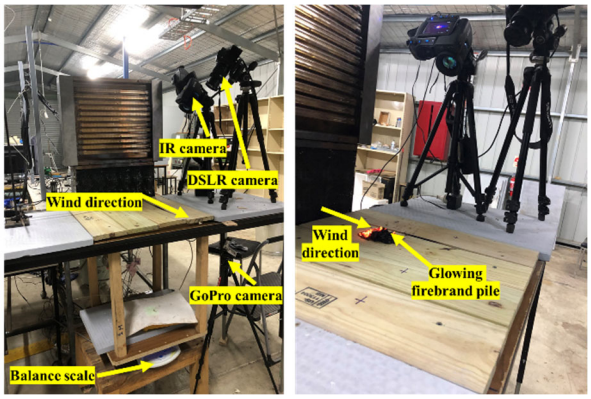

Fig. 1: Experimental set-up.

used in other recent studies [8, 9]. The tested pressure treated wood (PTW) specimen was 60cm x 60 cm and consisted of 4 boards with dimensions of 60cm x 14cm x 1.8 cm (LxWxD) each. The firebrand pile was deposited on the second board from the right (Fig. 1).

A system of 18 fans attached together in 3 rows was used to produce 1.4 m/sec and 2.7 m/sec wind, where a honeycomb was placed in front of the fans to reduce the level of turbulence intensity to <5 %. The airflow was always in the direction towards the glowing firebrand pile. One DSLR camera (Panasonic, Lumix S5) was used to observe firebrand exposure from right side, and two GoPro cameras (Hero4) are utilized to record from the back surface and the left side of the specimen (Fig. 1). An infrared camera (FLIR T1040) was used to measure the temporal and spatial variation of temperature on the back and top surface of the specimen. A scale was used to measure the mass loss (ML) and mass loss rate (MLR) of the sample. Combining MLR with measurements of heat of combustion using bomb calorimeter IKA C1, Heat Release Rate (HRR) was calculated. An experimental matrix is presented in Table 1. Six repetitions were conducted for each experimental condition.

3. Results and discussion

Probabilities of burn-through and back surface flaming ignition is presented in Fig. 2. The results are based on visual observations from the cameras used during experiments. It was found that 2.7 m/sec wind speed, 7 % MC, and 90° firebrand pile orientation resulted in higher likelihood of burn-through.

For the same wind speed and MC, firebrand pile orientation of 90° increases the probability of burn-through. For the same wind speed and pile orientation, decreasing MC from 26 % to 7 % increases the probability of burn-through. For the same MC and pile orientation, increasing the wind speed increases the probability of burn-through. Among all factors, wind speed has a greater effect on achieving a high probability of burn-through.

Applying 2.7 m/sec wind speed with either 90° pile orientation (S4), low MC (S7) or both (S8) resulted in 100 % of burn-through probability. It was observed that 83 % burn-through probability was achieved for S3 and S6 series, suggesting that 2.7 m/sec wind speed has the same effect as 7 % MC and 90° pile orientation combined.

Table 1: Experimental conditions.

Series	Repetitions	Wind speed (m/sec)	MC (%)	Pile orientation
S1	6	1.4	26	0˚
S2	6	1.4	26	90˚
S3	6	2.7	26	0˚
S4	6	2.7	26	90
S5	6	1.4	7	0˚
S6	6	1.4	7	90˚
S7	6	2.7	7	0˚
S8	6	2.7	7	90˚

The data in Table 1 was analyzed by comparing absolute difference of the burn-through probability by varying one variable (e.g. wind speed, MC % or firebrand pile orientation) while keeping the other two variables constant. This resulted in four pairs of conditions. For instance, varying firebrand pile orientation from 0° to 90° while keeping constant wind speed and MC, results in the following pairs: S2/S1, S4/S3, S6/S5, and S8/S7. The highest difference of 33 % was observed for different pile orientation, 7 % MC and 1.4 m/sec wind, followed by 17 % difference for pairs of 1.4 m/sec and 2.7 m/sec at 26 % MC. No difference was observed for 7 % MC and 2.7 m/sec wind. Similar analysis is employed also for the rest of the variables. It was determined that on average increasing wind speed has the highest influence on the probability of burn-though (42 %) compared to decreasing the MC % and changing the pile orientation from 0° to 90°, both having the same effect statistically (17 %). It can be assumed that 90° pile orientation has the largest exposed area to the airflow, and consequently, improving the combustion efficiency of the firebrand pile and the tested sample leading to higher probabilities of burn-through.

In terms of the initial back surface flaming, the highest probability was observed with 2.7 m/sec wind speed, 7 % MC, and 0° firebrand pile orientation. A total of 24 tests were performed at 1.4 m/sec with different configuration of MC and firebrand pile orientation, at which the back surface flaming was observed only once (S6: 1.4 m/sec; 7 %; 90°). The flaming at the back surface of the PTW sample mostly occurs when 2.7 m/sec wind speed was applied. Therefore, it can be assumed that 2.7 m/sec wind speed is the dominating parameter results in flaming ignition at the back surface.

One reason for this may be the amount of oxidizer supplied to the combustion zone. The airflow dynamics and combustion intensity on the back surface can be influenced by the orientation of the firebrand pile, and consequently the shape of the hole, and the wind speed (Fig. 3). For example, at a wind speed of 2.7 m/s with a 90° orientation, the wind cannot sufficiently penetrate the combustion zone due to the small longitudinal distance of the combustion zone along the airflow direction. As a result, less oxidizer is delivered to the combustion zone on the back surface, resulting in a lower probability of back flaming ignition at 90° orientation, as shown in Fig. 2. Similarly, a wind speed

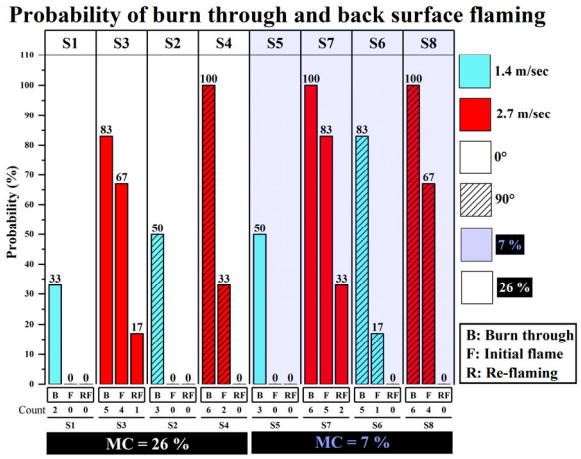

Fig. 2: Probability of burn-through and back surface flaming: Count is the number of times the event occurred out of 6 repetitions.

of 1.4 m/s does not provide enough oxygen at both orientations of the firebrand pile to initiate flaming ignition at the back surface. Alternatively, the longitudinal distance could affect on the convective heat transfer coefficient, subsequently changing the cooling effect through convection. However, these assumptions require further investigation.

Comparing S4 to S3, it was found that changing the pile orientation from 90° to 0° at 26 % MC and 2.7 m/sec wind was associated with a 34 % increase in the probability of back surface flaming. While changing the pile orientation at 7 % MC and the same wind speed (S8 and S7) resulted in 16 % increase in the probability of back surface flaming. Obviously, changing the orientation of the pile from 90° to 0° has the effect on increasing the probability of back surface flaming.

When comparing S4 to S8 (90° orientation and 2.7 m/sec wind), it was found that a decrease in MC from 26 % to 7% was associated with a 34 % increase in the probability of the back surface flaming. While for the 0° orientation (S3 and S7), a decrease in MC was only associated with a 16 % increase in the probability of back surface flaming. However, it should be noted that for the S3-S7 pair, the probability of flaming was the highest, 67% and 83 % respectively. Clearly, decreasing MC from 26 % to 7 % has an effect on increasing the probability of back surface flaming. It was observed that similar 67 % back surface flaming probability was achieved for S3 and S8 series suggesting that 0° pile orientation may have approximately similar effect as 7 % MC in terms of combustion efficiency.

Regarding the probability of back surface flaming, the interplay between 2.7 m/sec wind speed, 7 % MC, and 0° pile orientation, was examined in more detail. For a wind speed of 2.7 m/sec and a 90° pile orientation (S4/S8), a reduction in MC from 26% to 7% results in a 34% increase in the back surface flaming probability. Similarly, for a wind speed of 2.7 m/sec and 26 % MC (S4/S3), changing the firebrand pile orientation from 90° to 0° resulted in a 34% increase in the probability of back surface flaming. However, in cases when 2.7 m/sec wind speed was combined with 0° pile orientation (S3/S7), a reduction in MC from 26% to 7% resulted in only a 16% increase in the probability of back surface flaming. Likewise, if 2.7 m/sec wind speed was combined with 7 % MC (S8/S7), changing the pile orientation from 90° to 0° resulted in an increase in the probability of back surface flaming for only 16 %. It is clear that among 2.7 m/sec wind speed, 7 % MC and 0° pile orientation, applying only two parameters including 2.7 m/sec wind speed is sufficient in approaching a critical probability threshold of back surface flaming.

Similar to burn-though analysis, we compared pairs of back surface flaming for different wind speed while keeping same firebrand pile orientation and MC %. The highest difference of 83 % was observed for 7 % MC and 0° pile orientation (S7/S5), followed by 67 % difference for 0° pile orientation at 26 % MC (S3/S1), then by 50 % difference for 90° pile orientation at 7 % MC (S8/S6), and eventually by 33 % difference for 0° pile orientation at 26 % MC (S4/S2). Similar analysis was employed also for the rest of the variables. It was found that on average increasing wind speed had the highest influence on the probability of back surface flaming (58 %) compared to reducing the MC (17 %) and changing the pile orientation from 90° to 0° (8 %).

As represented in Fig. 2, the probability of re-flaming at the back surface of the PTW sample occurs only at 2.7 m/sec wind speed and 0° pile orientation. This result indicates that the increase in wind speed and 0° orientation are important parameters associated with back surface flaming ignition. Similar to back surface flaming ignition, the probability of re-flaming increases when MC decreases from 26% to 7%.

Our results are consistent with other studies [8-10], in which it was found that an increase in wind speed increases the probability of ignition and intensity of combustion of structural elements from firebrands. Also, the presented findings are in agreement with previous results that indicated that decreasing MC % is an important factor that increases the probability of ignition [11, 12]. Regarding the firebrand pile orientation, further analysis is required to identify the influence of the pile angle on the airflow dynamics in the combustion zone.

The back surface flaming duration is shown in Fig. **4**. The statistical analysis was performed based on 95 % confidence level represented by notches around the median of each group. The notches of all boxes overlap, indicating that their medians are not significantly different.

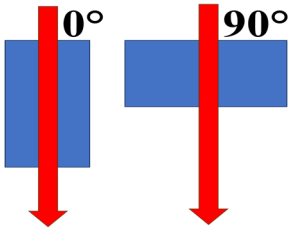

Fig. 3: Effect of firebrand pile orientation on the airflow dynamics. Blue rectangular is the firebrand pile orientation; and red arrow is the wind direction.

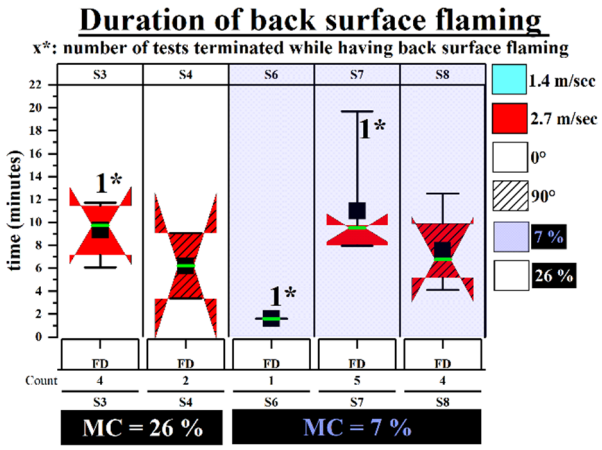

Fig. 4: Duration of back surface flaming: black square is the mean; green line is the median; Count is the number of times the event occurred out of 6 repetitions; and FD is the flaming duration.

The notches extend beyond the 25th and 75th percentiles, showing the uncertainty of the true median value. This occurs even for 4 and 5 repetitions, suggesting that a larger sample size is needed to identify the influence of the factors under study on flaming duration. There are statistically insignificant differences between medians, but it is still of value to compare absolute values between pairs. At the same wind speed and MC (S4/S3 and S8/S7), it was found that the back surface flaming duration increased by approximately 3.1 minutes by changing the firebrand pile orientation from 90° to 0°. At same wind speed and firebrand pile orientation (S3/S7 and S4/S8), it was found that the back surface flaming duration increased by approximately 0.4 minutes by reducing the MC from 26 % to 7 %. Since there was no back surface flaming observed at 1.4 m/sec, increase of wind speed is not discussed.

4. Conclusions

In this study we investigated the effect of MC %, wind speed, and firebrand pile orientation on burning behaviour of PTW samples. Conditions that resulted in the highest probability of burn-through and back surface flaming were associated with 2.7 m/sec wind speed, 7 % MC %, and pile orientation of 90° or 0°, respectively. Increasing wind speed plays a crucial role in elevating the likelihood of burn-through and is necessary for the occurrence of back surface flaming. 90° orientation possesses higher burning efficiency for the firebrand pile results in increasing the probability of burn-through as it has the highest exposed area to the airflow, resulting in higher probability of burn-through. After burn-through, the 0° orientation of the pile leads to an increased probability of back surface flaming and promotes longer flaming. It is assumed that the 0° orientation has better airflow dynamics towards the combustion zone on the back surface of the sample, as it has the greatest extent in the airflow direction. Re-flaming at the back surface occurred under 2.7 m/sec wind speed and 0° pile orientation, confirming the role of 0° firebrand pile orientation in improving the oxidation of the combustion products at the back surface. 7 % MC led to increased burn-through probability and back surface flaming and increased the probability of re-flaming. Wind speed and firebrand pile orientation have significant roles in the probability of back surface flaming, with wind speed being the dominant factor, where the airflow dynamics are mostly affected by the firebrand pile orientation. The back surface flaming duration data showed statistically insignificant differences among the implemented experimental conditions. Nevertheless, comparing medians of the groups show that the back surface flaming duration at 2.7 m/sec is only impacted by the firebrand pile orientation. However, conducting further tests is still needed to assess the impact of wind speed, MC %, and firebrand pile orientation on the back surface flaming duration of the tested samples. The combination of wind speed, MC %, and firebrand pile orientation leads to different combustion behaviours which affect the likelihood and duration of burn-through and back surface flaming. The findings reveal the complicated nature of interaction between firebrand piles and PTW, highlighting the importance of considering multiple factors for a better understanding.

5. Acknowledgments

Mohamed Mohamed was funded by the Underwriters Laboratories 'Firebrand Ignition of Building Materials' project. Alex Filkov was funded by the ARC Discovery 'Understanding the Origin and Development of Extreme and Mega Bushfires: Merging Fire Fronts' project.

6. References

[1] SFPE Handbook of Fire Protection Engineering, 5 ed., Springer New York, NY2016.
[2] L. Johnston, R. Blanchi, M. Jappiot, Wildland-Urban Interface, Encyclopedia of Wildfires and Wildland-Urban Interface (WUI) Fires2019, pp. 1-13.
[3] J.R. Meldrum, C.M. Barth, L.C. Falk, H. Brenkert-Smith, T. Warziniack, P. Champ, Living with wildfire in Log Hill Mesa, Colorado, U.S. Department of Agriculture, Forest Service, Rocky Mountain Research Station, 2013.
[4] J. Martin, T. Hillen, The Spotting Distribution of Wildfires, Applied Sciences 6 (2016).
[5] P. Omi, Forest Fires: A Reference Handbook, ABC-CLIO2005.
[6] G. Peterson, S. Prince, A. Rappold, Trends in Fire Danger and Population Exposure along the Wildland-Urban Interface, Environmental Science & Technology 55 (2021) 16257-16265.
[7] E. Koo, P.J. Pagni, D.R. Weise, J.P. Woycheese, Firebrands and spotting ignition in large-scale fires, International Journal of Wildland Fire 19 (2010).
[8] J.A. De Beer, J.A. Alascio, S.I. Stoliarov, M.J. Gollner, Analysis of the thermal exposure and ignition propensity of a lignocellulosic building material subjected to a controlled deposition of glowing firebrands, Fire Safety Journal 135 (2023).
[9] R.S.P. Hakes, H. Salehizadeh, M.J. Weston-Dawkes, M.J. Gollner, Thermal characterization of firebrand piles, Fire Safety Journal 104 (2019) 34-42.
[10] O. Matvienko, D. Kasymov, E. Loboda, A. Lutsenko, O. Daneyko, Modeling of Wood Surface Ignition by Wildland Firebrands, Fire 5 (2022).
[11] A.C. Fernandez-Pello, Wildland fire spot ignition by sparks and firebrands, Fire Safety Journal 91 (2017) 2-10.
[12] S. Wang, X. Huang, H. Chen, N. Liu, Interaction between flaming and smouldering in hot-particle ignition of forest fuels and effects of moisture and wind, International Journal of Wildland Fire 26 (2017) 71-81.
[13] S.L. Manzello, S. Suzuki, Experimental investigation of wood decking assemblies exposed to firebrand showers, Fire Safety Journal 92 (2017) 122–131.

Fires and Process Safety Paper 2
B. Z. Dlugogorski and A. R. Masri, Eds

Towards Clean Combustion and Decarbonisation
Proceedings of the Australian Combustion Symposium
26 – 29 November 2023, Darwin, Northern Territory, Australia

3D CFD modeling of the effect of sloped terrain on dynamics of wildfires in wildland urban interface

M. Ghodrat[1, *], A. Edalati-nejad[2] and A. Simeoni[3]
[1]School of Engineering & Technology, UNSW Canberra, Canberra, ACT 2600, Australia
[2]School of Science, UNSW Canberra, Canberra, ACT 2600, Australia
[3] Department of Fire Protection Engineering, Worcester Polytechnic Institute, Worcester MA, USA

Abstract

In this research a time-dependent investigation was conducted to numerically analyse the effects of wind-driven surface fire on nine structures representing a densely built area located on sloped terrains downstream of the fire source. A series of three-dimensional CFD simulations was carried out to analyse the effects of varying upslope terrain angles (0°, 10°, and 20°) on an inclined terrain with a constant wind velocity of 6 m/s. The numerical modeling was performed using FireFOAM, an integrated fire-atmosphere model that incorporates a large eddy simulation (LES) solver. To ensure the reliability of the numerical data, a rigorous validation process was undertaken, comparing the simulation results with real-world aerodynamic measurements taken from a full-scale building model, with no influence from fire-related effects. The results of the current work, highlight the fire-wind interactions and their impact on Wildland Urban Interface in the presence of flat and inclined terrain. The findings indicated that an increase in the inclined terrain angle results in a higher integrated temperature across the surfaces of all three rows of buildings.

Keywords: wildland urban interface, wind–fire interaction, terrain slope

1. Introduction

Wildfires are an inevitable natural disaster that inflicts substantial environmental and economic damage. The intricate interplay between complex terrains and the dynamics of wind flow significantly influences the behaviour of fires. The topographical features of an area can modify wind patterns, thereby affecting the spread and intensity of wildfires. Moreover, it is essential to consider the broader context of climate change, as it plays a crucial role in exacerbating wildfire risks. Climate change leads to alterations in temperature, precipitation patterns, and vegetation dynamics, creating favourable conditions for the ignition and rapid spread of wildfires. The combination of complex terrains and climate change-induced factors underscores the urgency to understand and mitigate the impacts of wildfires on both ecosystems and human societies.

The impact of terrain slope on fire spread rate in inclined plane has been examined by some researchers [1-3]. The interaction between wind and fire in sloped terrains is highly complex, with terrain slope playing a pivotal role in determining the rate of fire spread [4]. Recent studies have delved into the effects of terrain slope and wind on wildfire behaviour, revealing that an escalation in terrain slope corresponds to an increase in the rate of fire spread [5-7]. Moreover, investigations have reported that in windward inclined terrains, the acceleration of airflow contributes to more extensive fire propagation [8,9]. An essential area of wildfire research focuses on analysing the thermal and aerodynamic impact of fire-induced wind on urban building structures. He et al. [10], conducted a numerical investigation on the interaction between wind and structure in the presence of bushfire. In their study, Fire Dynamics Simulation (FDS) platform was used to investigate the enhancement of wind by fires and the impact on a single structure. The authors underscored the critical need for more comprehensive research on the influence of wind on fire dynamics and its effects on building structures, particularly when employing grid sizes smaller than the boundary layer thickness.

Sharples [11] examined the risks associated with bushfires and the behaviour of fires in mountainous regions. Their study focused on the mountain meteorology parameters and their potential influence on bushfire behaviour. Notably, they observed a correlation between the terrain slope and the flame's stream-wise velocity profile, as well as the fire-induced flow. In a complementary investigation, Mendes-Lopes et al. [12] conducted a series of experiments to gather data on the rate of spread, flame propagation, and associated characteristics. Their research provided valuable insights into these aspects of fire behaviour.

A numerical study using LES method is done by Ghader et al. [13] to simulate the interaction between an idealized cubic structure in the Wildland-Urban Interface and Wind-Driven Wildfire. The results showed that the presence of a building increases the growth and formation of buoyant instabilities, and consequently affects the behaviour of the fire's plume.

Edalati-nejad et al. [14] investigated the interaction of wind, fire intensity and downslope terrain for a single building in wildfire-prone areas. They found that at higher wind speeds, a single building located on steeper downslope inclinations is at an overall higher risk of bushfire attack, whereas at lower wind speed, a single building on steeper downslope terrain is at an overall lower risk of bushfire attack.

* Corresponding author:
Phone: (+61) 2 5114 5153
Email: m.ghodrat@unsw.edu.au

Prior studies have provided essential numerical insights into the influence of wind-driven surface fires on the dynamic behaviour of fires and temperature profiles downstream of the fire source. Nevertheless, there remains a significant knowledge gap regarding the underlying mechanisms that govern the interaction between horizontal wind flow, fire plumes, and their impact on the velocity profile surrounding a set of buildings situated on sloped terrains, as well as the surface temperature of each building downstream of the fire source.

This research seeks to address this gap by conducting a comprehensive and quantitative analysis of the factors that contribute to changes in surface temperature of buildings located on sloped terrains with varying slope angles.

2. Model Description

2.1 Geometrical model and boundary conditions

This study employs nine 6 × 6 × 6 m cubes to represent a wildland-urban interface (WUI) area affected by a wind-driven wildfire. The dimensions of each cubic structure match those utilized in the full-scale Silsoe cube experiment conducted by [15]. The WUI community under investigation is surrounded by a computational domain measuring 75 × 50 × 25 m, as depicted in Figure 1. To replicate a line fire configuration, a static fire source spanning the entire domain was positioned 15 m upstream of the first row of buildings. The fire line intensity is considered as 10 MW/m. At the inlet of the computational domain, a velocity profile following a power-law pattern was applied to represent the inflow, as described by Equation (1).

$$u^* = \frac{U(Z)}{U_{ref}} = \left(\frac{Z}{Z_{ref}}\right)^{\alpha} \quad (1)$$

Within the provided equation, Z_{ref} represents the reference height, which in this case corresponds to the building's height of 6m. U_{ref} denotes the reference velocity, set at 6 m/s. Alpha, a parameter influenced by terrain features, is assumed to have a value of 0.16 in this study. The top and outlet boundaries were assigned typical atmospheric pressure conditions, while the side boundaries were treated as free-slip boundaries.

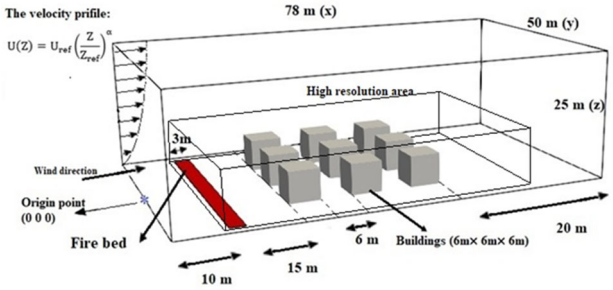

Fig. 1: Schematic of computational domain and the location of the buildings

The horizontal slope (domain attack) angle, θ, is considered as the angle of gravitational acceleration to the z coordinate of the computation domain, which is defined as two non-zero components:

$$g_x = -g\sin(\theta) \text{ and} \quad (2)$$
$$g_z = -g\cos(\theta)$$

For the current study, the selection of the power exponent α, which governs certain aspects of the terrain, is based on the terrain category. In this research, a value of 0.16 has been chosen for α, in accordance with the specific terrain conditions under investigation.

2.2 Numerical method

Numerical simulations were conducted using FireFOAM [16], an open-source software package that incorporates physical models related to heat transfer, combustion, and turbulent diffusion flames. FireFOAM, which is a large eddy simulation (LES)-based solver within the OpenFOAM framework, provides a versatile C++ toolbox for developing customized numerical codes [17]. One of the key advantages of FireFOAM is its integration of multiple systematic computational fluid dynamics (CFD) sub models, to simulate and solve fire dynamics problems. Its versatility is evident in successful applications, ranging from solid fuel pyrolysis, fire suppression, and fire-wall interactions [14]. [14].

Fire dynamics are commonly represented by solving the Favre-filtered equations of continuity, momentum, energy, species, and state, which pertain to fully compressible flow and presented in Eq 3-7:

$$\frac{\partial\bar{\rho}}{\partial t} + \frac{\partial(\bar{\rho}\tilde{u}_i)}{\partial x_i} = 0 \quad (3)$$

$$\frac{\partial(\bar{\rho}\tilde{u}_i)}{\partial t} + \frac{\partial(\bar{\rho}\tilde{u}_i\tilde{u}_j)}{\partial x_i} = \frac{\partial}{\partial x_j}\left[\bar{\rho}(\upsilon + \upsilon_t)\left(\frac{\partial(\tilde{u}_i)}{\partial x_j} + \frac{\partial(\tilde{u}_j)}{\partial x_i} - \frac{2}{3}\frac{\partial(\tilde{u}_k)}{\partial x_k}\delta_{ij}\right)\right] - \frac{\partial(\bar{P})}{\partial x_i} + \bar{\rho}\, g_i\,, \quad (4)$$

$$\frac{\partial(\bar{\rho}\tilde{h})}{\partial t} + \frac{\partial(\bar{\rho}\tilde{u}_j\tilde{h})}{\partial x_j} = \frac{D\bar{P}}{Dt} + \frac{\partial}{\partial x_j}\left[\bar{\rho}\left(\alpha_t + \frac{\upsilon_t}{Pr_t}\right)\left(\frac{\partial\tilde{h}}{\partial x_j}\right)\right] + \dot{q}''' - \nabla.\dot{q}_r'', \quad (5)$$

$$\frac{\partial(\bar{\rho}\widetilde{Y_m})}{\partial t} + \frac{\partial(\bar{\rho}\tilde{u}_j\widetilde{Y_m})}{\partial x_j} = \frac{\partial}{\partial x_j}\left[\bar{\rho}\left(D_c + \frac{\upsilon_t}{Sc_t}\right)\frac{\partial(\widetilde{Y_m})}{\partial x_j}\right] + \omega_m, \quad (6)$$

$$\bar{P} = \bar{\rho}R\tilde{T}, \quad (7)$$

In this context, the symbols "¯" and "~" represent spatial and Favre filtering, respectively. The variable p denotes static pressure, h represents total enthalpy, Y_m signifies the mass fraction of species m, and g denotes gravitational acceleration. Meanwhile, Pr_t, Sc_t, D_c , υ, υ_t, P, R, α_t, δ and ω_m correspond to the turbulent Prandtl number, turbulent Schmidt number, laminar diffusion coefficient, laminar viscosity, turbulent viscosity, density,

gas constant, thermal diffusion coefficient, Kronecker delta, and the production/sink rate of species m due to gas reaction, respectively.

2.3 Model validation

To validate the numerical model, a comprehensive comparison was performed between the mean pressure coefficients obtained in this study and the experimental measurements conducted by [18] as well as [15]. Furthermore, the numerical results of this study were cross validated with the findings from [10], as illustrated in Figure 2. We observe a deviation between the present study and experimental measurements, particularly in the region between points 1 and 2, corresponding to the turbulent flow at the roof's apex. While increasing mesh density could better capture smaller turbulent eddies at this location, it is worth noting that such adjustments would not significantly impact the temperature results, which remains the primary focus of our investigation. Furthermore, minor disparities in experimental measurements may be attributed to potential measurement errors. In summary, the disparities between our findings and those of He et al. [10] are attributable to variations in mesh density, turbulence models, or other potential numerical errors.

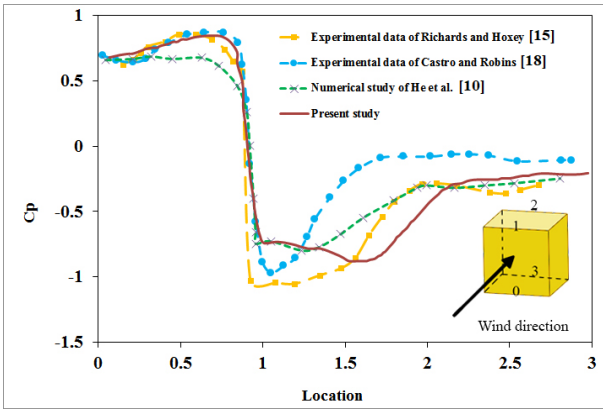

Fig. 2 Comparison of the mean pressure coefficient for the experimental studies of [15] and [18] and numerical simulation of [10]

2.4 Grid Sensitivity Analysis

To enhance the accuracy of the numerical calculations and reduce uncertainties, a meticulous sensitivity analysis of the mesh was performed on the entire domain, employing three distinct sets of structured mesh sizes: 9.1 million, 12.2 million, and 15.8 million cells. These meshes maintain uniformity in all directions. As previously mentioned, the subdomain mesh resolution was established to be five times finer than that of the primary domain. The primary domain mesh sizes were set at 0.5m, 0.165m, and 0.5m, while the subdomain mesh sizes were set at 0.165m in each dimension. The results obtained from the investigation of grid independence, as depicted in Figure 3, demonstrate that augmenting the number of grid cells initially leads to an increase in the area-weighted temperature of the buildings. However, further increments in the number of cells have only a marginal impact on this temperature index (integrated temperature). In other words, increasing the mesh number from 9.1 to 12.2 million changes the area-weighted temperature of the buildings, but a subsequent increase to 15.8 million does not significantly affect the temperature results. Based on this sensitivity analysis, the second mesh number was selected for the present study.

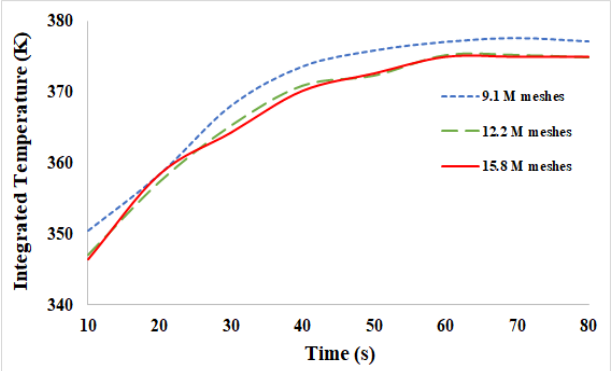

Fig 3. Comparison of the average temperature of the domain against time for three tested grid numbers

3. Results and Discussion

In this study, a comprehensive time-dependent investigation was conducted to analyze the impact of terrain slope on a fire bed and its downstream temperature distribution in the presence of three sets of three rows of buildings, under a wind-field of 6 m/s. Fig 4. shows the flat terrain (slope angle of zero) and Fig. 5 and Fig.6 show sloped terrain at 10 and 20 degrees respectively.

Comparing the results shown in Fig. 4 with those illustrated in Fig. 5 (slope angle 10°) and Fig. 6 (slope angle 20°), indicate the influence of terrain slope on the temperature distribution caused by the fire bed within the domain, considering wind speed of U_{ref} = 6 m/s and fire intensity of 10 MW/m.

The results reveal that as the terrain slope increases, the flame tilt angle induced by the buoyancy force also increases, subsequently leading to higher temperatures near the buildings. This phenomenon arises due to the generation of an amplified component of the buoyancy force on steeper terrain slopes, intensifying the tilt angle and resulting in elevated flame temperatures closer to the ground, particularly in the vicinity of the buildings. The increment of the flame tilt angle caused by an increase in the terrain slope can be seen in figures 4-6. Looking at the flame between the inlet of the domain and the first raw building, the flame tilt angle can be observed. In Fig. 4 it has wider angle compared to Fig. 5 as well as Fig6, which is considerably attached to the ground due to the increase in the terrain slope.

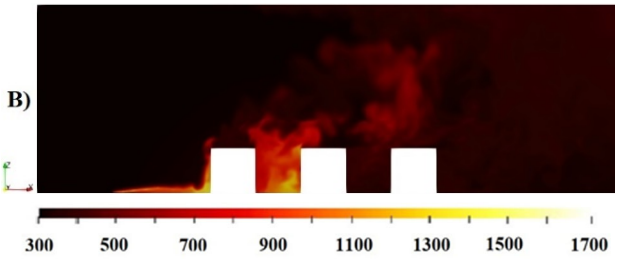

Fig. 4- Contour of temperature distribution for the case with U= 6 m/s and I= 10 MW/m at flat terrain (Slope 0)

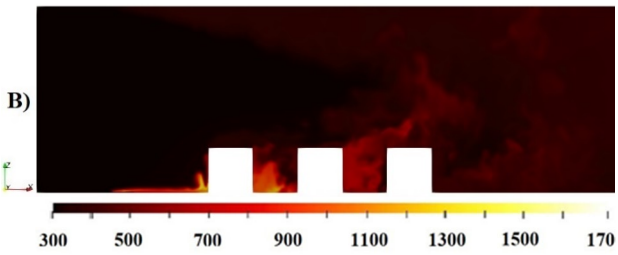

Fig. 5- Contour of temperature distribution for the case with U= 6 m/s and I= 10 MW/m, Slope 10

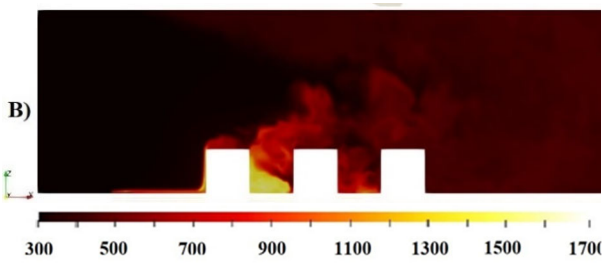

Fig. 6- Contour of temperature distribution for the case with U= 6 m/s and I= 10 MW/m, Slope 20

4. Conclusion

The present study focused on investigating the impact of inclined terrain with varying slope angles on a fire bed, its downstream temperature distribution in the presence of a set of nine building structures representing a densely built area in WUI. Slope angles of 0°, 10° and 20°were considered, along with specific wind-field condition at reference velocities of 6 m/s. The key findings of this investigation can be summarized as follows:

1. In inclined fields, an increase in the upslope terrain angle resulted in a greater tilt angle of the fire flame, primarily due to the buoyancy force. This, in turn, led to higher temperatures in the vicinity of the building.
2. Increasing the inclined terrain angle expanded the area with elevated ground temperatures, particularly in the direction toward the building.

5. Acknowledgments

The current work is supported by computational resources provided by the Australian Government in the University of New South Wales under the National Computational Merit Allocation Scheme (NCMAS).

6. References

[1] L.F. Hawley, J. For., 24, (1926), 756-763.
[2] A.L. Sullivan, Int. J. Wildland Fire, 18, (2009), 387-403.
[3] A.L. Sullivan, J.J. Sharples, S. Matthews, M.P. Plucinski, Environ. Model. Softw., 62, (2014), 153-163.
[4] M. Ghodrat, A. Edalati-nejad, A. Simeoni, Fire, 5, (2022), 208.
[5] N. Liu, J. Wu, H. Chen, X. Xie, L. Zhang, B. Yao, J. Zhu, Y. Shan, Int. J. Wildland Fire, 23, (2014), 1087-1096.
[6] F. Morandini, X. Silvani, J.L. Dupuy, A. Susset, Combust. Flame, 190, (2018), 158-170.
[7] P. Zhu, X.S. Wang, Y.P. He, C.F. Tao, X.M. Ni, Fuel, 184, (2016), 725-734.
[8] F. A. Albini, D. J. Latham, R. G. Baughman, USDA For. Serv. Res. Pap. INT-257, Intermt. For. and Range Exp. Stn., Ogden., (1982), 1-19.
[9] P.S. Jackson, J.C.R. Hunt, Q. J. R. Meteorol. Soc., 101, (1975), 929-955.
[10] Y. He, K.C.S. Kwok, G. Douglas, I. Razali, Fire Saf. Sci., 10, (2011), 1449-1462.
[11] J.J. Sharples, Int. J. Wildland Fire, 18, (2009), 737-754.
[12] J.M. Mendes-Lopes, J.M. Ventura, J.M. Amaral, Int. J. Wildland Fire, 12, (2003), 67-84.
[13] M. Ghaderi, M. Ghodrat, J.J. Sharples, Atmosphere, 12, (2020), 21.
[14] Edalati-nejad, A., Ghodrat, M., & Sharples, J. J. (2023). On the interaction of wind, fire intensity and downslope terrain with implications for building standards in wildfire-prone areas. International Journal of Wildland Fire.
[15] P.J. Richards, R.P. Hoxey, J. Wind. Eng. Ind. Aerodyn., 102, (2012), 72-86.
[16] Y. Wang, P. Chatterjee, J.L. de Ris, Proc. Comb. Inst., 33, (2011), 2473-2480.
[17] C.J. Greenshields, OpenFOAM User Guide, (2015), 473.
[18] I.P. Castro, A.G. Robins, J. Fluid Mech., 79, (1977), 307-335.

Fires and Process Safety Paper 3
B. Z. Dlugogorski and A. R. Masri, Eds

Towards Clean Combustion and Decarbonisation
Proceedings of the Australian Combustion Symposium
26 – 29 November 2023, Darwin, Northern Territory, Australia

Effect of fire intensity on wildfire interaction with multiple structures

M. Ghodrat[1,*] and A. Edalati-nejad[2]
[1]School of Engineering & Technology, UNSW Canberra, Canberra, ACT 2600, Australia
[2]School of Science, UNSW Canberra, Canberra, ACT 2600, Australia

Abstract

This paper presents a numerical modeling approach to investigate the effect of variation of fire intensity on the thermal heat flux and temperature profiles of an array of structures in a typical Wildland Uran Interface (WUI) scenario. To simulate the effects of wind-driven wildfires on a densely built suburban area, nine cubic structures, each measuring 6 × 6 × 6 m, were arranged in a grid of three rows of three, downstream of the fire source. The numerical modelling was conducted using an open source CFD code called FireFOAM which is a transient solver for fire dynamic simulation and turbulent diffusion flames supported by a large eddy simulation (LES) solver. The numerical data were verified using the aerodynamic measurements of a full-scale building model in the absence of fire effects. A set of two fire intensities, each corresponding to different types of grassland fuels was modelled to simulate fires burning with a relatively high wind speed of 12 m/s. The results show that at constant wind velocity of 12 m/s, an increase in fire intensity from I= 10 to 15 MW/m causes an increase in the surface temperature of all buildings, however, the temperature rise is higher on the first row of buildings compared to the rest.

Keywords: wildfire, large eddy simulation, wildland-urban interface, fire intensity, wind-structure

1. Introduction

While the concept of the wildland-urban interface (WUI) has been a longstanding concern, there has been a recent uptick in the frequency of fires occurring within WUI communities [1]. Extensive documentation of the consequences of this escalating wildfire phenomenon over the last few decades exists [2,3], and it is expected that these effects will become more pronounced due to climate change affecting regions worldwide. A critical aspect of addressing the WUI challenge and crafting effective solutions involves the analysis of how airflow behaves around built areas, the rate at which fires propagate, and their direct connection to fuel, which directly impacts fire intensity. These factors, to varying degrees, contribute to mitigating the impacts of wind-driven wildfires at the interface between wildland and urban areas. Through a comprehensive examination and understanding of these factors, we can formulate strategies to minimize the detrimental effects on WUI communities.

Depending on the specific environmental conditions, structures may catch fire as a wildfire approaches a Wildland Urban Interface (WUI) community [4]. Therefore, comprehending the impact of wind on the wildland urban interface is a crucial factor in predicting how fires behave. It's worth noting that there haven't been any experimental studies that have investigated the combined influence of fire and wind on buildings. Nonetheless, some researchers, like Richards et al. [5], conducted experiments and numerical analyses to understand how cube-shaped buildings respond to wind pressure, providing valuable insights into a building's aerodynamic behaviour in windy conditions without the presence of fire. Hostikka et al. [6] focused on numerical simulations to explore fire behaviour at the wildland urban interface, shedding light on the thermal effects of bushfires on structures. Their findings recommended a mesh size of 0.25 m for thermal radiation numerical simulations. Fryanova and Perminov [7] delved into the impact of fire intensity and wind speed on the likelihood of buildings catching fire, examining the thermal and fluid dynamics effects of wind on structures. Ghodrat et al. [8] and Ghaderi et al. [9] investigated the interaction between fire and wind on structures, analysing wind direction, terrain slope angles, and their influence on fire modeling. They also explored the transition from a wildfire to a Wildland–Urban Interface (WUI) situation, emphasizing the importance of considering how structural and wildland fuels combine in WUI simulations. Mell et al. [10] examined the WUI phenomenon and its associated challenges, concluding that physics-based models, supported by experimental data, can predict fire behaviour across a wide range of atmospheric and terrain slope conditions, which is invaluable for developing risk assessment and mitigation strategies in realistic WUI scenarios involving various fuels and environmental conditions.

Fuel moisture content (FMC) plays a key role in influencing the severity of fires [11]. It governs the conditions required for ignition, the quantity of fuel consumed, and the speed at which different types of fuel burn [12]. Empirical evidence demonstrates that elevating the fuel moisture content (FMC) from 5% to 70% can lead to a reduction in fire intensity of up to 70% [13]. This decrease in fire intensity can be attributed to the significant release of water vapor ahead of the fire, which effectively diminishes the supply of oxygen to the advancing fire front [12,14]. Additionally, the phase

* Corresponding author:
Phone: (+61) 2 5114 5153
Email: m.ghodrat@unsw.edu.au

transition of water into vapor necessitates a substantial amount of heat due to its high specific vaporization heat.

Numerous studies have underscored the connection between FMC and fire intensity and their impact on fire behaviour [15-20]. Clark et al. [21] examined the interactions between fire behaviour, fire intensity, canopy fuels, and turbulence and energy fluxes above the canopy. They explored how turbulence and energy fluxes were associated with fire behaviour and fuel consumption in wildfires, noting that more intense head fires led to greater consumption of shrubs and canopy fuels while also causing a notable increase in turbulence and heat flux above the canopy.

The existing review of literature highlights that, despite numerous studies on fire intensity and fuel content, there remains a need for more thorough investigation into the fundamental understanding of how wind-driven surface fires and their intensity affect building structures within the Wildland-Urban Interface.

Previous research has supplied essential insights into the influence of fuel energy content on fire behaviour and its spread. Nevertheless, we still lack a comprehensive understanding of the underlying mechanisms concerning how the intensity of wind-driven surface fires impacts buildings at the Wildland-Urban Interface (WUI) and how this variation affects temperature and wind velocity profiles both around and on the buildings. This study aims to bridge this knowledge gap by conducting a quantitative and systematic analysis of the factors that alter velocity profiles and surface temperatures of buildings at various fire intensity levels. This paper represents a numerical simulation to model the interaction between wind driven wildfire with a densely built area within a typical Wildland-Urban Interface setting covering a range of fire intensity values, using the FireFOAM solver.

2. Model Description

In this study, a simulated wildland-urban interface (WUI) impacted by a wind-driven wildfire is modelled using nine 6 × 6 × 6-meter cubic structures, matching those used in the Silsoe cube experiment [22]. The computational domain surrounding the WUI community measures 75 × 50 × 25 meters (see Figure 1). To replicate a line fire configuration, a stationary fire source with different fire intensities of 10 and 15 MW/m is placed 15 meters upstream of the initial row of buildings, which are approximately equivalent to fires burning in Australian Eucalyptus forests under very high fire intensity ratings. This is controlled through modification of model parameters in the numerical solver FireFOAM, corresponding to the burning of methane with a heat of combustion equal to 45 435 kJ/kg. The inlet of the computational domain features a power-law velocity profile, described by Equation (1), to represent inflow conditions.

$$u^* = \frac{U(Z)}{U_{ref}} = \left(\frac{Z}{Z_{ref}}\right)^{\alpha} \qquad (1)$$

In this equation, Z_{ref} corresponds to the building's height, which is 6 meters in this case. U_{ref} represents the reference velocity, set at 6 m/s. The parameter Alpha, influenced by terrain features, is assumed to have a value of 0.16 in this study. Boundary conditions were applied as follows: the top and outlet boundaries were set to typical atmospheric pressure conditions, while the side boundaries were designated as free-slip boundaries.

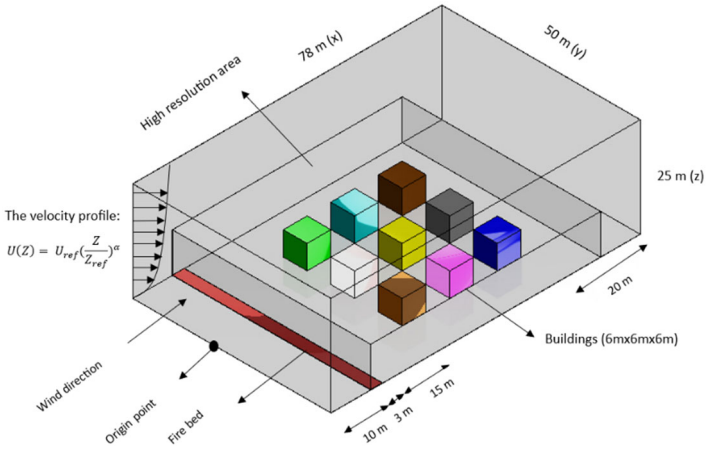

Fig. 1: Diagram illustrating the computational domain layout and the building positions.

2.1 Mathematical and Numerical Modelling

To address the equations governing the problem at hand, we have employed the FireFOAM [23] solver, an open-source software within the OpenFOAM framework. Specifically designed and developed for modeling turbulent buoyant flows and diffusion flames, FireFOAM excels in simulating the dynamic behaviour of fires and has proven to be an effective tool in wildfire modeling [24]. The combustion model of infinitely fast chemistry [25] is also employed. The single-step combustion reaction of methane is used:

$$CH_4 + 2\ O_2 \rightarrow CO_2 + 2\ H_2O$$

For simulating turbulent flows, we have applied the Large Eddy Simulation (LES) method. The wall-adapting local eddy (WALE)-viscosity method is also applied to describe sub-grid scale turbulence, because of its advantage in representing near-wall scaling of the eddy viscosity [26]. The current problem involves using the Favre-filtered formulation of the Navier-Stokes equations, which represent the dynamics of fire. These equations encompass momentum, mass conservation, energy conservation, and the mass fraction of chemical species. The equations governing continuity, momentum, energy, species, and state are detailed in Equations (3) to (7).

$$\frac{\partial \bar{\rho}}{\partial t} + \frac{\partial (\bar{\rho}\tilde{u}_i)}{\partial x_i} = 0 \qquad (3)$$

$$\frac{\partial(\bar{\rho}\tilde{u}_i)}{\partial t} + \frac{\partial(\bar{\rho}\tilde{u}_i\tilde{u}_j)}{\partial x_i} = \frac{\partial}{\partial x_j}\left[\bar{\rho}(\upsilon + \upsilon_t)\left(\frac{\partial(\tilde{u}_i)}{\partial x_j} + \frac{\partial(\tilde{u}_j)}{\partial x_i} - \frac{2}{3}\frac{\partial(\tilde{u}_k)}{\partial x_k}\delta_{ij}\right)\right] - \frac{\partial(\bar{P})}{\partial x_i} + \bar{\rho}\, g_i\,, \quad (4)$$

$$\frac{\partial(\bar{\rho}\tilde{h})}{\partial t} + \frac{\partial(\bar{\rho}\tilde{u}_j\tilde{h})}{\partial x_j} = \frac{D\bar{P}}{Dt} + \frac{\partial}{\partial x_j}\left[\bar{\rho}\left(\alpha_t + \frac{\upsilon_t}{Pr_t}\right)\left(\frac{\partial\tilde{h}}{\partial x_j}\right)\right] + \dot{q}''' - \nabla.\dot{q}_r'', \quad (5)$$

$$\frac{\partial(\bar{\rho}\widetilde{Y_m})}{\partial t} + \frac{\partial(\bar{\rho}\tilde{u}_j\widetilde{Y_m})}{\partial x_j} = \frac{\partial}{\partial x_j}\left[\bar{\rho}\left(D_c + \frac{\upsilon_t}{Sc_t}\right)\frac{\partial(\widetilde{Y_m})}{\partial x_j}\right] + \omega_m, \quad (6)$$

$$\bar{P} = \bar{\rho}R\tilde{T}, \quad (7)$$

In this context, the symbols "¯" and "~" represent spatial and Favre filtering, respectively. The variable p denotes static pressure, h represents total enthalpy, Y_m signifies the mass fraction of species m, and g denotes gravitational acceleration. Meanwhile, Pr_t, Sc_t, D_c , υ, υ_t, P, R, α_t, δ and ω_m correspond to the turbulent Prandtl number, turbulent Schmidt number, laminar diffusion coefficient, laminar viscosity, turbulent viscosity, density, gas constant, thermal diffusion coefficient, Kronecker delta, and the production/sink rate of species m due to gas reaction, respectively. $\dot{q}_r''$shows the total radiative heat flux (W/m^2) of the gas mixture, and $\dot{q}'''$ represents the heat generated by combustion [9] and meaning the reaction rate of fuel multiplied by the heat of combustion which can be defined as equation 8:

$$\dot{q}''' = \omega_m.\Delta H_c, \quad (8)$$

2.2 Model Validation

To validate the accuracy of our numerical model, we conducted a comprehensive comparison of mean pressure coefficients with experimental data from two separate sources: Castro and Robins [27] and Richards and Hoxey [22]. Furthermore, we corroborated our numerical findings with those of He et al. [28], as depicted in Figure 2. These experiments involved measuring pressure along both the vertical and horizontal centrelines of the Silsoe cube, which serves as a representation of an idealized building, under irrotational and sheared turbulent flow conditions. Additionally, our study's results were validated against He et al.'s [28] numerical investigation, which focused on modeling the interactions between bushfires, wind, and building structures using the Fire Dynamic Simulation (FDS) software package.

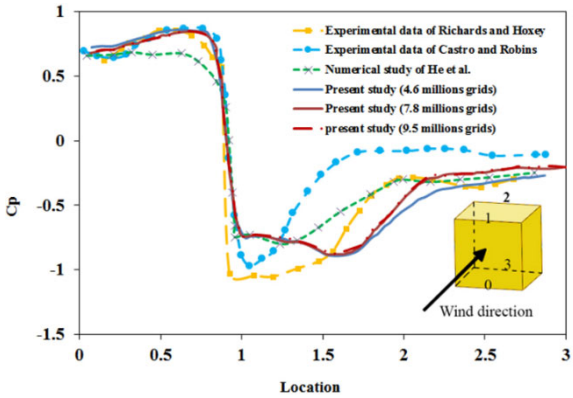

Fig 2. Model validation: Comparison of mean pressure coefficient of the present model with experimental studies of Richards and Hoxey [22] and Castro and Robin [27] and numerical simulation of He et al. [28]

2.4 Grid Sensitivity Analysis

To enhance the accuracy of our numerical computations and reduce uncertainties, we conducted a thorough sensitivity analysis of the mesh across the entire domain. We employed three distinct sets of structured mesh sizes: 9.1 million cells, 12.2 million cells, and 15.8 million cells, all designed to maintain uniformity in all directions. As previously mentioned, the subdomain's mesh resolution was intentionally set to be five times finer than that of the primary domain. The primary domain utilized mesh sizes of 0.5m, 0.165m, and 0.5m, while the subdomain featured mesh sizes of 0.165m in each dimension. The results collected from our investigation into grid independence, as shown in Figure 3, reveal that increasing the number of grid cells initially results in an elevation of the area-weighted temperature of the buildings. However, further increments in the number of cells have only a marginal impact on this temperature index (integrated temperature).

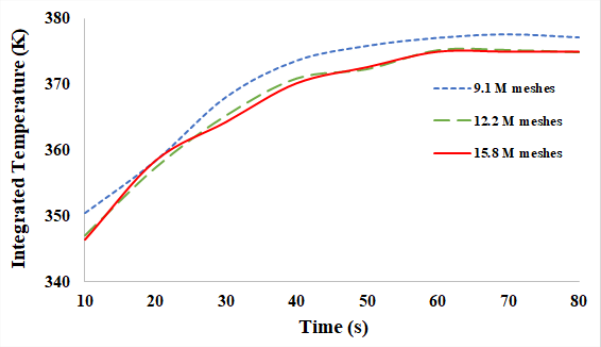

Fig 3. Comparison of the average temperature of the domain against time for three tested grid numbers

3. Results and Discussion

Comparing the temperature contours under fire intensities of 10 MW/m and 15 MW/m highlighted that the temperature on and around the three rows of buildings are intensified with raising fire intensities for

a constant wind speed of 12 m/s . Besides , an increased fire intensity has a notable impact on temperatures downstream, resulting in exceptionally high temperatures even behind the buildings.

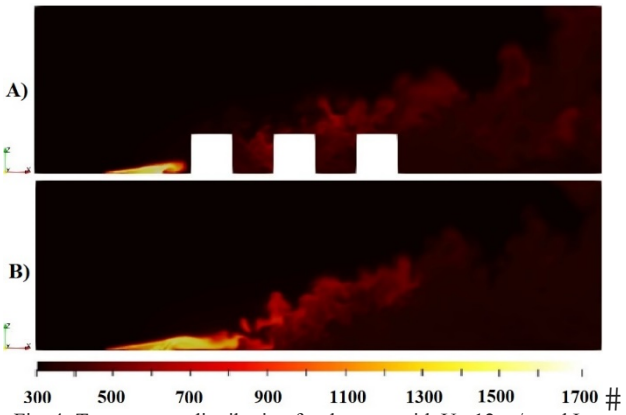

Fig. 4- Temperature distribution for the case with U= 12 m/s and I= 10 MW/m: B) cross section at y=0m C) cross section at y=6m.

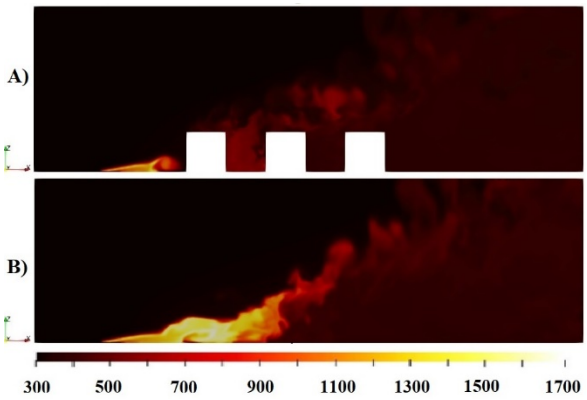

Fig. 5- Temperature distribution for the case with U= 12 m/s and I= 15 MW/m: B) cross section at y=0m C) cross section at y=6m.

Temperature distribution results presented in Figure 4 and Figure 5 pointed out that the temperature rise is higher on the first row of buildings compared to the second and the third.

4. Conclusion

This study presented a 3D computational fluid ıamics (CFD) analysis investigating the dynamic characteristics of wind-driven line fires and their impact on an array of nine cubic structures in the Wildland-Urban Interface (WUI). The primary focus was to examine how variations in fire intensity affect the multibuilding scenario in the WUI setting. Through a detailed comparison of line fire dynamics at different distances from the fire source and known wind velocities, it was observed that changes in fire intensity influence the plume geometry and characteristics. Moreover, the presence of multiple buildings significantly alters the plume attachment pattern. Increasing fire intensity resulted in a notable rise in temperature downstream of the fire source, to the extent that even at the back of the buildings, a zone of considerably higher temperature becomes apparent.

5. Acknowledgments

The current work is supported by computational resources provided by the Australian Government in the University of New South Wales under the National Computational Merit Allocation Scheme (NCMAS).

6. References

[1] S.E. Caton, R.S.P. Hakes, D.J. Gorham, A. Zhou and M.J. Gollner, Fire Technol. 53 (2016) 429–473.
[2] P.E. Dennison, S.C. Brewer, J.D. Arnold and M.A. Moritz, Geophys. Res. Lett. 41 (2014) 2928–2933.
[3] A.L. Westerling, Trans. R. Soc. B Biol. Sci. 371 (2016) 20150178.
[4] R.S.P. Hakes, S.E. Caton, D.J. Gorham and M.J. Gollner, Fire Technol. 53 (2) (2017) 475–515.
[5] P.J. Richards and R.P. Hoxey, J. Wind. Eng. Ind. Aerodyn. 102 (2012) 72–86.
[6] Hostikka, S., J. Mangs, and E. Mikkola, Fire Saf. Sci. 9 (2008) 1353–1364.
[7] K.O. Fryanova and V.A. Perminov, Mag. Civ. Eng. 75 (7) (2017) 15–22.
[8] M. Ghodrat, F. Shakeriaski, D.J. Nelson and A. Simeoni, Fire 4 (2) (2021) 27.
[9] M. Ghaderi, M. Ghodrat and J.J. Sharples, Atmosphere, 12 (1) (2021) 21.
[10] W.E. Mell, S.L. Manzello, A. Maranghides, D. Butry and R.G. Rehm, Int. J. Wildland Fire 19 (2) (2010) 238–251.
[11] D. Morvan, Fire Saf. J. 58 (2013) 121–131.
[12] N. Cheney, J. Gould and W. Catchpole, Int. J. Wildland Fire 3 (1) (1993) 31–44.
[13] T. Banerjee, W. Heilman, S. Goodrick, J. K. Hiers and R. Linn, Sci. Rep. 10 (1) (2020) 1–14.
[14] D. Morvan, Int. J. Wildland Fire 16 (5) (2007) 511–518.
[15] J. Gong, J. Cao, C. Zhai and Z. Wang, Appl. Therm. Eng. 179 (2020) 115651.
[16] D.R. Weise, E. Koo, X. Zhou, S. Mahalingam, F. Morandini and J.H. Balbi, Int. J. Wildland Fire 25 (9) (2016) 980–994.
[17] M.G. Cruz, M.E. Alexander and R.H. Wakimoto, Int. J. Wildland Fire 12 (1) (2003) 39–50.
[18] K. Moinuddin, N. Khan and D. Sutherland, Fire Saf. J. 125 (2021) 103422.
[19] A. Edalati-nejad, M. Ghodrat, S. A. Fanaee and A. Simeoni, Fire 5 (1) (2022) 17.
[20] M. Ghodrat, A. Edalati-Nejad, A. Simeoni, Fire, 5 (6) (2022) 208.
[21] K.L. Clark, W.E. Heilman, N.S. Skowronski, M.R. Gallagher, E. Mueller, R.M.; Hadden and A. Simeoni. Atmos. 11 (3) (2020) 242.
[22] P. Richards and R. Hoxey, J. Wind Eng. Ind. Aerodyn. 102 (2012) 72-86.
[23] Y. Wang, P. Chatterjee and J.L. de Ris, Proc. Combust. Inst. 33 (2) (2011) 2473–2480.
[24] M. El Houssami, A. Lamorlette, D. Morvan, R.M. Hadden and A. Simeoni, Combust. Flame 190 (2018) 12–24.
[25] S. Akaotsu, R. Ozawa, Y. Matsushita, H. Aoki, & W. Malalasekera, (2020). Fuel Processing Technology, 199, 106226.
[26] N. Ren, Y. Wang, S. Vilfayeau, & A. Trouvé (2013). In 7th International Seminar on Fire and Explosion Hazards.
[27] I. Castro and A. Robins, J. Fluid Mech. 79 (2) (1977) 307–335.
[28] Y. He, K.C.S. Kwok, G. Douglas, I. Razali, Fire Saf. Sci. 10 (2011) 1449–1462.

Fires and Process Safety Paper 4

B. Z. Dlugogorski and A. R. Masri, Eds

Towards Clean Combustion and Decarbonisation
Proceedings of the Australian Combustion Symposium
26 – 29 November 2023, Darwin, Northern Territory, Australia

An industrial-scale fire growth model for thin melting plastics

A. Krisman*
FM Global, MA 02062 USA

Abstract

Melting plastics are present in most building fires and represent the main fuel load in many large storage occupancies. Melting plastics fire growth is challenging to model due to the complex thermal decomposition process which involves melting and deformation in addition to pyrolysis, combustion, and heat transfer. This paper presents a simple model which captures the essential aspects of these processes for thin plastics in a manner that is: 1) computationally tractable, 2) scalable to industrial scale applications, and 3) extensible to also treat fire suppression dynamics. The model is implemented in FireFOAM, a fire modelling tool based on OpenFOAM with capabilities to capture the coupled dynamics of fire growth and suppression on unstructured and dynamic CFD meshes. The model is presented with respect to a standard plastic commodity used by FM Global to represent the fire hazard of unexpanded plastics, for which validation data is available, but may be generally applied to other geometries and related materials.

Keywords: warehouse fires, Class B fires, fire modelling, plastics decomposition in fires

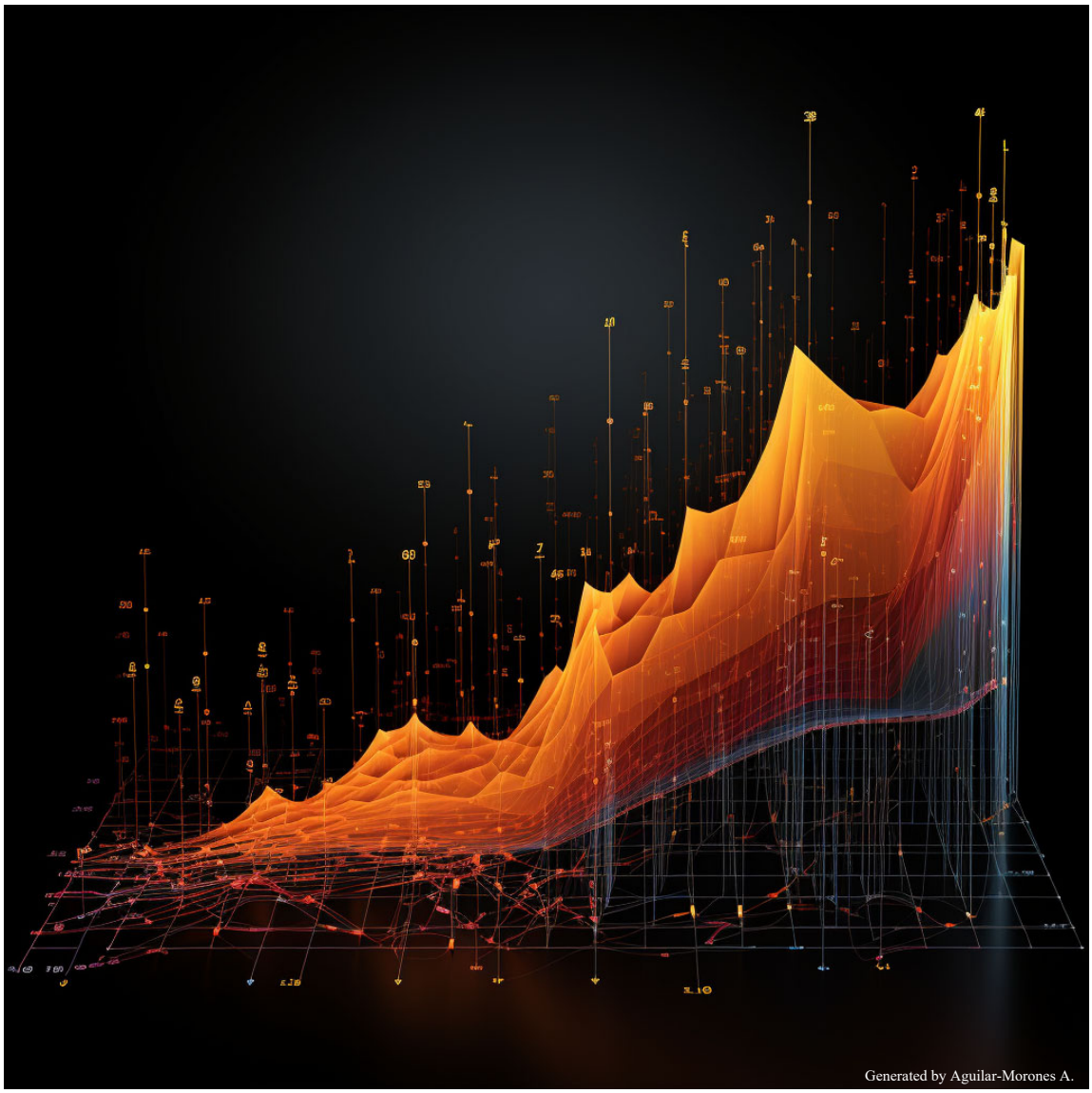

Artistic artificial intelligence images generated were based on the abstract content.

* Corresponding author:
Phone: (+61) 2 8273 1400
Email: alex.krisman@fmglobal.com

Fires and Process Safety Paper 5
B. Z. Dlugogorski and A. R. Masri, Eds

Towards Clean Combustion and Decarbonisation
Proceedings of the Australian Combustion Symposium
26 – 29 November 2023, Darwin, Northern Territory, Australia

Temperature and mixture fraction imaging in a vertical wall fire

V. Gupta[1,*], T. Xiao[1], M. J. Dunn[1], J. L. Torero[2] and A. R. Masri[1]
[1]School Aerospace, Mechanical, and Mechatronics Engineering, The University of Sydney, NSW 2006 Australia
[2]Department of Civil, Environmental and Geomatic Engineering, University College London, United Kingdom

Abstract

This paper presents the first laser-based measurements of temperature and mixture fraction in a vertical buoyancy-driven wall fire configuration. The objective of this paper was to explicitly measure near-wall flame structure and scalar gradients to understand flame-to-wall heat transfer mechanisms controlling both upward and downward fire spread. Gaseous methane is injected into a porous 3D-printed bronze burner at varying flow rates. Rayleigh scattering imaging of temperature and mixture fraction is undertaken using a high-energy laser sheet at 532 nm that is positioned adjacent to the burner surface. Through careful elimination of potential errors and interferences, scalars can be resolved from the flame leading edge onwards within 100 – 200 μm from the burner surface. The measurements within the laminar region of the flame reveal peak temperatures ranging from 1600 – 1800 K and large temperature and mixture fraction gradients that have plagued accurate quantification of the convective feedback. These gradients are sharpest towards the leading edge, likely contributing to its relative stability despite increased fuel injection rates. Future efforts will improve this database with additional fuels and calculations of the heat transfer modes.

Keywords: vertical wall fire, diffusion flame, temperature, Rayleigh scattering

1. Introduction

Boundary layer diffusion flames established over a fuel plate are highly relevant to understanding the phenomena of both opposed and concurrent flame spread [1]. Under both conditions, fuel is injected and then burned in a parallel oxidising flow, which may be provided by either forced convection over a horizontal plate through blowing or by natural convection over a vertical plate that is controlled by a buoyancy-induced flow. Analytical solutions by Kim et al. [2] and Kosdon et al. [3] provide a solution to the temperature and velocity profiles and, therefore, the heat flux from the flame to the fuel, under the assumption that the flow is laminar and that radiation is negligible. The thermal feedback from the flame is critical to describing flame spread rates of solids. For vertical wall flames, the onset of turbulence is non-trivial as increases in the flame length accelerate the buoyant flow, resulting in flow separation and a transition to a radiation-dominated in which self-similarity between the flow and heat transfer breaks down [4].

Upon the transition to a turbulent wall flame, computational models, including Large Eddy Simulation, are usually employed [5]. Due to the small length scales needed to resolve the flame-wall interaction, temperature gradients near the wall are seldom explicitly resolved. Most fire models employ wall heat transfer models in conjunction with an infinitely fast chemistry assumption. The modelling precision needed to model thermal feedback, along with the validity of any simplifying models for heat transfer, is not validated owing to the complexity of measuring near-wall scalar quantities. Consequently, existing modelling approaches require semi-empirical inputs that are predominately scale, geometry, temporally, and fuel chemistry dependent. Recent pushes to enrich the available database on vertical wall fires have yielded insights into flame radiation [6], soot formation rates [7], and velocity fields [7].

Further progress is challenged by a lack of experimental quantification into the flame structure, composition, and gas temperature. These are all critical variables defining convective feedback to the fuel surface and also mark the onset of turbulence, which has not been quantified hitherto. Accurate quantification of these variables is difficult as intrusive probes (e.g. thermocouples) are of a physical scale similar to the phenomena being measured, and therefore large uncertainty exists. This paper intends to address this gap by utilising a revised Sydney Wall Fire Burner set-up [8] and developing a laser-based Planar Rayleigh Scattering technique.

2. Methodology

2.1 Experimental set-up

The porous burner was manufactured using a laser metal additive manufacturing technique with a 74 mm x 78 mm front face with 2 mm porous unit cells. The burner features an embedded cooling coil and the porous mesh is 25 mm deep to ensure a uniform flow at the exit plane. The small unit cell size and low porosity enhance the thermal conductivity, permitting a uniform preheat of the fuel stream over the burner face and an effective control of the overall burner temperature by the cooling water. To prevent the condensation of water vapour forming on the burner surface, a counterflow heat exchanger system was developed that regulates the inlet water temperature to the burner to 40°C using a closed-water loop and a solenoid valve that regulates a separate chilled water stream to the heat exchanger.

* Corresponding author:
Phone: (+61) 2 93612835
Email: vinny.gupta @sydney.edu.au

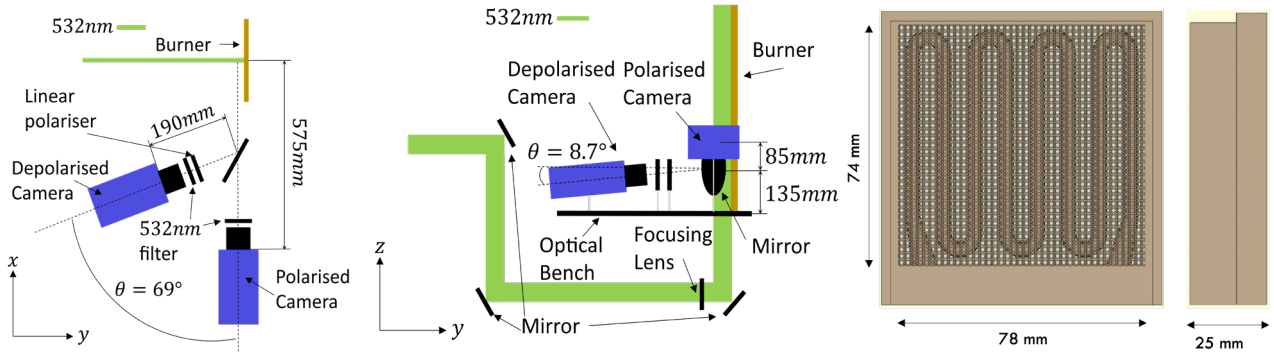

Fig. 1. (left) Schematic of the Rayleigh scattering optical set-up, and (right) the 3D-printed bronze burner.

Due to the increased inlet water temperature, the gas stream passing through the porous burner was preheated to approximately 38°C. This was an important parameter to monitor when doing air, helium and argon images during the experiment. The burner and plenum are mounted flush into a specially designed water-cooled steel plate that acts as a façade for the burner and enables air to be entrained into the leading edge. The outer plate temperature was also regulated to 40°C.

2.2 Planar Rayleigh Scattering

Simultaneous 2D measurements of temperature and mixture fraction were obtained by collecting both the polarised and depolarised Rayleigh scattering signal from the flame in regions where soot formation is low. The optical set-up is shown in Fig. 1. In this paper, only results for the polarised Rayleigh scattering are shown. Measurements of the depolarised Rayleigh scattering signal were obtained to mark the fuel/rich sides of the flame and to map the experimental Rayleigh signal to a flamelet manifold rather than a single flamelet. This will be shown in a future study. Rayleigh scattering was generated by the vertically polarised output of a frequency-doubled output of a pulsed Nd:YAG laser (Spectra Physics Pro 350) at 532 nm, yielding approximately 1 J at the probe volume. The beam orientation was shifted using a collection of mirrors to form a vertically oriented sheet passing normal to the burner. The Rayleigh beam was focused using a 300 mm cylindrical lens into a sheet that was 18 mm wide. The FWHM beam thickness was measured to be approximately 300 µm. The beam was positioned such that part of the Gaussian laser beam clipped the front surface of the burner. The polarised Rayleigh scattering signal was collected by a 50 mm $f_{\#}$1.8 lens and passed through a 532 nm FWHM interference filter onto an inter-line LaVision FlowMaster CCD camera. On-chip binning of 2x2 was utilised, with an effective pixel size of 128 µm/pixel. Chemiluminescence from the flame was completely rejected using both the interference filter and a camera gate of 1 µs.

Due to the proximity of the laser sheet to the burner surface and the resonant nature of Rayleigh scattering, significant efforts were placed in reducing interferences from scattering and reflections from solid surfaces and the burner itself. These interferences were brought down to a

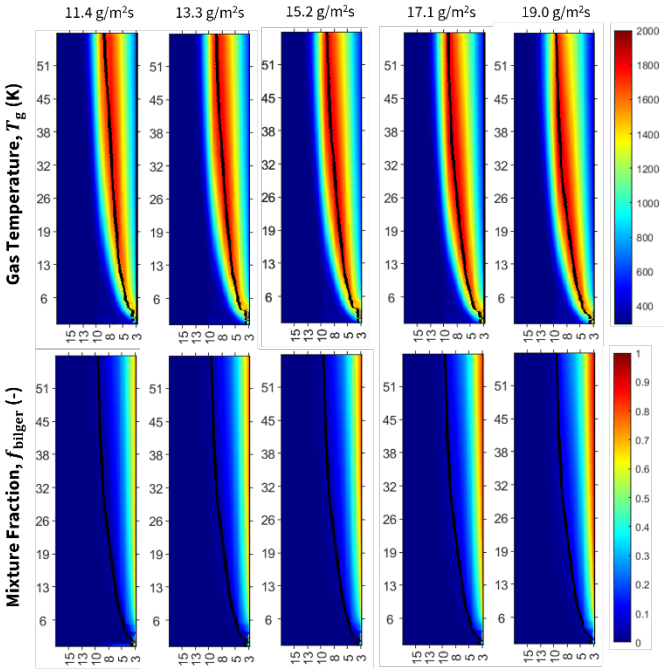

Fig. 2. Temperature and mixture fraction contours. Contours are ensemble mean of 100 shots. Black lines show the axial location of the stoichiometric mixture fraction. Units shown in the x- and y- axes of contour are in mm.

level that could be corrected using a laser reflection calibration shot obtained from flowing pure Helium through the burner, which possesses a small Rayleigh cross-section.

A suite of calibration shots was undertaken using a cold burner to determine the Rayleigh cross-sections for CH_4, DME, C_2H_6, O_2, N_2, Air, and Argon. Vertical wall flames were generated at a range of flow rates using methane, ethane, and dimethyl ether (DME). Images were taken at two axial locations, from x = 0 mm to x = 55 mm, and then from x = 50 mm to x = 95 mm (noting that the burner length is 74 mm). The imaging locations encompass both the laminar and transition regions of the boundary layer flame and correspond to locations where there is no significant soot formation in the fuels, which, if present, will pollute the signal due to Mie scattering and laser-induced incandescence.

This paper is focused on the development of the technique for a vertical wall fire, and therefore, data is reported for only the methane (CH_4) flame from x = 0 mm to x = 55 mm at a range of increasing fuel injection rates. Before taking images, the burner was allowed to preheat the water-cooling system to a stable 40 °C, at which a suite of 500 helium, argon and air shots were taken to provide accurate laser reflection and background corrections.

3. Results

Fuel injection rates corresponding to $\dot{m}_f'' = 11.4$ g/m^{2}s, 13.3 g/m^{2}s, 15.2 g/m^{2}s, 17.1 g/m^{2}s, and 19.0 g/m^{2}s were tested, with 1000 images taken for each case. Each image was corrected for camera dark noise, beam profile, and laser reflection. As the flames generated are purely buoyant and are injected at a relatively low bulk flow velocity, the presence of dust particles can generate strong scattering, particularly on the air side of the diffusion flame. To remove the interferences caused by particles, a particle masking algorithm was developed based on Monje [9], where unwanted dust particles are identified from thresholding the binarised Rayleigh image and then are masked using a combination of image dilation applied to each particle followed by comparing the resulting particle area to a 3 x 3 median filter to eliminate the resulting spurious particles. The removed data is then infilled using a natural interpolation algorithm of the neighbouring pixels. Each corrected Rayleigh image is normalised by the cold mean cold N_2 image: $\bar{s} = \left(S_{\mathrm{fl}}/S_{0,N_2}\right)$. The flame temperature is determined from:

$$T_{\mathrm{fl}} = \frac{T_{N_2}\sum_{i=1}^{j}(X_i\sigma_i)}{\bar{s}\sigma_{N_2}} \quad (1)$$

where X_i is the mole fraction of all the relevant species in the flame, and σ_i is the respective i^{th} species Rayleigh cross-section. Assuming constant pressure and the ideal gas law, the relative cross-sections of the flame species are determined through a 1D opposed-flow flame simulation of CH_4 and air in CHEMKIN Pro using the GRI Mech 3.0 mechanism for the fuel. Given that the flame is far from extinction, a strain rate of a = 5 s^{-1} was used to generate a lookup table. To complete the temperature mapping, it is necessary to demarcate the Rayleigh image of the vertical boundary layer diffusion flame into the lean and rich side in physical coordinates such that the correct lookup table solution can be applied. This is done by identifying the minima in the Rayleigh signal for each pixel along the length of the burner, which is assumed to correlate to the largest temperature and, therefore, the stoichiometric mixture fraction. This approximation will not be necessary in future due to the presence of a depolarised Rayleigh signal to directly map the fuel concentration. The Bilger mixture fraction is also computed in terms of the normalised Rayleigh signal.

Figure 2 shows ensemble mean (100 images) spatial images showing both the temperature and mixture fraction images of the CH_4 flames at increasing fuel injection rates. The black line in each contour marks the stoichiometric mixture fraction that was also used to demarcate the streams for the temperature mapping process. The temperature plots show a characteristic laminar boundary layer structure along the fuel plate that is dominated by thermal expansion. The high-temperature zone region (> 1000 K) is quite broad, with the stoichiometric mixture fraction line located towards the air side owing to its low value for methane. At low flow rates, this high-temperature region sits quite closely to the burner surface, indicating that convective feedback is stronger. However, as the fuel injection rate increases, the reaction zone pushes further away from the fuel plate, which corresponds to an increase in the mixture fraction on the burner side. However, the temperature on the fuel side does not reach the injection temperature (~ 311 K), suggesting strong effects of thermal expansion and diffusion even close to the burner. This is reinforced by the large mixture fractions at the corresponding location, suggesting that reactions are not occurring that close to the burner. Increased blowing does not alter the stability of the flame, which is firmly attached at the leading edge.

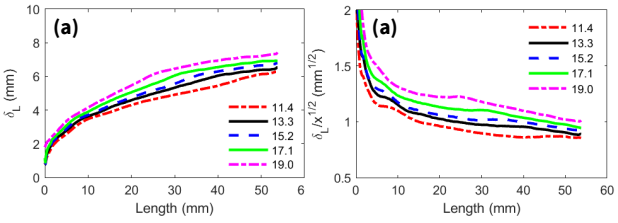

Fig. 3. Flame stand-off distance profiles for various fuel rates.

The flame stand-off distance is quantified by tracing the location of f_{st} along the axial flame direction and is shown in Fig. 3a. The flame stand-off distance displays a parabolic type profile axially, with an almost constant value irrespective of fuel supply rate at the leading edge. However, this trend shifts monotonically, with an increased stand-off distance of 2 mm as $\dot{m}_f''$ increases from 11.4 to 19.0 g/m^{2}s. The increase in stand-off distance is expected as the fuel concentration increases on the fuel side, thus shifting the location of f_{st}. Scaling the stand-off distance thickness by $x^{1/2}$ highlights the effects of increased fuel injection. However, in all cases, the profile is stable, and therefore the flow is laminar.

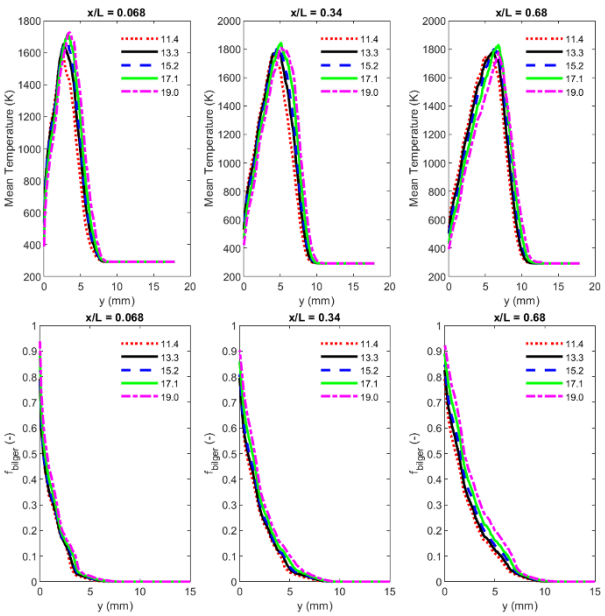

Fig. 4. Temperature and mixture fraction profiles normal to the wall at x/L = 0.068, 0.34, 0.68.

Profiles of the temperature and mixture fraction normal to the burner surface are shown in Fig. 4 at x/L = 0.068, 0.34, 0.68. The results show peak temperatures ranging between 1600 K and 1800 K. Close to the leading edge, increasing the fuel flow rate increases the maximum temperature from 1600 K to 1725 K. The magnitude of the differences diminishes further downstream; however, it is interesting that the largest peak temperatures are found at a flow rate of 17.1 g/m^{2}s at x/L = 0.34 and 0. 68. The location of the peak temperatures shifts further from the burner surface as the flame stand-off distance increases. On the air side of the flame stoichiometric mixture fraction, the temperature dramatically decreases to ambient conditions. This is quite different to the low slope temperature decline observed with thermocouple measurements by other authors [10] for other fuels. However, it is important to emphasise that methane possesses a small stoichiometric mixture fraction. Therefore, the data for ethane and DME will be quite revealing as to the accuracy of existing probe-based measurements in buoyant wall fires. Significantly large temperature and mixture fraction gradients are identified from the burner surface to the peak temperature zone. The temperature gradient profiles do not appear to take the commonly assumed parabolic profile, and the mixture fraction also varies non-linearly in the normal direction. The temperature and mixture fraction gradients are the sharpest close to the leading edge, with the gradients monotonically decreasing further downstream. Due to the sensitivity in calculating the gradient to noise, a wavelet denoising algorithm will be applied to the images shortly before calculating the temperature gradients and convective heat fluxes on the burner surface.

4. Conclusions

This paper presents the first non-intrusive measurements of gas temperature and mixture fraction in a buoyant wall fire configuration through a Rayleigh scattering technique. Boundary layer flames generated from methane are measured at varying fuel injection rates. The laminar leading-edge region is first studied. The measurements enable the quantification of the flame stand-off distance based on the location of the stoichiometric mixture fraction location. It is shown that the stand-off distances for the various fuel injection rates collapse at the leading edge but diverge monotonically further downstream due to the buoyancy-generated boundary layer flow. The leading edge remains stabilised at larger injection velocities, and the flame retains its laminar structure for the entirety of the measurement window. Peak temperatures ranging from 1600 K to 1800 K are identified, and the locations of these temperatures shift away from the wall further downstream and with increased fuel injection rates. Extremely large temperature and mixture fraction gradients with non-linear profiles are measured near the wall, which are fundamental to accurate quantification of flame-to-wall heat transfer. The scalar gradients are significantly more prominent towards the leading edge. Future work will analyse the depolarised Rayleigh signal to enable more accurate quantification of scalars in the leading edge and turbulent regions of the flame for a variety of fuels with increasing densities.

5. Acknowledgments

This work is supported by the Australian Research Council (DP200103609). The authors would like to acknowledge the assistance of Andrew R.W. Macfarlane for his technical advice regarding the experimental setup.

6. References

[1] A.C. Fernandez-Pello, T. Hirano. Combust. Sci. Technol. 32 (1983) 1–31.

[2] J.S. Kim, J. de Ris, F. William Kroesser. Symp. Combust. 13 (1971) 949–961.

[3] F.J. Kosdon, F.A. Williams, C. Buman. Symp. Combust. 12 (1969) 253–264.

[4] P.J. Pagni, T.M. Shih. Symp. Combust. 16 (1977) 1329–1343.

[5] N. Ren, Y. Wang, S. Vilfayeau, A. Trouvé. Combust. Flame. 169 (2016) 194–208.

[6] D. Zeng, G. Xiong, G. Agarwal, Y. Wang. Proc. Combust. Inst. 38 (2020) 4477–4484.

[7] A. Valencia, M. Talbaut, J. Yon, G. Godard, C. Gobin, A. Coppalle. Proc. Combust. Inst. 36 (2017) 3219–3226.

[8] V. Gupta, T. Xiao, M.J. Dunn, J.L. Torero, A.R. Masri. Fire Saf. J. (in press). (2023).

[9] I.T. Monje, Experimental Investigation of Highly Turbulent Premixed Jet Flames, The Ohio State University, 2022.

[10] J.L. De Ris, G.H. Markstein, L. Orloff, P.A. Beaulieu. Fire Saf. Sci. (2003) 259–270.

Fires and Process Safety Paper 6
B. Z. Dlugogorski and A. R. Masri, Eds

Towards Clean Combustion and Decarbonisation
Proceedings of the Australian Combustion Symposium
26 – 29 November 2023, Darwin, Northern Territory, Australia

LES/flamelet model for sooting turbulent ethylene fires

J. Lin[1,*], H. Zhou[2] and E. R. Hawkes[1]
[1]School of Manufacturing and Mechanical Engineering, The University of New South Wales, NSW 2052 Australia
[2]Institute for Aero Engine, Tsinghua University, Beijing 100084 China

Abstract

This study incorporates a two-equation soot model into the radiative flamelet/progress variable framework. The soot model considers acetylene and benzene as soot precursors, and the soot source terms are closed using the presumed filtered density function (FDF) method by assuming that the FDFs of gas-phase and soot quantities are independent. Large eddy simulations are performed on the FM burner ethylene sooting fire. The predictions of soot volume fractions and temperature reasonably agree with experiment, validating the proposed treatment for soot formation. The soot particles are found to generate upstream due to nucleation. Moving downstream, the soot volume fraction increases as a combined result of coagulation, surface growth and oxidation. The inherent intermittency of soot is found to be much larger than that of gas-phase quantities.

Keywords: soot, flamelet/progress variable, soot evolution, intermittency

1. Introduction

Soot modelling is pivotal in high-fidelity simulations of fires. Yet, it remains a challenge due to the complex soot production mechanisms and the significant non-linear interactions between gas-phase thermochemical states, soot, turbulence, and radiation [1]. In fire modelling, the laminar smoke point (LSP) formation model is commonly used. The LSP model is often integrated with the eddy dissipation model (EDM), operating under the infinitely fast chemistry assumption [2-4]. A limitation of this approach is its explicit omission of the intricate physical and chemical processes of soot formation, including nucleation, surface growth, coagulation, and oxidation [2].

For a more precise representation of soot formation, it is essential to incorporate detailed gas-phase chemistry. Flamelet models emerge as a promising method for considering detailed chemistry while maintaining a reasonable computational cost. Over recent years, flamelet models have been increasingly popular as a combustion model in fires, as seen in Ref. [5-7]. While incorporating soot into flamelet models has shown potential in engine-related combustion studies [8], its application in fire conditions has been sparse. Recently, Nmira et al. [1] delved into the turbulence-soot interaction in an ethylene fire with flamelet/soot models, and Domino et al. [9] integrated a soot module into their flamelet model suite to perform simulations on a large-scale pool fire. Despite these advances, literature on soot/flamelet model in fire research remains limited, and a comprehensive investigation into the soot production mechanism under fire conditions is still wanting.

Therefore, the objective of this study is twofold. The first aim is to integrate and validate a soot model into a radiative flamelet/progress variable (RFPV) code [5]. This newly incorporated model is then employed to investigate the soot evolution pattern in a buoyancy-driven turbulent sooting fire. This study highlights the complexities of soot dynamics and illustrates the potential of the proposed method to be applied in more complicated sooting flames.

2. Methodology

2.1 Soot model

A two-equation model is implemented in an in-house LES solver in OpenFOAM-7 to predict soot in fires. In this model, the soot number density $\widetilde{N_s}$ and the soot mass fraction $\widetilde{Y_s}$ are solved with the following governing equations,

$$\frac{\partial \overline{\rho}\,\widetilde{N_s}}{\partial t}+\frac{\partial\,\overline{\rho}\,\widetilde{u_i}\,\widetilde{N_s}}{\partial x_i}=\frac{\partial}{\partial x_i}\left(\overline{\rho}\,D_t\frac{\partial\,\widetilde{N_s}}{\partial x_i}\right)+\overline{\dot{\omega}_{N_s}^{ncl}}-\overline{\dot{\omega}_{N_s}^{coag}}, \quad (1)$$

$$\frac{\partial \overline{\rho}\,\widetilde{Y_s}}{\partial t}+\frac{\partial\,\overline{\rho}\,\widetilde{u_i}\,\widetilde{Y_s}}{\partial x_i}=\frac{\partial}{\partial x_i}\left(\overline{\rho}\,D_t\frac{\partial\,\widetilde{Y_s}}{\partial x_i}\right)+\overline{\dot{\omega}_{Y_s}^{ncl}}+\overline{\dot{\omega}_{Y_s}^{sg}}-\overline{\dot{\omega}_{Y_s}^{ox}}, \quad (2)$$

where ρ is the density, u is velocity, and t is the time. D_t is the turbulent diffusivity, and the molecular diffusivity is neglected as in Ref. [1]. The physico-chemistry of soot comprises four stages: nucleation, surface growth, coagulation and oxidation. Their associated source terms are denoted as $\dot{\omega}_{-}^{ncl}$, $\dot{\omega}_{-}^{sg}$, $\dot{\omega}_{-}^{coag}$, and $\dot{\omega}_{-}^{ox}$. The expressions of these soot source terms align with Lindstedt's work in Ref. [10], which considers acetylene/benzene as soot precursors. The closure of these source terms in the context of LES is introduced in subsequent sections. The soot volume fraction (SVF) can be derived by $\widetilde{f_v}=\frac{\overline{\rho_s}}{\overline{\rho}}\,\widetilde{Y_s}$, where ρ_s is the soot density and is taken as $1740\ kg/m^3$.

2.2 Combustion model

With the flamelet concept, the local thermochemical states such as density, viscosity, diffusivity, temperature and mass fractions of species can be retrieved from the pre-tabulated solution of flamelet equations. In this work, the extended radiative flamelet progress variable approach [11] is applied. The application of this model in fires has been validated in our previous work [5]. In this model, the parameterising variables are the mixture fraction (Z), the progress variable (C) and the total enthalpy (H), such that $\phi=\phi(Z,C,H)$.

In the presence of soot, the RFPV model can be extended to the following format, $\phi=\mathcal{G}(Z,C,H)\mathcal{K}(\phi_s)$

* Corresponding author:
Email: jianhong.lin@unsw.edu.au

[8]. In this expression, $\mathcal{G}(Z, C, H)$ is the gas-phase related part, while $\mathcal{K}(\phi_s)$ is the soot related component. Here, ϕ_s denotes soot scalars, and in the context of the current two-equation model, it corresponds to N_s *and* Y_s. It is worth noting that soot is considered in a one-way coupled manner. This means that the consumption of precursors is not reflected in the computation of flamelet solutions [1]. While a more comprehensive two-way coupling is our ongoing work, the current simplified treatment can be justified by its reasonable performance for C1-C3 hydrocarbon diffusion flames [1].

2.3 Closure: presumed FDF

In the context of LES, a presumed filtered density function (FDF) method is introduced to close the filtered quantities,

$$\tilde{\phi} = \int\int\int\int \mathcal{G}(Z,C,H)\mathcal{K}(\phi_s)\,\tilde{P}(Z,C,H,\phi_s)\,d\phi_s dH dC dZ. \quad (3)$$

Because of the different time scales between the gas-phase and the soot states, this is further simplified to Eq. (4) by assuming that the FDFs of gas-phase and soot quantities are independent, according to Ref. [8],

$$\tilde{\phi} = \int\int\int \mathcal{G}(Z,C,H)\,\widetilde{P}(Z,C,H)dH dC dZ \times \int \mathcal{K}(\phi_s)\,\tilde{P}(\phi_s)d\phi_s. \quad (4)$$

For the gas-phase thermochemical scalars, such as temperature, $\mathcal{K}(\phi_s) = 1$ applies and it is simply closed with $\tilde{\phi} = \tilde{\phi}\,(\tilde{Z},\ \widetilde{Z''^2},\ \tilde{C}, \tilde{H})$, where $\widetilde{Z''^2}$ stands for the subgrid mixture fraction variance. Governing equations are solved for these parametrising variables, details of the model can be found in Ref. [5]. To close the soot source terms $\overline{\dot{\omega}_s}$, it is assumed that $\tilde{P}(\phi_s) = \delta(N_s - \widetilde{N_s})\delta(Y_s - \widetilde{Y_s})$ and therefore,

$$\overline{\dot{\omega}_s} = \mathcal{K}(\widetilde{N_s},\ \widetilde{Y_s})\,\overline{\rho}\int_{Z_s}^{1}\frac{\mathcal{G}(Z,\tilde{C},\tilde{H})}{\rho}\beta(Z)dZ, \quad (5)$$

where a beta distribution is assumed for mixture fraction and delta distribution is assumed for C and H. The beta distribution of mixture fraction is widely presumed in flamelet/soot modelling applications [1, 8]. In fire modelling, both the beta and top-hat distributions have demonstrated similar performance in turbulent line fires [12], suggesting that this is a reasonable assumption. Please consider that Z_s here signifies the location at which acetylene is entirely consumed in a flamelet solution [1].

2.4 Radiation model

In this work, only water vapor, carbon dioxide and soot are considered as participating media. The radiative absorption coefficients of CO_2 and H_2O are fitted from the RADCAL model [13]. For soot, the coefficient is given by $\kappa_{soot} = C_{soot} f_v\, T$, where T is the temperature and $C_{soot} = 700\, m^{-1}K^{-1}$ [14]. The radiative transfer equation is solved using fvDOM, and the turbulence-radiation interaction is addressed with the presumed FDF method [5].

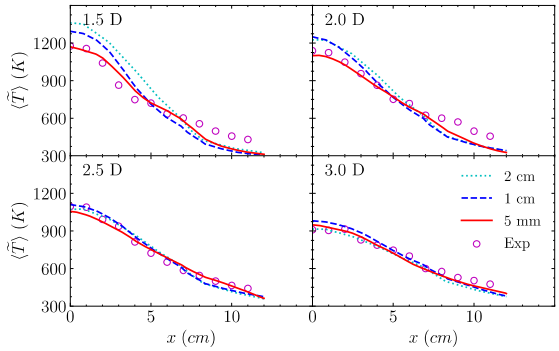

Figure 1 Radial distributions of the predicted mean temperature with various axial distances (1.5 D, 2.0 D, 2.5 D and 3.0 D) above the burner compared with experimental data.

3. Experimental/numerical settings

3.1 FM burner

The FM burner is a target experiment at the MaCFP workshop, which was experimentally studied at FM Global [15]. This configuration features a buoyancy-driven ethylene diffusion flame. While the experiment has investigated different oxygen concentrations, only the normal air case is considered in the current work. The fuel is supplied from a round burner whose outer diameter is D = 15.2 cm at a fixed flow rate of 0.318 g/s. The coflowing air is supplied from a 1.22 m × 1.22 m sandbed surface with a fixed velocity of 0.041 m/s. Measurements of mean temperature with a two-thermocouple probe and soot volume fraction via laser induced incandescence are available for comparison.

3.2 Numerical setting

The chemistry mechanism used in this study is based on the work of Narayanaswamy et al. [16], comprising 158 species and 1804 reactions. The computational domain is defined as 1.22 m × 1.22 m × 2.0 m. Grids are uniformly distributed with cubic cells up to a height of 0.6 m from the burner and gradually expand towards the domain outlet. Three different meshing schemes are tested, characterised by cubic cell dimensions of 2 cm, 1 cm and 5 mm, respectively. For boundary conditions, ethylene and air are introduced in accordance with the experiment, while open boundaries are set on the sides and the outlet. All simulations run for 30 seconds, but statistics are derived from the final 20 seconds of data. The turbulence model applied is a dynamic one-equation model [17]. The time step is approximately 0.5 ms, ensuring that the maximum Courant-Friedrichs-Lewy (CFL) number remains below 0.6.

4. Results and Discussion

4.1 Validation of simulation results

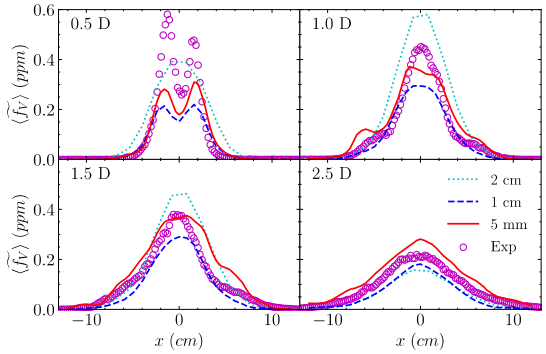

Figure 2 Radial distributions of the predicted mean soot volume fraction with various axial distances (0.5 D, 1.0 D, 1.5 D and 2.5 D) above the burner compared with experimental data.

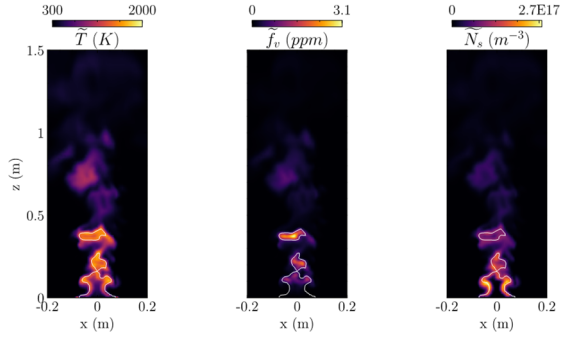

Figure 3 Instantaneous fields of $\widetilde{T}$, $\widetilde{f_v}$ and $\widetilde{N_s}$. The white lines mark the locations of $\widetilde{Z} = Z_{st}$.

The LES results for the FM burner case are compared with available experimental measurements to validate the numerical models. Specifically, Fig. 1 illustrates the mean temperature, while the mean soot volume fraction at various axial distances is depicted in Fig. 2.

As depicted in Fig. 1, elevated flame temperatures are observed around the centreline (x = 0 cm), reaching approximately 1200 K at an axial distance of 1.5 pool diameter (1.5 D) and decreasing to about 900 K downstream at 3.0 D. With an increase in radial distance, the mean temperature diminishes across all axial distances. All meshing schemes capture this trend, with the refined mesh providing enhanced accuracy.

Compared to temperature, the soot volume fraction prediction is markedly influenced by grid size, as evidenced in Fig. 2. The higher values predicted with the 2 cm grid case imply the overshoot of the soot source terms due to the underprediction of subgrid variance of mixture fraction. However, all three grids produce soot predictions that deviate insignificantly from the experimental results, indicating a reasonable agreement given the intricate nature of soot phenomena. Refinement to a 1-cm and 5-mm grid allows the simulation to more accurately depict the 'M' shaped distribution of soot upstream at 0.5 D.

In summary, Figs. 1 and 2 present reasonable predictions of both temperature and soot distributions of the FM burner, thus validating the numerical models. Subsequent discussions will focus on the results derived from the 1-cm grid.

4.2 Soot evolution and its intermittency

The instantaneous fields of soot quantities are presented in Fig. 3. A comparison reveals markedly

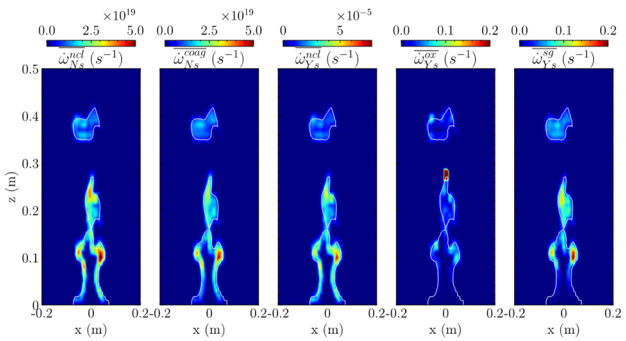

Figure 4 Instantaneous fields of the soot source terms (left to right: nucleation of $\widetilde{N_s}$, coagulation of $\widetilde{N_s}$ nucleation, oxidation, and surface growth of $\widetilde{Y_s}$). The white lines mark the locations of of $\widetilde{Z} = Z_{st}$.

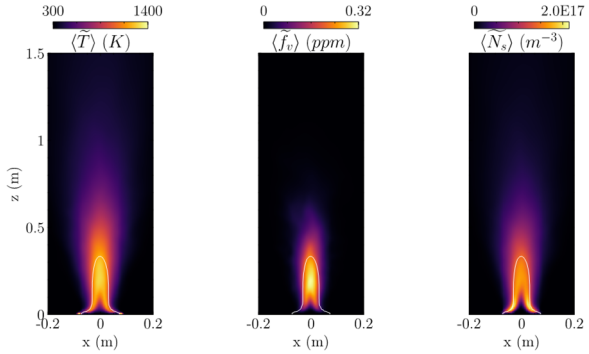

Figure 5 Time-averaged fields of temperature, soot volume fraction and soot number density. The white lines mark the locations of of $\langle\tilde{Z}\rangle = Z_{st}$.

different evolution patterns between the soot volume fraction and the soot number density, shedding light on the soot growth mechanism in this fire. Specifically, the soot number density rapidly attains its peak value upstream (z < 0.1 m) and subsequently diminishes downstream. In contrast, the soot volume fraction is negligible upstream but then gradually increases, peaking at approximately 0.4 m. To understand how soot develops in this flame, the soot source terms, including nucleation, coagulation, surface growth and oxidation, are presented in Fig. 4, focusing on the flame zone (0 – 0.5 m). At upstream locations, nucleation stands as the predominant production source term, leading to the rapid rise of Ns by generating numerous small particles. However, the effect of nucleation on Ys and SVF is less prominent, as its magnitude is considerably smaller than the surface growth source term, which aligns with predictions reported in Ref. [1], explaining the lower SVF near the inlet. As depicted in Fig. 4, oxidation remains almost zero upstream, allowing the downstream SVF to accumulate and increase beyond 0.1 m. Consequently, the influence of the surface growth source term becomes prominent after 0.1 m, further amplifying the SVF downstream. Coagulation also starts to play a larger role beyond z > 0.1 m, causing the soot number density to decrease gradually. Soot is eventually consumed by oxidising species (O_2 and OH) on the soot particle surface. As soot continues moving downstream, the soot surface area increases, leading to intensified oxidation, which peaks around 0.25 m. It is worth noting that the oxidation effect is prominent near stoichiometry, resulting in the SVF becoming almost negligible in lean mixtures, as illustrated in Fig. 3.

Figure 5 displays the time-averaged fields of soot volume fraction and soot number density. The trends in these mean fields closely resemble the instantaneous patterns shown in Fig. 3. However, it is worth noting that the peak value of the time-averaged SVF is substantially lower than that in the instant presented in Fig.3, which can be seen as an indicator of soot intermittency. The temperature field, representing the gas-phase thermochemical states, is presented in Fig. 3 and Fig. 5 as a reference. As can be seen, high temperatures are observed near the isoline of stoichiometric mixture fractions, indicating its homogeneity at a given mixture fraction. In comparison, SVF presented is much less homogeneous in the mixture fraction space. Therefore, the intermittent behaviour is more of the nature of soot

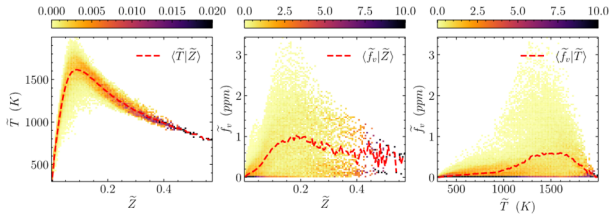

Figure 6 Conditional mean and PDF of temperature and soot volume fraction at 1.5 D.

rather than a result from gas-phase phenomena. This intermittency can be attributed to both the influence of local scalar dissipation rate on soot formation and the absence of molecular diffusivity in soot [8].

Figure 6 offers a quantitative analysis of soot intermittency at the height of 1.5 D. While the conditional mean of temperature on mixture fraction aligns closely with areas of higher conditional probability density function (PDF) distribution, the dispersion of the soot volume fraction is noticeably broader than that of the temperature. This observation is in line with previous qualitative assessments, highlighting the much more pronounced intermittency in soot than temperature. The conditional mean and PDF of $\widetilde{f_v}$ on $\tilde{T}$ are also depicted in Fig. 6, revealing a limited correlation between the two fields. Soot appears absent in most instances, as highlighted by the highest conditional PDF at $\widetilde{f_v}|\tilde{T} = 0$. In comparison, the conditional mean $\langle \widetilde{f_v}|\tilde{T} \rangle$ is located significantly above 0, especially when temperature is higher than 1000 K. This disparity further emphasises the significant intermittent nature of soot in this flame.

5. Conclusion

A two-equation soot model is incorporated with radiative flamelet/progress variable (RFPV) in LES to simulate the FM burner configuration, focussing on the analysis of soot evolution and soot intermittency in fires. The numerical models are first validated by the reasonable agreement in the predicted temperature and soot volume fraction with experimental data. In terms of the evolution of soot, the soot particles are formed upstream due to soot nucleation. Moving downstream, the soot fraction begins to increase as a combined result of surface growth, coagulation and oxidation. In this flame, strong soot intermittency is observed, and this is inherent to soot nature, as such intermittent behaviour is not observed in the gas-phase.

6. References

[1] F. Nmira, A. Bouffard, J.-L. Consalvi, Y. Wang, Proc. Combust. Inst., 39 (2023) 3959-3968.
[2] Z. Chen, J. Wen, B. Xu, S. Dembele, Fire Saf. J., 64 (2014) 12-26.
[3] P. Chatterjee, Y. Wang, K.V. Meredith, S.B. Dorofeev, Proc. Combust. Inst., 35 (2015) 2573-2580.
[4] P. Chatterjee, D. Zeng, Y. Wang, Proc. Combust. Inst., 38 (2021) 4987-4994.
[5] J. Lin, PhD Thesis, UNSW Sydney, 2023
[6] L. Ma, F. Nmira, J.-L. Consalvi, Combust. Theory Model., 26 (2022) 613-636.
[7] R. Xu, V.M. Le, A. Marchand, S. Verma, T. Rogaume, F. Richard, J. Luche, A. Trouvé, Fire Saf. J., 120 (2021) 103101.
[8] M.E. Mueller, H. Pitsch, Combust. Flame, 159 (2012) 2166-2180.
[9] S.P. Domino, J. Hewson, R. Knaus, M. Hansen, Phys. Fluids, 33 (2021).
[10] H. Bockhorn, Soot formation in combustion: mechanisms and models, Springer Science & Business Media, 2013.
[11] M. Ihme, H. Pitsch, Phys. Fluids, 20 (2008) 055110.
[12] R. Xu, PhD Thesis, University of Maryland, 2021
[13] W.L. Grosshandler, Calculations in a Combustion Environment, NIST Technical Note, 1402 (1993).
[14] P. Narayanan, A. Trouvé, Proc. Combust. Inst., 32 (2009) 1481-1489.
[15] D. Zeng, P. Chatterjee, Y. Wang, Proc. Combust. Inst., 37 (2019) 825-832.
[16] K. Narayanaswamy, G. Blanquart, H. Pitsch, Combust. Flame, 157 (2010) 1879-1898.
[17] W.-W. Kim, S. Menon, in: 33rd Aerospace Sciences Meeting and Exhibit, American Institute of Aeronautics and Astronautics, 1995.

Fires and Process Safety Paper 7
B. Z. Dlugogorski and A. R. Masri, Eds

Towards Clean Combustion and Decarbonisation
Proceedings of the Australian Combustion Symposium
26 – 29 November 2023, Darwin, Northern Territory, Australia

Integrated ML-CFD analysis of light gas dispersion in semi-confined spaces

H. Liu[1,*], J. Mohammadpour[1], R. Abbassi[1], M. Asadnia[1] and F. Salehi[1]
[1] School of Engineering, Macquarie University, NSW 2109 Australia

Abstract

This study presents a new model to enhance the prediction of low-density gas distribution inside a lab-scale dispersion chamber. The approach combines machine learning (ML) techniques with computational fluid dynamics (CFD) analysis. The CFD simulation data is utilised through CFD code FLACS for different ventilation velocities, slope angles and leakage rates. Three different ML models are adopted to predict spatial distributions of gas concentration: k-Nearest Neighbour (k−NN), Random Forest (RF) and eXtreme Gradient Boosting (XGB). All models demonstrated good capacities in predicting the gas concentration under different operating conditions. By harnessing the power of machine learning, the current research offers a comprehensive exploration of the intricate gas dispersion patterns, which is crucial for ensuring safety and optimising operations in various industrial applications.

Keywords: machine learning, computational fluid dynamics, light gas dispersion

1. Introduction

The transformation from fossil fuels to carbon-free fuels like hydrogen is of great interest in Australia. Hydrogen can be produced using renewable energy resources such as solar and wind energy, while various challenges, including the safety and reliability of hydrogen systems, still need to be addressed to enable scaling hydrogen in energy sectors. Accidental hydrogen leakage is a key issue that may result in catastrophic consequences if ignored during the planning stage. Understanding the distribution and dispersing behaviour of light gases such as hydrogen within confined spaces is paramount for preventing accidents and developing effective emergency response strategies. However, capturing the accurate physical behaviours of gas dispersion, especially in complex scenarios, presents formidable challenges.

Various studies have been conducted on hydrogen dispersion in confined spaces employing experiments, numerical simulations, or a combination of both. Sommersel et al. [1] used experimental techniques to investigate hydrogen dispersion and combustion in a tunnel-like channel with a large aspect ratio. However, large-scale experimental studies on hydrogen dispersion and explosions often face cost and safety constraints. To address this issue, helium, a non-combustible substitute for hydrogen, has been frequently employed in larger-scale dispersion investigations [2], including this study. Carefully designed and conducted experimental studies could provide accurate representations of a given accidental scenario; however, often limited to the cost and scale of the laboratory facilities, it is not feasible to re-produce every complex scenario with experiments.

Numerical methods have also been utilised to analyse the safety aspects of hydrogen, such as leakage and dispersion. Huang et al. [3] applied computational fluid dynamics (CFD) simulations to examine hydrogen leaks and diffusion in an actual-sized underground parking garage. Shibani et al. [4] also used large eddy simulations (LES) to explore potential fires stemming from hydrogen fuel cell vehicles in tunnels.

In recent years, the integration of CFD techniques and machine learning (ML) approaches has significantly advanced our ability to simulate and visualise gas dispersion in intricate settings. A key requirement for ML models is reliable and comprehensive datasets, which can be achieved through precise numerical CFD simulations. Ni et al. [5] examined different ML algorithms to predict toxic gas dispersion based on CFD simulations. The cornerstone of our approach lies in the utilisation of advanced machine learning algorithms to develop predictive models capable of extrapolating gas dispersion patterns from CFD-generated data. Using comprehensive and validated datasets, these models aim to decipher the intricate relationships between key parameters influencing gas distribution, such as chamber geometry, flow rates, and initial conditions.

Through the synergy of numerical simulation and machine learning, this study aims to bridge the gap between detailed CFD analyses and real-time predictive capabilities. It presents ML-CFD models to predict the distribution of low-density gas in confined spaces, further enhancing our understanding of gas dispersion dynamics to promote safe utilisations of hydrogen energy. The remainder of this paper is organised as follows: Section 2 provides an overview of the gas dispersion chamber, while Section 3 details the methodology, encompassing experimental and numerical approaches. Workflows and architecture of the predictive ML are also covered in this section. Section 4 presents the results of our experiments, evaluating the performance and accuracy of the machine learning predictions against the CFD simulations. Finally, Section 5 discusses the implications of our findings and outlines potential avenues for future research.

* Corresponding author:
Phone: (+61) 2 9850 9147
Email: hengrui.liu@mq.edu.au

2. Problem definition

2.1 Experimental setup

The measurements were conducted using the Macquarie Dispersion chamber (4m × 0.3m × 0.3m) to provide a set of experimental data for CFD model validation. Due to safety concerns, helium was utilised as a surrogate of hydrogen during experimental research, given its similar physical properties and behaviours within a dispersion chamber. A photo of the experimental rig is shown in Fig. 1. The camber is equipped with 12 sensors (XEN-5320) in total where 7 sensors are installed on the ceiling and 5 sensors are located on side walls. The gas sensors measure concentrations based on the thermal conductivity of the gas, and the data-gathering frequency was 3.3 Hz. The inaccuracy of gas concentration readings from the current sensors is 1%. Helium was injected into the dispersion chamber upwards along the Z axis via a 4mm nozzle connected to a dedicated gas cylinder. A ventilated dispersion scenario with helium dispersing to the chamber at a leakage rate of 67.27L/min and 0.25m/s ventilation velocity was constructed and investigated in the present study as the validation case for CFD models. For this base case, the jet Reynolds number is around 3240, and the inlet Reynolds number is 5080, indicating a turbulent He jet and cross flow. It should be noted that the current study focusses more on the safety perspective, while the physics underlying the jet in a crossflow scenario is also of great interest [6]. Sensor readings obtained from the downstream chamber ceiling were used as validation points, where quasi-steady state conditions were established. It is worth noting the gas concentration near the nozzle is very unsteady due to the effect of wind and injected jet. A schematic detailing the sensor locations and gas concentration distribution at steady state is shown in Fig. 2.

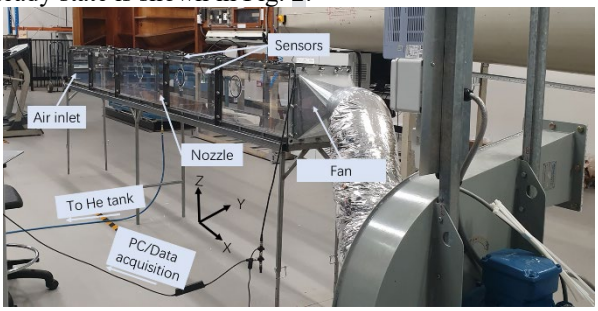

Fig. 1 Schematic of the dispersion chamber setup

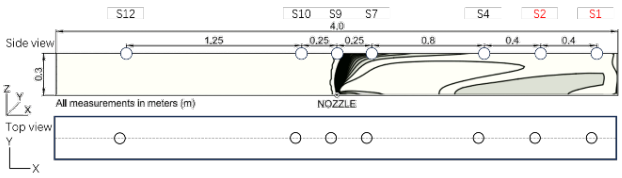

Fig. 2 Schematic of the sensor locations and stabilised gas distribution; sensor locations used as validation are marked in red

2.2 Numerical simulation

FLACS-CFD V22.1r2 was employed for the current dispersion study. The conservation equations of mass, momentum, energy, and species were solved in FLACS using the standard k−ε turbulence model and SIMPLE algorithm for pressure-velocity coupling. All simulations were conducted on a computational domain with 87K mesh following a mesh sensitivity analysis [7]. Based on the experimental configuration, a numerical model was constructed with a core domain (4 m × 0.3 m × 0.3 m) representing the dispersion chamber with its enclosed walls and an extended domain (5 m × 0.5 m × 0.5 m) emulating the surrounding ambient environment. To keep consistency with the experiment, simulations were also conducted using helium. The simulation duration spanned 150 seconds, including an initial 15-second period for establishing a fully developed flow field before introducing helium injection. The injection phase lasted 120 seconds, followed by a subsequent 15-second period designated for purging. In total, 42 simulation cases with a combination of different helium leakage rates (67.27 L/min, 80.73 L/min and 94.19 L/min), wind velocities (0.25 m/s, 0.71 m/s and 1.5 m/s) and slope angles (0%, 1%, 3% and 5%) were considered.

2.3 ML regression models

ML algorithms can significantly reduce the computational cost of developing multi-variable CFD problems. In the current work, three individual ML techniques, including extreme gradient boosting (XGB), Random Forest (RF), and k-Nearest Neighbours (k-NN), were explored due to their proven accuracy and broad application in nonlinear regression [8]. For each ML model, their key hyperparameters were also optimised to give the best regression results.

The k-NN algorithm is a straightforward non-parametric ML technique used for implementing both classification and regression models. It determines the classification or value based on the majority class or average value of its nearest neighbours. In the k-NN algorithm, the outcomes are influenced by the number of predictor weights and the quantity of neighbours (k). It is, therefore, necessary to optimise their values to ensure precision in prediction [9].

Random Forest is also widely used for classification and regression tasks. It constructs multiple decision trees during training, and each tree is trained on a subset of the data and makes independent predictions. The final output is determined by aggregating these predictions, often through a majority vote for classification or averaging for regression. These combined predictions enhanced the accuracy and mitigated the overfitting problem. This also makes RF robust and good at handling noisy data. In this study, we examined the number of estimators, the maximum number of features for node splitting (max features), and the maximum number of decision levels (max depth) [9].

Extreme Gradient Boosting (XGB) is an extension of the Gradient Boosting Machine, derived from K Classification and Regression Trees. XGB operates by fitting initial weak learners, typically decision trees, to the entire dataset, followed by modelling second learners on the first residuals to address limitations. This iterative approach continues until a pre-defined stopping criterion is met, leading to a prediction based on the sum of each

learner's contribution. The hyperparameters utilised in this study are the number of estimators and the learning rate, which is the step size decrease for every step to prevent overfitting [9].

3. Methodology

In the current study, 42 CFD simulations were initially performed with varying operational parameters to generate the dataset, which is a crucial input for the ML. Then, the concentrations of helium at different locations were extracted from simulations for the ML step. The integration of ML algorithms is expected to reduce computational time. In order to obtain the best algorithm for the CFD data set, three different MLAs, including XGB, RF, and k-NN are examined in the present study.

In the present study, the available dataset of 500 samples is randomly divided into a training set, comprising 75% of the data, and a testing set, which accounted for the remaining 25%. The testing data were used to validate the ML models with optimum performance. This randomised allocation ensures that both datasets are representative subsets of the original data. It should also be noted that the same random state is used for all models to ensure uniformity and consistency. The independent variables in the machine learning model include the helium leakage rate, wind velocity, sensor location, and slope angle, while the helium concentration is considered as the objective. Correlation coefficient (R) and the root mean square error (RMSE) are used to statistically evaluate the performance of the ML models and defined using Eqs. (1) and (2).

$$R = \frac{\sum_{i=1}^{n}(M_i - M_{avg})(E_i - E_{avg})}{\sqrt{\sum_{i=1}^{n}(M_i - M_{avg})^2 \sum_{i=1}^{n}(E_i - E_{avg})^2}} \quad (1)$$

$$RMSE = \sqrt{\frac{1}{n}\sum_{i=1}^{n}(M_i - E_i)^2} \quad (2)$$

where M_i represents measured values, E_i refers to predicted values, and M_{avg} and E_{avg} are the average values of measured and predicted values, respectively.

4. Results and discussion

This section presents the validation of CFD models against experimental results and then analyses three distinct ML algorithms to obtain the most proficient regression model for the subsequent optimisation phase.

4.1 Validation of CFD model

Helium concentration at sensors mounted to the ceilings obtained via both experiment and CFD simulation are compared in Fig. 3 for leakage rate of 67.27L/min and 0.25m/s ventilation velocity, and no slope.

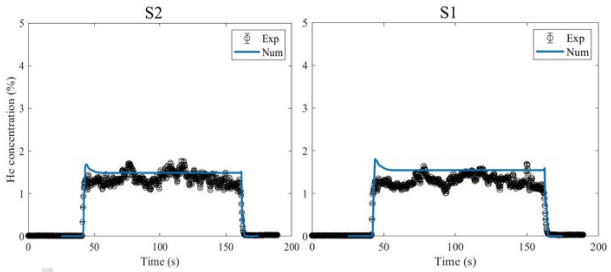

Fig. 3 Helium concentration with time at downstream sensor locations

It is seen that a reasonable agreement between experimental and numerical data was achieved (the difference in average gas concentration values at quasi-steady state are within 15%), indicating that the simulation successfully captured the helium dispersion behaviour inside the chamber. The observed discrepancy could be due to the unstable nature of interaction between a high-speed jet and orthogonal ventilation, as reflected by the fluctuation in the experimental result, while the RANS based k−ε turbulence model tends to give a time-averaged value.

4.2 Machine learning results

The comparison between predicted and measured values is shown in Fig. 4 for the three regression models. Evidently, the agreement between predicted and measured values is highly favourable across most data. However, the RF regression model stands out for its exceptional accuracy, as observed in both training and test datasets ($R_{training}$=0.9902 and $R_{testing}$=0.9847). Tuning hyperparameters in ML regression models optimises model performance by adjusting settings that impact the learning process, enhancing accuracy and generalisation. It tailors the model to data characteristics, enhancing predictive power and minimising overfitting. Table 1 presents the best configuration hyperparameters for all the considered ML algorithms optimised using GridsearchCV, a tool in the Scikit-learn library. The learning rate controls the step size at each iteration while moving toward a minimum of the loss function. The number of estimators defines the quantity of boosting rounds or decision trees.

Table 1 Best Hyperparameters for the ML models

XGB	Learning rate	Number of estimators	
	0.5	10	
RF	Max depth	Max features	Number of estimators
	10	3	490
k-NN	Number of neighbours		
	2		

The Max. depth determines the number of nodes at each decision tree, influencing the model's capacity. The Max feature is crucial for specifying the features considered at each tree split, affecting diversity and randomness. Finally, the number of neighbours specifies the number of nearest data points to consider when making predictions.

RMSE is a statistical parameter that shows the standard deviation of predicted values, and R provides an improved assessment of the relationship between the predicted results.

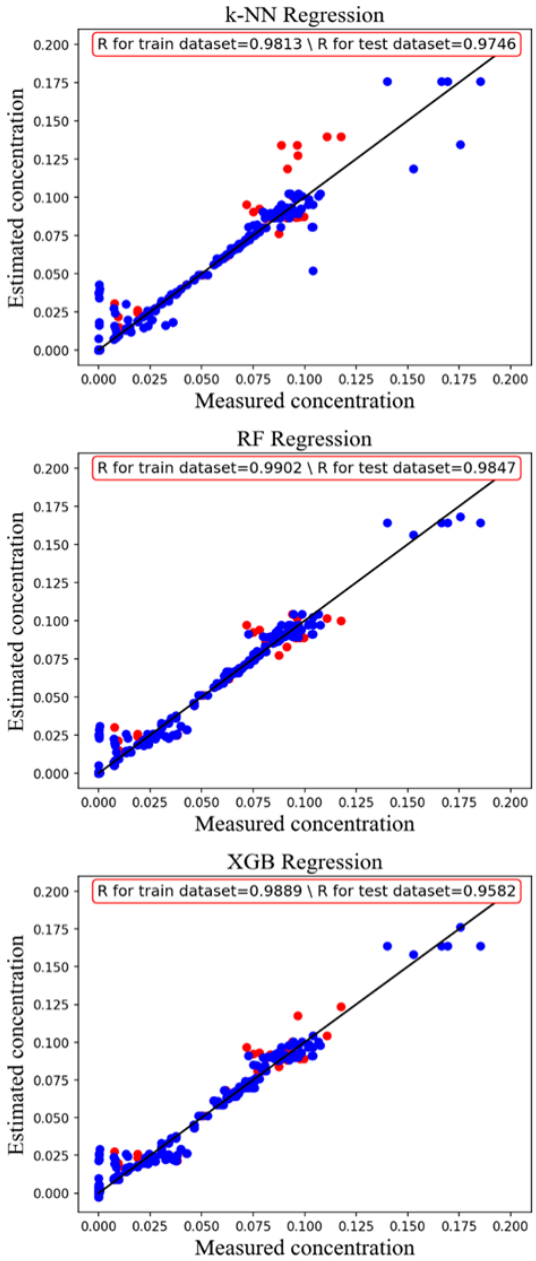

Fig. 4 Comparing the performance of k-NN, RF, XGB regression models (blue and red circles represent train and test datasets, respectively).

Table 2 Comparing RMSE values for the ML models

ML algorithms	**RMSE**	
	Train data	Test dataset
XGB	0.0055	0.0063
RF	**0.0051**	**0.0063**
k-NN	0.0071	0.0071

Table 2 shows a comparison of RMSE values across different ML algorithms, evaluating their predictive performance on both training and test datasets. The RMSE values quantify the average discrepancy between predicted and actual values, with lower values indicating better accuracy. The XGB and RF algorithms demonstrate consistent performance, with RMSEs of 0.0055 and 0.0051 on the training data, respectively, and 0.0063 on the test data for both. These models show effective fitting and generalisation capabilities. However, the k-NN algorithm yields slightly larger RMSE values of 0.0071 for both training and test datasets, suggesting comparatively weaker generalisation ability. It can be concluded that the ML models excel in rapid predictions and domain adaptability, offering advantages over CFD's time-consuming and complex simulations and limited adaptability.

5. Conclusions

This study utilised computational fluid dynamics analysis and advanced machine learning techniques to enhance helium distribution and concentration prediction in a dispersion chamber. The validity of the CFD results was confirmed via in-house experiments.

Three ML regression models, namely k-nearest neighbours (k-NN), random forest (RF), and eXtreme Gradient Boosting (XGB) were assessed. The ML results reached good agreement with simulation results across various operating conditions. Among the ML models investigated, RF outperformed the other two in forecasting average gas concentrations. Optimum values for all the ML algorithms were also identified and suggested. This study emphasises the capabilities of predicting gas dispersion trends, which hold significant importance in ensuring safety and operational efficacy in various industrial applications.

6. References

[1] O.K. Sommersel, D. Bjerketvedt, K. Vaagsaether, T.K. Fannelop, Experiments with release and ignition of hydrogen gas in a 3m long channel, International Journal of Hydrogen Energy 34 (2009) 5869-5874.
[2] T. Gelain, C. Prevost, Experimental and numerical study of light gas dispersion in a ventilated room, Nuclear Engineering and Design 293 (2015) 476-484.
[3] T. Huang, M. Zhao, Q. Ba, D.M. Christopher, X. Li, Modeling of hydrogen dispersion from hydrogen fuel cell vehicles in an underground parking garage, International Journal of Hydrogen Energy 47 (2022) 686-696.
[4] Shibani, J. Rajkumar, V. Aryai, F. Salehi, R. Abbassi, M. Ghodrat, M. Dadashzadeh, Computational fluid dynamics modelling of a hydrogen fire safety in a scaled tunnel environment, Safety in Extreme Environments, doi:10.1007/s42797-021-00049-7(2022).
[5] J. Ni, H. Yang, J. Yao, Z. Li, P. Qin, Toxic gas dispersion prediction for point source emission using deep learning method, Human and Ecological Risk Assessment: An International Journal 26 (2020) 557-570.
[6] R.M. Kelso, T.T. Lim, A.E. Perry, An experimental study of round jets in cross-flow, Journal of Fluid Mechanics 306 (2006) 111-144.
[7] H. Liu, F. Salehi, R. Abbassi, T. Lau, G. Heng Yeoh, F. Mitchell-Corbett, V. Raman, Experimental and numerical analysis of low-density gas dispersion characteristics in semi-confined environments, Journal of Loss Prevention in the Process Industries 86 (2023).
[8] D.R. Cahanap, J. Mohammadpour, S. Jalalifar, H. Mehrjoo, S. Norouzi-Apourvari, F. Salehi, Prediction of three-phase product yield of biomass pyrolysis using artificial intelligence-based models, Journal of Analytical and Applied Pyrolysis 172 (2023) 106015.
[9] J. Mohammadpour, S. Husain, F. Salehi, A. Lee, Machine learning regression-CFD models for the nanofluid heat transfer of a microchannel heat sink with double synthetic jets, International Communications in Heat and Mass Transfer 130 (2022) 105808.

Fires and Process Safety Paper 8
B. Z. Dlugogorski and A. R. Masri, Eds

Towards Clean Combustion and Decarbonisation
Proceedings of the Australian Combustion Symposium
26 – 29 November 2023, Darwin, Northern Territory, Australia

Water mist fire suppression of the Sydney buoyant turbulent fire burner

T. Xiao[1,*], V. Gupta[1], M. J. Dunn[1] and A. R. Masri[1]
[1]School of Aerospace, Mechanical and Mechatronic Engineering,
The University of Sydney, Darlington, NSW 2006 Australia

Abstract

This study presents a characterisation of a canonical experiment that observes the interactions of water mist sprays with a buoyant turbulent diffusion flame. A compressed natural gas (CNG) buoyant diffusion flame is stabilized on the Sydney Turbulent Buoyant Fire Burner which is surrounded by a low-velocity air co-flow that is seeded with fine water mist droplets ($D_{32} \sim 38\mu m$). PDPA measurements are made across the wind tunnel exit plane to define the boundary conditions of both droplet velocity and size distributions. Flame extinction stability limits of the experimental setup are identified. Extinction is defined by characteristic times at which the flame lifts off the burner and subsequently extinguishes under the influence of injecting a certain amount of water through the spray injectors. Simultaneous highspeed images of flame chemiluminescence and Mie scattering of droplets qualitatively convey the complex interactions between droplets and the flame sheet showing complete droplet evaporation in the presence of a flame front. This experimental setup with its well-defined boundary conditions, forms the beginnings of a platform for advancing capabilities to model complex flame spray interactions.

Keywords: buoyant turbulent flames, fire suppression, water mist

1. Introduction

Given the elevated risks associated with mass timber for construction alongside highly energy efficient insulation products used in modern building envelopes, it is necessary to revisit and ultimately advance modern fire suppression and firefighting strategies. Water mist systems are increasingly viewed as a viable alternative to conventional fire protection systems, such as sprinklers. Fine water mist has extended residence times in a flame while providing a larger surface area for latent cooling. The mechanisms behind water mist suppression are gas-phase cooling, oxygen dilution, surface wetting and radiation attenuation [1].

Previous studies have shown variations in water mist suppression performance due to changes in spray characteristics, leading to the consensus that suppression performance is highly dependent on configuration [2]. It is also noted that gas phase cooling primarily dominates with large dependence on the proximity of droplet evaporation to the flame front [3,4]. Considering this insight, it is crucial to prioritize the study of spray-flame interactions when developing CFD models for predicting water mist suppression performance. Given the wide range of existing literature, most studies are limited to small scale configurations of laminar diffusion flames or turbulent jet flames [5–7], which are not representative of real fires consisting of a wide range of physical length scales [8]. While recent studies have investigated realistic large-scale turbulent fires, they lack the near field detailed characterization and/or controlled conditions necessary for model validation [9–11]. With the current limitation in literature, it is imperative to eliminate the dependence on spray/experimental configuration, especially misting systems with high droplet momentum making near field diagnostics of water mist interactions in turbulent flames extremely difficult.

The present work aims to provide an experimental study of water mist fire suppression on a buoyant turbulent diffusion flame in a mist laden co-flow configuration, enabling near field diagnostics of spray flame interactions. This features a well characterized canonical turbulent diffusion flame [12] with well-defined boundary conditions amenable for CFD modelling. A unique feature of the burner is that fuel turbulence can be controlled using a perforated plate that can slide within the fuel stream. Detailing the complex interactions between fine water mist droplets and turbulent flames in a canonical laboratory sized experiment are fundamental towards achieving a performance-based design approach on water mist fire protection systems.

2. Experimental Setup

2.1 Burner and Water Mist Co-flow Design

The experiment consists of the canonical Sydney buoyant turbulent fire burner seated inside a square cross sectional 250mm x 250mm wind tunnel with an induced surrounding air co-flow of approximately 0.2m/s. The burner has an exit plane diameter of 35mm, a tube length of 130mm and produces 10-40kW CNG buoyant turbulent diffusion flames with varying levels of fuel turbulence. For details on burner assembly, refer to reference [12]. In this study, heat release rates (HRRs) of 10-30kW are chosen for analysis, with CNG supplied through a mass flow controller. Figure 1 shows a schematic of the fire burner sitting at the centre of the wind-tunnel with 10mm protruding above the wind-tunnel exit plane. Three layers of 10mm thick and 19mm cell

* Corresponding author:
Email: tony.xiao@sydney.edu.au

sized aluminium mesh screens are placed in the wind tunnel to straighten the mist laden co-flow. Fine water mist is produced by six hollow cone nozzles (red type KBN) evenly distributed radially around the burner. The nozzles are recessed 350mm below the burner exit plane to reduce the effects of droplet momentum, allowing for homogenous mixing between the water droplets and air co-flow. Each nozzle produces a hollow cone spray of fine water mist with a cone angle of 80 degrees. The nozzles are pressurized by a gear pump that draws water from an upstream reservoir with a water pressure regulator allowing for controllability of the mass flux of water mist. The wind tunnel sits approximately 1.5m below an exhaust hood ensuring minimal effect of exhaust velocities on flame dynamics. The experimental setup is enclosed to prevent atmospheric draft.

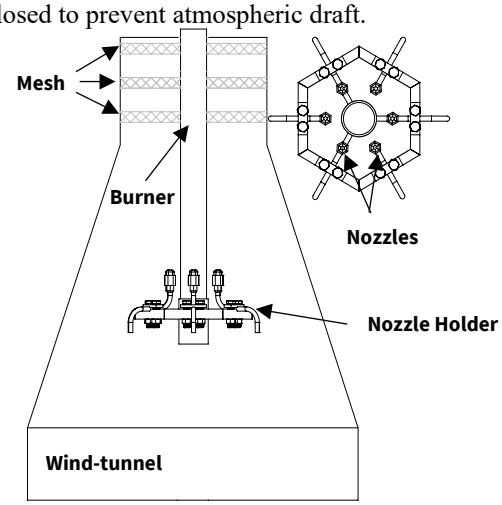

Figure 1. Schematic of burner co-flow configuration with water mist injectors.

2.2 PDPA Measurements

A commercial PDPA system (TSI Model FSA 4000) was used for the single-point measurements of velocity and droplet size distributions. An Argon-ion laser feeds a two-channel fibre optics assembly to the transmitter while the 300 mm focal length receiver was positioned in a 31° forward scattering configuration with a 3.74 µm fringe spacing. Two pairs of beams with wavelengths 514.5 nm and 488.0 nm are used for measuring the axial and radial components of velocity, respectively [12]. Built-in probe volume correction (PVC) in the software (FlowSizer) has been implemented to correct for lower detectability of small droplets at the edge of the probe volume. Point measurements of the mean axial velocities and droplet size distributions of pure water mist were taken along radial profiles at the exit plane of the wind tunnel.

2.3 High Speed Mie Scattering of Droplets and Flame Chemiluminescence

The optical setup employed for high-speed imaging of droplet Mie scattering is shown in Fig. 2. Droplet Mie scattering at 532nm is generated by a frequency doubled 15W Nd:YAG laser at a repetition rate of 500Hz and a 9ns pulse duration. The beam passes through a 1000mm horizontally focused cylindrical lens and expended in the vertical direction for form a laser sheet approximately 150mm in height with a nominal thickness of 1mm across the probe volume. The scattering signal is collected orthogonally to the laser sheet with a 50 mm f# = 1.8 Nikkor lens connected to a high-speed CMOS camera (Photron FASTCAM SA-X2). Chemiluminescence of the flame is also captured simultaneously with a camera exposure time of 50µs.

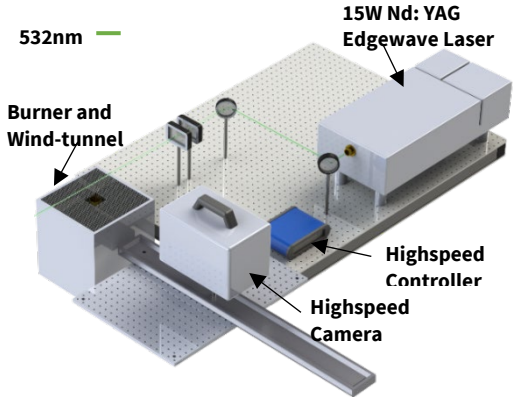

Figure 2. Schematic of highspeed flame chemiluminescence and Mie scattering of droplets.

3 Experimental Results

3.1 Droplet Velocities and Size Distributions

Radial profiles of mean droplet velocities and droplet size distributions (D_{32} and D_{10}) at the wind-tunnel exit plane with no flame is presented in Fig. 3. The walls of the burner sit at radial positions x = -17.5mm and x = +17.5mm, with the mean droplet axial velocities for varying nozzle flow rates across the centre plane of the wind-tunnel (Fig. 3(a)) varying between 0.7-1.3m/s near the walls of the burner. At the edges of the wind tunnel (x = -100mm and x = +100mm) droplet velocities are near zero, whilst directly above the burner at x = 0mm, velocities are negative due to a recirculation zone created by the presence of the burner at the exit plane.

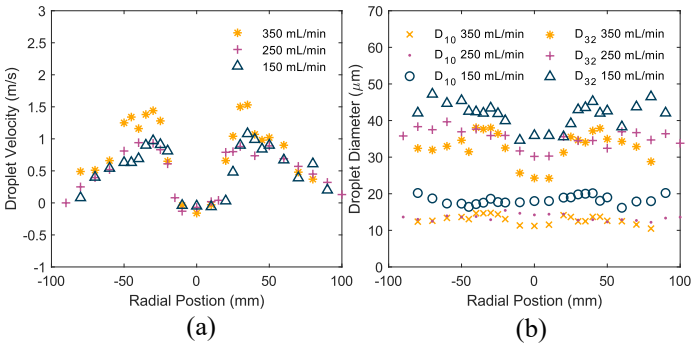

Figure 3. PDPA measurements at the wind-tunnel exit plane of (a) droplet velocities and (b) droplet diameters.

Droplet velocities are seen to increase from the edge of the wind-tunnel in a parabolic manner towards the burner wall. Varying the nozzle flow rates between 150mL/min and 250mL/min seem to have minimal to no effect on the velocity profiles, whereas increasing the mass flow rate to 350mL/min increases peak velocities

from 1m/s to 1.3m/s. Interestingly, if conditioned to droplet sizes of 1µm to 5µm, the velocity profiles remain unchanged. Assuming that such small droplets are representative of the gas flow, this suggests that there is momentum transfer from the droplets to the air co-flow increasing the gas phase velocity from the set 0.2m/s to higher values as shown in Fig. 3(a). Figure 4 shows a point measurement scatterplot of droplet velocities against diameters at a nozzle flow rate of 150mL/min. The average velocity for any given range of droplet diameters from 1µm to 80µm remains unchanged at 1.09m/s.

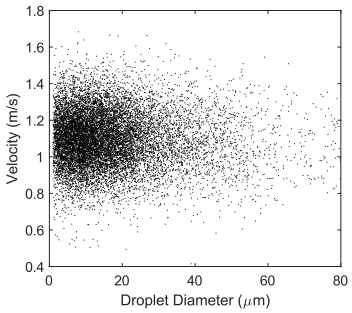

Figure 4. Single point PDPA measurements of droplet velocity vs diameter.

Figure 3(b) shows droplet diameters of D_{32} and D_{10} radially across the centre of the wind tunnel. Interestingly, the droplet size distributions are relatively constant along the exit plane of the wind tunnel. The average D10 along the exit plane vary between approximately 13µm to 19µm for flow rates of 150mL/min and 350mL/min respectively. The D_{32} however varies greatly from 23µm to 44µm because the burner sits in the centre of tunnel which corresponds to the drop in D_{32}. Smaller droplets have lower Stokes numbers allowing them to follow the entrainment field and recirculation zone above the burner exit plane, which results in the lower D_{32}. The larger droplets have more momentum preventing entrainment of large droplets into the region above the burner exit plane.

3.2 Flame Suppression Limits

For a given HRR and mass flux of water mist, the flame undergoes two regimes of stability before complete extinction as shown in Fig. 5. The first regime consists of the flame anchored at the exit plane (labelled "anchored"). The second regime where the flame stays stably lifted above the burner exit plane with a given lift-off height (labelled "Lifted"). The "Baseline" case is a 20kW flame without the turbulence generator in the burner in an absence of water mist in the co-flow. A small addition of water mist into the co-flow (130mL/min) is shown in the anchored regime of Fig. 5. A reduction in flame luminosity is observed in this regime compared to the baseline case, this is possibly attributable to a reduction in soot incandescence [2]. Increasing the mass flux of water mist to 150mL/min eventuates in flame detachment from the burner exit plane. The lifted regime shows a widening of the flame brush due to an increase in unburnt fuel downstream of the burner exit plane. Once lifted, the flame becomes highly chaotic, extremely sensitive to atmospheric flow conditions.

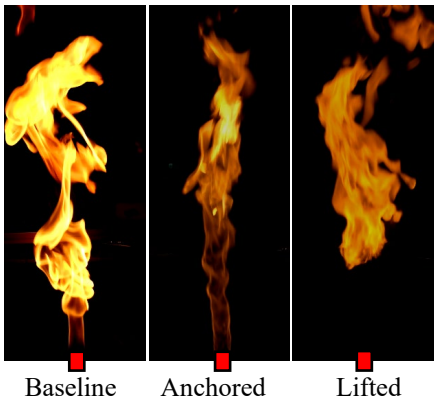

Figure 5. DSLR images of different suppression regimes of a 20kW flame, with the burner position in red.

Figure 6 shows a stability map of the two operating regimes (Fig. 5.) with varying mass fluxes of water mist and flame HRRs (10-30kW). The solid lines represent the mass flux of water required to transition the flame from the anchored regime to the lifted regime with the associated time taken. The dashed lines represent the water mass flux limit for which the flame fully extinguishes from the lifted regime. It's observed that with a reduction in the mass flux of water for a given flame, the time taken to transition between regimes goes up exponentially. This is due to not only the complex transient spray-flame interactions, but also environmental factors such as atmospheric turbulence and all the small associated error bars with fuel flow rate and the mass flux of water mist. With increasing HRR, the extinction stability curves translate linearly with mass flux of water.

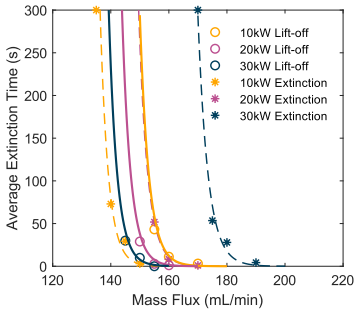

Figure 6. Flame suppression stability limits for anchored and lifted regimes at varying flow rates of water mist.

Flame lift-off is inversely proportional to HRR, this suggests that increasing the exit plane strain rate, reduces the amount of water mist required to lift the flame off the exit plane. Whereas with complete extinction, increasing the HRR increases the amount of water mist required to suppress the flame. Interestingly, at 10kW, a hysteresis phenomenon is observed where the extinction limit occurs at a lower mass flux than the lift off limit. Once the flame lifts off the burner exit plane, it is unable to stay stably lifted unless the mass flux of water is reduced to below the lift-off limit. All flame cases regardless of HRR, and flame operating regimes follow an asymptotic correlation between the time (t) it takes for the flame to lift off the burner or for complete extinction of a lifted flame. This correlation is described in Eq. (1) following a exponential decay with a constant exponent of -1, where $\dot{m}$ is the mass

flux of water mist (mL/min) and c_1 is the asymptotic infinite time to extinction flow rate specific to HRR. This characteristic curve marks the region of extreme instabilities present in flame extinction.

$$t(s) = 180(\dot{m} - c_1)^{-1} \quad (1)$$

3.3 High Speed Mie Scattering of Droplets and Flame Chemiluminescence

Figure 7 shows a time series of instantaneous images of a 20kW flame in the anchored regime with a steady co-flow of water mist with the nozzle flow rates set at 140mL/min. The series of images below show the wind-tunnel and burner exit planes with a cropped image size of 300mm in height and 200mm in width. The droplets are seen to populate the airside with no droplets on the fuel side. This suggests that droplet evaporation occurs whenever there is a flame front. A standoff distance between the droplets and the flame front is observed, however, since chemiluminescence is line of sight integrated, it cannot be quantified. The series of images above is located 300-600mm downstream of the burner exit plane. At 8ms, a local extinction zone is observed in the flame with a stream of droplets being entrained into the fuel side. Once the droplets have penetrated to the fuel side, they no longer evaporate in this instance and get advected downstream in the fuel jet as seen at 16ms. With droplets reaching within millimetres of the flame front, it can be inferred that droplet evaporation is a primary driver of flame extinction. Further work on simultaneous planar imaging techniques of the flame front with droplet Mie scattering is key to quantitatively identify relative droplet positions to the flame sheet, identifying the dominant suppression mechanism of water mist fire suppression.

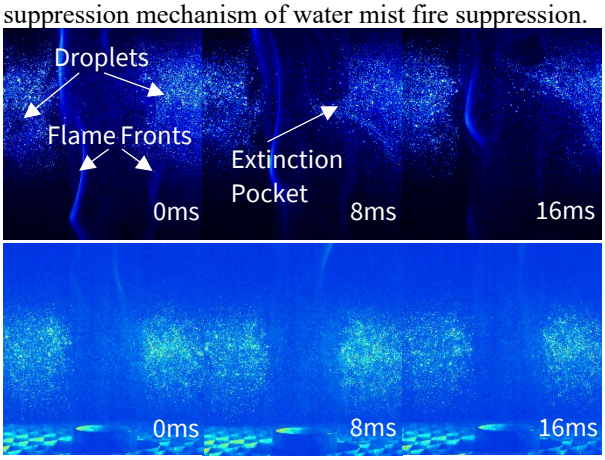

Figure 7. Time series of simultaneous highspeed flame chemiluminescence and Mie scattering of droplets.

4. Conclusions

This paper presents the characterisation of a novel setup consisting of a canonical burner with a mist laden co-flow that enables the study of spray flame interactions with well-defined boundary conditions. Droplet velocities, size distributions and concentrations are quantified from PDPA measurements of the wind-tunnel exit plane and their variations with different nozzle flow rates. A stability map is generated for different flame HRRs showing the sensitivity of mass flux of water mist with average time to extinction. This work provides valuable measurements and characterisations of a canonical experiment of water mist fire suppression, this develops a platform for future quantitative measurements where the water is mixed with a range of metal salts to enhance the physical suppression of water with chemical inhibition mechanisms.

5. References

[1] Z. Liu, A.K. Kim, Review of water mist fire suppression systems - fundamental studies, J. Fire Prot. Eng. 10 (2000) 32–50.

[2] J.P. White, S. Verma, E. Keller, A. Hao, A. Trouvé, A.W. Marshall, Water mist suppression of a turbulent line fire, Fire Saf. J. 91 (2017) 705–713.

[3] R. Ananth, R.C. Mowrey, Ultra-fine water mist extinction dynamics of a co-flow diffusion flame, Combust. Sci. Technol. 180 (2008).

[4] A. Yoshida, K. Kashiwa, S. Hashizume, H. Naito, Inhibition of counterflow methane/air diffusion flame by water mist with varying mist diameter, Fire Saf. J. 71 (2015).

[5] S. Asano, A. Yoshida, Liftoff height of turbulent diffusion flame in water-mist-laden coflowing air stream, Combust. Flame. 230 (2021) 111425.

[6] Y. Liu, J. Shen, J. Ma, G. Li, Z. Zhao, X. Ni, X. Wang, Laser-based measurement and numerical simulation of methane-air jet flame suppression with water mist, Process Saf. Environ. Prot. 148 (2021) 1033–1047.

[7] R. Matsuo, H. Naito, A. Yoshida, Extinguishment of counterflow diffusion flame stabilized in turbulent airflow by polydisperse water mist, Proc. Combust. Inst. 37 (2019) 4239–4246.

[8] S. Tieszen, On the fluid mechanics of fires, Annu. Rev. Fluid Mech. - Annu REV FLUID MECH. 33 (2001) 67–92.

[9] S.C. Kim, H.S. Ryou, An experimental and numerical study on fire suppression using a water mist in an enclosure, Build. Environ. 38 (2003).

[10] C.S. Jeong, C.Y. Lee, Experimental investigation on spray characteristics of twin-fluid nozzle for water mist and its heptane pool fire extinguishing performance, Process Saf. Environ. Prot. 148 (2021).

[11] Y. Liu, Z. Fu, G. Zheng, P. Chen, Study on the effect of mist flux on water mist fire extinguishing, Fire Saf. J. 130 (2022) 103601.

[12] T. Xiao, V. Gupta, A.R.W. Macfarlane, C. Kennedy, M.J. Dunn, A. Kourmatzis, J.L. Torero, A.R. Masri, On the Structure of Buoyant Fires with Varying Levels of Fuel-Turbulence, Combust. Flame. 257 (2023) 112993.

Fires and Process Safety Paper 9
B. Z. Dlugogorski and A. R. Masri, Eds

Towards Clean Combustion and Decarbonisation
Proceedings of the Australian Combustion Symposium
26 – 29 November 2023, Darwin, Northern Territory, Australia

Computational modelling of Sandia cryogenic hydrogen jet

J. Mohammadpour[1, *] and F. Salehi[1]
[1] School of Engineering, Macquarie University, Sydney, NSW 2109, Australia

Abstract

Liquid hydrogen offers a promising strategy for achieving high-density hydrogen storage and efficient on-site distribution. Nevertheless, the possibility of catastrophic consequences due to hydrogen leakages necessitates comprehensive investigations into cryogenic liquid hydrogen to evaluate the potential hazards associated with accidental releases precisely. The present research aims to model the cryogenic gas release experiment conducted by Sandia. We consider four tests with varying stagnation pressures (2 to 5 bar) and stagnation temperatures (50 to 56 K). RANS simulations are carried out in OpenFOAM with a developed solver. The under-expanded jet is solved using a notional nozzle approach. The numerical results show good agreement with the experimental data, including mole fraction contours, temperature profiles, and normalised inverse temperature decay rate. While the mole fraction and temperature contours are accurately predicted in both axial and lateral directions, there is slight overprediction in the axial direction, which could be due to the model's accuracy. The present computational model holds the potential for further analysis of cryogenic hydrogen in large-scale facilities and modelling delayed ignition and consequence of hydrogen fire and explosion.

Keywords: cryogenic hydrogen, under-expanded jets, OpenFOAM, CFD simulation

1. Introduction

Hydrogen is emerging as a promising fuel for the mobility sector while adopting sustainable distribution and storage techniques, such as liquid hydrogen, is crucial for a cleaner future [1]. Urban areas encounter complex compliance challenges [1]. Separation requirements for urban areas include 15 m from lot lines, ignition sources, and overhead utilities, as well as 23 m from building openings and assembly spaces. Updates are required to handle the distances between hydrogen storage tanks [2]. Scientific studies on cryogenic hydrogen are necessary for safe and effective storage processes.

Cryogenic hydrogen dispersion modelling has been studied by different research teams [3, 4]. Giannissi et al. [5] examined the impact of atmospheric humidity on vapour dispersion resulting from liquified hydrogen spills reported in the Health Safety Laboratory. Fluctuating wind direction was also considered, confirming its significant impact on hydrogen dispersion. Their computational results aligned with experiments showed that humidity and slip effect had strong influence on cloud buoyancy. Recent research at Sandia National Laboratories studied upward vertical releases of cryo-compressed hydrogen to investigate the effect of reservoir temperatures and pressures and nozzle diameters on dispersion [1]. The results can offer a scientific foundation to support prospective modifications to separation distances recommended by NFPA 2: "Hydrogen Technologies Code for liquid hydrogen handling". Giannissi et al. [6] numerically studied the Sandia cryogenic hydrogen jet. Using an integral model, they could accurately validate their computational fluid dynamics (CFD) codes to predict the Sandia hydrogen jet, including radial H_2 dispersion, normalised temperature decay rate, and mole fraction contours. Later, Ba et al. [7] investigated cryogenic hydrogen jets with stagnation pressure and temperature set at 50 K and 2-10 bar, respectively. They captured shock structures adjacent to the nozzle in the case of under-expanded cryogenic H_2 jets. Ren et al. [8] focused on predicting the nearfield flow physics of the under-expanded cryogenic H_2 jet using direct numerical simulations. They demonstrated the emergence of complex acoustic waves adjacent to the under-expanded jets. Moreover, their observations revealed localised liquefaction resulting from the expansion of pressurised cryogenic H_2 gas jet flow. Chowdhury and Hecht [9] extended their earlier research on cryogenic hydrogen gas release [1] to unintended leakage through cracks instead of round nozzles. They studied aspect ratios of 16 and 32 and found that the decay of centerline concentrations was similar to the round nozzles when stagnation pressures ranged from 3 - 5 bar.

This study introduces an accurate approach to simulating Sandia's vertical cryogenic hydrogen jet release with a particular focus on addressing challenges related to standards and codes for liquid hydrogen. To efficiently capture the underlying physics, a solver is developed based on 'rhoPimpleFoam' while the necessary libraries are adopted to handle the species mass fraction equations and thermal properties. The present research offers a deeper understanding of under-expanded jet flow. The impacts of different operating parameters are also discussed while a detailed comparison against the experimental data is given. While this study primarily focuses on modelling cryogenic non-reacting hydrogen jet releases, it holds relevance to the broader field of hydrogen fire and safety. Understanding the behaviour of non-burning hydrogen jets is a crucial aspect of ensuring safety in hydrogen storage and distribution systems. For modelling delayed ignition and consequence fire and explosion modelling, it is essential to understand the cryogenic jet development. So, the computational model developed in this study can serve as a foundational framework for future research that may involve the modelling of ignition and subsequent combustion processes in hydrogen-rich environments.

* Corresponding author:
Phone: (+61) 2 424806584
Email: javad.mohammadpour@mq.edu.au

2. Problem definition

Fig. 1 shows a schematic view of Sandia's experiment setup. Four experiments have been performed for hydrogen release at the nozzle diameter of 1 mm. The reservoir pressures and temperatures are set at 2-5 bar and 50-58 K, respectively. The vertical upward gas release is surrounded by low-velocity air co-flow (0.3 m/s) to eliminate room currents, having a negligible impact on simulations [6]. The two cameras, one for nitrogen and another for hydrogen, captured light scattered by a laser focused into an 18-mm high sheet using lenses. Through analysing the Raman signals, collected by the two cameras, from known pure gas flows and correcting for laser intensity, the camera's response is linearised, enabling quantification of gas concentration [1].

3. Methodology

To effectively capture the fundamental principles of physics, simulations are conducted using a solver developed based on the 'rhoPimpleFoam' framework. This solver incorporates essential libraries tailored to handle the species mass fraction equations and thermal properties for simulating the supersonic cases. A Reynolds-averaged technique is applied to solve the conservation of mass, momentum, energy, and species [6]:

$$\frac{\partial \rho}{\partial t} + \frac{\partial \rho u_i}{\partial x_i} = 0 \quad (1)$$

$$\frac{\partial \rho u_i}{\partial t} + \frac{\partial \rho u_i u_j}{\partial x_j} = -\frac{\partial P}{\partial x_i} + \frac{\partial}{\partial x_j}\left((\mu + \mu_t)\left(\frac{\partial u_i}{\partial x_j} + \frac{\partial u_j}{\partial x_i}\right)\right) + \rho g_i \quad (2)$$

$$\frac{\partial \rho h}{\partial t} + \frac{\partial \rho u_i h}{\partial x_i} = \frac{dP}{dt} + \frac{\partial}{\partial x_i}\left((\lambda + \lambda_t)\frac{\partial T}{\partial x_i}\right) + \frac{\partial}{\partial x_i}\left(\rho \sum_{k \neq a} D_{q_k}\left(h_{v_k} - h_{v_a}\right)\frac{\partial q_{v_k}}{\partial x_i}\right) + \frac{\partial}{\partial x_i}\left(\sum_k \frac{\mu_t}{Sc_t} h_k \frac{\partial q_k}{\partial x_i}\right) \quad (3)$$

$$\frac{\partial \rho q_p}{\partial t} + \frac{\partial \rho u_j q_p}{\partial x_j} = \frac{\partial}{\partial x_j}\left(\left(\rho D_p + \frac{\mu_t}{Sc_t}\right)\frac{\partial q_p}{\partial x_j}\right) \quad (4)$$

where ρ is the mixture density, u is the velocity, P is the pressure, g is the gravity, T is temperature, μ is laminar viscosity, μ_t turbulent viscosity, λ is laminar thermal conductivity, λ_t is turbulent thermal conductivity, Sc_t is turbulent Schmidt number is 0.72, D is molecular diffusivity, h is enthalpy, and q is the total mass fraction.

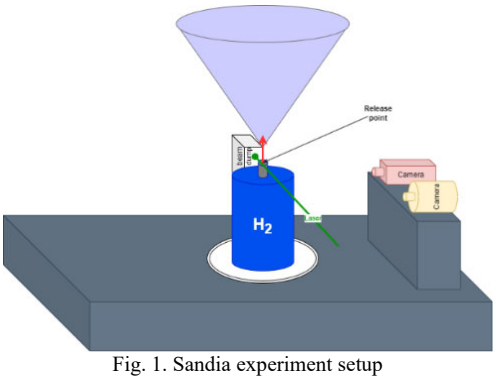

Fig. 1. Sandia experiment setup

Both k-ε and RNG k-ε turbulence models were previously recommended for modelling cryogenic jets [6]. We conducted a comprehensive comparison between the predictions of these two turbulence models against experimental data. This comparison included various aspects of the jet development, such as concentration and temperature profiles, flow patterns, and other relevant characteristics. This thorough analysis revealed that the k-ε model consistently aligns more closely with the experimental observations and hence the former is adopted here.

The pressure-implicit with splitting of operators (PIMPLE) algorithm is adopted for solving the pressure-velocity coupling. This method is developed based on the PISO technique and incorporates the feature of under-relaxation at each step, similar to the SIMPLE method. This combination enhances the stability of the PIMPLE algorithm in simulations and enables it to handle larger time steps, resulting in faster and more efficient [10]. For enhanced accuracy and model stability, a maximum Courant number of 0.5 is maintained across the entire domain. An under-relaxation factor of 0.7 is adopted to enhance the stability of the solution algorithm by mitigating its nonlinearity. This moderates the convergence rate while increasing the stability.

The jet flow is significantly dependent on the ratio of the stagnation pressure (P_0) to the ambient pressure (P_a), denoted as the nozzle pressure ratio (NPR). Based on the NPR value, the jet flows are typically classified in the following classification: (1) subsonic jet when NPR=1; (2) moderately under-expanded jet at 1<NPR≤2; and (3) highly under-expanded jet when NPR>2. Hence, Test 1 can be classified within the moderately under-expanded jet group, while the other tests fall into the category of highly under-expanded jets.

When a jet of fluid is released into an atmosphere with higher pressure, the jet expands rapidly and creates a shock wave. This shock wave can have a significant impact on the behaviour of the jet flow. The notional nozzle technique is a simplified method for modelling under-expanded jets. It replaces the actual nozzle with a hypothetical nozzle that has the same mass flow rate as the actual nozzle. This allows the CFD simulation to be simplified and made more computationally efficient while still maintaining accuracy. Here, a notional nozzle technique method is applied that solves the mass, momentum, and energy balance equations from the throat to the notional nozzle. Table 1 shows the boundary conditions in Sandia's experiment and the prediction at the notional nozzle [1, 6]. For Test 1, with NPR≈2, close to the critical pressure ratio, the leak forms a perfectly expanded supersonic jet, while in the cases with pressures ranging from 3 to 5 bar, the leaks result in under-expanded supersonic jets. In all scenarios, the flow remains supersonic, as indicated by Mach numbers (speed of flow/speed of sound) exceeding one.

Table 1. Stagnation, throat, and notional nozzle conditions

	Stagnation		Throat			Notional nozzle		
Test	P (bar)	T (K)	P (bar)	T (K)	U (m/s)	T (K)	U (m/s)	d (mm)
1	2	58	1	43.9	535.3	43.9	535.3	1
2	3	56	1.457	41.9	533.3	36.1	633.1	1.03
3	4	53	1.94	39.6	516.4	30.7	665.1	1.08
4	5	50	2.422	37.4	498.2	26.8	671.5	1.14

4. Numerical setup

The notional nozzle is located at the position of the actual nozzle. The Mach disk forms when a supersonic flow, such as a jet flow, interacts with the ambient air. The Mach disk is a normal shock wave resulting from the difference in static and ambient pressures. The height of the first Mach disk (H_{disk}), for ambient jets, is calculated using the following equation [11].

$$\frac{H_{disk}}{d} = 0.65\sqrt{\frac{P_0}{P_a}} \quad (5)$$

where d is the nozzle diameter.

The maximum H_{disk} in this study is equal to 1.45 mm. Therefore, as shown in Fig. 2, the release gas point is considered at (0, 2, 0 mm). The computational domain is extended around the release point from -0.05 to 0.05 m in the x direction, 0 to 0.14 m in the y direction, and 0 to 0.1 m in the z direction, consistent with previous studies [6].

The wall condition is applied to the bottom surface (green), while the symmetry condition is considered in the xy plane (blue) to reduce computational costs. The inflow is maintained with a constant velocity at the inlet, and the remaining faces are outflow (red).

The characteristics of an ideal gas govern the properties, except for the under-expanded zone where the National Institute of Standards and Technology (NIST) equation of state is adopted to account for the high pressures characteristic of this region [6]. Hecht and Panda [1] demonstrated that the ideal gas law can effectively correlate gas concentration with mole fraction and temperature, with only a slight margin of error when comparing the ideal gas assumption to real gas behaviour. The domain is initialised with air, which contains 77% of N_2 and 23% of O_2. Furthermore, ambient conditions of 1 bar pressure and 297 K temperature are initially implemented. Thermophysical properties for H_2, N_2, and O_2 are determined using the NIST WebBook [12, 13].

Structured mesh configuration with hexahedral cells is generated with finer mesh adjacent to the release point, as shown in Fig. 2. Proper mesh independence study is individually carried out for each test, resulting in 560 K, 540 K, 510 K, and 500 K cells for Test 1, Test 2, Test 3, and Test 4, respectively.

5. Results and discussion

Fig. 3 shows 2D contour plots of the hydrogen mole fraction for the considered tests. A reasonable agreement between the simulation and measurement data is achieved. While slight overprediction is observed in the central spreading, the model precisely captures lateral spreading in all cases. The results are also significantly better than the previous RANS simulation of this experiment [6] (not shown here). The greatest deviation in lateral spreading prediction is observed in Test 4 at a mole fraction of 0.04. The observed overprediction might arise from the k-ε model in overestimating the turbulent diffusion [2].

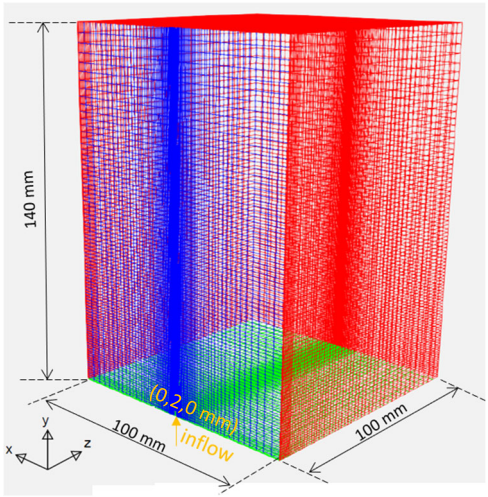

Fig. 2. The present computational domain

Fig. 4 presents 2D contour plots of temperature for the considered tests. Consistent with Fig. 3, the axial cold temperature penetration is slightly overpredicted for most cases, while the lateral temperature distribution is well captured. However, the temperature profile of 140 K in Test 4 is underpredicted.

The normalised inverse temperature decay rate (NITDR) is calculated to visualise and compare how the temperature decays along the flow. It is valuable for understanding the thermal behaviour of the jet, heat exchange with the surrounding environment, and the overall energy distribution within the flow. Fig. 5 shows, for all four tests, an acceptable agreement between the predicted NITDR and measured values which are plotted versus the normalised distance. The fitted line has a proportionality of 0.032, closely predicted compared to Sandia's report. The differences compared to the experimental data in the axial direction are consistent with the overprediction observed in Fig. 4 and previous studies [6]. This discrepancy can be attributed to the presence of ice accumulation on the nozzle or the presence of warmer jets during experimentation, which lead to shifting from the centreline and thereby contributing to variations in measurements [1]. Despite this, it is worth noting that Giannissi and Venetsanos [14] demonstrated that the impact of humidity can be neglected when the jets have a densimetric release of Froude number (Fr) above 1000. For the considered tests, the densimetric Fr number ranged from 5204 to 22,771. Hence, it is expected that the humidity to have insignificant effects on the results while further investigation is needed.

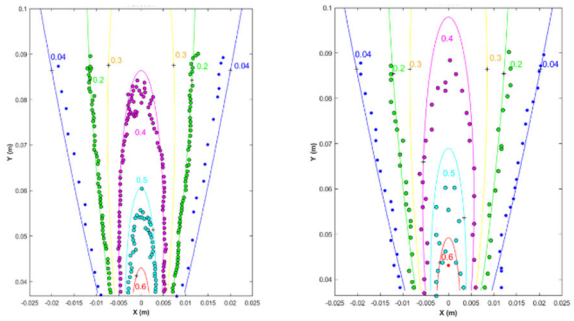

(a) Test 1 (b) Test 2

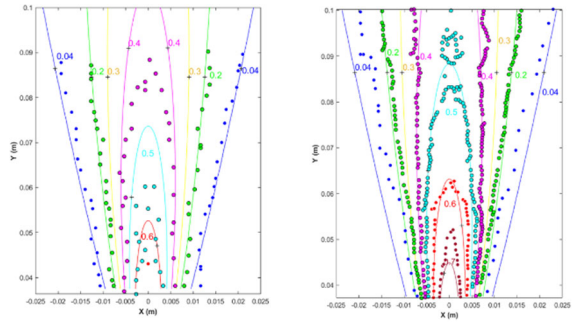

(c) Test 3 (d) Test 4

Fig. 3. Comparing mole fraction contours of simulation (lines) and Sanida's experiment (circles)

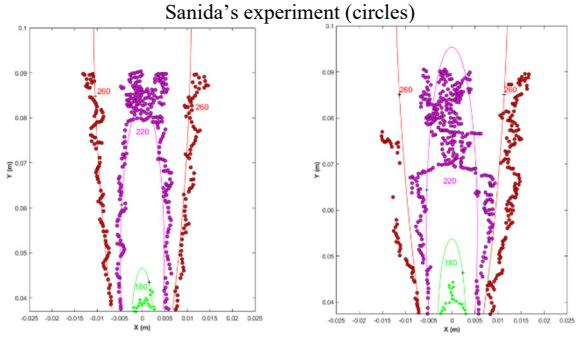

(a) Test 1 (b) Test 2

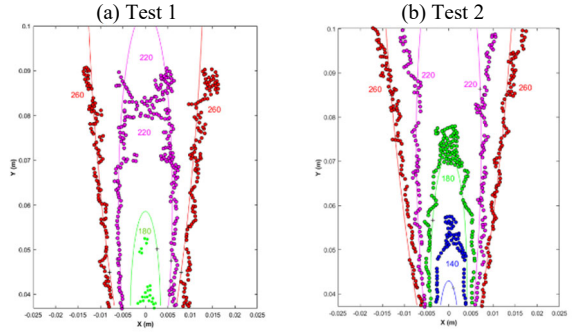

(c) Test 3 (d) Test 4

Fig. 4. Comparing temperature contours of simulation (lines) and Sanida's experiment (circles)

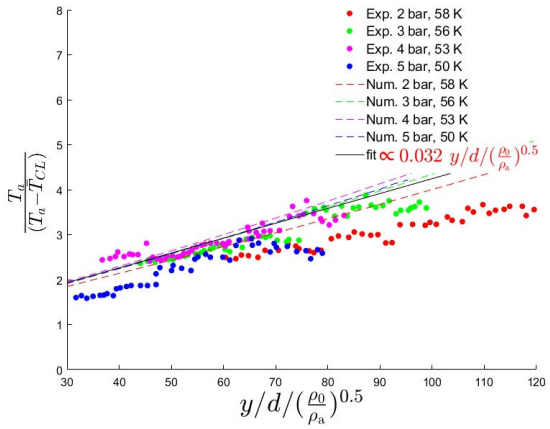

Fig. 5. Normalised inverse temperature decay rate.

6. Conclusion

This study aimed to further analyse cryogenic hydrogen dispersion. The developed solver was developed in OpenFoam to model Sandia's experiment focusing on a cryogenic hydrogen gas release. The preliminary investigation showed that the k-ε model outperformed the RNG k-ε model in the prediction of hydrogen dispersion. Therefore, the simulations were carried out using the k-ε turbulence model. The notional nozzle approach was employed to reduce computational costs.

The numerical results showed a reasonable agreement with the experimental findings in predicting the hydrogen mole fraction and temperature contours, and normalised inverse temperature decay rate. Despite slight overprediction of the mole fraction and temperature profiles in the axial direction, the numerical results are well-predicted in the lateral direction.

This research has the potential to facilitate the development and enhancement of safety codes and standards applicable to liquid hydrogen facilities.

7. Acknowledgments

The authors acknowledge computing support from the National Computational Infrastructure (NCI) in Australia.

8. Reference

[1] E.S. Hecht, P.P. Panda, Mixing and warming of cryogenic hydrogen releases, International Journal of Hydrogen Energy 44 (2019) 8960-8970.
[2] C. Rivkin, R. Burgess, W. Buttner, Hydrogen technologies safety guide, National Renewable Energy Lab.(NREL), Golden, CO (United States), 2015.
[3] M. Ichard, O.R. Hansen, P. Middha, D. Willoughby, CFD computations of liquid hydrogen releases, International Journal of Hydrogen Energy 37 (2012) 17380-17389.
[4] A. Venetsanos, S. Giannissi, Release and dispersion modeling of cryogenic under-expanded hydrogen jets, International Journal of Hydrogen Energy 42 (2017) 7672-7682.
[5] S. Giannissi, A. Venetsanos, N. Markatos, J. Bartzis, CFD modeling of hydrogen dispersion under cryogenic release conditions, international journal of hydrogen energy 39 (2014) 15851-15863.
[6] S.G. Giannissi, A.G. Venetsanos, E.S. Hecht, Numerical predictions of cryogenic hydrogen vertical jets, International Journal of Hydrogen Energy 46 (2021) 12566-12576.
[7] Q. Ba, Q. He, B. Zhou, M. Chen, X. Li, L. Cheng, Modeling of cryogenic hydrogen releases, International Journal of Hydrogen Energy 45 (2020) 31315-31326.
[8] Z. Ren, J.X. Wen, Numerical characterization of under-expanded cryogenic hydrogen gas jets, AIP Advances 10 (2020).
[9] B.R. Chowdhury, E.S. Hecht, Dispersion of cryogenic hydrogen through high-aspect ratio nozzles, International Journal of Hydrogen Energy 46 (2021) 12311-12319.
[10] Y. Deng, L. Zhang, D. Sun, B. Yu, Development of an efficient large time step unsteady solver for incompressible flows using the IDEAL algorithm in OpenFOAM, Journal of Computational Science 61 (2022) 101692.
[11] S. Crist, D. Glass, P. Sherman, Study of the highly underexpanded sonic jet, AIAA journal 4 (1966) 68-71.
[12] P.J. Linstrom, W.G. Mallard, The NIST Chemistry WebBook: A Chemical Data Resource on the Internet, Journal of Chemical & Engineering Data 46 (2001) 1059-1063.
[13] P. Linstorm, NIST chemistry webbook, NIST standard reference database number 69, J. Phys. Chem. Ref. Data, Monograph 9 (1998) 1-1951.
[14] S. Giannissi, A. Venetsanos, A comparative CFD assessment study of cryogenic hydrogen and LNG dispersion, International journal of hydrogen energy 44 (2019) 9018-9030.

Fires and Process Safety Paper 10
B. Z. Dlugogorski and A. R. Masri, Eds

Towards Clean Combustion and Decarbonisation
Proceedings of the Australian Combustion Symposium
26 – 29 November 2023, Darwin, Northern Territory, Australia

Venting of 18650 lithium-ion batteries during thermal runaway

V. Gupta[1, *], M. J. Dunn[1], C. Avila Jiminez[2], A. Macfarlane[1], S. Galindo Lopez[1], A. R. Masri[1]
[1]School of Aerospace, Mechanical and Mechatronics Engineering, The University of Sydney NSW 2006 Australia
[2]Clean Combustion Research Center, King Abdullah University of Science and Technology (KAUST) Thuwal 23955-6900 Saudi Arabia

Abstract

While the thermal runaway of lithium batteries continues to pose a high risk for fires, the characteristics of the thermal runaway process and the resultant venting of material and flame ejection from batteries remain only vaguely understood. This paper introduces a novel experimental rig designed to study the complex physical and chemical processes defining the venting process during thermal runaway and the structure of ensuing flames. Preliminary results are presented for a single 18650 battery cell where thermal runaway is induced with high-speed optical measurements employed to characterise the near-field of the vented jet close to the battery exit plane. Results show that the thermal runaway process is characterised by a sporadic release of hot pyrophoric particles, which may lead to autoignition of surrounding gases vented from the battery. Velocities of the particles ejected from the battery based on streak velocimetry are found to be in the range of 15-25 m/s. This work forms an initial platform for further research to shed more light on this important safety issue.

Keywords: lithium-ion battery, thermal runaway, battery fires

Artistic artificial intelligence images were generated based on the abstract content.

* Corresponding author:
Phone: (+61) 2 93612835
Email: vinny.gupta@sydney.edu.au

Towards Clean Combustion and Decarbonisation
Proceedings of the Australian Combustion Symposium
26 – 29 November 2023, Darwin, Northern Territory, Australia

The impact of octane numbers on the thermal efficiency and driving cycle fuel consumption of a gasoline turbocharged direct-injection engine

Zhicheng Ling[1], Jamie Terence Slaymaker, Yi Yang*, Zhenbiao Zhou and Michael Brear
[1]Department of Mechanical Engineering, The University of Melbourne, Victoria 3010 Australia

Abstract

The efficiency of modern spark-ignition engines is constrained by engine knock and the fuel octane ratings. This paper investigated the impact of the Research Octane Number (RON) and Motor Octane Number (MON) on the knock resistance of a 2.3-L gasoline turbocharged direct-injection (GTDI) engine and determined the octane impact on drive cycle fuel consumption of a conventional vehicle powered by this engine. Four fuels of different octane numbers (91.5RON/80.7MON, 91.6RON/83.4MON, 91RON/86MON, 95.4RON/86.6MON), were tested over the entire engine operation map at both normal and high intake temperatures. The vehicle fuel consumption was determined for standard EPA drive cycles and hot-weather towing tests with each fuel. The engine results show that a higher RON consistently improves the anti-knock performance and engine thermal efficiency. The effect of MON is more complex, in that higher MON improves the knock resistance at part loads and thus increases thermal efficiency, whereas a lower MON performs better at high loads and/or high temperatures. Driving cycle analysis shows that increasing RON and decreasing MON can lead to up to 11.2% and 4.7% reduction in fuel consumption, respectively, for hot-weather towing, but there is no noticeable change in the standard drive cycles among the test fuels.

Keywords: octane numbers, anti-knock ability, GTDI engine, driving cycle, fuel consumption

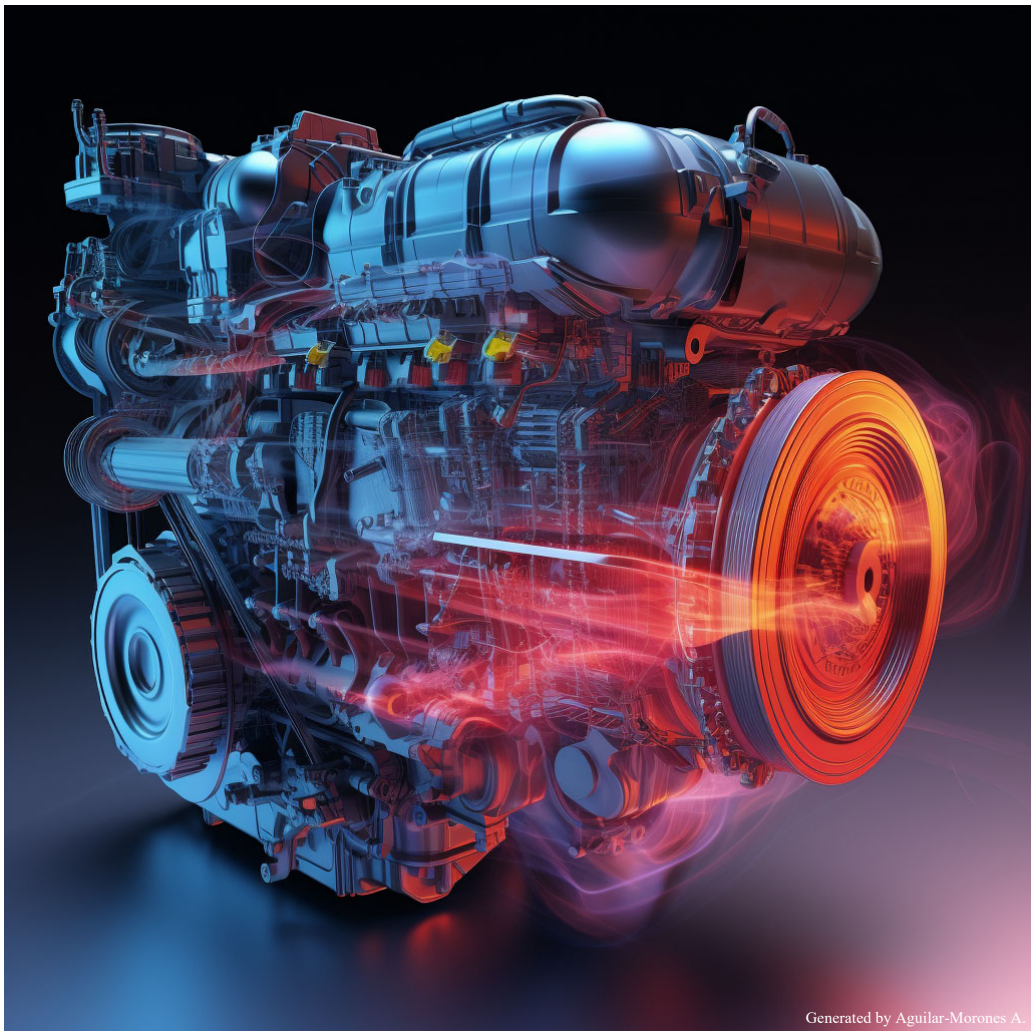

Artistic artificial intelligence images generated were based on the abstract content.

* Corresponding author:
Phone: (+61) 403153056
Email: yi.yang@unimelb.edu.au

Circularity and Hydrocarbon Fuels Paper 2

B. Z. Dlugogorski and A. R. Masri, Eds

Towards Clean Combustion and Decarbonisation
Proceedings of the Australian Combustion Symposium
26 – 29 November 2023, Darwin, Northern Territory, Australia

Natural gas-diesel dual-fuel direct-injection in compression-ignition condition

Quancen Wan[1], Yijun Lin[1], Cheng Wang[1], Guan Heng Yeoh[1], Sanghoon Kook[1] and Qing Nian Chan[1,*]
[1] School of Mechanical and Manufacturing Engineering, University of New South Wales, NSW 2052, Australia

Abstract

This work investigates the impact of ambient temperature on the ignition and combustion characteristics of methane (CH_4, a natural gas surrogate) and *n*-heptane (a diesel surrogate) in late direct-injection compression-ignition engine conditions. Two converging single-hole injectors were employed to introduce the fuels into an optically accessible constant-volume combustion chamber. Ambient temperatures ranging from 780 K to 1060 K were the varied parameters. High-speed schlieren imaging and pressure trace measurements were conducted. The findings reveal that at the lowest temperature, where pilot ignition followed the pilot end-of-injection (EOI), the flame initially shifted upstream post-ignition, eventually progressing downstream. At higher temperatures, where pilot ignition occurred before its EOI, the flame initially stabilised near the intersection of the jets. Specifically, at 890 K, the upper flame boundary shifted upstream after pilot EOI before gradually moving downstream. At 1060 K, the CH_4 flame exhibited an upstream shift after pilot EOI but stabilised at a fixed distance from the nozzle over time. These observations suggest that the combustion products from pilot ignition play a role in flame stabilisation, with the extent influenced by ambient temperature. An explanation of the lift-off response is offered based on the interaction between the CH_4 jet and the low-momentum combustion products of the diesel surrogate near the nozzle.

Keywords: methane compression-ignition, dual-fuel, direct-injection, flame stabilisation

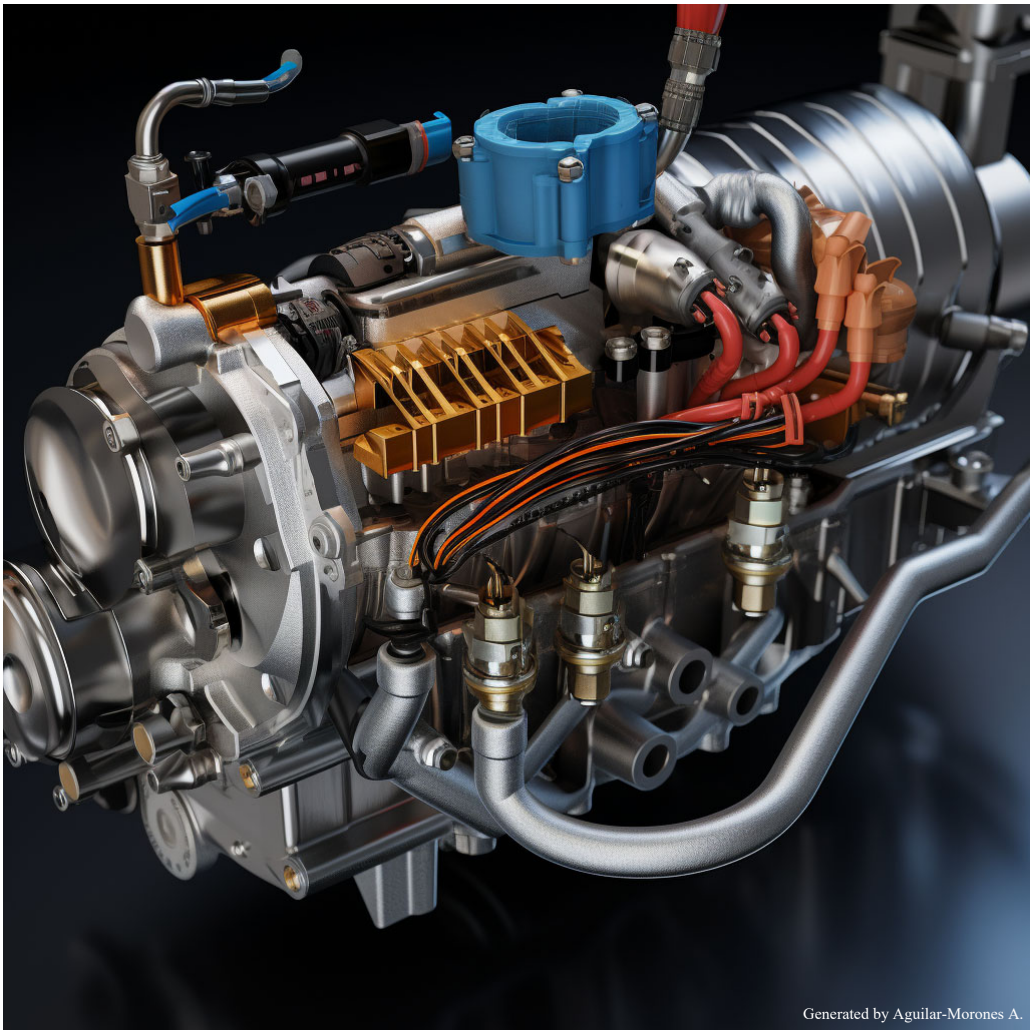

Artistic artificial intelligence images generated were based on the abstract content.

* Corresponding author: Qing Nian Chan
Email: qing.chan@unsw.edu.au

Circularity and Hydrocarbon Fuels Paper 3
B. Z. Dlugogorski and A. R. Masri, Eds

Towards Clean Combustion and Decarbonisation
Proceedings of the Australian Combustion Symposium
26 – 29 November 2023, Darwin, Northern Territory, Australia

Stabilisation of spent tyre pyrolysis liquid as a stable fuel oil

Junzhi Wu[1,2,*], Zhezi Zhang[2] and Dongke Zhang[2]
[1] Shanxi Institute of Energy, Taiyuan, Shanxi, 030006, China
[2] Centre for Energy (M473), The University of Western Australia, 35 Stirling Highway, Crawley, WA 6009, Australia

Abstract

Aiming to produce a stable fuel oil for use in internal combustion engines from spent tyres, raw spent tyre pyrolysis liquid was subjected to a set of chemical treatments including aqueous washing using deionised water, NaOH and HCl; esterification by reacting with methanol and ethanol and catalysed by H_2SO_4 or NaOH; and saponification by reacting with halogenoalkanes. The raw liquid and samples after each treatment were subjected to chemical speciation using HPLC and GC-MS techniques, and fuel quality and ageing tests. The results showed improved stability under accelerated ageing, with the amount of ageing precipitates formation decreased by more than half in the alkali and acid washed and esterified liquids. The esterification of the raw liquid not only significantly improved the stability but also converted otherwise "troublesome" organic acids into combustible esters. HPLC analysis indicated the conversion of nitrogen-containing species to surfactants was successful, albeit complex and inefficient treatment process. Among the various treatments, alkaline wash showed the best performance in stabilising the raw liquid. In addition to the stability, alkaline washing was also shown to greatly improve fuel properties such as flash point and total acid number.

Keywords: aqueous washing; fuel oil; esterification, pyrolysis liquid, spent tyres, stability

1. Introduction

With the rapid development of automobile industry, the demand for new tyres and output of spent tyres are on the rise worldwide. It is estimated that 13.5 million tonnes of waste tyres are scrapped every year[1]. Pyrolysis has been considered by many as one of the favourable methods to valorise spent tyres[2]. Pyrolysis of spent tyres produces three raw products[3], namely, a non-condensable fuel gas consisting mainly of hydrogen and methane, a condensate (or pyrolysis liquid) rich in complex hydrocarbons, and a solid residue rich in carbon. Clean and beneficial utilisation of these products has been a subject of on-going R&D and, in working with industry partners, the UWA Centre for Energy has researched and developed a suite of methods and technologies that can turn the raw pyrolysis products into various value-added products and services. One of these developments is a method to stabilise the raw pyrolysis liquid into a stable fuel oil for energy applications.

One of many challenges confronting the use of pyrolysis liquid as a fuel is its complex and reactive oxygenated and nitrogen-containing organic constituents, which cause instability and have a short-shelf-life of the liquid. In searching for a simple, cost-effective and environmentally responsible way to stabilise spent tyre pyrolysis liquid, several treatment strategies were conceptualised and evaluated in the present work. The approaches included 1) selective removal of "troublesome" organic acid species (e.g. benzoic acid, methyl benzoic acid, palmitic acid, oleic acid and stearic acid) with deionised water, acid or alkali washing treatments; 2) conversion these organic acids in the pyrolysis liquid to esters via esterification with methanol or ethanol catalysed by either H_2SO_4 or NaOH; and 3) conversion of nitrogen-containing species, particularly amines, to surfactant-like amine salts. The resultant fuel oils after the aforementioned treatments, respectively, were tested for their fuel properties such as flash point, viscosity and acid number, as well as the amount of precipitates formed in accelerated ageing tests. The present contribution outlines the treatment methods and shares the new and interesting findings.

2. Experimental

Raw spent tyre pyrolysis liquid was obtained from a commercial spent tyre retort kiln operated by our industry partner. The retort is air-tight and operates at slightly above atmospheric pressure and 500℃ with a typical solid retention time of ca. 20 minutes. The volatile stream is condensed through a chilled water (4℃) cooled condenser to be separated into a non-condensable fuel gas, which is burnt on-site for heat and power, and the raw pyrolysis liquid, which is the subject of the work described in this paper. The as-received pyrolysis liquid was stored at room temperature prior to treatments or analyses. The sample has a boiling point range between 85℃ (the initial boiling point) and 392 ℃ (the final boiling point).

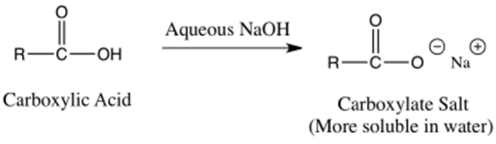

(R1)

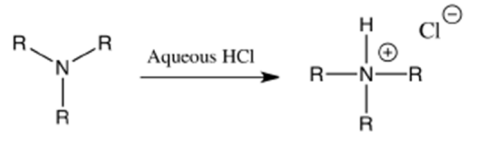

(R2)

Aqueous washing of the raw pyrolysis liquid was conducted using deionised (DI) water, NaOH or HCl,

* Corresponding author:
Phone: (+61) 8 6488 7600
Email: junzhi.june.wu@foxmail.com and dongke.zhang@uwa.edu.au

respectively, to remove any "troublesome" species. The acid and alkali treatments were to convert the organic acids and bases to water soluble salts for extraction, following Reactions 1 and 2. In a typical run, a pyrolysis liquid was washed with DI water equal volume 3 times, before alkaline wash (0.1M NaOH, equal volume, 3 times) or acidic wash (0.1M HCl, equal volume, 3 times). The mixture was shaken for at least 15 minutes and allowed to settle into two layers with the bottom discharged and the upper portion subjected to the next step of washing desired. Any excess water in the treated liquid was removed using anhydrous sodium sulphate and filtered through a microfiber glass filter to remove particulates prior to subsequent analysis.

Similarly, the raw pyrolysis liquid was subjected to esterification by methanol and ethanol with H_2SO_4 or NaOH as catalyst, which is expected to not only quench the detrimental effect of the acids on the stability of the raw pyrolysis liquid but also enhance the combustion characteristics of the resulting fuel oil, as esters are more akin to biodiesel[4]. Reaction R3 below shows a typical acid catalysed esterification reaction. The raw retort liquid was well mixed with methanol (ratios 1:1, 2:1, 4:1 and 8:1) and 0.5 wt% H_2SO_4, heated to the boiling point of methanol and refluxed for 72 hours. Progression of the reaction was monitored by taking samples at 4, 8, 24, 48 and 72hrs. The mixture was then neutralised with a stoichiometric alkaline solution (NaOH) and washed three times with DI water to remove excessive methanol. Excess water in the treated liquid was then removed using anhydrous sodium sulphate and filtered through a microfiber glass filter to remove any particulates prior to any further analysis.

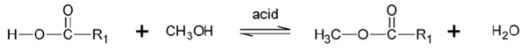

(R3)

Similar procedures were applied to alkali catalysed esterification.

The raw pyrolysis liquid was also reacted with halogenoalkanes to convert tertiary amines and other nitrogen-containing species to surfactants, or saponification[5], which are simultaneously hydrophilic and hydrophobic, that may act as stabilising agents for long-term storage of the resulting fuel oil. The presence of a small amount of surfactant in the fuel oil also eliminates the formation of biological gums in the fuel as water is no longer available to support bacteria growth to cause blockage and/or corrosion to the handling and storage facilities.

Tertiary amines, which are the most common nitrogen-containing compounds in the raw liquid, can be converted into a surfactant salt by reacting with halogenoalkanes (R4). The charges and the alkane chains will make the salt amphiphilic thus improve the overall fuel stability. Conversion of nitrogen-containing species to surfactant-like amine salts was conducted by mixing excess iodobutane (5 vol%) with the raw retort liquid. The mixture was heated to 100 °C while stirred, for 10 hours in a sealed container. The mixture after reaction was extracted with DI water and the aqueous phase was analysed using HPLC to confirm the formation of amine salts.

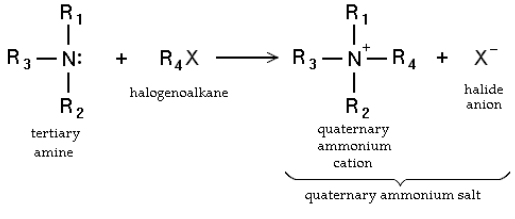

(R4)

The raw liquid sample and samples after each treatment were subjected to chemical speciation using HPLC (Agilent 1200 HPLC-DAD fitted with an Eclipse XDB-C18 column and using a mixture of 70% water and 30% acetonitrile isocratic as the mobile phase at a flow rate of 0.6 ml min^{-1}) and GC-MS (Agilent 7890a-5975 fitted with a HP-5MS column, 30m×0.25mm×0.25µm housed in an oven, which was held at the initial temperature of 32 °C for 8 mins followed by 2 °C min^{-1} ramping to 90°C and held for 8 mins; and finally heated at 5 °C min^{-1} to 300°C and held for 1 min) techniques and fuel quality and ageing tests, following relevant standards. In particular, the ageing test following the ASTM-D2274 (Standard Test Method for Oxidation Stability of Distillate Fuel Oil (Accelerated Method)) was a primary gauge for the stability of the treated fuels.

Results and Discussion

Table 1 summarises the ageing precipitates and key properties of the raw and treated pyrolysis liquids, along with those for commercial fuels of relevance including marine gas oil, marine diesel oil, intermediate fuel oil 180, intermediate fuel oil 380, and non-road diesel, for comparison.

Aqueous washing

The stability of the liquid was only marginally improved after washing with deionised water (DI washing). The ageing precipitate was reduced slightly from 2290 mg/100ml in the raw liquid to 1790 mg/100ml after DI washing. Interestingly, the stability was substantially improved after the alkaline wash and acidic wash, with the ageing precipitate reduced to 500 mg/100ml and 845 mg/100ml, respectively.

A number of organic acids were identified in the raw pyrolysis liquid using an Obitrap MS (Thermo Fusion), such as benzoic acid, methyl benzoic acid, palmitic acid, oleic acid and stearic acid. These acids are normally added as additives in the production of automobile tyres. When washing the raw pyrolysis liquid with 0.1 M NaOH solution, reactions with some long chain organic acids, especially palmitic acid and stearic acid, formed soap emulsions.

Esterification

Improved stability was also seen in the esterified samples. The amount of precipitate from the ageing test of the treated pyrolysis liquid after esterification (1100 mg/100ml) was almost halved. The additional benefit of

this treatment is that it converts other troublesome compounds into combustible esters that are similar to biodiesel. Fig. 1 shows the typical GC-MS spectra, which clearly indicate the formation of methyl benzoate, methyl palmitate and methyl stearate resulting from the esterification with methanol and H_2SO_4 at 65 °C.

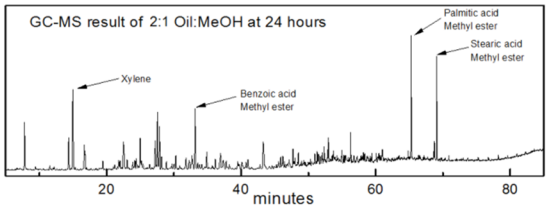

Figure 1 Typical GC-MS spectra of a pyrolysis liquid after esterification at 65 °C

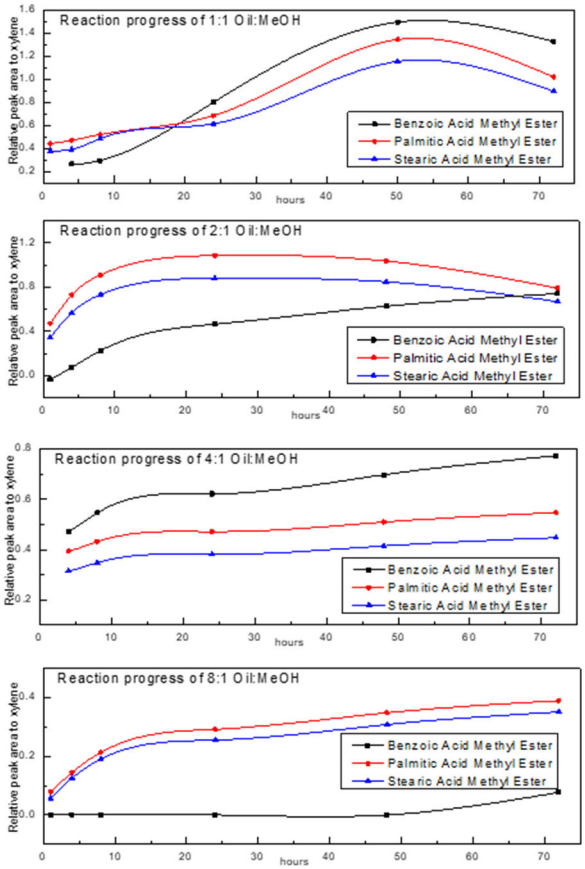

Figure 2 Temporal variation of the major easter products measured using GC-MS for different oil:CH_3OH ratios

The total acid number of the esterified pyrolysis liquid was reduced to ca. 5 mgKOH/g, suggesting an extensive conversion of organic acid to esters. Ageing tests of the treated liquid yielded ~1100 mg/100 ml precipitates, much less than the result of raw pyrolysis liquid (~2290 mg/100 ml). Figure 2 shows the dynamic progressions of the major ester products during methanol esterification process with their peak areas nominalised against an inert species – xylene, for cross comparison.

Esterification using ethanol was also trialled and the results showed the acids could be successfully converted into esters, as shown in Figure 3.

NaOH catalysed esterification of the pyrolysis liquid in methanol failed to yield any esters, even after 3 days of reaction.

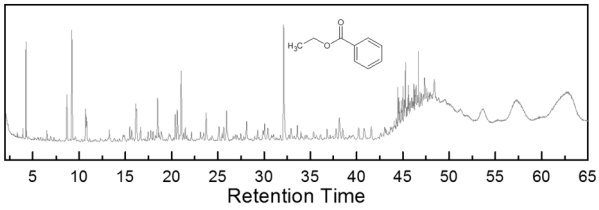

Figure 3 GC-MS result shows that ethanol also works for esterification.

Saponification

Saponification required excess halogenoalkanes to react with tertiary amines and other nitrogen-containing species present in the raw pyrolysis liquid to form surfactants[6]. However, there is no easy way to remove the excess unreacted halogenated reactant after the saponification treatment, which would compromise the subsequent characterisation. As such, the stability of pyrolysis liquid after saponification was not assessed. However, DI water was used as a probe to extract any water soluble species or the surfactants from the pyrolysis liquid before and after the saponification reaction, and HPLC with Diode Array Detector was employed to analyse the DI water extracts. The new peaks highlighted in the HPLC chromatograph are newly formed species which has similar retention time on the HPLC chromatograph of 1-Butylquinolium iodide, the product of quinoline (one of the major N-containing species) with iodobutane, are believed to be the surfactants formed after reaction (Fig. 4). Complete conversion is unlikely, as the concentration of nitrogen-containing species in the raw liquid is low (~800 ppm) and some of the major species, such as nitriles and thiazoles, will not convert to surfactants. However, these "salty" compounds imply at least some degree of conversion of the nitrogen-containing species to surfactants.

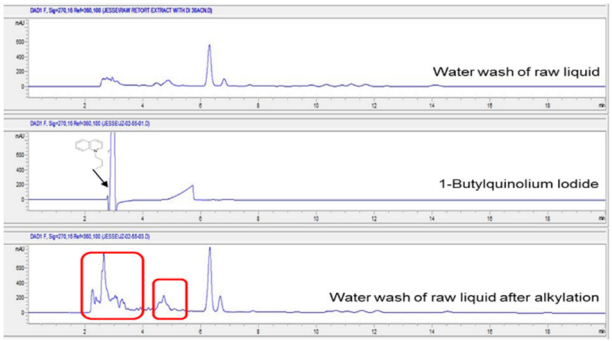

Figure 4 HPLC analysis of the DI water extract before and after the saponification with halogenoalkanes

Although saponification of the raw pyrolysis liquid achieved the initial scientific and technical intent, that the excessive amount of halogenoalkanes required to achieve the conversion, and the complexity involved in the inefficient processing suggests saponification would not be recommended as a means of pyrolysis oil stabilisation.

Fuel stability and quality

The fuel properties of the pyrolysis liquid after each of the aforementioned treatment were either the same or

improved compared to the raw pyrolysis liquid (Table 1). The flash point increased after all treatments, while the pour point remained the same. The viscosity was reduced after all treatments with the exception of the esterification treatment, which showed a marginal increase. A comparison of the properties of the liquid after each treatment indicated alkaline washing as the most promising. Additional fuel property testing, including total acid number, carbon residue content, resins content and Cetane index, were conducted on the alkaline washed liquid. Compared to the raw pyrolysis liquid, the alkaline washed liquid had improved Cetane index, ca. 50% reduction in carbon residue, ca. 75% reduction in the resins content and dramatic reduction of total acid number.

4. Conclusions

Various treatments to raw spent tyre pyrolysis liquid to enhance the stability were assessed. The samples after each treatment all showed improved stability under accelerated ageing, with the amount of aging precipitates formation decreased by more than half in the alkali and acid washed and esterified liquids. The esterification of the raw liquid not only significantly improved the stability but also converted otherwise "troublesome" organic acids into combustible esters. HPLC analysis indicated the conversion of the nitrogen-containing species to surfactants was successful. Among the various treatments, alkaline wash showed the best performance in stabilising the raw liquid. In addition to the improved stability, the stabilised fuel oil shows comparable qualities to those of commercial marine gas oil, marine diesel oil, intermediate fuel oil 180, intermediate fuel oil 380, and non-road diesel.

5. Acknowledgments

This research received financial supports from Australian Research Council under the ARC Linkage Projects scheme (LP160100035) and ARC Discovery Projects scheme (DP210103766 and DP220100116). Wu gratefully acknowledges the Postdoctoral Research Fellowship provided by the China Scholarship Council.

5. References

[1] Borówka, G., Bytnar, K., Krzak, M., Walendziewski, J., Zmuda, W. ***Journal of. Energy Resources Technology***, 2019;141(4):042207
[2] Rodriguez, I., Laresgoiti, M., Cabrero, M., Torres, A., Chomón, M., Caballero, B., ***Fuel Processing Technology,*** 2001;72:9-22.
[3] Han, W., Han, D., Chen, H., ***Polymers,*** 2023;15(7):1604.
[4] Masudi, A., Muraza, O., Jusoh, N., Ubaidillah, U., ***Environmental Science and Pollution Research***, 2023;30:14104–14125.
[5] Nivet J., Bernelin R., Blanc M., Riess J., ***European Journal of Medicinal Chemistry***, 1992;27:891-898.
[6] Jin, Z., Dong J., Kong, L., ***Academic Journal of Materials & Chemistry***, 2023;4:28-33.

Table 1 Ageing precipitate and properties of the raw and treated pyrolysis liquids

	Raw retort liquid	Water washed liquid	Alkaline washed liquid	Acid washed liquid	Esterified liquid	Marine Gas Oil	Marine Diesel Oil	Intermediate Fuel Oil 180	Intermediate Fuel Oil 380	Non-road diesel
Precipitate (mg/100ml)	2290	1790	500	845	1100	25	25	N/A	N/A	N/A
Flash Point (°C)	14.8	35	40.5	30	30	60	60	60	60	61.5
Pour Point (°C)	-30	-30	-30	-30	-30	-6	0	30	30	6
Viscosity @ 40°C (cSt)	4.77	3.07	4.56	2.85	4.99	6	11	180	380	1.4-20
Total Acid Number	22.54	-	0.55	-	4.98	0.5	0.5	2.5	2.5	N/A
Carbon residue (wt%)	1.1	-	0.63	-	-	N/A	0.3	15	18	N/A
Cetane Index	29	-	34.3	-	-	40	35	N/A	N/A	35
Resins content (mg/100ml)	40018	-	11380	-	-	N/A	N/A	N/A	N/A	10
Sulphur content %	0.73	-	-	-	-	-	-	-	-	-
Nitrogen content %	0.01	-	-	-	-	-	-	-	-	-

Circularity and Hydrocarbon Fuels Paper 4
B. Z. Dlugogorski and A. R. Masri, Eds

Towards Clean Combustion and Decarbonisation
Proceedings of the Australian Combustion Symposium
26 – 29 November 2023, Darwin, Northern Territory, Australia

Traverse combustion and smouldering front propagation in a column of coal gangue in an upward flow of O_2/N_2 mixture

Junzhi Wu[1,2*], Zhezi Zhang[2], Shuoshuo Zhou[3], Jian Gao[4] and Dongke Zhang[2, *]
[1] Shanxi Institute of Energy, Taiyuan, Shanxi, 030006, China
[2] Centre for Energy (M473), The University of Western Australia, 35 Stirling Highway, Crawley, WA 6009, Australia
[3] Hisense R&D Institute, 399 Songling Road, Qingdao, 266000, China
[4] College of Urban Transportation and Logistics, Shenzhen Technology University, Shenzhen, China

Abstract

Traverse combustion and propagation of smouldering front in a bed of coal gangue (CG) in a vertical quartz tube with a constant upward flow of O_2/N_2 mixture were experimentally studied. Once ignited from the top, a thin layer of glowing coal gangue undergoing smouldering is established and traverses downwards against the oxidant gas flow at a fairly constant velocity. Upon reaching the bottom of the bed, the counter-current smouldering front is transformed into a thicker layer of burning front, composed of glowing particles in the lower portion and bright flame in the upper portion, and commences concurrent propagation upwards, following the oxidant gas flow at a constant, albeit lower, velocity. The burning rate and propagation velocity of the burning front were measured against the particle size, O_2 concentration and flowrate. The mass burning rate decreases with increasing particle size during counter-current propagation but is invariant with particle size during concurrent propagation. Similarly, the downward propagation velocity decreases with increasing particle size while the upward propagation velocity is not sensitive to the particle size. The mass burning rate, and both downward and upward propagation velocities increase linearly with increasing O_2 concentration and gas flowrate.

Keywords: coal gangue, heterogeneous combustion, smouldering, traverse flame propagation, volatile combustion

1. Introduction

Coal gangue is a coal mining waste in gigantic quantities globally and poses a significant environmental problem wherever coal is mined[1]. Still containing combustible matter, coal gangue stockpiles often incur spontaneous combustion[2], emitting CO_x, SO_x, NO_x, VOCs as well as particulate matter (PM)[3]. Understanding the mechanisms and progression of spontaneous combustion in coal gangue stockpiles is of fundamental interest in combustion science and informs the formulation of countermeasure strategies to contain or even prevent spontaneous combustion.

Generally-speaking, spontaneous combustion is initiated when the rate of heat release from a localised oxidation zone within a stockpile is persistently greater than the rate of heat dissipation from the oxidation zone [4, 5] As the heat accumulates and the temperature rises, the oxidation accelerates, causing the combustion zone to propagate, expand and spread in the stockpile. Meanwhile, large temperature gradients between the burnt zone and the rest of the stockpile as well as the ambient induce natural convections around the combustion front, further complicating the heat and mass transfer environments and the spontaneous combustion processes. For a real solid fuel of interest such as coal gangue, the oxidation reactions are far more complex because different combustible components (e.g. volatile matter and fixed carbon) and different reactions (e.g. surface carbon oxidation, pyrolysis and devolatilization, and gas phase combustions) are simultaneously involved in a highly transient, constantly changing process. This makes the study of the transient combustion and burning front propagation process in a bed of coal gangue both interesting and challenging.

Recent literature has seen some significant progress in the understanding of burning front propagation in packed beds of combustible solid particles[6-9], which we term as traverse combustion. The present contribution extends our previous work to examine traverse combustion in a bed of coal gangue, which has significantly less combustible material and therefore much lower heating value as compared to the fuels examined before. A particular attention is paid to the influence of particle size, O_2 concentration and the gas flowrate.

2. Experimental

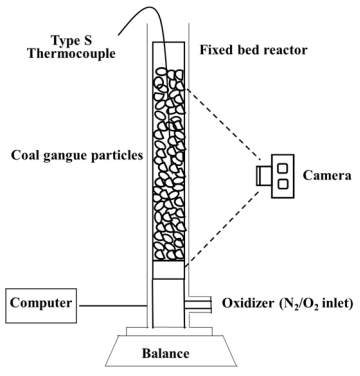

Figure 1 A schematic of the experimental setup

Figure 1 shows a schematic of the experimental setup, consisting of a vertical quartz tube reactor (ID: 1.4 cm) sitting on an electronic balance, a thermocouple and a digital camera. A coal gangue sample was collected from Shuozhou coal mine, Shanxi Province, China. The

* Corresponding authors:
Phone: (+61) 8 6488 7600
Email: junzhi.june.wu@foxmail.com and dongke.zhang@uwa.edu.au

as-received coal gangue sample was dried in air, milled and then sieved into size fractions of 0.6-0.9, 0.9-1.25, 1.25-1.6,1.6-2.0 and 2.0-2.5 mm. Table 1 presents the proximate and ultimate analysis data of the coal gangue.

Table 1 Proximate and ultimate analysis of coal gangue

Proximate analysis (wt%, a.r.)				Ultimate analysis (wt%, a.r.)				
Mois	VM	FC	Ash	C	H	N	S	O*
1.2	22.2	13.4	63.2	24.7	1.9	0.8	4.5	3.7

* Calculated by difference

In a typical experimental run, a coal gangue sample is loosely packed into the quartz column to a consistent height without compaction. A flow of O_2/N_2 mixture enters the column from the bottom and through a perforated plate that supports the coal gangue bed above it. Ignition is initiated by dropping a small burning charcoal particle to the top of the bed, in the meantime, the digital camera begins to record the burning front propagation while mass and centre-point temperature are continuously recorded on a computer. At the conclusion of the experimental run, the video clip, electronic balance and thermocouple readings are analysed offline to obtain the mass burning rate, burning front propagation velocity as well as the flame temperature as the burning front passes through the centre of the bed where the thermocouple is situated, which are correlated against coal gangue particle size, gas flow, and O_2 concentration.

3. Results and Discussion

Figure 2 shows typical sequential photographs of burning front propagation through a bed of 0.6-0.9 mm coal gangue with a flow of pure O_2 at 0.3 L min^{-1}. Upon ignition, a thin, regular and glowing burning front is established and begins to propagate downwards. When the burning front reaches the bottom of the bed, the burning front becomes thicker and begins to traverse upwards. The upward propagating burning front seems to be composed of two layers, i.e., glowing particles in the lower portion and bright flame in the upper portion.

The coal gangue bed appears to be still black behind the burning front as it propagating downwards. In this stage, the combustion appears to be dominated by particle surface smouldering with no volatile flame can be observed. As seen in Fig. 3, the total weight loss during the downwards propagation accounts for ca. 70% of the total weight lost, which suggests substantial pyrolysis and devoloatilesation also occurred in this stage. However, due to the heat lost to the cold surrounding, as well as forced convection from the cold oxidising gas, volatile flame could not be initiated and sustained. As the burning front propagating upwards, bed becomes grey indicating depletion of the combustible matter. In this stage, the glowing particles in the lower portion of the burning front is due to the heterogenous surface combustion while bright flame in the upper portion is due to the gas phase volatile combustion. The grey colour signifies ash formation as the burning front moves upwards and the whole process ends as the burning front reaches the top of the coal gangue bed. These interpretations seem to corroborate well with the mass burning rates and burning front propagation velocity data. Fig. 3 depicts a typical temporal mass loss profile of a burning bed, showing a faster burning rate as the burning front traverses downwards and a slower burning rate as the burning front traverses upwards.

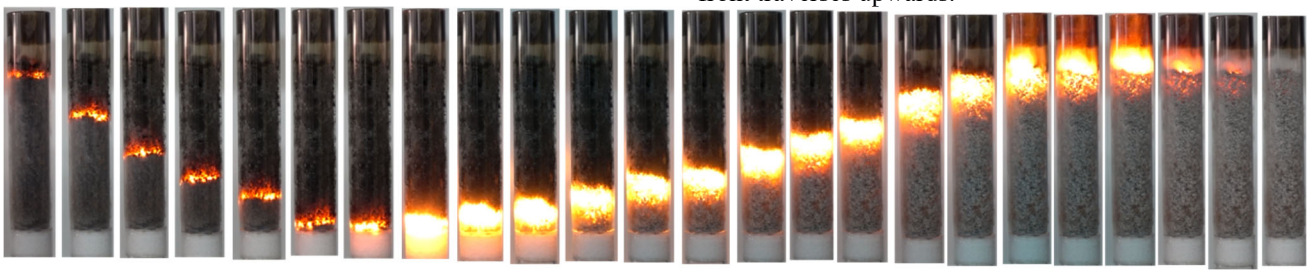

Figure 2 Sequential photographs showing the burning front propagation, firstly downwards and then upwards, through a bed of 0.6-0.9 mm coal gangue with a flow of pure O_2 at 0.3 L min^{-1}

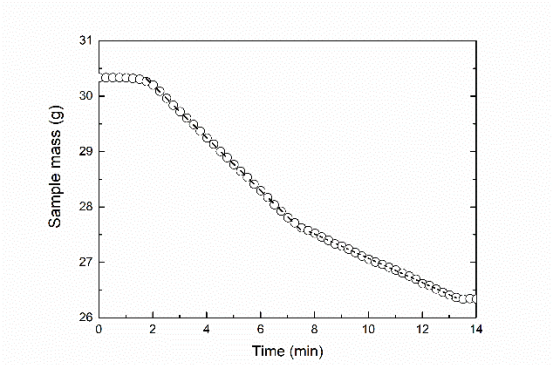

Figure 3 Typical mass loss profile for a bed of 0.6-0.9 mm coal gangue with a flow of pure O_2 at 0.3 L min^{-1}

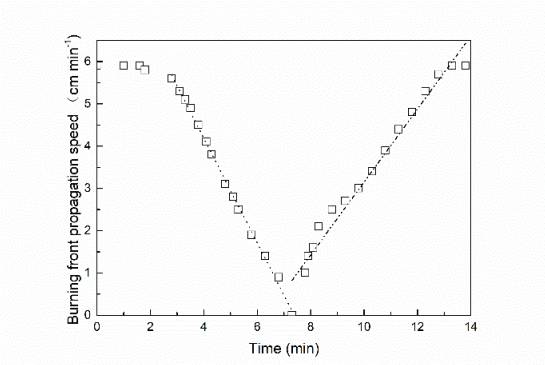

Figure 4 Downwards and upwards flame propagation velocities in a bed of 0.6-0.9 mm coal gangue with a flow of pure O_2 at 0.3 L min^{-1}

Figure 4 presents typical downwards and upwards flame propagation velocities in a bed of 0.6-0.9 mm coal gangue with a flow of pure O_2 at 0.3 L min^{-1}. It is evident that upwards front propagation velocity is slower than the downward propagation, corresponding to the slower mass burning rate during upwards flame propagation.

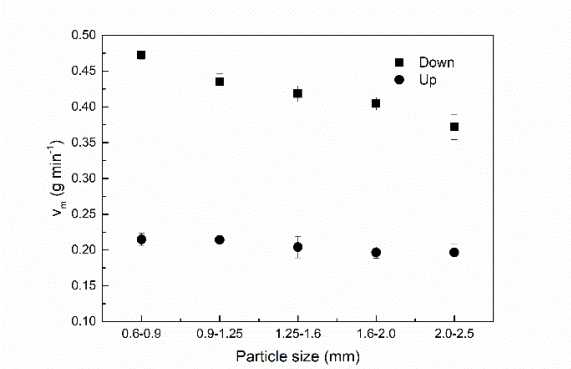

Figure 5 Mass burning vs particle size in a flow of pure O_2 at 0.3 L min^{-1}

The effect of particle size on the mass burning rate is illustrated in Fig. 5, where it can be seen that the burning rate during downwards propagating front decreases with increasing particle size while that of the upward propagating front is insensitive to particle size. Similarly, the burning front propagation velocity also decreases with particle size during downward propagation but less sensitive during upward propagation, as shown in Fig. 6. The downward propagation of burning front is dominated by heterogeneous oxidation on the coal gangue particle surface. Both particles and gas are cold ahead of the burning front. Larger particles have less surface area and take more energy to heat up. As such, it would be harder to sustain the burning in a bed of larger particles. However, during the upward propagation, the particles and burnt gas ahead of the burning front are already hot and particles are undergoing devolatilization. This explains why the burning front has a glowing heterogeneous combustion portion and on top of it a homogeneous gas phase flame portion. Consequently, the burning front propagation velocity is less sensitive to the particle size.

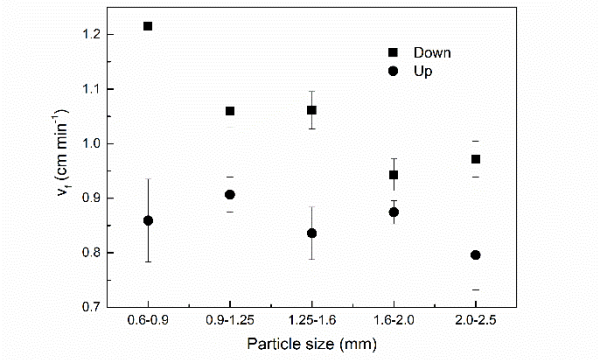

Figure 6 Burning front propagation velocity vs particle size in a flow of pure O_2 at 0.3 L min^{-1}

Increasing the pure O_2 flowrate causes an increase in both the mass burning rate and burning front propagation velocity, no matter downwards or upwards, as evident in Figs. 7 and 8.

The effect of O_2 concentration on the mass burning rate and burning front propagation velocity is illustrated in Figs. 9 and 10 respectively below, showing a positive correlation.

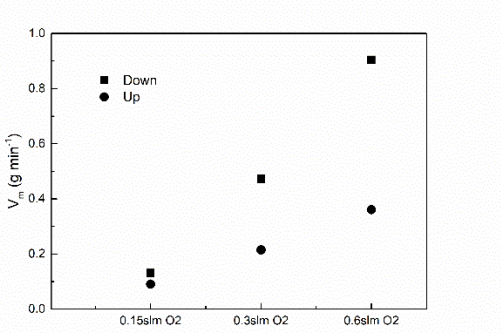

Figure 7 Mass burning rate vs O_2 flowrate (slm = Standard Litre per Minute)

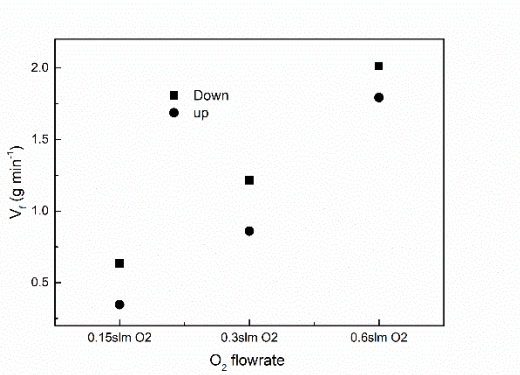

Figure 8 Burning front propagation velocity vs O_2 flowrate (slm = Standard Litre per Minute)

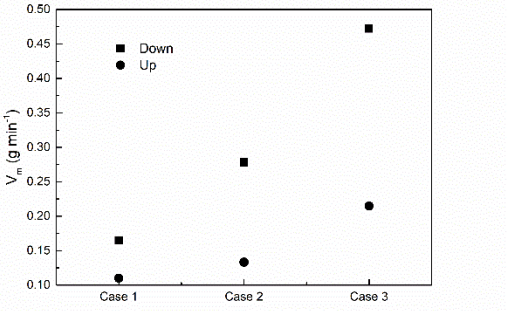

Figure 9 Mass burning rate vs O_2 concentration (Case 1 50%O_2:50%N_2; Case 2 75%O_2:25%N_2; Case 3 100%O_2: 0%N_2)

An increase in either O_2 concentration or flowrate leads to an increase in the availability of O_2 to execute the oxidation of the bed material of coal gangue, resulting in increased mass burning rate and flame propagation velocity. These observations and interpretation suggest that the combustion in the coal gangue bed is limited by the O_2 availability. It follows that limiting O_2 supply is a most effective way to combat spontaneous combustion in a stockpile of combustible solid. Adopting small gradient low slope sides,

compacting around the bases and top, and fine particle surfacing of combustible stockpiles are some practical measures to prevent spontaneous smouldering incidents.

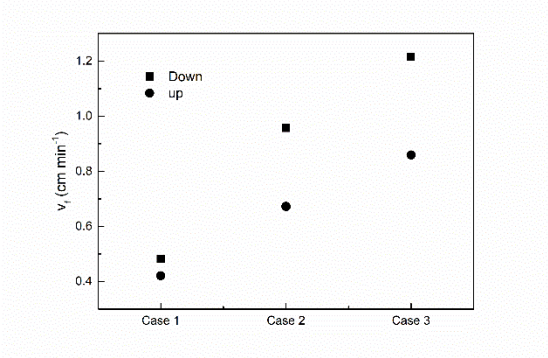

Figure 10 Burning front propagation velocity vs O_2 concentration (Case 1 50%O_2:50%N_2; Case 2 75%O_2:25%N_2; Case 3 100%O_2: 0%N_2)

The thermocouple registers the maximum burning front temperature as it passes through the centre of the bed. It was observed that the particle size has a minimal influence on the maximum flame temperature. However, as shown in Fig. 11, increasing O_2 concentration or flowrate results a high flame temperature as the combustion becomes intense with an increased O_2 availability. The maximum burning front temperature is always lower during downward flame propagation than during upward flame propagation, consistent the burning intensity determined by the O_2 availability. A larger portion of the heat from the heterogeneous combustion is spent on preheating the layer of cold particles ahead of the burning front as it traverses downwards, resulting in a lower maximum flame temperature. Conversely, the bed has already been preheated by the time when the burning front traverses upwards and therefore, the maximum flame temperature is higher.

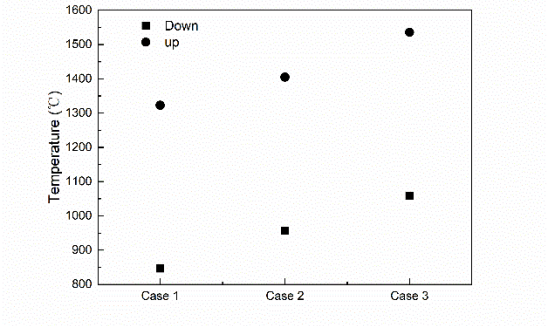

Figure 11 Maximum flame temperature versus O_2 concentration (Case 1 50%O_2:50%N_2; Case 2 75%O_2:25%N_2; Case 3 100%O_2: 0%N_2)

4. Conclusions

Traverse combustion and propagation of smouldering front in a bed of coal gangue (CG) in a vertical quartz tube with a constant upward flow of O_2/N_2 mixture have been systematically examined experimentally. Heterogeneous surface oxidation dominates during downward, counter-current burning front propagation into a layer of cold particles ahead of the burning front and against the oxidant gas flow. During downward propagation, the mass loss is due to both devolatilization and surface oxidation, and both mass burning rate and burning front propagation velocity decrease with increasing particle size.

The upward, concurrent smouldering front is of a thicker burning layer composed of glowing particles in the lower portion and bright flame in the upper portion. During the upward propagation, the burning front traverses into the already preheated hot layer of coal gangue particles, both the heterogeneous surface oxidation and devolatilization, and homogeneous gas phase combustion, are taking place, resulting in the two-layered burning front structure. During this stage of traverse combustion, both mass burning rate and burning front propagation velocity are less sensitive to the particle size.

The maximum burning front temperature registered by the thermocouple is around 900℃ during the downward propagation and is as high as 1500℃, and both increase with increasing O_2 concentration and the flowrate. Likewise, the mass burning rate, and both downward and upward propagation velocities increase linearly with increasing O_2 concentration and the flowrate. The traverse combustion is limited O_2 availability.

5. Acknowledgments

This research received financial supports from Australian Research Council under the ARC Discovery Projects scheme (DP210103766 and DP220100116), and the Future Energy Exports CRC (Project Number: 21.RP2.0059). Wu gratefully acknowledges the Postdoctoral Research Fellowship provided by the China Scholarship Council.

5. References

[1] Li J, Wang J, ***Journal of Cleaner Production,*** 2019;239:117946.
[2] Jiang X, Yang S, Zhou B, Cai J, ***Combustion Science and Technology***, 2021:1-15.
[3] Wu, J., Cheng, F., Zhang, D, ***International Journal of Energy for a Clean Environment***, 2021;22(5):33–49.
[4] Sujanti, W, Zhang, D, ***Fuel***, 1999;78(5):549 – 556.
[5] Sujanti, W, Zhang, D, Chen, X, ***Combustion and Flame***, 1999;117(3):646 – 651.
[6] Qi X, Zhou S, Gao J, Zhu M, Zhang Z, Zhang D, ***Proceedings of the Combustion Institute***, 2021;38:4251-9
[7] Zhou S, Gao J, Wu J, Zhang D, ***Combustion and Flame***, 2022;246:112396
[8] Gao, J., Qi, X., Zhang, D, Matsuoka, T, Nakamura, Y, ***Proceedings of Combustion Institute,*** 2021;38:5023–5032
[9] Zhou, S, Qi, X, Gao, J, Huang, X, Zhang, D, ***Combustion Science and Technology***, 2023, DOI:10.1080/00102202.2022.2160633

Circularity and Hydrocarbon Fuels Paper 5
B. Z. Dlugogorski and A. R. Masri, Eds

Towards Clean Combustion and Decarbonisation
Proceedings of the Australian Combustion Symposium
26 – 29 November 2023, Darwin, Northern Territory, Australia

Debromination of tris(tribromophenoxy)triazine by pyrolysis with calcium hydroxide

Caleb O. Ojo[1], Angel A. Aguilar-Morones[1], Vinuthaa Murthy[1], Suresh N. Thennadil[1], Sergei Levchik[2], Joel Tenney[2] and Bogdan Z. Dlugogorski[1, *]

[1]Energy and Resources Institute, Charles Darwin University, Darwin, Australia, 0909
[2]R&D, ICL-IP America, 769 Old Saw Mill River Rd, Tarrytown, USA, NY 10591

Abstract

Metal oxides and hydroxides reduce the emission of brominated compounds during pyrolysis of plastics containing brominated flame retardants (BFR). Calcium hydroxide is very effective when used with legacy BFR but is yet to be tested with novel BFR. This study investigates the effectiveness of calcium hydroxide in capturing bromine from 2,4,6-tris-(2,4,6-tribromophenoxy)-1,3,5-triazine (TTBP-TAZ) across a range of pyrolytic temperatures. We combine the thermogravimetric analysis with differential scanning calorimetry and record infrared spectra of the evolved gases and the solid residues. The results demonstrate significant differences in the decomposition of TTBP-TAZ with and without $Ca(OH)_2$. The volatilisation of neat TTBP-TAZ proceeds mainly in one dominant step, whereas that with $Ca(OH)_2$ comprises three stages. Calcium hydroxide captures all HBr produced in the pyrolysis of TTBP-TAZ and greatly reduces the emission of brominated phenols, capturing 67 % Br initially present in TTBZ-TAZ as $CaBr_2$.

Keywords: chemical recycling of plastics, novel brominated flame retardants, bromine circularity, pyrolysis, HBr

1. Introduction

Brominated flame retardants (BFR) constitute essential additives in manufacturing circuit boards and plastic casing for electrical and electronic equipment [1]. During thermal decomposition of BFR, the released bromine radicals delay the ignition process and slow down the subsequent development of flaming combustion [2]. While very effective in preventing unwanted fires, many first-generation BFR displayed toxicological and environmental disadvantages that prompted the industry to develop novel BFR [3], such as 2,4,6-tris-(2,4,6-tribromophenoxy)-1,3,5-triazine (TTBP-TAZ). This agent exhibits high effectiveness in delaying the ignition of acrylonitrile butadiene styrene (ABS) and high impact polystyrene (HIPS), replacing the once popular polybrominated diphenyl ethers [4], in these applications. The ICL Group is the biggest manufacturer of TTBP-TAZ at its plant in Israel, exporting the chemical to Korea, Europe, USA and China.

The thermal treatment of e-waste containing BFR produces volatile brominated organic species, as well as HBr. No economically viable technology exists to recover bromine from BFR-laden plastics forcing these materials to be either directed to landfills or incinerated. Reckless and unregulated combustion of e-waste containing BFR can form brominated trace pollutants such as polybrominated dibenzo-*p*-dioxins and dibenzofurans (PBDD/F) [1]. There is an urgent need to recover bromine from BFR plastics and convert their hydrocarbon matrices to low-bromine hydrocarbon feedstocks, to make these plastics suitable for the circular economy of the future [5,6].

Numerous studies have demonstrated the ability of metal compounds to reduce the emission of brominated volatile organic species during the pyrolysis of plastics laden with BFR. The capture of bromine comes to pass by the formation of metal bromides or oxybromides [5], with calcium hydroxide found as the most effective of these metal compounds [1,7-9]. Studies involving pyrolysis of tetrabromobisphenol A (TBBPA) abound, but the feasibility of recycling bromine from novel BFR, such as TTBP-TAZ, remains unknown.

The following work investigates the pyrolysis of pure TTBP-TAZ with calcium hydroxide, emphasising the fixation of the bromine in the solid residue.

2. Materials and Methods

2.1 Materials

The flame-retardant tris(tribromophenoxy)triazine (Fig. 1) was donated by the ICL Group, while the calcium hydroxide and bromide standards were purchased from Sigma Aldrich.

2.2 Thermogravimetry and differential scanning calorimetry

We conducted three types of experiments to collect measurements from thermogravimetry (TGA) and differential scanning calorimetry (DSC), using the Netzsch simultaneous thermal analyser (STA) 449 F3 Jupiter: (i) To obtain the TGA and DSC curves illustrated in Fig. 2, we placed 10 mg samples in an alumina crucible and subjected them to a temperature ramp of 10 °C/min from room temperature to 600 °C under argon gas flowing at a rate of 50 mL/min (30 mL/min purge and 20 mL/min protective [10]). (ii) To determine the bromine fixation by calcium hydroxide, we placed 100 mg of samples in a 3.4 mL crucible positioned on the top of the Netzsch S-type sample carrier, at a constant heating rate of 10 °C/min to the final temperature of up to 650 °C, with the argon purge gas flowing at 50 mL/min. The samples contained

* Corresponding author:
Phone: +61 (0) 408 965 978
Email: Bogdan.Dlugogorski@cdu.edu.au

the atomic ratio of Ca:Br of 1:2, as this reflects the stoichiometry of Br capture. The crucible carrier permits large sample sizes but has no sensor for energy flow measurements. Evacuation and refilling of the furnace were performed thrice to reduce the concentration of oxygen present in the system. Once the heating stops, the system rapidly cools, preventing secondary reactions. (iii) To obtain the infrared (IR) spectra of the evolved gases, we transferred the gases from the TGA to an IR spectrometer, as described in Section 2.4. The sample size amounted to 10 mg, with the TGA operated up to 900 °C with the temperature ramp of 10 °C/min.

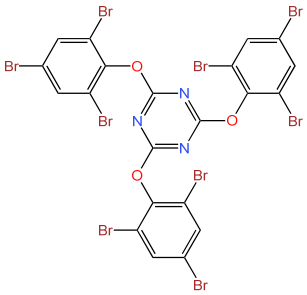

Figure 1: Tris (tribromophenoxy)triazine.

2.3 Analysis of solid residue

We leached the pyrolysis residue with 50 mL of distilled water to recover calcium bromide, with the leachate filtered and then analysed for Br anions by a Metrohm 930 ion chromatograph (IC). The atomic absorption spectrophotometer (AAS Agilent 55B AA) determined the calcium concentration in extracted water, to verify the stoichiometry between Ca^{2+} and Br^- in solution. We also air-dried the residues, after the removal of water-soluble species, and obtained the abundances of C, H and N with a Thermo Scientific™ FlashSmart™ analyser. The Bruker Invenio X Fourier transform–infrared spectrophotometer (FTIR) facilitated the characterisation of the functional groups in the solid residues using an attenuated total reflectance device operated at a resolution of 4 cm^{-1} with an average of 32 scans. These residues originated from the TGA runs interrupted at preset temperatures, with the oven cooled afterwards.

2.4 Analysis of gaseous products

A 1 m coupling line (Netzsch) between TGA and Fourier transform IR expedited the analysis of the evolved gases. We kept the transfer line at 290 °C to prevent condensation while keeping the 2.4 m multipass gas cell of 0.1 L in volume at 200 °C. We periodically acquired the IR spectra and named them after the instantaneous temperature in the TGA. Thus, for example, the spectrum denoted as "650 °C" would document the gas species that left the TGA between approximately 610 °C and 650 °C. This reflects thrice the formal residence time (i.e., 3 × 1.3 min) of the gases in the cell, and the temperature ramp of 10 °C/min. The IR spectra covered the range of 4000 cm^{-1} – 400 cm^{-1}, averaged over 16 scans at the spectral resolution of 1 cm^{-1}.

3. Results and Discussion

3.1 TGA results

Figure 2 presents the characteristic thermogravimetric and heat flow measurements of neat TTBP-TAZ and its mixture with $Ca(OH)_2$. A single step dominates the decomposition of the neat BFR between 300 and 460 °C with a mass loss of 93 %, concurring with the results of Lörchner et al. [10]. On the other hand, the mixture of TTBP-TAZ and $Ca(OH)_2$ reacts in three stages: The first stage occurs between 300 and 340 °C with a mass loss of 6.5 %, while, in the second stage, a mass loss of 43.6 % befalls in the temperature window of between 370 and 440 °C. A mass loss of 8.5 % characterises the final stage between 440 to 600 °C, double the mass loss of the pure BFR at the same temperature range.

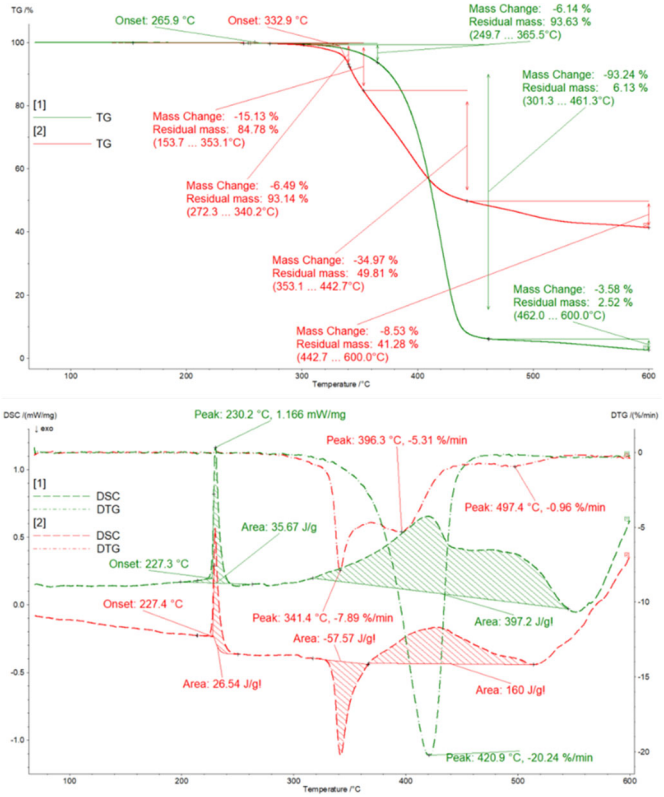

Figure 2: TGA (in top pane), DSC and DTG (both in bottom pane) curves for the thermal decomposition of neat TTBP-TAZ (green) and a mixture of TTBP-TAZ and $Ca(OH)_2$ (red), in argon carrier gas flowing at 50 mL/min at the rate of 10 °C/min.

The onset of mass loss of the neat BFR falls at about 389 °C, and for the mixture at 333 °C, showing that the additive initiates early decomposition of the BFR. The latter occurs just after the melting point of TTBP-TAZ at 227 °C. The differential thermogravimetric (DTG) curve indicates the maximum degradation rate of the neat BFR to fall at 421 °C. Compared to the single DTG peak of the neat BFR, the mixture displays three peaks - two strong maxima at 341 °C and 396 °C and a minor crest at 497 °C. The pyrolysed residue of TTBP-TAZ retains 3 % of the original mass at 600 °C, while this quantity is as high as 41 % for the mixture.

3.2 DSC results

The enthalpy of fusion of the pure BFR amounts to 36 J/g, while for the mixture, it corresponds to 27 J/g. This is because the instrument calculates the specific enthalpy based on the combined mass of TTBP-TAZ and $Ca(OH)_2$. The presence of $Ca(OH)_2$ converts the endothermic decomposition of the neat BFR, characterised by the enthalpy of 397 J/g, to a combination of exothermic and endothermic processes with values of -58 J/g and 160 J/g, respectively. Our figure for the decomposition enthalpy of neat TTBP-TAZ is about twice the value of 212 J/g for hexabromocyclododecane (HBCD) and more than three times the amount of 119 J/g for TBBPA published by Barontini et al. [13].

3.3 Bromine and calcium in pyrolysis char

Figure 3 shows the calcium hydroxide capturing 31 wt% of the initial Br in the solid residue at 400 °C. This value rises to 67 wt% at 650 °C, with critical transitions at 450 to 500 °C and 600 to 650 °C. This low fixation could result from scarcity of H atoms to form HBr with Br radicals. The amount of formed HBr is relatively small, and most Br escapes as compounds of organic bromine, like 2,4,6-tribromophenol [10]. This poses a technological challenge due to the contamination of the pyrolysis oil with bromine [12], requiring a separate unit operation to debrominate the oil in an industrial operation.

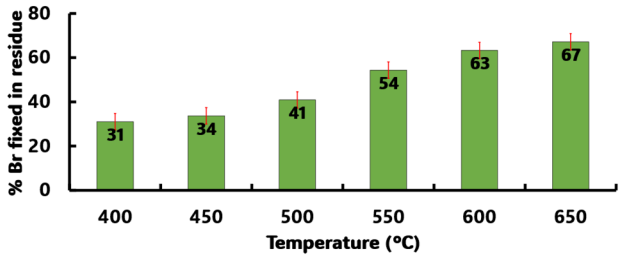

Figure 3: Inorganic bromine fixed in the solid residue from co-pyrolysis of TTBP-TAZ with $Ca(OH)_2$ from 400 to 650 °C.

If all calcium removed in the leachate were initially bound to bromine, we could compute the expected stoichiometric amount of bromine. This means that, if all Ca is present as $CaBr_2$, the bromine corresponding to the reaction stoichiometry should equate to the bromide determined by the ion chromatography. This is indeed the case for 550 °C and above, in Fig. 4, revealing that the bromide in the solution represents the dissolved $CaBr_2$. Higher quantities of calculated Br that arise at lower temperatures probably represent the formation of calcium oxybromides, as the dissolution of unreacted CaO and $Ca(OH)_2$ would affect equally the measurements at both low and high temperatures.

3.4 Elemental analysis of C, H and N

The elemental analysis of C, H and N, as documented in Table 1, provides insights into the effectiveness of capturing bromine by $Ca(OH)_2$. The abundance of C grows monotonically with the temperature increase and is proportional to the rise in Br fixation, signifying the intensification of Br removal from the BFR. The abundance of nitrogen and hydrogen remains relatively constant until 550 °C. This constancy means that equal and consistent amounts of nitrogen and hydrogen leave the crucible, as shown in the TGA-FTIR results (Fig. 5), but not significant enough (due to the high Br in the residue) to influence their proportion. However, above 550 °C, all C-Br bonds break and Br is removed from the char, so changes in the content of N and H become significant. Elevating the temperature beyond 600 °C induces a minor change in the composition of the residue. The infrared spectra confirm this comportment above 600 °C (Fig. 5), reporting the presence of C-N bonds.

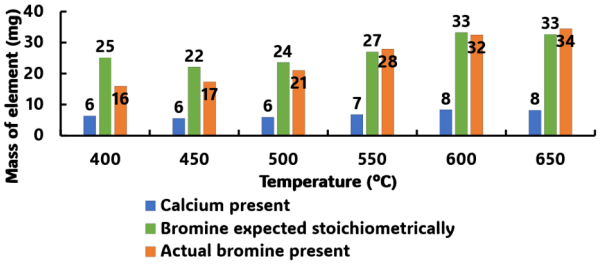

Figure 4: Amount of calcium in the leachate extracted from the solid residue (blue), calculated bromine assuming all bromine is present as calcium bromide (green) and bromide measured in the solutions by ion chromatograph (orange).

Table 1: CHN composition of solid residue at different temperatures after removing soluble species.

Temperature (°C)	% Nitrogen	% Carbon	% Hydrogen
25* (feed)	3.1	18.2	1.4
400	2.7	24.5	1.4
450	2.2	25.9	1.4
500	2.1	26.8	1.4
550	2.0	34.4	1.4
600	4.9	45.3	3.1
650	5.2	45.7	3.6

3.5 IR spectra of solid residue

Figure 5 illustrates the IR spectra of the pyrolysis residue. There is a gradual reduction in bands related to C-N, C-O and C-Br from 400 to 500 °C. A sharp reduction in IR peaks is seen from 500 to 550 °C. Above 550 °C, the important bonds break, correlating well with the changes in the elemental analysis documented in Table 1. The plots show calcium carbonate impurity and evidence of the appearance of the band at 1585 cm^{-1} which signifies the presence of aromatic nitrogen species, consistent with the elemental analysis.

3.6 IR spectra of evolved gases

The vibration bands of NCO at 2270 cm^{-1} dominate the IR spectra (Fig. 6). The library matches the spectrum well with benzene isocyanate. At a low temperature of 400 °C for the neat BFR, we confirm the presence of isocyanuric acid. Higher temperatures and the presence of calcium hydroxide prompt the release of isocyanic acid [10] (Fig. 7). We also observe the rotational bands of HBr between 2400 and 2600 cm^{-1} from 409 to 650 °C for the neat BFR. Interestingly, Lörchner et al. [10] did not find HBr peaks, probably due to the use of a lower resolution or the less sensitive gas cell. In the presence of $Ca(OH)_2$, the HBr peaks are absent at all temperatures indicating the

complete removal of HBr by calcium hydroxide. The OH peaks and peaks in the fingerprint region confirm the presence of organic bromine compounds such as tribromophenol as expected from the structure of TTBP-TAZ. When we introduce $Ca(OH)_2$ (Fig. 7), we observe reduced intensities of these brominated organic compounds.

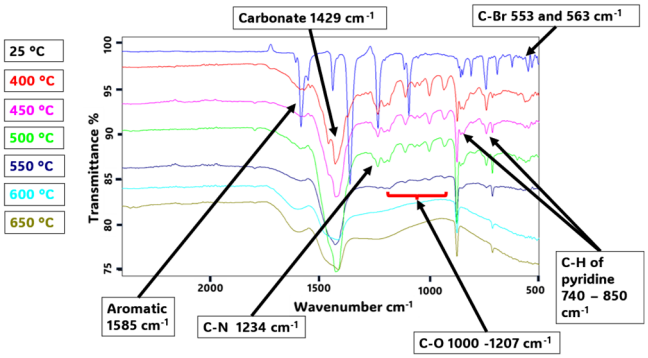

Figure 5: Infrared spectra of the residue from the pyrolysis of combined TTBP-TAZ and $Ca(OH)_2$ after leaching and drying. The trace at 25 °C is for pure TTBP-TAZ (offset for clarity).

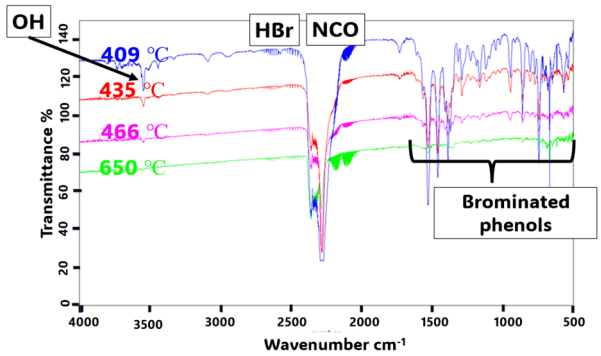

Figure 6: FTIR spectra of decomposition products of the pyrolysis of TTBP-TAZ without $Ca(OH)_2$ at different temperatures (offset for clarity).

We recommend that future studies investigate higher heating rates and introduce an adsorber bed after the pyrolysis, to debrominate the gas-phase phenols and to increase the capture of bromine. Elemental mass balance on carbon and bromine must be performed, together with the calculation of uncertainties, to verify the veracity of the measurements. This will require gas-chromatographic analysis of liquid products. We also recommend performing transmission electron microscopy–selected area electron diffraction, as the crystal sizes will probably be too small for the powder X-ray diffraction, and X-ray absorption fine structure spectroscopy, to investigate the possible formation of calcium oxybromide species that appear to limit the capture of bromine at low temperatures. Finally, the present results, supplemented by the density-functional-theory calculations, should easily establish the reaction mechanisms for the decomposition of TTBP-TAZ, with and without $Ca(OH)_2$.

4. Conclusions

Calcium hydroxide transforms the one-stage endothermic decomposition of TTBP-TAZ into a three-stage complex process, revealing an exothermic reaction at around 341 °C. We demonstrated that $Ca(OH)_2$ captures up to 67 % of bromine initially present in TTBP-TAZ. At temperatures above 550 °C, the collected data suggested the formation of $CaBr_2$. The infrared analyses of the solid residue and the evolving gases detected the formation of unidentified nitrogen species, and isocyanic acid, respectively. The isocyanuric acid arises only in the pyrolysis of neat TTBP-TAZ and at low temperatures near 400 °C. We identified polybrominated phenols, produced at temperatures below 500 °C, as the reason for the incomplete capture of bromine in $CaBr_2$.

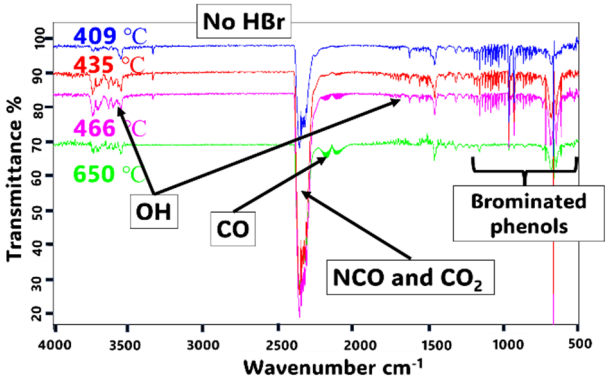

Figure 7: FTIR spectra of decomposition products of the pyrolysis of TTBP-TAZ with $Ca(OH)_2$ at different temperatures (offset for clarity).

5. Acknowledgments

We thank Mr Stephen Poole, Manager of the Water Laboratories of DITT of the NT Government, for access to an ion chromatograph. We thank Dr Hao Wang for assistance with laboratory work. COO and AAA-M recognise CDU, NAFRA and AINSE for Scholarships.

6. References

[1] M.S. Kuttiyathil, L. Ali, O.H. Ahmed, M. Altarawneh, Environ. Sci. Pollut. Res. 30 (2023) 98300-98313.
[2] M. Altarawneh, A. Saeed, M. Al-Harahsheh, B.Z. Dlugogorski, Prog. Energy Combust. Sci. 70 (2019) 212-259.
[3] E.A.R. Zuiderveen, J.C. Slootweg, J. de Boer, Chemosphere 255 (2020) 126816.
[4] D. Lörchner, W. Kraus, R. Köppen, Chemosphere 229 (2019) 77-85.
[5] S. Oleszek, S. Kumagai, M. Grabda, K. Shiota, T. Yoshioka, M. Takaoka, J. Hazard. Mater. 409 (2021) 124972.
[6] O. Terakado, R. Ohhashi, M. Hirasawa, J. Anal. Appl. Pyrol 91 (2011) 303-309.
[7] L. Ali, M.S. Kuttiyathil, O.H. Ahmed, M. Altarawneh, Sep. Purif. Technol 307 (2023) 122836.
[8] S.H. Jung, S.J. Kim, J.S. Kim, Fuel. Process. Technol. 96 (2012) 265-270.
[9] S. Kumagai, G. Grause, T. Kameda, T. Yoshioka, J. Mater. Cycles Waste Manag. 19 (2017) 282-293.
[10] D. Lörchner, D. Dittmann, U. Braun, L.W. Kroh, R. Köppen, J. Anal. Appl. Pyrol. 141 (2019) 104635.
[11] F. Barontini, K. Marsanich, L. Petarca, V. Cozzani, Ind. Eng. Chem. Res. 43 (2004) 1952-1961.
[12] R.T. Gao, B.Y. Liu, L. Zhan, J. Guo, J. Zhang, Z.M. Xu, J. Hazard. Mater. 392 (2020) 122447.
[13] Barontini, F., Marsanich, K., Petarca, L., Cozzani, V., 2004. Ind. Eng. Chem. Res. 43, 1952-1961.

Circularity and Hydrocarbon Fuels Paper 6
B. Z. Dlugogorski and A. R. Masri, Eds

Towards Clean Combustion and Decarbonisation
Proceedings of the Australian Combustion Symposium
26 – 29 November 2023, Darwin, Northern Territory, Australia

Thermal decomposition mechanism of F-3020, end-capped brominated epoxy flame retardant

Angel A. Aguilar-Morones[1], Caleb O. Ojo[1], Vinuthaa Murthy[1], Suresh Thennadil[1], Sergei Levchik[2], Joel Tenney[2] and Bogdan Z. Dlugogorski[1,*]

[1] Energy and Resources Institute, Faculty of Science and Technology, Charles Darwin University, NT 0909 Australia
[2]R&D, ICL-IP America, Tarrytown, New York, USA

Abstract

This contribution investigates the mechanism of thermal decomposition of end-capped epoxy oligomers of tetrabromobisphenol A (TBBPA), denoted as F-3020, commonly deployed to control flammability of styrenic polymers. The aim is to assist with the development of co-pyrolysis processes for recycling plastics containing brominated flame retardants (BFR). The experiments combine thermogravimetric analysis and differential scanning calorimetry, with attenuated total reflectance of the residue and on-line infrared analysis of pyrolysis gases and. F-3020 decomposes in three stages including, (Stage 1) volatilisation that commences at around 260 °C, followed (Stage 2) by dissociation of ether linkages, with the accompanying emission of 2,4,6-tribromophenol (from end caps) and methane and acetone (from hydroxypropanediyl linkages). Stage 2 also includes the formation of CH_3Br and HBr from intramolecular reactions. The rate of pyrolysis in Stage 2 peaks at around 360 °C. Stage 3 commences at around 412 °C and releases debrominated or partly-debrominated fragments of F-3020, with declining discharge of CO_2, CO and H_2O, and ceased release of CH_4 and CH_3COCH_3. The present measurements suggest that success of the co-pyrolysis process will depend on the effectiveness of inorganic adsorbers for fixing HBr and for debrominating CH_3Br, bromophenols and volatilised molecules of F-3020 at temperatures as low as 260 °C.

Keywords: brominated epoxy flame retardants, decomposition mechanism, debromination, FTIR, evolved gases

1. Introduction

Brominated flame retardants (BFR) reduce risk of ignition of plastic components in electrical and electronic equipment (EEE) [1]. According to Forti et al., in 2019, the world economy generated 53.6 Mt of EEE waste (WEEE or e-waste), increasing at a rate of 1.8 Mt per year [2]. Recycling BFR plastics poses critical challenges, as environmental regulations mandate the threshold of BFR of 1000 mg/kg in recycled products [3]. While this level strictly applies to most legacy BFR, like polybrominated diphenyl ethers (PBDE), for practicality and cost-saving, it serves as a universal benchmark for the bromine content in recycled plastics [4].

The novel processes that handle BFR plastics, called "advanced recycling" comprise (i) solvent-based operations, for example, supercritical water oxidation, dissolution precipitation and hydrolysis [3]; (ii) thermal methods, such as gasification, pyrolysis, microwave-assisted pyrolysis, co-pyrolysis and catalytic pyrolysis [4]; and (iii) recently developed techniques, like hydrocracking and non-thermal plasma treatment [5, 6]. Among these processes, pyrolysis shows the most promise, as the process operates under inert atmosphere that significantly lowers the formation of potential pollutants. Pyrolysis scales up easily between laboratory experiments and industrial treatment and thus can be adopted to operate at throughputs imposed by existing facilities. It has "High" technology readiness level (TRL) [7]. These considerations have prompted us to investigate pyrolysis for recovering bromine from BFR and from plastics laden with BFR.

Among polymers exploited in the manufacture of EEE, the share of high-impact polystyrene (HIPS) and acrylonitrile butadiene styrene (ABS) amounts up to 55 % [8]. These plastics require BFR to display no blooming (migration), to offer good processability and high impact, as well as thermal and UV stability. These requirements make end-capped brominated epoxy oligomers, like those of tetrabromobisphenol A (TBBPA or 2,2',6,6'-tetrabromo-4,4'-isopropylidene diphenol) an excellent and commonly used choice. For convenience, we denote this oligomer as F-3020, a commercial name coined by the ICL Group that manufactures it (Fig. 1). In F-3020, the end caps are 2,4,6-tribromophenoxys, and the TBBPA monomers are bridged by links of 2-hydroxypropane-1,3-diyls, which we abbreviate as hydroxypropanediyl. These links also bridge the end caps with the oligomer backbone (Fig. 1).

The present study develops the pyrolysis mechanism of F-3020 based on the experimental measurements from three hyphenated techniques, (i) TGA-DSC (thermal gravimetric analysis - differential scanning calorimetry); (ii) Fourier transform infrared spectroscopy of gases evolving from the TGA-DSC apparatus (FTIR-EGA); and (iii) attenuated total reflectance of solids produced in interrupted pyrolysis of F-3020 (FTIR-ATR). This study brings an insightful understanding of the production of brominated organic and inorganic species, to progress designing strategies to remove, fix and recover the bromine from WEEE to reach Br circularity.

* Corresponding author:
Phone: +61 (0)8 8946 7704
Email: Bogdan.Dlugogorski@cdu.edu.au

2. Experimental

2.1 Materials

The ICL Group donated F-3020 as powder, with its chemical structure illustrated in Fig. 1. F-3020 contains 57 % Br and displays molar mass of 2300 g/mol, which corresponds, on average, to 2.6 monomeric units [9] as marked in Fig. 1. Air Liquid Group supplied ultra-high purity argon (99.9999 %).

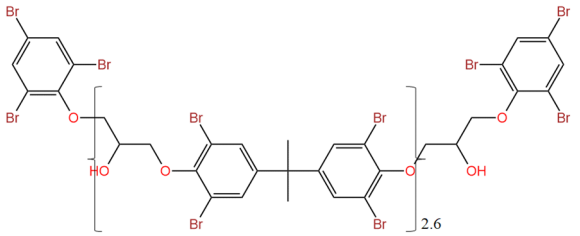

Figure 1. Chemical structure of F-3020.

2.2 Analytical details

2.2.1 TGA-DSC

A simultaneous thermal analyser, Netzsch 449 F3 Jupiter, served to perform the synchronised measurements of thermogravimetric analysis and differential scanning calorimetry. The instrument operated at a heating ramp of 10 °C/min, within the temperature range of 70 °C to 700 °C, flowing argon at 50 mL/min (30 mL/min around the sample and 20 mL to protect the balance mechanism), as measured at 25 °C and 1.013 bar. We placed samples of up to 10 mg in circular Al_2O_3 crucibles of 6.8 mm in diameter and 85 µL, housed in a platinum TGA furnace of 96 cm^3 and capable of reaching 1500 °C. The product gases proceeded to a long-path gas cell, as described in Section 2.2.2. We evacuated the TGA furnace three times to a pressure of about 1 Pa, flooding it with argon after each evacuation, to minimise the concentration of the residual oxygen.

2.2.2 FTIR-EGA and FTIR-ATR

A transfer line manufactured by Netzsch, 1 m in length and heated to 290 °C, connected the outlet from the TGA oven to the long-path (multipass) gas cell positioned in the sample compartment of a Bruker Invenio X Fourier transfer infrared (FTIR) spectrometer. The volume of the transfer line corresponded to 8.7 mL, resulting in the residence time of product gases in the line of 10.4 s. The gas cell, from PIKE Technologies, featured 2.4 m path length, a volume of 100 mL, and a heating jacket. We operated the cell at 200 °C to prevent condensation of pyrolysates, resulting in the nominal residence time of gases in the cell of 76 s. Each FTIR spectrum, collected every 48 s, represented an average of 16 scans acquired at the spectral resolution of 1 cm^{-1}, between 4000 cm^{-1} and 400 cm^{-1}.

To investigate the transformation of F-3020 during the pyrolysis, we arrested the decomposition process by stopping the heating at 360 °C, 400 °C and 600°, and cooling the reactor. The solid residues were grounded and analysed with the ATR accessory from Bruker (Platinum ATR). The accessory incorporated a high-pressure attachment for mounting samples and featured a diamond crystal plate set for a single reflection with the incidence angle of the incoming beam of 45°. We plan additional measurements with a germanium crystal plate, as the negative peaks revealed in some of the spectra suggest high refractive indices of the residue. The Bruker Invenio X FTIR functioned at the spectral resolution of 4 cm^{-1} and averaged 32 scans for each acquisition, for the range of wave numbers between 4000 cm^{-1} and 400 cm^{-1}.

3. Results and Discussion

3.1 Analysis of TGA-DSC measurements

Figure 2 illustrates the TGA, DTG and DSC curves of the pyrolysis of F-3020. The term DTG denotes the derivative thermogravimetry reflecting the instantaneous slope in the TGA profile. The decomposition of F-3020 proceeds sequentially in Stages 1-3: Stage 1 - below 331 °C (mass loss 6.6 %), Stage 2 - 331 °C – 412 °C (77.2 %), and Stage 3 - above 412 °C up to the maximum experimental temperature of 700 °C (7.6 %). An onset temperature for the mass loss in Stage 1 corresponds to 280 °C, with minor but noticeable change of mass starting at around 260 °C. The maximum loss rate occurs in Stage 2 at 360 °C.

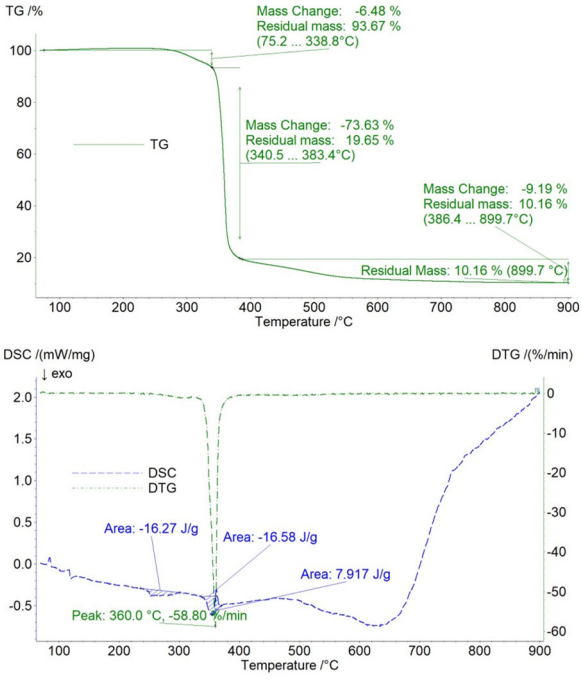

Figure 2. TGA (top pane), DSC and DTG (both in bottom pane) plots of decomposing F-3020.

Luda et al. [10] measured 274 °C and 339 °C, for the onset and maximum temperature, respectively, for non-capped diglycidyl ether of TBBPA (inert atmosphere, 20 °C/min, sample size 10 mg – 15 mg). A closer examination of the TGA curve in Luda's et al. paper suggests evaporation commencing at around 215 °C. Thus, the addition of end caps increases the evaporation and breakdown temperatures by ≈ 25 °C.

Except at above 650 °C, the DSC baseline falls below the zero line, indicating an exothermic effect. As heating constitutes an endothermic process, we suspect interference from nickel impurities left on the walls of the reference crucible from the DSC calibration. The main decomposition segment (Stage 2) in the DTG curve translates into overlapping exothermic (≈ 340 °C – 356 °C) and endothermic (≈ 356 °C – 370 °C) phenomena in the DSC measurements. The fronting exotherm (-16.6 J/g) morphs into a tailing endotherm (8.0 J/g), whereas normally one would expect an endothermic pyrolysis process characterised by ≈ 100 J/g – 500 J/g [11, 12]. In the IR spectrum of neat F-3020 we observe minor peaks due to the C-O-C and CH vibrations in oxirane, at around 924 cm^{-1} and 3081 cm^{-1}, respectively. Thus, it is possible that catalysed polymerisation of residual epoxide groups takes place at lower temperatures (i.e., < 340 °C), and that the self-polymerisation of the epoxy groups at around 356 °C blurs the determination of heat consumed in the main pyrolysis step.

3.2 Decomposition mechanism

The analysis of the FTIR-EGA spectra acquired at 260 °C and 266 °C (Fig. 3), and the FTIR-ATR bands for the neat F-3020 (not shown), suggests that Stage 1 involves four types of volatilisation reactions. This analysis considers peaks with *S/N* (signal to noise) > 2. (1) The elimination of water from the hydroxypropanediyl bridges that leads to formation of C=C bonds in the solid phase [13]; see the water bands around 3750 cm^{-1} and 1625 cm^{-1}. (2) The transfer of residual 2,4,6-tribromophenol or TBBPA from solid to gas phases, as FTIR-ATR detects a broad band centred on 3563 cm^{-1}, indicating the presence of OH vibration in the neat FTIR consistently with the appearance of a sharp peak at 3548 cm^{-1} in the FTIR-EGA spectrum. (3) The emission of CO_2 (2349 cm^{-1} and 667 cm^{-1}), which we suspect to originate, at this temperature, from the presence of an unknown aromatic ester in neat F-3020, as evidenced by a band at 1725 cm^{-1} collected by FTIR-ATR. (4) Elimination of a ketone and/or aldehyde species, such as acetone (from hydroxypropanediyl links) or acrolein (from glycidol impurity), is evidenced by a band between 1720 cm^{-1} and 1680 cm^{-1}.

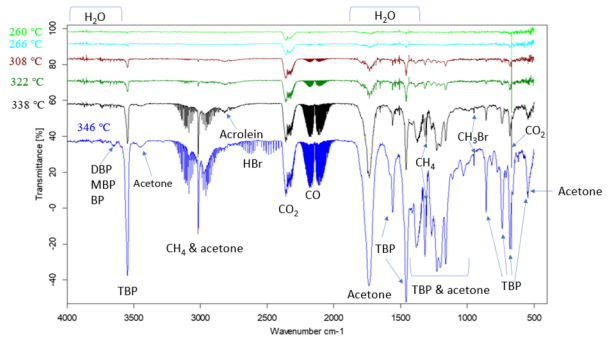

Figure 3. FTIR of the evolved gases in the neat F-3020 at different temperatures

As the temperature reaches 308 °C, the FTIR-EGA spectra document the onset of Stage 2 decomposition of F-3020, accompanied by significant emissions of CH_4 (rotational spectrum around 3000 cm^{-1}), CO_2, CO (rotational fine structure of between 2210 cm^{-1} and 2060 cm^{-1}), 2,4,6-tribromophenol, acetone (characteristic ketone peak at 1715 cm^{-1}), at the continued evolution of H_2O. All these species arise from the molecular rearrangements of the hydroxypropanediyl bridges. While details of these transformations remain to be established from the density-functional-theory calculations, Scheme 1 summarises these observations. The emissions of CO_2 are too substantial, to be explained away by the ester impurity mentioned in the preceding paragraph. The ether C-O bonds are characterised by a relatively low bond dissociation energy (BDE) of 271 kJ/mol. In contrast, the aliphatic C-C bonds exhibit more resistance to breakage at low temperature as their BDE amounts to 338 kJ/mol [14]. We note that C-O bond is weakened by double bond formed after water elimination [13].

Stage 2 also includes: (1) The evolution of minor amounts of acrolein from the residual epoxide groups, with acrolein emissions subsiding just above 346 °C, as demonstrated by the band around 2800 cm^{-1}, in agreement with the TGA-DSC measurements discussed in Section 3.1. (2) The emission of HBr that commences just above 322 °C, corroborated by the appearance of its rotational spectrum between 2700 cm^{-1} and 2400 cm^{-1}. Hydrogen bromide forms by the intramolecular reaction between OH in hydroxypropanediyl bridges and the ortho-Br [15], as OH in TBBPA is quite acidic and/or by the HBr elimination engendered by the tautomerisation of phenol-cycloxadienone. (3) The intramolecular reaction between OH in hydroxypropanediyl bridges and the ortho-Br also releases CH_3Br, but amount of this species is smaller than that of CH_4. As the discharge of HBr declines prior to 378 °C, the production of CH_3Br ceases around this temperature. (4) Between 338 °C and 346 °C, the main bromophenol species switch from 2,4,6-tribromophenol to 2,4-dibromophenol, monobromophenols and phenol, as the bottom spectrum in Fig. 3 illustrates minor peaks at 3653 cm^{-1} and 3453 cm^{-1} attributed to the OH groups in 2,6-dibromophenol, and phenol, in that order. Evidently, isopropylidene-phenyl bond [16] commences to cleave off below 346 °C, and the resulting species undergo subsequent debromination.

The gas-phase spectra of Stage 3, recorded at temperatures above 412 °C (not shown), substantiate the disappearance of methane and acetone, and greatly reduced discharge of CO_2, CO, H_2O and HBr. Several of hydroxyaromatic species form, fully or partly debrominated, but the bands are too small for positive identification.

Although, relatively simple to perform, EGA does not separate the gases prior to their analysis, as done by gas chromatography – mass spectrometry (GC-MS). This prevented us from positively identifying propen-1-ol [10], also expected from the decomposition of the residual oxirane. By the same token, EGA did not identify short brominated aliphatics (but for CH_3Br), anticipated to arise as well from the thermal decomposition of F-3020 [10].

While we have no room to show the results from the FTIR-ATR measurements, the solid residue from the partly-pyrolysed F-3020 contains aromatic rings up to 400 °C (1528, 1441 cm^{-1}) and has no *ν*Ar-O and *ν*ArO-C

(1231, 994 cm^{-1}) at this temperature. This suggests the removal of ether oxygens early in the pyrolysis process. We detect no C-Br at 400 °C, with δAr-H barely visible at 734 cm^{-1}. Charring manifests itself by the appearance of peaks at 1596 cm^{-1}, 880 cm^{-1} (ωAr CH), 819 cm^{-1} (ω neighbouring Ar CH) and 752 cm^{-1} due to the bending of out-of-plane CH in substituted aromatics. These features were also reported by Luda et al. [10]. The spectra of neat F-3020 and those reflecting the partly-pyrolysed material, up to 360 °C, involve two peaks around 3563 cm^{-1} and 3351 cm^{-1} assigned to stretching vibration of OH in ArOH (as discussed above) and in hydroxypropanediyl bridges. No detection of these bands at 400 °C concurs with the cession of acetone emission, observed in the high-temperature FTIR-EGA spectra.

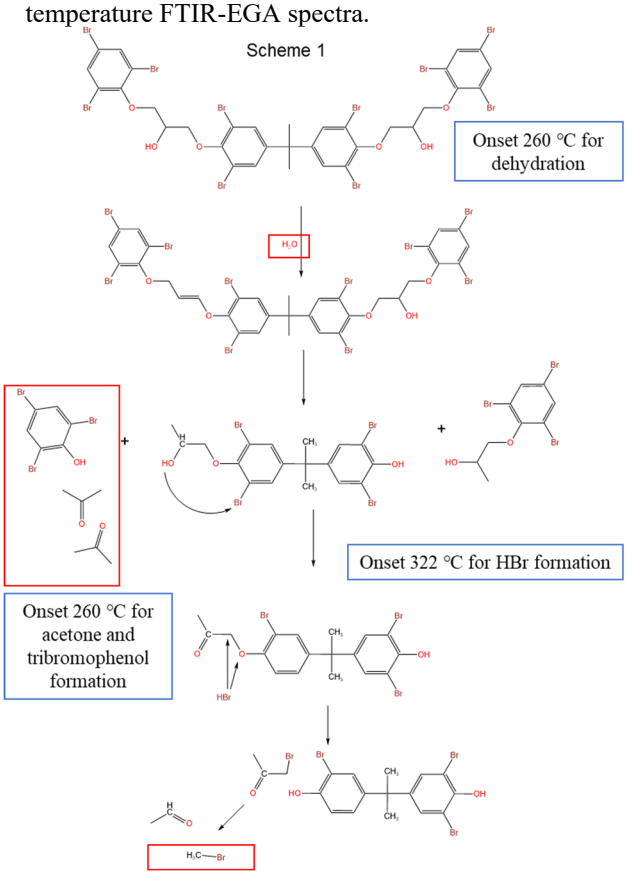

Scheme 1. Decomposition mechanism of neat F-3020 based on the species detected (black boxes) through FTIR in the evolved gases.

4. Conclusions

The results presented in this contribution demonstrate expediency of TGA, DSC and FTIR-based techniques (EGA and ATR) for identifying the key mechanistic features of the thermal decomposition of brominated flame retardants. The end-capped F-3020 is more stable to thermal breakdown by about 25 °C than the diglycidyl terminated oligomers of TBBPA studied by Luda et al. [10]. We observed minor peaks due to residual oxirane in the IR spectrum of the neat F-3020, and detected acrolein, but not propen-1-ol in the evolved gases. The key bromine-containing species included brominated phenols, bisphenols or their fragments, CH_3Br and HBr. Large amounts of methane and acetone arise from rearrangements of hydroxypropanediyl bridges. The maximum rate of pyrolysis occurs at 360 °C and char forms by 600 °C.

5. References

[1] B. Riise Recovering Plastics from Electronics Waste, in *Energy Technology 2020: Recycling, Carbon Dioxide Management, and Other Technologies,* Chen X et al. Editors, Springer Link, 295-306 (2020).

[2] V. Forti, C.P. Balde, R. Kuehr, G. Bel, *The Global E-waste Monitor 2020: Quantities, Flows and the Circular Economy Potential*, UNU/UNITAR/ITU/ISWA (2020).

[3] P. Das, J.-C.P. Gabriel, C.Y. Tay, J.-M. Lee, Chemosphere 269 (2021) 129409.

[4] C. Jia, P. Das, I. Kim, Y.-J. Yoon, C.Y. Tay, J.-M. Lee, J Ind Eng Chem (2022).

[5] M.A. Charitopoulou, K.G. Kalogiannis, A.A. Lappas, D.S. Achilias, Environ Sci Pollut Res 28 (2021) 59190-59213.

[6] J. Song, J. Wang, J. Sima, Y. Zhu, X. Du, P.T. Williams, Q. Huang, Chemosphere 338 (2023) 139535.

[7] M. Solis, S. Silveira, Waste Manage 105 (2020) 128-138.

[8] X. Yang, L. Sun, J. Xiang, S. Hu, S. Su, Waste Manag 33 (2013) 462-473.

[9] ICL Group, https://www.icl-ip.com/f-3020/ (accessed Oct 2023).

[10] M.P. Luda, A.I. Balabanovich, M. Zanetti, J Anal Appl Pyrol 88 (2010) 39-52.

[11] F. Barontini, K. Marsanich, L. Petarca, V. Cozzani, Ind Eng Chem Res 43 (2004) 1952-1961.

[12] C.O. Ojo, A.A. Aguilar-Morones, V. Murthy, S.N. Thennadil, S. Levchik, J. Tenney, B.Z. Dlugogorski, ACS 2023 (submitted)

[13] S.V. Levchik, E.D. Weil, Polym Int 53 (2004) 1901-1929.

[14] Y.-R. Luo, *Handbook of Bond Dissociation Energies in Organic Compounds*, CRC Press LLC2003.

[15] M. Blazsó, Z. Czégény, C. Csoma, J Anal Appl Pyrol 64 (2002) 249-261.

[16] M.P. Luda, A.I. Balabanovich, A. Hornung, G. Camino, Polym Adv 14 (2003) 741-748.

Fundamentals and New Concepts Paper 1
B. Z. Dlugogorski and A. R. Masri, Eds

Towards Clean Combustion and Decarbonisation
Proceedings of the Australian Combustion Symposium
26 – 29 November 2023, Darwin, Northern Territory, Australia

Particle residence time measurements in a flash reactor

X. Bi[1,2,*], E. W. Lewis[1,2], G. J. Nathan[1,2] and Z. Sun[1,2]
[1]Centre for Energy Technology, The University of Adelaide, SA 5005 Australia
[2]School of Electrical and Mechanical Engineering, The University of Adelaide, SA 5005 Australia

Abstract

The particle residence time distribution, $E(t)$, was measured in a lab-scale flash reactor for a pulse of particles added to a continuous jet issuing into a counter flow at room temperature. The measuring range is from the jet exit to two different downstream locations (x/d_{exit} = 62 and 124) for a series of systematically varied initial flow conditions ($\overline{U}_j/\overline{U}_c \approx 31 - 636$ for a constant $\overline{U}_c$ = 0.008 m/s and $\overline{U}_c/\overline{U}_j \approx 0.016 - 0.517$ for a constant $\overline{U}_j$ = 0.248 m/s, where $\overline{U}_j$ is the jet flow velocity and $\overline{U}_c$ is the counter flow velocity). The measurements were performed using light absorption of continuous laser beams positioned at the three aforementioned locations to allow the derivation of $E(t)$ for the two measuring ranges both starting from the exit plane. The $E(t)$ has been evaluated for the 1st and 60th percentiles, $\tau_{p,1}$ and $\tau_{p,60}$, respectively, which characterise the leading edge and the bulk flow. It was found that the characterised particle residence time has a non-monotonic relationship with the normalised jet velocity, with the values of $\overline{U}_j/\overline{U}_c$ for their ($\tau_{p,1}$ or $\tau_{p,60}$) minimum values increasing as the x/d_{exit} decreases. This is deduced to be associated with the effect of particle "group" reducing aerodynamic drag for bulk particles, while this effect can be minimised by sufficiently high jet velocity. Counter flow was found to broadly increase the particle residence time, although its effect is strong for downstream locations, while weak for the upper stream. Industrial-scale particle-based systems need to consider these different flow regimes to optimise design.

Keywords: residence time distribution, particle-laden flow, and flash reactor

1. Introduction

The residence time distribution (RTD) of particles through a reactor is a critical criterion characterising the overall performance of systems, such as thermal-chemical reactions and solid mixing in fluidised beds [1, 2], microchannels [3], solar particle reactors [4] and flash reactors [5]. The RTD of particles has been introduced to describe the probability function of the residence time of particles within a region of interest and operating conditions. However, this function is challenge to measure because it cannot be derived directly from local measurements of velocity and because of the challenges of performing any in-situ measurements in high temperature industrial reactors. The processes within them are complex, involving multi-mode heat and mass transfer that is non-linearly coupled with particle and fluid dynamics, and an inaccessible environment for most of the available measuring techniques [6]. Therefore, there is currently a lack of reliable measurements providing data for such systems, in turn inhibiting the processes of optimisation, upscaling and design. The overall aim of this work is to meet this need through developing and applying a method to reliably measure RTD within an industrially relevant, lab-scale reactor.

Flash reactors employing particle-laden flows are widely used in industry for high temperature processes such as ironmaking, alumina and cement calcination [7-9]. One type of these reactors consists of a vertical chamber with a set of inlets at the top to feed raw material, through which particles fall under the influence of gravity, and outlets at the base to collect processed product. The simplicity of this device also makes it relevant to model validation, and hence will also support the development of other types of more complex reactor.

The challenges of measuring RTD in particle flow reactors have led to previous measurements. Early work was typically performed using different types of tracers [1]. Despite the usefulness of this method in providing data of relevance to particles that are sufficiently small to approach perfect flow tracers or identical to main particles in the flow, it is unable to account for two-phase effects. More recently, Davis *et al.* [4] developed a method in which a small burst of particles was introduced into a steady-flowing gas stream as both the tracer and the medium being traced. This is an important development in that it accounts for two-phase flow effects, albeit it being limited to dilute phase regime. Nevertheless, those measurements were limited to inflow and outflow through a swirling reactor, so there is a need to extend this to provide better understanding of in-situ distributions through jet-like flow reactors, whose flow-fields are better understood.

To meet this need, the present investigation aims to improve understanding the RTD of particles through a well characterised, lab-scale jet-flow environment that is both directly relevant to a particular class of flash reactor and also well suited to the development and validation of numerical models. This is performed for a systematically varied series of particle inlet and internal reactor flows.

2. Experimental Approach

Figure 1 presents the experimental arrangement used to allow optical measurement of the RTD of the pulse of particles through a lab-scale flash reactor at room temperature. The reactor body is a vertically-aligned acrylic pipe with inner diameter d_{pipe} = 190 mm, with a coaxial stainless-steel pipe jet of exit diameter d_{exit} = 10.2 mm used to feed particles from the top of the system.

* Corresponding author:
Phone: (+61) 452 480 427
Email: xiaopeng.bi@adelaide.edu.au

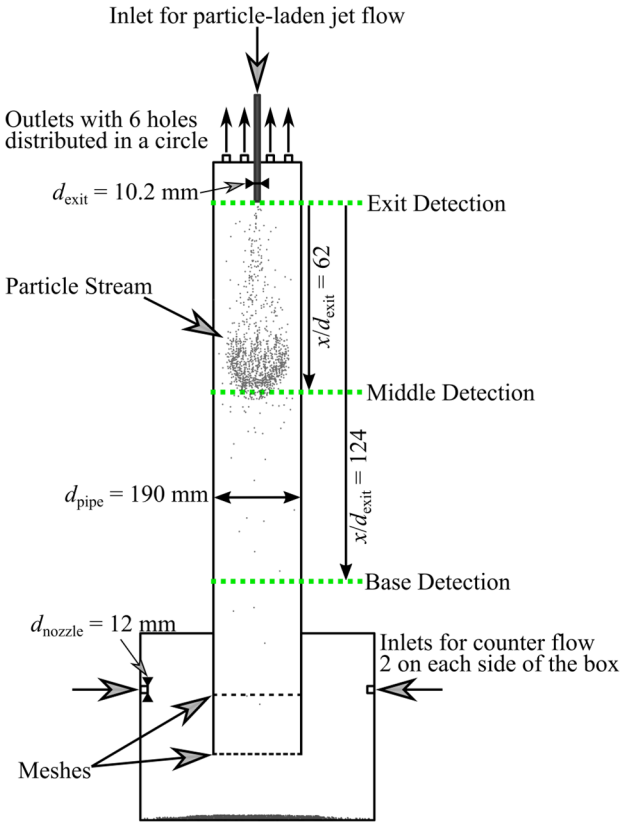

Figure 1. Experimental arrangement with three levels of optical detection to determine the particle residence time distribution for a pulse particle-laden jet flow in a lab-scale flash reactor. The particle flow is injected with compressed air from a top central tube, while a counter flow is supplied and evenly distributed by eight nozzles symmetrically positioned at each side of the cubic wall of a bottom box.

Particles were released into a continuous flow of carrier air via a ball valve, to generate a pulse of particles within a continuous jet. The particles issue downward to an upward (counter) flow of air supplied from eight nozzles (d_{nozzle} = 12 mm) evenly distributed on the side walls of a plenum, which also doubles as the particle collection box. Two mesh screens were used at the bottom section of the rig with eight mesh cups covering the inlets of the counter flow to generate a spatially uniform counter flow

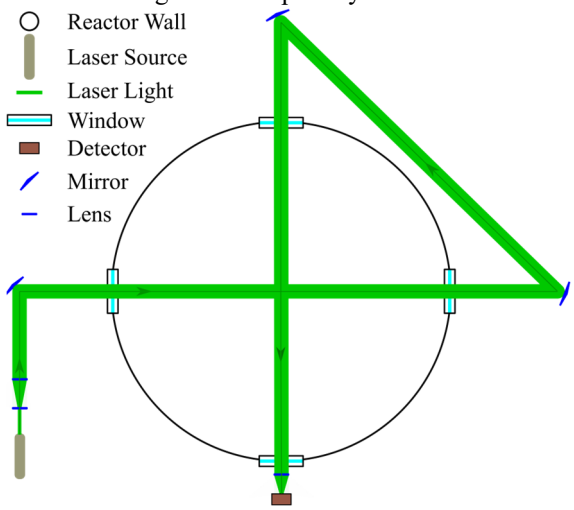

Figure 2. Optical arrangement detecting particle signals for deriving particle residence time distribution. The laser beam is arranged to cross the reactor centerline twice to detect the bulk flow of dispersed particles. Note that the exit detection channel only consists of a single beam as it is sufficiently large to cover the jet exit.

within the system. Separate mass flow controllers were used to control the flow rates through the jet and counter flow, to provide bulk velocities in the range 0.248 m/s ≤ $\bar{U}_j$ ≤ 5.101 m/s and 0.008 m/s ≤ $\bar{U}_c$ ≤ 0.128 m/s, respectively. PMMA particles (microbeads spheromers) with density of 1200 kg/m^3, particle diameter $\bar{d}_p$= 80 μm and bulk volume of 0.5 mL were used for each pulse of particles.

Figure 2 presents the optical arrangement used to transmit the laser through each of the measurement planes to detect the passage of the pulse of particles. These were arranged at the three downstream distances (x) from the jet exit plane, x/d_{exit} = 0, 62 (middle) and 124 (base). All of the optical parts were mounted to an external aluminium frame around the main rig.

A continuous 532 nm laser beam (Thorlabs CP5532), with a beam power of ~ 4.5mW was expanded to provide a collimated beam of ~ 20 mm diameter. This laser beam was double crossed at the centre of the reactor by a series of optical mirrors to extend the beam path length used for particle signal detection. At the end of the beam path, a light detector (DET100A2) was used to continuously detect the intensity of the laser light beam during the measurement. Note that this arrangement of double laser beam was only applied to the middle and base detection channels, while the exit detection used a single laser beam, with all the other settings same as the double beam arrangement. This is because the cross-sectional area of a single beam is sufficiently large to detect the whole exit of the particle discharge tube.

The RTD of particles was derived using the well-known convolution-deconvolution method [4, 6, 10, 11]. This method assumes the outlet concentration of particles is the result of convolution of the inlet particle concentration with the particle RTD within this section. The equation is given as follows,

$$o(t) = i(t) * E(t) = \int_0^t i(t-t')E(t')dt', \qquad (1)$$

where, i(t) and $o(t)$ are the inlet and outlet particle concentration as a function a time for a certain study region, and $E(t)$ is the RTD of particles within a reactor. A fast Fourier transform was performed on the measured particle signals that are intensity-based particle concentration to derive the $E(t)$ for the distance between detection channels, i.e., x/d_{exit} = 0 ~ 62 and 0 ~ 124.

3. Results and Discussion

Figure 3 presents a typical measurement of the temporal profile of particle signal distribution, normalised by area, calculated from the light extinction measurement for the flow with $\bar{U}_j$ = 1 m/s and $\bar{U}_c$ = 0.008 m/s. A narrow temporal distribution can be identified for the exit (0 ~ 1 s), while it spreads for the base (1.1 s ~ 6.7 s). This indicates that the initial particle pulse disperses gradually through the system.

It can be also seen from Fig. 3 that the detected particle signals are highly skewed, with a rapid rise followed by a lower decay rate (the tail). This is because the leading-edge particles are densely laden due to the high initial

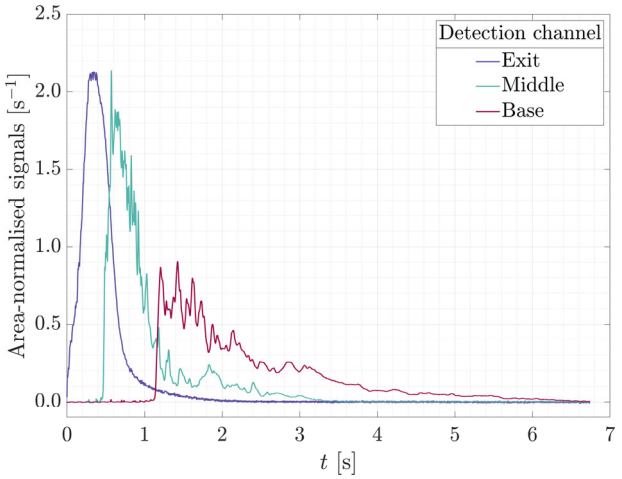

Figure 3. Measured particle signals in the time domain for three levels of detection. Here, $\bar{d}_p$ = 80 µm, $\bar{U}_j$ = 1 m/s, $\bar{U}_c$ = 0.008 m/s.

volume fraction when the pulse is introduced and the high gradient in number density, followed by a long wake. This non-linear phenomenon has been explained with a detailed force balance in a study of free-falling particle flows [12], that include the formation of a particle "group" at the front where drag mainly acts on the exterior side due to the short particle-particle distance within the bulk particles, and a discrete particle "tail" due to turbulent wake (see Fig. 1). The difference in the decay and rising rate of particle signal becomes more significant with downstream distance as a result of the integration of these effects with time and distance.

Figure 4 presents the particle residence time distribution $E(t)$ that is derived using the convolution-deconvolution method in Eq. (1). These are consistent with their corresponding area-normalised particle signals. This implies that the temporal profile of particle signal at the exit level from a near-perfect plug flow (Fig. 3), has only a small effect on the profile of $E(t)$. The sharp rise of the $E(t)$ indicates that the peak concentration occurs ~ 0.1 s after the leading edge of particles, with trailing particles passing up to ~ 3 s later.

Figure 5 presents statistical measures of the cumulative $E(t)$ including $\tau_{p,1}$ and $\tau_{p,60}$ as a function of a

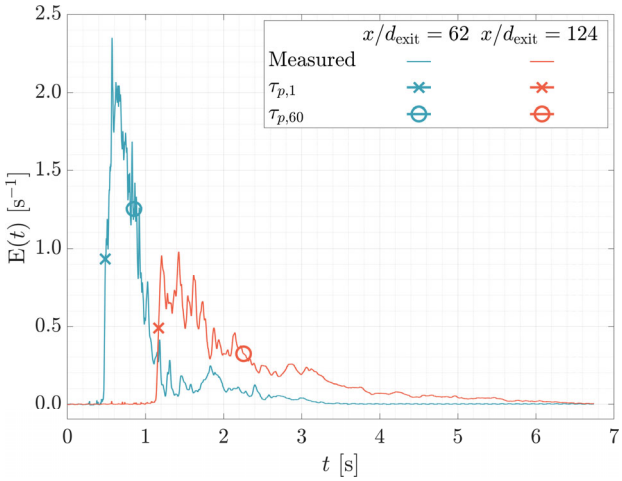

Figure 4. Particle residence time probability distribution, $E(t)$, from the jet exit to x/d_{exit} = 62 and 124 with markers identifying the 1% and 60% cumulative $E(t)$, denoted by $\tau_{p,1}$ and $\tau_{p,60}$, respectively. Here, $\bar{d}_p$ = 80 µm, $\bar{U}_j$ = 1 m/s, $\bar{U}_c$ = 0.008 m/s.

series of normalised $\bar{U}_j$ and $\bar{U}_c$ for x/d_{exit} = 62 and 124. These corresponding to 1% and 60% values of the cumulative $E(t)$ function, namely $\tau_{p,1}$ and $\tau_{p,60}$, defined as $\int_0^{\tau_{p,1}} E(t)dt = 0.01$ and $\int_0^{\tau_{p,60}} E(t)dt = 0.6$, respectively. Both $\tau_{p,1}$ and $\tau_{p,60}$ at x/d_{exit} = 124 are greater than twice that of x/d_{exit} = 62 for all subfigures, demonstrating that the particles generally decelerate between the two falling distances. This is because particle-air interaction is expected to increase with downstream distance as particles continuously disperse, reducing the "group" effect, while the axial counter flow distribution is relatively uniform, impeding the particle fall. The error bar based on one standard deviation calculated from five repetitions is shown. This provides confidence in the repeatability of the measurement.

Figure 5 (a) presents a plot of the dependence of that $\tau_{p,1}$ and that $\tau_{p,60}$ on the velocity ratio of jet to counter flow $\bar{U}_j$ /$\bar{U}_c$ at two downstream locations. It can be seen that $\tau_{p,1}$ for x/d_{exit} = 62 decreases monotonically with an increase in $\bar{U}_j$ as expected because an increase in initial velocity will reduce the time needed for particles to move through the pipe. However, further downstream at x/d_{exit} = 124, the trend is non-monotonic. After the initial decrease from $\tau_{p,1}$ = 2.36 s to 1.13 s for $\bar{U}_j$ = 0.248 m/s and 1.996 m/s, respectively, $\tau_{p,1}$ then increases for $\bar{U}_j$ = 3.5 m/s and 5.1 m/s to $\tau_{p,1}$ = 1.32 s and 1.76 s. A plausible explanation is that velocity is sufficient to cause a decrease in the aforementioned particle "group" effect, thereby inducing greater particle-air interaction, increasing the $\tau_{p,1}$. This phenomenon can be also observed for $\tau_{p,60}$ for both falling ranges. While the trends in all data sets are broadly consistent, the value of $\bar{U}_j/\bar{U}_c$ for the minimum defined particle residence time can be seen to increase with the decrease in distance, and may even be beyond the range of present data for the $\tau_{p,1}$ at x/d_{exit} = 62. That is, for this case, the value of $\bar{U}_j/\bar{U}_c$ for the minimum $\tau_{p,1}$ may locate outside the current scope of the velocity ratio, potentially indicating a strong particle "group" effect for particles that $\tau_{p,1}$ characterises. This is consistent with $\tau_{p,1}$ characterises the leading edge of the pulse of particles, whilst $\tau_{p,60}$ characterises the bulk flow behaviour. However, more data is needed to better understand these effects, particularly the influence of all of these parameters on the particle "group".

Figure 5 (b) shows that the counter flow extended the particle residence time at all studied falling distances, as expected. This is because the counter flow generates upwards air momentum impeding particle fall. For x/d_{exit} = 124, $\tau_{p,60}$ can be increased by 140% when $\bar{U}_c/\bar{U}_j$ is increased from 0.016 to 0.517. This effect is only weak for $\tau_{p,1}$ of x/d_{exit} = 62, plausibly due to the top section is still in the jet momentum influential region and particles at the leading edge in this region are self-dominated by particle momentum.

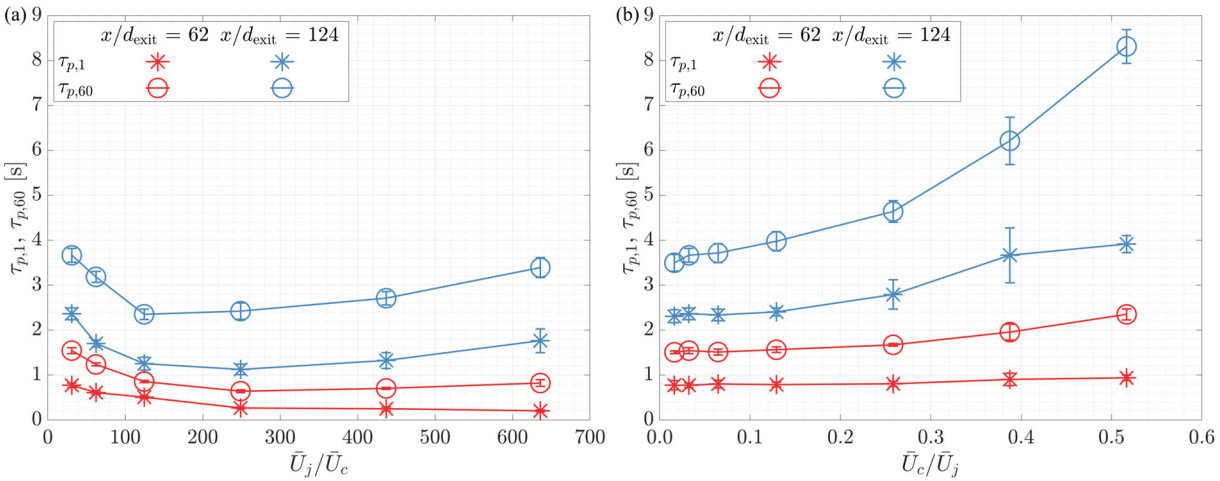

Figure 5. The statistical measures of particle residence time for x ranges of 0 - 0.63 m and 0 - 1.26 m under different flow conditions. The influence of normalized jet flow velocity on 1% and 60% cumulative $E(t)$ is presented in (a) with a constant $\bar{U}_c$ = 0.008 m/s, while (b) shows the effect of normalized counter flow velocity on them with a constant $\bar{U}_j$ = 0.248 m/s. Particle diameter is kept constant with $\bar{d}_p$ = 80 µm.

4. Conclusions

New insights of the effects of the jet flow and counter flow on the particle residence time of a pulse particle flow between particle exit to two different downstream locations (x/d_{exit} = 62 and 124) in a confined lab-scale flash reactor have been provided. The $\tau_{p,60}$ (characterise the bulk particle flow) of x/d_{exit} = 62 and 124, and $\tau_{p,1}$ (characterise the leading-edge particles) of x/d_{exit} = 124 were found to be non-monotonically dependent on the normalised jet velocity with the values of $\bar{U}_j/\bar{U}_c$ for their ($\tau_{p,1}$ or $\tau_{p,60}$) minimum values increasing as the x/d_{exit} decreases. The $\tau_{p,1}$ of x/d_{exit} = 62 was found to be monotonically dependent on the $\bar{U}_j/\bar{U}_c$ possibly because the jet velocity used in the present study was not sufficient to break their "group" effect, which is deduced to be responsible for the trend of the characterised particle residence time. However, more work is needed to better understand and confirm the controlling influences. Counter flow was found to broadly increase the particle residence time, although its effect is strong for downstream locations, while weak for the upper stream. For other industrial systems employing particle flows, this work suggests a direct in-situ measurement of flow field is important for understanding the efficacy of relevant parameters in engineering processes.

5. References

[1] A. Harris, J. Davidson and R. Thorpe, Chem. Eng. Sci. 58 (11) (2003) 2181-2202.

[2] K. Chen, P. Bachmann, A. Bück, M. Jacob and E. Tsotsas, Powder Technol. 345 (2019) 129-139.

[3] S. Chen, Q. Lin, N. Pan, M. Hao, Y. Jiang, Y. Xie, Y. Ba, X. Bian and K. Liu, Phys. Fluids 35 (8) (2023).

[4] D. Davis, M. Troiano, A. Chinnici, W.L. Saw, T. Lau, R. Solimene, P. Salatino and G.J. Nathan, Chem. Eng. Sci. 214 (2020) 115421.

[5] S. Xiu, Z. Li, B. Li, W. Yi and X. Bai, Fuel 85 (5-6) (2006) 664-670.

[6] P.V. Danckwerts, Chem. Eng. Sci. 50 (24) (1995) 3857-3866.

[7] F. Chen, Y. Mohassab, T. Jiang and H.Y. Sohn, Metall. Mater. Trans. B 46 (1) (2015) 1133-1145.

[8] J.R. Fernandez, S. Turrado and J.C. Abanades, Reaction Chemistry & Engineering 4 (12) (2019) 2129-2140.

[9] A. Kontopoulos, K. Krallis, E. Koukourakis, N. Denaxas, N. Kostis, A. Broussaud and O. Guyot, Appl. Therm. Eng. 17 (8-10) (1997) 935-945.

[10] Y. Gao, F.J. Muzzio and M.G. Ierapetritou, Powder Technol. 228 (2012) 416-423.

[11] A.H. Essadki, B. Gourich, C. Vial and H. Delmas, Chem. Eng. Sci. 66 (14) (2011) 3125-3132.

[12] Y. Wang, X. Ren, J. Zhao, Z. Chu, Y. Cao, Y. Yang, M. Duan, H. Fan and X. Qu, Powder Technol. 292 (2016) 14-22.

Fundamentals and New Concepts Paper 2
B. Z. Dlugogorski and A. R. Masri, Eds

Towards Clean Combustion and Decarbonisation
Proceedings of the Australian Combustion Symposium
26 – 29 November 2023, Darwin, Northern Territory, Australia

Characterisation of a long-distance microscope lens for shadow imaging of 80-250 μm diameter particles

E. W. Lewis[1, *], G. J. Nathan[1] and Z. Sun[1]
[1]School of Electrical and Mechanical Engineering, University of Adelaide, SA 5005 Australia

Abstract

Particle shadow imaging using a long-distance microscope lens has been shown to provide high-resolution imaging of particles with diameters in the range of 80-250 μm. The sharpness of the particle image was analysed for these particles at a series of distances from the focal plane, for two different lens magnifications. The particle image quality was seen to change significantly with particle material, shape, and magnification. The depth-of-field of the image was then shown to be able to be defined using a threshold of the two-dimensional gradient of the image intensity, with a resultant depth of field calculated to be 0.5 mm and 2 mm for a resolution of 1.4 and 5.4 μm per pixel, respectively.

Keywords: optical techniques, experimental, particle-laden flow

Nomenclature

ϕ_v – Particle volumetric loading (-)
$\dot{V}_p$ – Volumetric flow rate of particles (m^3/s)
$\dot{V}_f$ – Volumetric flow rate of fluid (m^3/s)
d_p – Particle diameter (m)
WD – Working distance from lens to particle (m)
I – Intensity detected by camera (counts)
G – 2-dimensional gradient of camera intensity ($pixel^{-1}$)
G_{Lim} – Calculated threshold for gradient ($pixel^{-1}$)
x, y, z – Co-ordinate system

1. Introduction

Flows laden with solid particles are found in many high-temperature industrial systems, such as calciners for mineral processing in which the particles react to form a useful product [1] and as solid fuels for combustion [2]. The particle-fluid interactions in such systems is highly complex with the flow typically having strong velocity and temperature gradients, which are challenging to resolve numerically or measure accurately. Furthermore, spatial variations in the particle size, shape, and number density can significantly affect the local flow conditions. In a reactor, these complexities are compounded by coupling between the two phases, with particles adsorbing or releasing energy by radiation and convection, and with gases being released by, or adsorbed by, the particles in certain temperature ranges.

Industrial particle-laden systems commonly operate with high particle volumetric loadings ($\phi_v > 10^{-4}$), where $\phi_v = \dot{V}_p/\dot{V}_f$, $\dot{V}_p$ and $\dot{V}_f$ are the respective particle and fluid volumetric flow rates. Consequently, it is challenging to isolate individual particles for measurements of velocity, particle size, and concentration. The commonly used particle scattering measurements require a known or constant local light flux for reliable measurement of particle size and number density. The combined influences of multiple scattering, attenuation, signal trapping, and background interference present in densely loaded flows leads to significant uncertainty in such measurements [3].

These interferences can be dramatically reduced using the method of shadow imaging, although the measurement with a conventional arrangement is integrated over a relatively long path length. Resultantly, the method is susceptible to the alternative interference from overlapping shadows on a common optical path [4]. Digital holography for particle imaging utilises the interference patterns generated by the combination of coherent light from a reference source and the particles, however the particle detection is limited to systems with sufficiently low particle volumetric loadings to avoid significant overlap of the fringe patterns [5, 6].

The influence of overlapping particles can alternatively be mitigated using a long-distance microscope lens by utilising the narrow depth of field in which particles are sharply imaged, together with image processing to reject particles outside of the focal plane [7]. This method has been shown to provide high-resolution imaging of particles from 1-1000 μm with a depth dimension of approximately 0.5mm [4, 8]. However, little information is available of the details of the parameters that control the spatial resolution in this technique.

To meet this need, the present paper presents a systematic characterisation of resolution from a long-distance microscope lens for particle detection and image depth-of-field. Images were recorded for a series of particle diameters, working distances, fields-of-view, and particle positions relative to the focal plane.

Method

The particle shadow imaging was performed using a long-distance microscope lens (Questar QM1) attached to a PCO.2000 CCD camera. Particles were adhered to the surface of a glass plate, as presented in the arrangement in Figure 1. The particles investigated were

* Corresponding author:
Email: elliott.lewis@adelaide.edu.au

of two types, namely: 1) monodisperse plastic (PMMA) spheres (microbeads spheromers) with diameters of 80 and 250 µm (1 standard deviation of approximately 10%), which are partially transparent, and 2) aluminosilicate ceramic (Carbo) particles with a mean diameter of 160 µm and a sphericity of approximately 0.9, which are opaque.

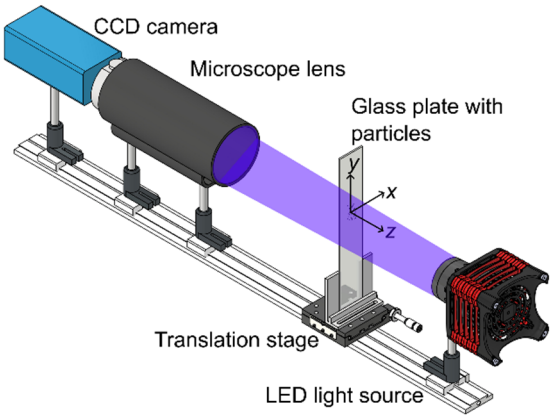

Figure 1: Arrangement used to characterise particle imaging for a series of distances from the focal plane.

Illumination was provided by a high-power LED array (Thorlabs SOLIS 445 nm) with a pulse width set to be 10 µs, similar to what is required for typical velocity measurements for flows with expected velocities <10 m/s. The glass plate was mounted to a translation stage, to allow fine control of the distance between the particles and focal plane of the image. The position of the focal plane was determined to within about ±0.3mm by eye, following which images of particles on the plate were then captured for a series of distances of -8 mm < z < 8 mm from this position to assess the depth-of-field of the camera for particle imaging. Two different working distances (WD) were investigated: 1) WD = 1150 mm with no additional zoom lens, with a resultant field-of-view of 11 mm, resolution of 5.4 µm per pixel, and F-number of ~14, and 2) WD = 560 mm with an additional 2× Barlow lens, with a resultant field-of-view of 2.8 mm, resolution of 1.4 µm per pixel, and F-number of ~8.4.

Image processing:

- Dark-charge (DC) images were collected with the lens cap on. The time-averaged dark charge intensity was subtracted from all subsequent images.
- Time-averaged reference background (BG) images were collected under the same

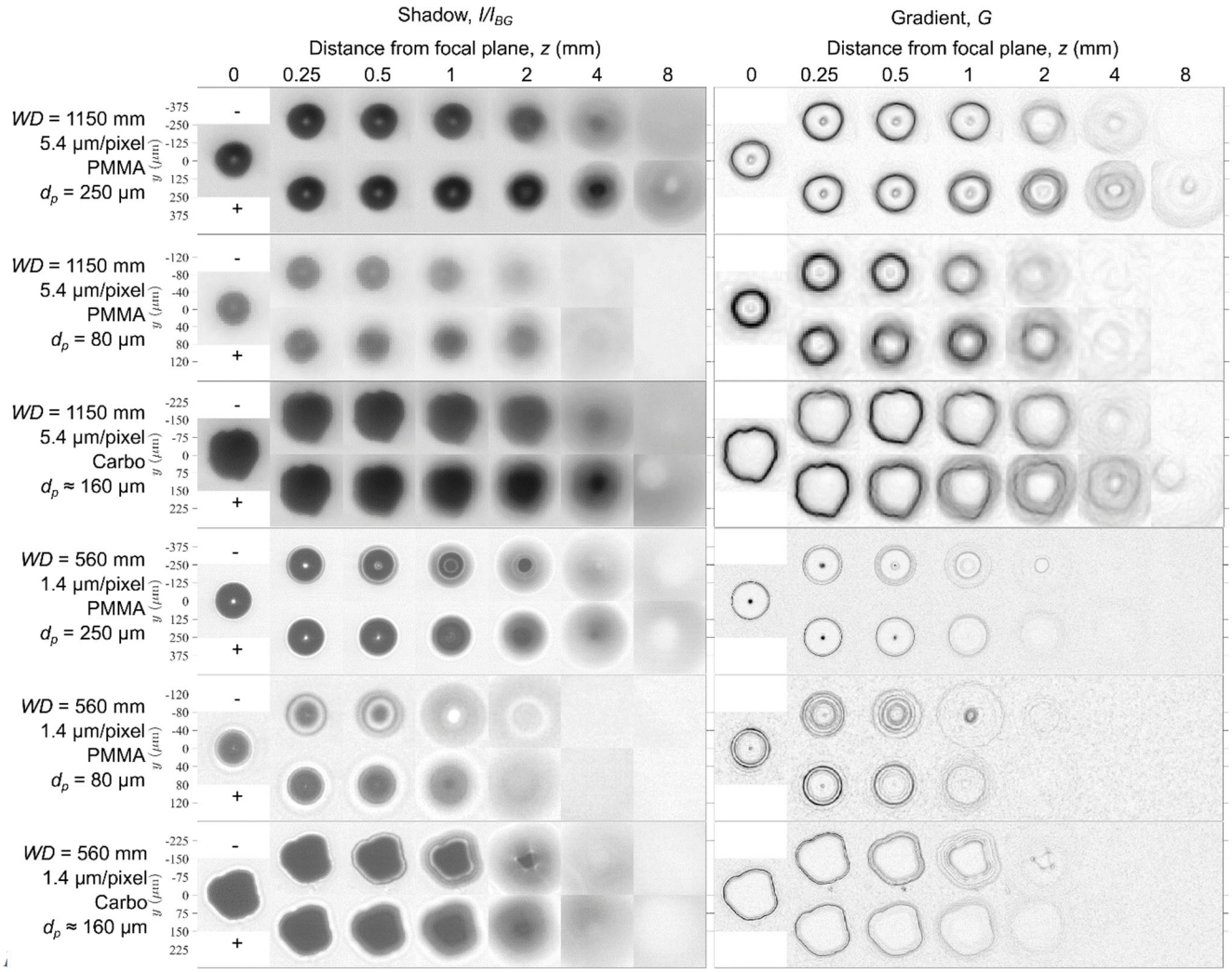

particle diameters (d_p), and particle materials investigated.

conditions as the experiment with no obstructions between the LED and lens.
- The relative shadow intensity was then calculated using the ratio of the instantaneous DC-corrected shadow and background images.

Results

Figure 2 presents the shadow image (left) and calculated two-dimensional gradient intensity (right) for a series of individual particles as they are translated through the range -8 < z < 8 mm. Images are presented for each particle investigated at the working distances of 1150 and 560 mm. The particle image can be seen to change significantly with the distance from the focal plane, with a decrease in both intensity and gradient with increasing $|z|$.

The sharpness of the images can also be seen to reduce with distance from the focal plane, consistent with previous work. The d_p = 80 µm particles imaged at WD = 560 mm can be seen to be only sharply focussed within a region of z = ± 0.5 mm, with differences between these images and z = 0 mm suggesting that it may be possible to reduce this depth resolution further.

Each of the spherical PMMA particles has a bright spot on the centre of the particle, attributed primarily to the diffraction of light by the particle. Additionally, diffraction patterns are imaged around the outside edge of the particles as they move out of focus. These patterns are stronger for the particles closer to the camera than those away from it. This is particularly evident for the small-FOV case with a resolution of 1.4 µm per pixel, and can also be seen around the edge of the non-spherical, opaque carbo particle. The presence of diffraction patterns is strongly dependent on the distance between the LED light source, particle, and detector, as well as the alignment of the light source with the detector. The greater the distance between the LED and detector, the closer the illumination that is detected becomes to a point source. Further systematic analysis is required to fully understand the effect of LED position on the shadow and diffraction reaching the camera.

The depth-of-field in which particles are identified can be varied by using different thresholding values for the gradient and shadow intensity. The apparent depth-of-field in which particles are sharply imaged can be seen to increase with increasing working distance, consistent with expectation, as well as with increasing particle diameter. Therefore, for systems where a narrow depth resolution is required (e.g., flows with strong spatial gradients), a shorter working distance should be preferred, with the trade-off being a smaller field-of-view.

Figure 3 presents a cross-section of the shadow intensity and gradient for the d_p = 80 µm particle imaged at WD = 560 mm, for a series of values of z. The intensity detected by the camera can be seen to decrease by up to half in the darkest regions of shadow when the particle is in focus, with a sharp increase towards the background value beyond the particle boundary. The regions of strong gradient on the particle edge correspond closely to the average particle diameter measured using a Malvern Mastersizer, as indicated by the vertical dashed lines.

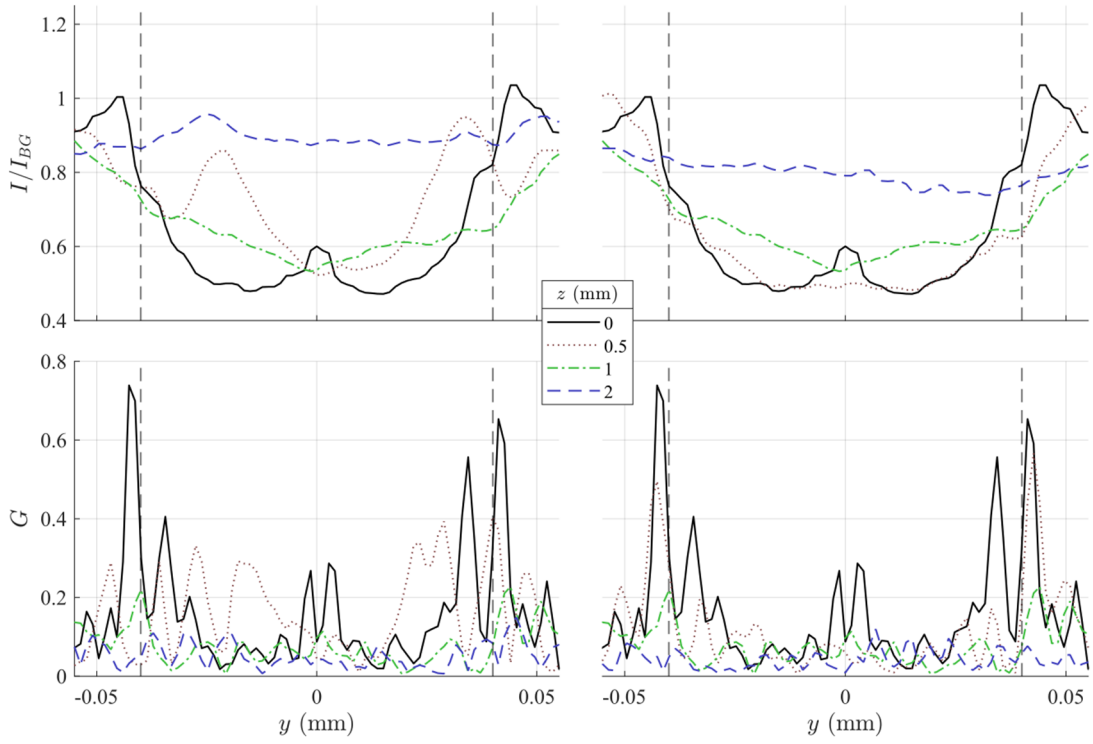

Figure 3: The image intensity I/I_{BG} (top) and gradient G (bottom) through the centre of a single 80 µm particle imaged with a WD = 560 mm, for a series of distances from the focal plane (z). The vertical dashed lines indicate the average diameter of the particles.

Figure 4 presents an example of a gradient intensity calculation, which could be used as a threshold for

particle detection, as a function of the distance from the focal plane. The edge-of-particle gradient, G_{Lim}, was defined here by the minimum gradient measured within a one-pixel thick particle edge in a square region ($2d_p \times 2d_p$) around the particle. (This is the same area around the particles that is presented in the individual tiles of Figure 2). That is, the intensity was calculated from $G_{Lim} = quantile(G, \frac{\pi d_p * 1}{(2d_p)^2})$, with the resultant values of $95 < \frac{\pi d_p}{(2d_p)^2} < 99.5$ calculated for the presented particle diameters. It can be seen that the value of G_{Lim} peaks on the focal plane, decreasing significantly with increasing $|z|$. The decrease is greater for WD = 560 mm than WD = 1150 mm, agreeing with the expectation of a decreasing depth-of-field with the working distance. The resultant depth of field, calculated from values within 80% of the peak, is approximately 0.5 mm and 2 mm for WD = 560 and 1050 mm, respectively. The values of G_{Lim} are also typically non-symmetric about z = 0 mm. This means that thresholds must be carefully selected to measure particles within a pre-defined region.

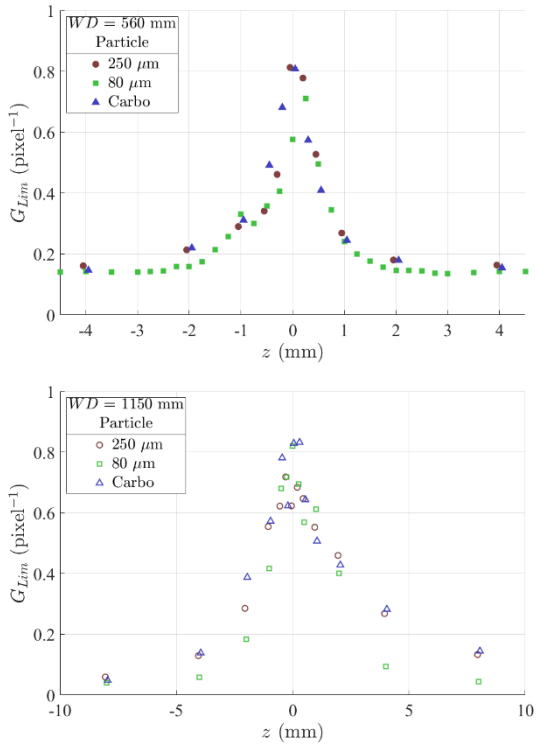

Figure 4: Value of the calculated gradient limit, measured in the square region of side length 2×d_p around a single particle, as a function of distance from the focal plane for the series of particles investigated at WD = 560 mm (top) and WD = 1150 mm (bottom).

Conclusions

Particle shadow imaging using a long-distance microscope lens has been shown to provide high-resolution images for particles with diameter from 80-250 µm. The depth in which particles were sharply imaged was shown to be as little as ±0.5 mm, demonstrating the potential for imaging within densely-loaded flows in which there is strong scattering and attenuation of incident light. For systems where a narrow depth resolution is required, for example measurements in systems with strong spatial gradients, the working distance should be made as short as practical.

The gradient of the shadow has been shown to be a useful measure for identifying the edges of the particle, with the desired depth-of-field for particle detection able to be controlled through careful selection of threshold values. The transparent, spherical PMMA particles and opaque granular Carbo particles displayed significantly different shadow properties, with stronger diffraction patterns seen around the edges of the spherical particles as well as a bright spot on the centre of the particle when in focus. For application in low volumetric loadings these additional diffraction patterns may prove useful for obtaining additional information about particle shape or position, although experience with imaging in densely laden flows suggests that they will tend to be overwhelmed by interference in such environments.

References

[1] F. Williams, H.W. Schmidt, Flash- and CFB calciners, history and difficulties of development of two calcination technologies, 2012, pp. 135-140.

[2] T. Li, C. Geschwindner, A. Dreizler, B. Böhm, Particle-resolved optical diagnostics of solid fuel combustion for clean power generation: a review, Measurement Science and Technology, (2023).

[3] P.A.M. Kalt, C.H. Birzer, G.J. Nathan, Corrections to facilitate planar imaging of particle concentration in particle-laden flows using Mie scattering, Part 1: Collimated laser sheets, Appl. Opt. 46 (2007) 5823-5834.

[4] S. Khodaparast, N. Borhani, G. Tagliabue, J.R. Thome, A micro particle shadow velocimetry (µPSV) technique to measure flows in microchannels, Experiments in Fluids 54 (2013) 1474.

[5] G. Brunnhofer, A. Bergmann, A. Klug, M. Kraft, Design and Validation of a Holographic Particle Counter, Sensors (Basel) 19 (2019).

[6] U. Schnars, C. Falldorf, J. Watson, W. Jüptner, Digital Holography and Wavefront Sensing: Principles, Techniques and Applications, 2nd 2015 ed., Springer Berlin / Heidelberg, Berlin, Heidelberg, 2014.

[7] S. Han, Z. Sun, Z.F. Tian, T. Lau, G. Nathan, Particle velocity measurement within a free-falling particle curtain using microscopic shadow velocimetry, Opt. Express 29 (2021) 10923-10938.

[8] S. Han, Z. Sun, C. de Jacobi du Vallon, T. Collins, M. Boot-Handford, M.G. Sceats, Z.F. Tian, G.J. Nathan, In-situ imaging of particle size distribution in an industrial-scale calcination reactor using micro-focusing particle shadowgraphy, Powder Technology 404 (2022) 117459.

Fundamentals and New Concepts Paper 3

B. Z. Dlugogorski and A. R. Masri, Eds

Towards Clean Combustion and Decarbonisation
Proceedings of the Australian Combustion Symposium
26 – 29 November 2023, Darwin, Northern Territory, Australia

Influence of flame stability on nanoparticle growth during flame spray pyrolysis

C. M. Kennedy[1,*], Y. Zhang[1], M. J. Dunn[1] and A. R. Masri[1]

[1]School of Aerospace, Mechanical and Mechatronic Engineering, The University of Sydney, Darlington, NSW 2008, Australia

Abstract

This work provides an experimental analysis of nanoparticle agglomeration and growth during flame spray pyrolysis (FSP). The particular novelty of the work lies in relating flame stability regimes to detailed particle characteristics including size and morphology. A rapid thermophoretic sampling device is designed and calibrated in order to extract iron oxide nanoparticle samples from an FSP flame under varying synthesis conditions. The samples are then analysed via transmission electron microscopy (TEM). Sampling at various heights above the burner (HAB) provides the means to segregate zones of primary particle formation, growth and agglomeration. Resultant data regarding these particle regimes is essential input to validate models and can further act as a calibration tool for the application of non-intrusive diagnostics. In addition, the analysis provides novel insight into the influence of flame stability on product particle characteristics.

Keywords: flame spray pyrolysis, thermophoretic sampling, flame synthesis

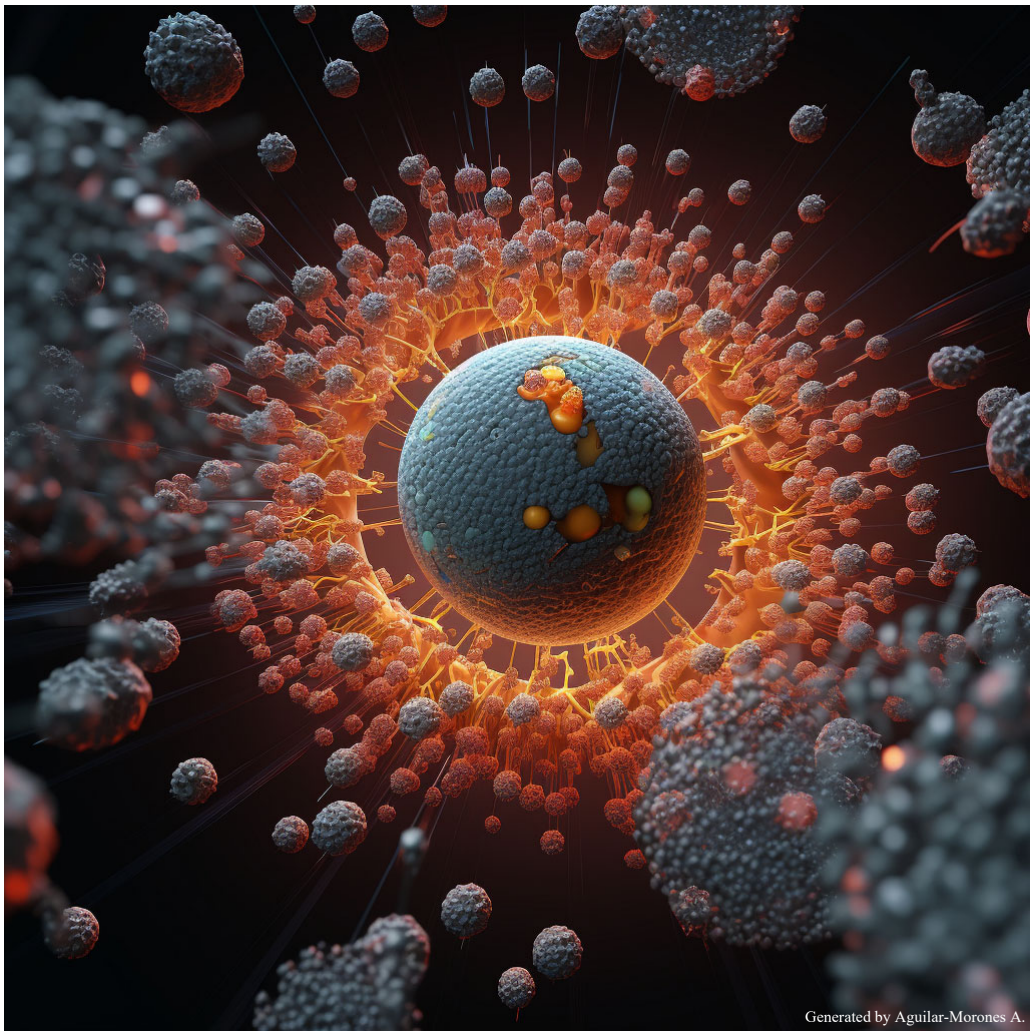

Artistic artificial intelligence images generated were based on the abstract content.

* Corresponding author:
Email: callum.kennedy@sydney.edu.au

Fundamentals and New Concepts Paper 4
B. Z. Dlugogorski and A. R. Masri, Eds

Towards Clean Combustion and Decarbonisation
Proceedings of the Australian Combustion Symposium
26 – 29 November 2023, Darwin, Northern Territory, Australia

Effect of outlet boundary conditions and temperature gradient on the maximum transient growth for linear and nonlinear systems

Xinyu Zhao[1], Dan Zhao[1, *] and Hui Rong[1]
[1]Department of Mechanical Engineering, University of Canterbury, Christchurch 8041 New Zealand

Abstract

Combustion instability is common in propulsion and power generation systems. It manifests as large-amplitude acoustic oscillations and results in undesirable consequences like structural damage, performance deterioration, and even mission failure. This study focuses on the maximum transient growth of acoustic energy in different systems. The model is a straight tube with an acoustically compact heat source and a mean temperature gradient over the heat source. Its inlet is acoustically open and its outlet is acoustically open or closed. The flow disturbance is described by a Galerkin expansion technique and the unsteady heat release is modelled using a modified King's law. Via the linearization of delayed velocity at the heat source, the nonlinear system transforms into the linear-delay and the linear system. With the increased mean temperature gradient, the maximum initial energy growth rises in the open-closed tube and drops in the open-open tube. The maximum initial energy growth of the open-closed tube is higher than that of the open-open tube. For nonlinear systems, with the increased mean temperature gradient, maximum energy growth over a long time becomes higher or its required initial energy becomes lower. Compared to the open-open tube, the initial energy that the open-closed tube requires to retain a high level of acoustic energy after a long time is lower. It may imply that the triggering may be easier to occur under higher mean temperature ratios and the open-closed tube is more sensitive to the triggering than the open-open tube.

Keywords: transient energy growth, linear system, nonlinear system, outlet boundary condition, triggering

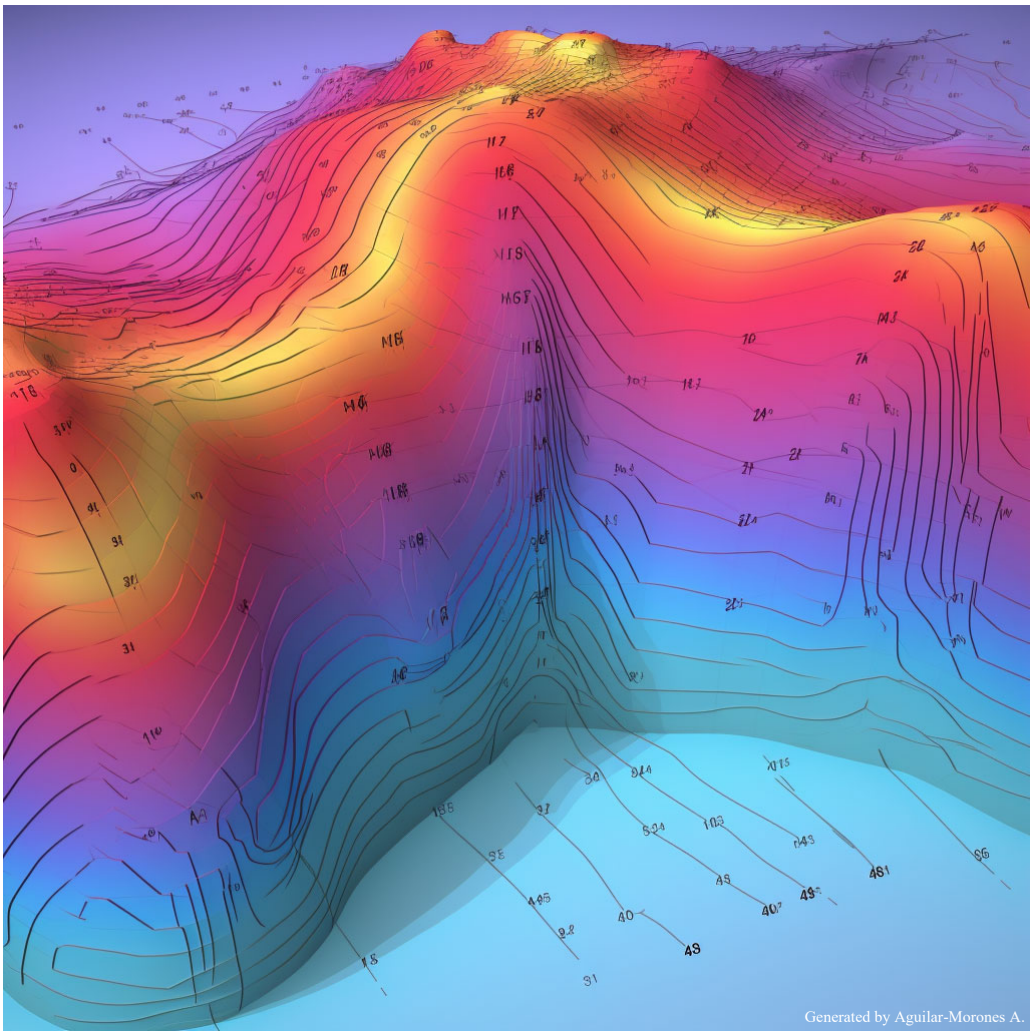

Artistic artificial intelligence images generated were based on the abstract content.

* Corresponding author:
Phone: (+64) 0224550340
Email: dan.zhao@canterbury.ac.nz

Fundamentals and New Concepts Paper 5
B. Z. Dlugogorski and A. R. Masri, Eds

Towards Clean Combustion and Decarbonisation
Proceedings of the Australian Combustion Symposium
26 – 29 November 2023, Darwin, Northern Territory, Australia

Plasma-assisted combustion for aerospace propulsion: A review

Abishek Shrestha[1*]
[1] abishek.stha@outlook.com

Abstract

Combustion plays a significant role in the energy and Aerospace sectors. The push towards electrification of aerospace propulsion in the aviation sector is being made to comply with the environmental goals. However, it will likely take decades to achieve this goal. Meanwhile, the newly growing and promising field of plasma-assisted combustion has grabbed attention to exploring its capability for combustion enhancement and pollution control. Scientists and engineers have carried out numerous investigations and experiments on using this technology in aerospace engines, particularly in the field of aviation engines, aiming to achieve an emission-free sector. The aim of this comprehensive paper is to summarize and discuss the development, and importance of non-thermal plasma to enhance combustion efficiency and emission control for the aerospace propulsion sector. The impact of plasma on different stages of combustion such as ignition, flame propagation, flame stability, and emissions are compiled in the research paper based on findings of prior research in the field. The primary focus of this summary is on the use of plasma-aided technology for air-breathing aviation engines.

Keywords: plasma assisted combustion, propulsion efficiency, aerospace Propulsion, emission control

1. Introduction

1.1 Combustion Overview

In the present energy market, the use of combustion-based systems to extract energy is more than 80%[1, 2]. Attempts are being made to electrify airplanes using highly efficient batteries. However, it will not be feasible in the short term. Because of the high energy density fuel being used in combustion engines and its advantage of being re-fuelled easily, combustion is preferred for Aero-propulsion[2]. Although combustion has played a major role in aerospace vehicle development, it still has a low energy conversion efficiency and has contributed to air pollution and climate change directly[3]. It is estimated that aviation accounts for 2.5% of global (Carbon Dioxide) CO2 emissions and 3.5% of non-CO2 emissions. The latest statistics for (Q1&Q2) the year 2023 show that the global aviation sector including Passenger (Domestic and International) and air freight contributed 3,249,527,795 tonnes of CO2 alone[4]. The data on the NOx emission suggest that 70-80% of total airport NOx emission is contributed by the aircraft. The NOx emission reduction goal of 60% by 2026 AD, has been highlighted in the ICAO Doc 9887 compiled by the Committee on Aviation Environmental Protection(CAEP)[5]. The direction for the development of future engines is to make them more fuel-efficient and pollution-free. It makes them economically and environmentally fit for civil aviation[6]. The attempts being made for the technological development of cleaner engines are shown in table 1.

Table 1: Types of technology as a potential for emission control to comply with ICAO and CAEP goals[5]. Along with the pros, cons, and effectiveness of emission reduction.

Methods	Pros	Cons	Reduction
Rich burn quick quench lean burn (RQL)	Lower cost and complexity, Conversion to Neutral N_2, High reliability, and service history	Need for airflow optimization, Need for redesign of injectors	50-70% for small engine, 55-65% for medium-sized engines
Double Annular Combustor (DAC)	Lean combustion at high power reduced fuel-choking	Control of pattern factor, excessive fuel burn, reduced efficiency in mid-power range	20% for Low overall pressure ratio, 40% margin obtained at OPR=24.6
Axially Staged Combustor (ASC)	A lower level of NOx at high power	Fuel choking risk, high casing strength, and stiffness	40-50% in a 2-stage combustor

1.2 Plasma Assisted Combustion (PAC)

In the last two decades, research on using plasma to enhance the combustion process & and for pollutant control has been ongoing. Due to its ability to produce active species, heat, and modify transport species[2]. The ability of the plasma state to excite a neutral atom and increase its particle velocity makes it a viable option in applications such as aerospace propulsion to achieve energy and environmental sustainability goals.

Although the studies have demonstrated the effectiveness of plasma in attaining the environmental and economic goals for propulsion systems by fuel reformation, combustion, and emission control, it is still unclear about the type of plasma to be used in different combustion environments. One of the contributors to this uncertainty is the variation of the plasma properties and complicated interaction between the combustion chemistry, plasma,

* Corresponding author:
Phone: +61 (0)406895208
Email: abishek.stha@outlook.com

species transport, and aerodynamics[1]. From the control perspective, the complex nature of plasma makes it difficult to understand the suitable control mechanisms and quantification of plasma properties in a highly volatile combustion application. The focus of the review is to discuss the following:

- Progress made in PAC in emission control of aerospace propulsion.
- Different types of plasma (non-thermal and thermal) for pollution control.
- The effect of plasma on different stages of combustion.
- Application of plasma to air-breathing aerospace engines.

2. Plasma

It is considered the fourth state of matter, which is a gas in an excited state due to interaction with a high-energy particle generated by a magnetic field [2]. Plasma can be subdivided into two classes for use in combustion applications: Equilibrium or Thermal Plasma and Non-Equilibrium or Non-thermal Plasma [2, 7].

2.1 Equilibrium Plasma

The thermal plasma comprises species that are in thermal equilibrium with each other. These plasmas are fully ionized plasma and have equally excited electrons, neutral species, and ions [7]. One of the major drawbacks to this type of plasma is the heat energy loss from the transition of glow-like discharge into sparks or arcs. The equilibrium plasmas have some direct applications currently in the automotive spark plug and plasma cutting applications [2, 7, 8].

2.2 Non- Equilibrium Plasma

The non-thermal plasma has electrons in the excited state compared to the ions and neutral species, causing the plasma temperature to be close to the ambient temperature. The low temperature allows ease of achieving the direction of energetic-electron energy, without heat loss in the process. The non-equilibrium plasmas most of the electron energy is utilized in the dissociation of neutral molecules and the production of ions. Thus, enabling the conversion of discharge plasma into chemical energy [7].

The non-thermal plasma rapidly produces electronically and vibrationally excited species faster than the keychain-branching processes of combustion at low and intermediate temperatures. Hence, eliminating the ignition delay. The experimental results have established the fact that non-equilibrium plasma can enable direct ignition to flame transition without extinction limit as suggested by the S curves. Besides, the researchers suggest that the plasma plays a significant role in the production of active species at a lower temperature, which aids in the activation of fuel oxidation even at lower temperatures, which is not possible in a conventional combustion process [9].

In non-thermal plasma (NTP), the discharge energy goes into the excitation of the energetic electrons more than the ion and neutron heating. Thus, energy is consumed for electron impact dissociation rather than ionization of background gas to produce radicals which decompose the toxic molecules near room temperature by avoiding the energy loss to background gas heating. Some of the NTP formation methods such as Electron beam irradiation, Electrical discharge, Dielectric barrier discharge, and Pulse power discharge have been recognized as solutions to the removal of hazardous pollutants.

Methods like Electron beam dry scrubbing have been researched to eliminate the need for the expensive catalyst for NO_x (Nitrous oxides) removal. Its ability to convert pollutants into byproducts for use in fertilizers has been an advantage and the tests on these types of systems could remove significant amounts of NO_x and SO_2 (Sulphur oxides) from power plants, municipal waste incinerators, and combustion boilers[10]. In contrast to the electron beam excitation of plasma formation, the electric discharge method has the potential to form a non-thermal plasma in atmospheric pressure gases by use of (DC, AC, or pulse power sources. Dielectric barrier discharge (DBD) and pulse power discharge are the most developed technologies to date.

Research has shown that Pulsed discharge-controlled NOx emission is more efficient in comparison with DC corona discharge, as the pulsed discharge restricts the transfer into arc discharge. Researchers suggest that short-duration pulses influence preventing loss due to heating by terminating the voltage before the non-thermal plasma shifts to a thermal plasma. It can be established from experiments that; the shorter pulse time provides more energetic electrons and higher energy. The development of pulsed power discharge has enabled the reduction of the pulse duration to 5 nanoseconds[10]. Compared to a general pulsed discharge it has proven to have more NO removal efficiency. Data obtained from one of such experiments is shown in Table 1. The energy efficiency of the nanosecond pulsed power is found to be highest in recent experiments about pollution control by non-thermal plasma.

Table 2: Experimental results from the comparison of general pulsed discharge with nanosecond pulse discharge[10]

	General Pulsed discharge	Nano-Second pulsed discharge.	
Pulse Duration	50 ns	5 ns	2ns
NO removal efficiency (220 ppm)	0.37 mol/kWh	0.52 mol/kWh	0.89 mol/kWh
Ozone Yield	30 g/ kWh	400 g/kWh	470 g/kWh

3. Effect of plasma on Combustion

The use of the fourth state of matter has many advantages in improving combustion efficiency [11]. The improvement in plasma technology and laser diagnostics seen in recent years has helped us understand the

enhancement mechanisms of plasma-assisted combustion [12].

Ignition:

The study on increasing and constant active components on the ignition boundary of the combustor has suggested that the increase of active species can broaden the lean ignition boundary[6]. The studies on spark ignition and plasma-assisted ignition on ignition delay time have shown that the plasma jet ignition delay time is much shorter than that for the spark ignition. The minimum plasma jet ignition delay showed an 88.74% reduction time in ignition delay compared to spark ignition[6].

Flame propagation:

Some experiments have suggested the use of PAC to boost ignition and lean burn limit. The use of microwave is suggested to enhance the effect in oxygen-rich combustion, then that in fuel-rich conditions[1]. Additionally, plasma aided ignition kernel development but except the flamer speed. Decades of research have shown that the flammability limit is caused by the radiation heat loss during combustion.[2]

Flame stability:

The blowout air flow is the main indicator of the flame stability and the high blowout achieved from the DBD generated plasma activated Propane-air flame, shows that combustion continues to occur under very lean burn conditions[12]. The temperature environment with variable pressure pilots and flame motivated the research for non-thermal plasma using microwave and hybrid approaches of both thermal and non-thermal plasma being employed for combustion stabilization[7].

Emission:

Research has shown that the implementation of PAC enables the concentration of CO (Carbon Monoxide) volume fraction in the main combustion zone of the combustor and is reduced in the downstream mixing zone. This indicates that the active particles in the chemical reaction in the main combustion zone accelerate the combustion reaction and ensure complete combustion of fuel. This milestone of reaching a complete combustion level reduces the emissions significantly[6].

4. PAC for Air Breathing Engines.

The Gas turbine engines, which operate at 9+ Km altitude still have issues of high-altitude ignition and afterburner. PAC enables jet engine design modifications with reduced chamber volume, improved air-fuel mixture, increased flame propagation, and improved emissions. The gas turbine combustors with piloted flame stabilization using non-equilibrium plasma provide a better performance, wider turndown ratios, and lower emission of Carbon and nitrogen oxides. It also supports the reduction in flame dynamics and reduces pressure fluctuations[6].

The study of emission characteristics of aviation kerosene in an aero engine combustor using volume dielectric barrier discharge configuration and investigations conducted by temperature and emission measurement concluded that CO emission was reduced for fuel-rich, stoichiometric, and fuel-lean kerosene-air mixture. In contrast, NOx emission was reduced only in the case of a fuel-rich mixture. It has been shown in experiments that the DBD discharge can produce Ozone (O_3). This is believed to be the primary reason for the increment in NOx emission. It shows the limitation of the DBD in achieving the goals of PAC for emission control.

The research on the effect of nano-pulsed discharge on the combustion instabilities concluded that, with the activation of plasma discharge and the pulse repetition frequency, the flame stabilizes in the burner passage[1]. The nano pulsed discharge is believed to be effective in radical generation and high speed of penetration requiring less power measured at 0.01-1 J/Pulse.

Research on a novel aero-engine combustor using PAC has shown that using PAC reduces the emission significantly for all three major pollutants NOx, CO, and HCs[6].It is evident that even with such a low power consumption, a significant amount of emission reduction is possible.

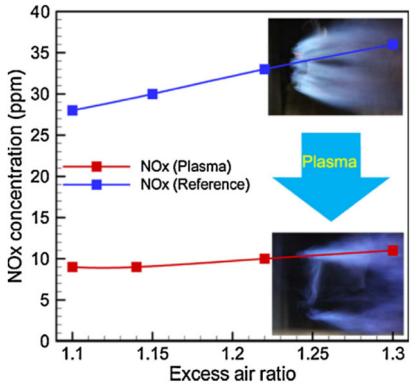

Fig.1: Experimental demonstration of plasma-assisted combustion using nano-second plasma discharge and the NOx concentration (ppm) at different excess air ratios[6]. The experiment demonstrates the ability of NPD to reduce NOx emissions.

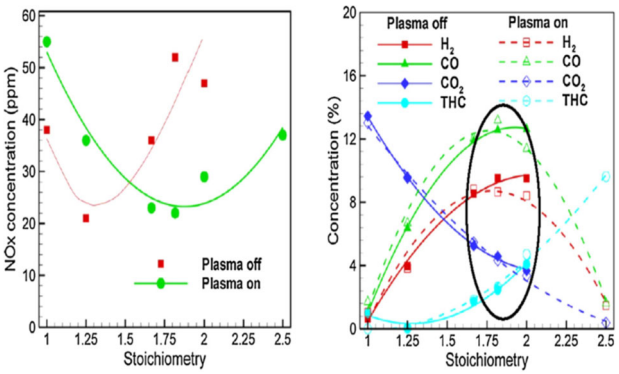

Fig. 2: Pollutants (NOx, CO, THC) generated with and without Plasma. The power consumed for plasma generation was 150 watts[6].

The high-speed flow of air in Scramjet engines operating above MACH 5 causes many complications when it comes to the mixing of air and fuel[13]. Additionally, ignition, flame stabilization, and cooling at high temperatures are some other requirements. In the present context, kerosene-fuelled scramjet engines are considered suitable for high-speed propulsion. In this case, a small amount of Hydrogen or pyrophoric liquid is used as pilot

igniters. However, they have added the complexity of storing and delivering these in high-speed flow conditions.
The application of the gliding arc plasma on a scramjet engine showed an increase in wall pressure and combustion zone[14]. At such high Mach numbers, the flow residence time is much shorter than the autoignition time of the jet fuels at 900 Kelvin[2]. The flow residence time is quite short even when the fuel is ignited. Attempts have been made to reach this unity using plasma torches and combining these with the dielectric barrier discharge (DBD). This technology is predicted to be the future of aerospace travel and ensures the application of PAC in the improvement of combustion and emission control for a sustainable future.

5. Conclusion & Discussion

Non-equilibrium plasmas will be the dominant method of plasma-assisted combustion due to the dissociation of most of the neutral atoms without having any heat loss. Over the years, many improvements have been made in understanding plasma magic and its dynamics and chemistry. In addition, the plasma has been shown to have a positive impact on the different stages, such as a reduction in ignition delay, Stable flame, and reduced emissions. The emission control objective of the Aviation industry can be achieved using PAC. From the study of the PAC in the case of air-breathing, the only way to achieve the stringent environmental needs of the aerospace industry can only be achieved with the help of PAC. The NOx concentration, which is a major problem in the current aerospace industry can be solved with the current systems available if the plasma technology is implemented in it.

6. Future works

The direction of the research on PAC will be towards the applicability of the PAC systems to the current existing propulsion systems. As discussed in the paper the research on the PAC systems in the case of the current Gas turbine, is the milestone to reaching carbon neutrality. As discussed earlier, one of the major hurdles to applying plasma technology directly to applications such as propulsion is the knowledge gap in the type of plasma discharge suitable for it[1]. The missing reaction pathways for the plasma-assisted combustion and the mechanisms have not been validated practically[1]. The fulfillment of this gap will be a game-changer in this field and will enable the sector to flourish.
This will be the direction of the research in this field.

7. References

[1] W.S. Yiguang Ju, Plasma assisted combustion: Dynamics and chemistry, Progress in Energy and Combustion Science 48 (2015) 21-83.

[2] K.K. K. Chavda *, Plasma Assisted Combustion: A Review, IOSR Journal Of Applied Physics (IOSR-JAP) 13 (2021) 26-35.

[3] G.D. Gohardani Amir S.*, Riti Singh, Challenges of future aircraft propulsion: A review of distributed propulsion technology and its potential application for the all-electric commercial aircraft, Progress in Aerospace Sciences 47 (2011) 369-391.

[4] M.H. Oksana Ovdiienko, Volodymyr Marchuk, Dmytro Bugayko, An assessment of the aviation industry's impact on air pollution from its emissions: worldwide and the Ukraine, Environmental & Socio-economic Studies 9 (2021) 1-10.

[5] X.S. Yize Liu, Vishal Sethi, Devaiah Nalianda, Yi-Guang Li, Lu Wang Review of modern low emissions combustion technologies for aero gas turbine engines, Progress in Aerospace Sciences 94 (2017) 12-45.

[6] Z.W. Mengzhe Li, Rongguang Xu, Xiaoliang Zhangc, Zhitong Chenc, Qiu Wange, Advances in plasma-assisted ignition and combustion for combustors of aerospace engines, Aerospace Science and Technology 117 (2021).

[7] I.B. Matveev, Plasma Assisted Combustion, Gasification and Pollution Control, Outskirts Press Inc. , Denver, Colorado, 2013.

[8] I.C. I V Adamovich, N Jiang, J-H Kim, S Keshav, W R Lempert, E Mintusov, M Nishihara, M Samimy and M Uddi, Plasma-assisted ignition and high-speed flow control: non-thermal and thermal effects, PLASMA SOURCES SCIENCE AND TECHNOLOGY 18 (2009).

[9] J.K.L. Yiguang Ju, Christopher B. Reuter,Sang Hee Won, Xueliang Yang, Suo Yang, Wenting Sun, Zonglin Jiang, Qi Chen, Plasma Assisted Low Temperature Combustion, Plasma Chem Plasma Process 36 (2016) 85-105.

[10] D.W. Takao Matsumoto, Takao Namihira and Hidenori Akiyama, Non-Thermal Plasma Technic for Air Pollution Control, in: B. Haryanto (Ed.), Air Pollution - A Comprehensive Perspective2012.

[11] V.B. A. Ktinnov, V. Bityurin, V. Vinogradov, D. Vanwie, Plasma Assisted Combustion, 39th AIAA Aerospace Sciences Meeting and Exhibition, AIAA, Reno, NV, 2001

[12] W.S.a.Y. JU, Non Equilibrium Plasma-Assisted Combustion: A Review of Recent Progress, Journal of Plasma Fusion Research 89 (2013) 208-219.

[13] K.M.P. Gautam Choubey, Ambarish Maji and TuhinDeshamukhya, A brief review on the recent advances in scramjet engine, International Conference on Functional Materials, Characterization, Solid State Physics, Power, Thermal and Combustion Energy, AIP Publishing, 2017.

[14] K.A.V. A. Siva Nagaraju, Krishna Murari Pandey, Darpahari Das, Numerical analysis of plasma combustion in scramjet engine-A review, Materials Today: Proceedings 45 (2021) 6838-6851.

Towards Clean Combustion and Decarbonisation
Proceedings of the Australian Combustion Symposium
26 – 29 November 2023, Darwin, Northern Territory, Australia

Gaussian particle selection pairing for the generalised binomial Langevin multiple mapping conditioning model

Matthew du Preez and Andrew P. Wandel*
School of Engineering, University of Southern Queensland, QLD 4350 Australia

Abstract

Stochastic implementations of mixing models typically use particles where mixing is modelled by ultimately calculating weighted averages of particle pairs. The method for pairing particles is the principal difference between most of the mixing models. Pairs of particles are sometimes only permitted to mix within a given distance of another particle but there is rarely any bias to which a particle within an acceptable distance is selected, with the closest particle the most common method if any bias is applied. An approach used by the authors is uniform particle selection, where particles within a certain distance are equally likely to be paired. A comparison between uniform and Gaussian particle pairing selection was investigated for the binomial-Langevin Multiple Mapping Conditioning model using homogeneous nonreacting DNS as a test case. No significant differences between the two selection pairing methods were found for the range of parameters tested, but the effect of the method in a reactive case is not yet investigated.

Keywords: micro-mixing model, modified Curl's model, multiple mapping conditioning

1. Introduction

A micro mixing model is used to model diffusion processes. There are two extreme implementations. First, any particle can pair with any other particle, which is Modified Curl's mixing [1]. This can lead to unphysical behaviour such as mixing across a flame front. Second, particles may only pair with neighbours. This is problematic when streams are segregated as mixing does not occur quickly enough. A compromise is obtained by many advanced mixing models with varying strengths and weaknesses e.g., Euclidean Minimum Spanning Tree [2], Multiple Mapping Conditioning [3], binomial Langevin Multiple Mapping Conditioning (BLM-MMC) [4].

It has previously been shown [5-6] that randomly pairing particles that are within the diffusion length scale is an effective technique, but this method does not account for inter-particle distance within that kernel window. An alternative kernel is investigated, where a Gaussian kernel makes it more likely that close particles will be paired. This Gaussian kernel within BLM-MMC is compared with the standard uniform pairing method in BLM-MMC. The Gaussian particle pairing is inspired by the kernel model KerM [7], which was applied to a Modified Curl's mixing model, but no direct comparison is made here to KerM, and the model used here is not KerM.

2. Generalised BLM-MMC Method

The BLM-MMC is broken down into sub-components and the main aspects are highlighted.

2.1 binomial Langevin model

The binomial Langevin equation [4,6,8,9] describes the transport of the scalar η

$$\mathrm{d}\eta^{*p} = A\,\mathrm{d}t + (2\langle N\rangle B_\eta)^{1/2}\,\mathrm{d}\omega_{\mathrm{bin}} \tag{1}$$

where the drift A and diffusion B coefficients for a homogeneous case are

$$A = G_\eta\,\omega\,(\eta^{*p} - \langle\eta\rangle) \tag{2}$$

$$G_\eta = -\left(K_\eta\left(1 - \left\langle\left(\frac{\eta'^{(*p)}}{\eta'_*}\right)^2\right\rangle\right) + 1\right) \tag{3}$$

$$B_\eta = K_\eta\left(1 - \left(\frac{\eta'^{(*p)}}{\eta'_*}\right)^2\right) \tag{4}$$

with K_η and $\mathrm{d}\omega_{\mathrm{bin}}$ given elsewhere [6] and the fluctuations defined to be

$$\eta'^{(*p)} = \eta^{*p} - \langle\eta\rangle^{*p} \tag{5}$$

$$\eta'_* = \begin{cases} \eta'^{(*p)}_{\max} & \eta'^{(*p)} > 0 \\ \eta'^{(*p)}_{\min} & \eta'^{(*p)} < 0 \end{cases} \tag{6}$$

with the averages defined to be

$$\langle\eta\rangle^{*p} = \min(\eta \mid \eta = \eta^{*p}) + \left(\langle\eta\rangle - \min(\eta \mid \eta = \eta^{*p})\right) \times \frac{\max(\eta \mid \eta = \eta^{*p} - \min(\eta \mid \eta = \eta^{*p})}{\max(\eta) - \min(\eta)} \tag{7}$$

and Eq. (7) is numerically calculated using 20 bins where previously the conditional min and max were used. This allows the particles to drift away from their stream at an appropriate rate when the PDF is close to a double δ-function.

2.2 Reference variable

The standard definition for the reference variable ξ is used, namely that it is a standard Gaussian. It is defined by mapping to η so that ξ monotonically increases with η.

2.3 MMC model

The MMC equation for a stochastic particle for a nonreacting scalar Z is only a function of the mixing model S

$$\mathrm{d}Z^{*p} = S\mathrm{d}t \tag{8}$$

* Corresponding author:
Phone: (+61) 7 4631 2230
Email: andrew.wandel@usq.edu.au

2.4 Modified Curl model

Modified Curl's model [1] is selected as the mixing model to mix quantity ϕ of particles p and q an amount a where $0 \le a \le 1$.

$$\begin{aligned} \phi^{*p}_{k+1} &= \phi^{*p}_{k} + a\left(\phi^{*q}_{k} - \phi^{*p}_{k}\right) \\ \phi^{*q}_{k+1} &= \phi^{*q}_{k} - a\left(\phi^{*q}_{k} - \phi^{*p}_{k}\right) \end{aligned} \quad (9)$$

Particles are mixed using Modified Curl with a trapezoidal probability density function (PDF)

$$A(a) = 2(2 - 3\langle a\rangle) + 6(2\langle a\rangle - 1)a \quad (10)$$

which is sampled by

$$a = \frac{3\langle a\rangle - 2 + ((3\langle a\rangle - 2)^2 + 3(2\langle a\rangle - 1)\mathrm{U})^{1/2}}{3(2\langle a\rangle - 1)} \quad (11)$$

where U = (0,1) is a uniform random number and mean $\langle a\rangle = 0.4$ is used for all simulations here.

2.5 Closure for mixing

BLM-MMC is closed [10] by mixing until the mixture fraction variance $\langle Z'^2\rangle$ matches the binomial Langevin variance $\langle \eta'^2\rangle$. This is performed by mixing using Modified Curl until it causes over mixing, and then the mixing amount for the last pair for equally weighted particles is [10]

$$a_i = 1 - \left(1 + 2n\frac{\langle \eta'^2\rangle - \langle Z'^2\rangle_{i-1}}{\left(Z^q_k - Z^p_k\right)^2}\right)^{1/2} \quad (12)$$

3. Particle Selection Kernels

The different methods for pairing particles investigated in this article are described in this section, beginning with the uniform distribution (which has been used previously), followed by the new method based on a Gaussian kernel (where inter-particle distance completely controls the pairing likelihood). The Gaussian kernel is appealing because the probability of selecting a particle is continuously distributed, so does not arbitrarily exclude a particle that has an almost identical state to a particle that is included for consideration.

3.1 Uniform distribution

Uniform particle selection means any pair of particles within the mixing length in reference-variable space [5-6]

$$L = (B\Delta t)^{1/2} \quad (13)$$

has equal probability of being paired, where Δt is the time step and

$$B = \langle N\rangle \left\langle \left(\frac{\partial Z}{\partial \xi}\right)^2 \right\rangle^{-1} \quad (14)$$

3.2 Gaussian distribution

Gaussian particle selection is inspired by the process used in KerM [7], in that the kernel used for selecting particle pairs is Gaussian, which causes closer particles to be more likely to be paired. We choose the probability of pairing the second particle as

$$k^{pq} = \exp\left(\frac{-\left(d^{pq}\right)^2}{c^2\sigma^2}\right) = \exp\left(\frac{-\left(d^{pq}\right)^2}{c^2 B\Delta t}\right) \quad (15)$$

where $d^{pq} = \xi^q - \xi^p$ is the distance between particle pairs (and $k = 0$ when $p = q$), c is a constant and $\sigma = \mathrm{L}$ is used to close the model. The kernel in KerM specifies the denominator to be some variable, but was only specified to be a constant in the published results to date, with different values tested [7]. The denominator is proportional to the mean dissipation rate, as in Eq. (15), if and only if the distribution of ξ is Gaussian [11] or a joint normal [12]. For each particle p, the probability of particle q being paired is determined by normalising k:

$$\mathrm{P}^{pq} = \frac{k^{pq}}{\sum_q k^{pq}} \quad (16)$$

and random sampling from this CDF is used to select q. As demonstrated using KerM [7], if c is small, then k approaches 0 (neighbour pairing) and if c is large then k approaches 1 (Modified Curl).

We next want to determine the value of c that produces the same variance in k^{pq} as occurs in the uniform distribution. The variance of the uniform PDF is

$$\int_{-L}^{+L} x^2 \frac{1}{2L}\mathrm{d}x = \frac{x^3}{6L}\Big|_{-L}^{+L} = \frac{1}{6L}\left(L^3 + L^3\right) = \frac{L^2}{3} \quad (17)$$

and so a uniform distribution is equivalent to the Gaussian distribution when $c = 3^{-1/2}$.

4. Comparison with KerM

The differences between the model here (using Sect. 3.2) and KerM [7] are described here. In general, the differences are semantics: it is possible to adopt the methods described here in KerM and *vice versa*.

The first difference is the selection of the conditioning variable. Both methods use a mixture fraction for this purpose, but while KerM uses the mixture fraction solved within the system (in a manner resembling Conditional Moment Closure [13]), the current model uses the binomial Langevin mixture fraction as a separate mixture fraction. A further difference is that the reference variable is mapped from the binomial Langevin mixture fraction so that the reference variable has a Gaussian distribution.

The PDF for the mixing amount in KerM follows the traditional approach for Modified Curl's model: a uniform distribution for all possible values. In the current work, the PDF is trapezoidal to bias the likelihood of no mixing occurring, which reduces the over-prediction of the kurtosis of the scalars.

The other difference is the method used to determine the number of particle pairs that mix each timestep. In KerM, an estimation-correction method based on EMST [2] is used to determine the mean amount of variance decay caused by each particle pair, which yields the number of pairs required to produce the decay indicated by the turbulent scalar mixing frequency. In the current work, the pairs are mixed until variance of the MMC

mixture fraction matches the variance of the binomial Langevin mixture fraction.

5. Comparison between Uniform and Gaussian Particle Selection Pairing

5.1 Setup

Simulations of BLM-MMC are performed using a homogeneous decaying scalar field from a Direct Numerical Simulation (DNS) case F2C [14]. It was selected because it has an initial scalar field close to a double δ-function distribution which is a difficult initial condition. The initial mixture fraction Z in the current simulations are initialised to match the DNS PDF (Fig. 6) The mixing frequency used in the current simulations is calculated from the DNS variance (Fig. 10) and dissipation rate (Fig. 11) Time was normalised using [14] (Table 1) $l/u = 0.38$. These numerical procedures were used to ensure the behaviour differences between the DNS and BLM-MMC was due to the different particle selection methods. Simulations are performed with 40k particles.

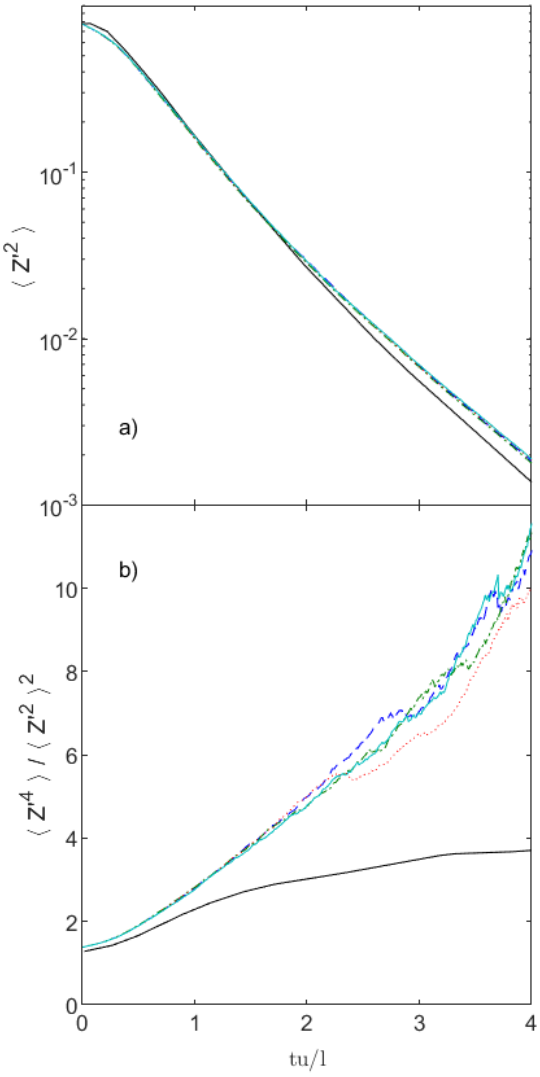

Figure 1: a) variance b) kurtosis. (line style, case number): (-- uniform), (-. Gaussian $c = 3^{-1/2}$, (: Gaussian $c = 1$), (- Gaussian $c = 4$), (- DNS [14]).

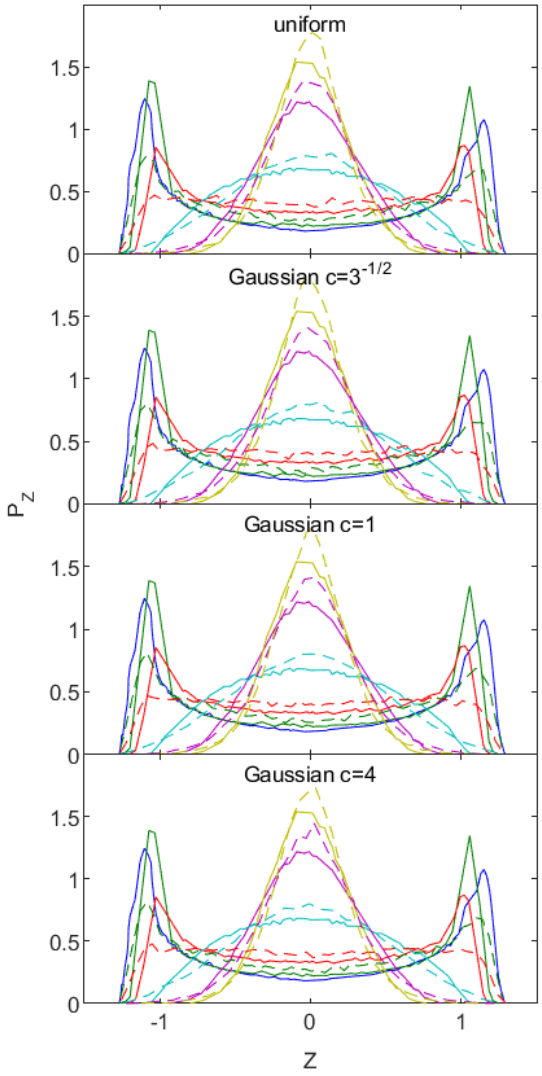

Figure 2: PDF. At same times as DNS [14] for case F2C. Solid line DNS, dashed line MMC. tu/l = (--- 0.22, -- 0.42, -- 0.83, -- 1.28, -- 1.49).

Kahan summation [15] is performed to minimise rounding error to better represent the mathematical algorithm and avoid the influence of the numerical implementation from confusing the results. Random numbers are drawn from the xoroshiro256++ uniform random number generator [16]. The bin sizes of the PDFs in Fig. 2 were computed based on the data [17]. The cases tested are 1) Uniform, 2) Gaussian $c = 3^{-1/2}$ (equivalent c to uniform), 3) Gaussian $c = 1$, 4) Gaussian $c = 4$.

5.2 Discussion

The history of the MMC mixture fraction variance (Fig. 1a) is the same for all simulations. This is expected as the particles mix until the reference variance equals the scalar variance [10].

Increasing c increases the kurtosis slightly. This is expected as larger values of c increase the range of particles available for selection. However, there is no significant difference in kurtosis before $tu/l = 2$ as low variance causes statistical noise to cause kurtosis variations later as seen in Fig. 1b and so there are only

minute differences between the cases in Fig. 2 which are only visible in the tails for the final distributions shown.

Two statistical tests are performed to check the difference between the different Gaussian c values. The Kolmogorov–Smirnov test [18] evaluates if the samples belong to the same continuous population, which was implemented using the MATLAB R2023a function kstest2.

The Mann–Whitney U test [19] evaluates if the samples from one group are typically larger than the samples from the other group; if not, then the medians are equal. The MATLAB R2023a function ranksum was used in the current analysis. The null hypothesis for both tests is that the distributions are identical. The significance level that the hypothesis can be rejected is shown in Table 1. The values found here are much higher than the standard value of α which is 0.05 indicating that it is very difficult to reject either hypothesis for the values of c tested here.

Table 1: Significance level α at which the hypothesis is rejected. Each Gaussian c value is compared with the uniform selection method. K: Kolmogorov–Smirnov. M: Mann–Whitney.

time tu/l	$c = 3^{-1/2}$		$c = 1$		$c = 4$	
	K	M	K	M	K	M
0.22	0.999	>0.999	0.990	0.998	0.877	0.994
0.42	0.996	0.999	0.928	0.995	0.728	0.991
0.83	0.763	0.943	0.802	0.899	0.380	0.887
1.28	0.651	0.963	0.925	0.901	0.489	0.858
1.49	0.807	0.997	0.592	0.783	0.247	0.821

The Kolmogorov-Smirnov test significance value α is occasionally smaller than the Mann–Whitney significance value showing that it is easier to reject the hypothesis that the samples belong to the same continuous population than to reject the hypothesis that the medians of the two samples are equal. This is expected because the tails appear to have greater differences between uniform and each Gaussian than the medians at $tu/l = 1.28$ and 1.49 and the Kolmogorov–Smirnov test is less sensitive to differences in the tails but more sensitive to differences in the middle of the distribution.

6. Conclusions

There was no significant difference between the standard uniform and the Gaussian particle selection methods for the range of values of c that were tested. In the limit $c \to 0$, particles will mix with their neighbour—as commonly used in many MMC implementations—while in the limit $c \to \infty$, Modified Curl's mixing is reproduced. The Gaussian method requires more computations because of Eq. (15) and the fact that more particles q need to be considered as having a non-zero kernel probability k^{pq}. However, given the significant computational time required for chemistry calculations, it is unlikely that this extra time would add more than a fraction of one per cent to the overall computational time.

7. Acknowledgment

M. du Preez was funded by an Australian Postgraduate Award.

8. References

[1] J. Janicka, W. Kolbe and W. Kollmann, J. Non-Equilb. Thermodyn. 4 (1977) 47-66.
[2] S. Subramaniam and S.B. Pope, Combust. Flame 115 (1998) 487.
[3] A.Y. Klimenko and S.B. Pope, Phys. Fluids 15 (2003) 1907.
[4] A.P. Wandel and R.P. Linstedt, Proc. Combust. Inst. 34 (2013) 1365.
[5] A.P. Wandel, Combust. Theory and Model. 17 (2013) 707.
[6] M. du Preez, A.P. Wandel, D. Bontch-Osmolovskaia and R.P. Lindstedt, Phys. Fluids 33 (2021) 045109.
[7] X. Su, J. Wei, H. Zhou, E.R. Hawkes and Z. Ren, Combust. Flame. 255 (2023) 112916.
[8] L. Valino and C. Dopazo, Phys. Fluids A 3 (1991) 3034.
[9] A.P. Wandel and R.P. Lindstedt, Proc. Combust. Inst. 37 (2019) 2151.
[10] M. du Preez, A.P. Wandel and R.P. Linstedt, A method for solving two-stream mixing using the generalised binomial-Langevin multiple mapping conditioning model, Australian Combustion Symposium (2021).
[10] A.P. Wandel, A stochastic micromixing model based on the turbulent diffusion length scale, Australian Combustion Symposium (2011).
[11] F. Gao, Phys. Fluids A 3 (1991) 2438.
[12] A.P. Wandel, Phys. Fluids 35 (2023) 041703.
[13] A.Y. Klimenko and R.W. Bilger, Prog. Energy Combust. Sci. 25 (1999) 595.
[14] V. Eswaran and S.B. Pope, Phys. Fluids 31 (1988) 506.
[15] W. Kahan, Commun. ACM 8 (1965) 40,48.
[16] D. Blackman and S. Vigna, ACM Trans. Math. Softw. 47 (2021)
[17] K.H. Knuth, Digital Signal Processing 95 (2019) 102581.
[18] F.J. Massey, J. Am. Stat. Assoc. 46 (1951) 68.
[19] H.B. Mann and D.R. Whitney, Ann. Math. Stat. 18 (1947) 50.

Fundamentals and New Concepts Paper 7
B. Z. Dlugogorski and A. R. Masri, Eds

Towards Clean Combustion and Decarbonisation
Proceedings of the Australian Combustion Symposium
26 – 29 November 2023, Darwin, Northern Territory, Australia

MMC-IEM with varying particle weights: A numerically-conservative method for a single reference variable

Andrew P. Wandel*
School of Engineering, University of Southern Queensland, Qld 4350 Australia

Abstract

The Multiple Mapping Conditioning model using the Interaction by Exchange with the Mean closure (MMC-IEM) promises a consistent approach to modelling turbulent combustion processes by using the mean of two other particles to determine the conditional mean towards which a particle's scalar should relax. However, a limitation of the approach occurs when the weights of the particles are different to each other, which is a common occurrence in inhomogeneous implementations. The approach proposed here produces conservation to the desired numerical precision, while still maintaining the necessary condition of the process being well-mixed. This is achieved by iteratively normalising the columns then rows of the mixing matrix so that it is made to be conservative then well-mixed on each iteration. It is proven that the chosen error tolerance in the conservation of the mixing process controls the overall error in the conservation of the results. It is shown for a homogeneous isotropic case that the approach does not substantially change the predictions of MMC-IEM compared to the original transport equations, so this approach is suitable for application to inhomogeneous flows.

Keywords: multiple mapping conditioning, interaction by exchange with the mean, conservative mixing

1. Introduction

The Multiple Mapping Conditioning (MMC) model [1] has been implemented for a wide variety of cases. The variants of MMC best suited to model local extinction-reignition phenomena are probabilistic MMC [2] formulations. The Modified Curl's model [3,4] is used as the closure model for the mixing term for most implementations of MMC, while the Interaction by Exchange with the Mean (IEM) model [5,6] is also used for a number of implementations. The variants are:

1. What will be called "MMC-Curl" in this paper, where the standard transport equation for the reference variable is solved and the Modified Curl's model is used with non-neighbouring particles paired and not all particles mixing [7,8].
2. The binomial Langevin–MMC (bL-MMC) model, where the binomial Langevin model [9] is used to define the reference variable [10–13]. The mixing is identical to MMC-Curl.
3. What is an MMC-Curl-IEM model because it simultaneously mathematically satisfies both Modified Curl's and IEM models by special selection of the Modified Curl's mixing amount [14–16]. (This model has variously been called "MMC-Curl" and "MMC-IEM" in the literature.) This is the model used in MMC-LES where particles are paired using a k-dimensional tree algorithm, while in RANS implementations neighbouring particles in reference space are paired. All particles mix every timestep.
4. What will be called "MMC-IEM" in this paper, where IEM is used with the conditional mean computed using the nearest two particles in reference space. Where there is a single reference variable, the nearest two particles are the immediate neighbours either side of the chosen particle [17–19], while for multiple reference variables, the two closest particles are chosen [20]. All particles mix every timestep.

Inhomogeneous simulations introduce challenges for accurate and computationally-efficient simulations. The nature of turbulent flows typically causes stochastic particles to cluster in various parts of the flow, while they disperse in other parts of the flow. To ensure statistical validity, a minimum number of particles is required at each location, while to manage computational load, it is desirable to not have too many particles at each location. To achieve this balance, simulations typically assign a "weight" (i.e. a probability of existing) to each particle. If there are too few particles at a location, the heaviest particles are split, with the new particles having the same state as the parent, but their weights adding to the parent's weight. If there are too many particles at a location, particles are either randomly chosen for deletion, or randomly combined in the reverse process to splitting.

Having different weights does not challenge Modified Curl's because the pairwise nature of Modified Curl's—particles relax to a state that is solely defined by the particles relaxing to that state—ensures that the mixing process is conservative (even if triplets are used) [11]. However, MMC-IEM has a challenge because the state to which a particle relaxes is defined by particles that do not relax to the same state. In Sect. 2, the key principles of mixing that need to be satisfied are presented, and the consequences of these principles for MMC-IEM are derived in Sect. 3.1. A method to enable MMC-IEM to satisfy the principles for a single reference variable is presented in Sect. 4, with an assessment of the impact of this method on the outcomes presented in Sect. 5.

2. Key Numerical Principles for Mixing

There are two fundamental numerical principles that good mixing models satisfy: being well-mixed and

* Corresponding author:
Phone: (+61) 4 4631 2230
Email: andrew.wandel@unisq.edu.au

conservative. Let the new value for variable x for particle i at timestep k+1 be:

$$x_i^{k+1} = \sum_j L_{ij} x_j^k \tag{1}$$

where L_{ij} is the interaction matrix between all particles j and particle i. In other words, L_{ij} defines how other particles j contribute to the new value of particle i.

The well-mixed criterion requires the mixing method to be numerically stable by not introducing fluctuations numerically that do not exist physically; a consequence of this criterion is that a uniform field remains uniform. Mathematically, the well-mixed criterion is satisfied by:

$$\forall_i \sum_j L_{ij} = 1 \tag{2}$$

In practice, the well-mixed criterion is inherently satisfied by mixing models via the formulation of their transport equation. The well-mixed criterion is essential for a mixing method: if it is violated, the results are almost certainly unreliable—if any results are obtained at all!

The conservation criterion requires the mean to remain unchanged by the mixing process; this reflects the physical nature of a passive process. Mathematically, the conservation criterion is satisfied by:

$$\forall_j \sum_i w_i \left[\delta_{ij} - L_{ij} \right] = 0 \tag{3}$$

which becomes:

$$\forall_j \frac{1}{w_j} \sum_i w_i L_{ij} = 1 \tag{4}$$

where w_i represents the weight of particle i. The weight is not explicitly required for the well-mixed criterion because it is embedded in the formulation of L_{ij}, but it must be explicitly included in the conservation criterion because the behaviour of L_{ij} for different i is not coupled in the formulation of L_{ij}. While the conservation criterion is not necessary for the mixing method to produce results, the inherent bias caused by its violation can result in significant accumulated errors.

3. MMC Theory

The test case has a passive scalar (mixture fraction, Z), a single reactive scalar (non-dimensional temperature, T), and a single reference variable (ξ) linked to Z. The homogeneous, stochastic form of MMC [1] is used here:

$$\begin{aligned} d\xi_i &= A_i dt + \sqrt{2B}\, d\omega_i \\ dZ_i &= S_i dt \\ dT_i &= S_i dt + W_i dt \end{aligned} \tag{5}$$

where $d\omega_i$ is a Wiener process, S_i represents the mixing model, and W_i is the chemical source term. The drift coefficient A_i and diffusion coefficient B are [1]:

$$\begin{aligned} A_i &= B\left(\xi_i - \langle \xi \rangle\right) \\ B &= \langle N \rangle \left\langle \left(\frac{dZ}{d\xi} \right)^2 \right\rangle^{-1} \end{aligned} \tag{6}$$

where the formula for A_i takes its simplest form because ξ has a Gaussian distribution [21–24], $N = D(\nabla Z)^2$ is the scalar dissipation rate and D is the molecular diffusivity of Z. The second factor in the formula for B is modelled using the numerical scheme [8] implemented in all subsequent MMC simulations.

3.1 MMC-IEM Model

The IEM model [5,6] can be directly applied using a conditional mean conditioned on a scalar (in this case, the reference variable) instead of the unconditional mean, so long as the dissipation timescale represents the conditional fluctuations' decay instead of the unconditional fluctuations' decay:

$$S_i = -\frac{Z_i - \langle Z | \xi_i \rangle}{\tau_{\min}} \tag{7}$$

Here $\tau_{\min}$ is the minor dissipation timescale, as opposed to the major dissipation timescale

$$\tau_{\text{maj}} = \langle Z'^2 \rangle / \langle N \rangle \tag{8}$$

The two timescales are related to the fluctuations [8]:

$$\frac{\tau_{\min}}{\tau_{\text{maj}}} = \frac{\left\langle \left(Z - \langle Z | \xi \rangle \right)^2 \right\rangle}{\left\langle \left(Z - \langle Z \rangle \right)^2 \right\rangle} = \frac{\langle Z''^2 \rangle}{\langle Z'^2 \rangle} \tag{9}$$

and this ratio is fixed to 1/8 [7] in this paper, consistent with almost every implementation of MMC.

If there is a single reference variable, the MMC-IEM procedure for computing the conditional mean in Eq. (7) is to sort the particles in reference space, and to compute the conditional mean by computing the (weighted) mean of the two particles immediately neighbouring particle i on either side within reference space [17,18]. In other words, if ξ_i monotonically increases with i,

$$\langle Z | \xi_i \rangle = \frac{w_{i-1} Z_{i-1} + w_{i+1} Z_{i+1}}{w_{i-1} + w_{i+1}} \tag{10}$$

This model produces an asymmetric tridiagonal L_{ij}, while Modified Curl's is symmetric (when the off-diagonal elements are multiplied by the particle's weight) with only a single non-zero off-diagonal element per row/column.

To close the model, the boundary conditions for $i = 1$ and $i = n_p$ (the final particle) need to be specified because particles i–1 and i+1 respectively do not exist. The approach [19] is to use the boundary particle ($i = 1$ or $i = n_p$) as a ghost particle, replacing the non-existent particle in Eq. (10).

This model is mathematically well-mixed—it satisfies Eq. (2). If all of the weights w_i are equal, then this model is mathematically conservative—it satisfies Eq. (4). However, if any of the weights w_i are different, the scheme as formulated is not conservative. Consider the first few particles ($n_p > 3$):

$$L_{\{1-3\},\{1-3\}} = \begin{bmatrix} 1 - \frac{\Delta t}{\tau_{\min}} \left(1 - \frac{w_1}{w_1 + w_2} \right) & \frac{\Delta t}{\tau_{\min}} \frac{w_2}{w_1 + w_2} & 0 \\ \frac{\Delta t}{\tau_{\min}} \frac{w_1}{w_1 + w_3} & 1 - \frac{\Delta t}{\tau_{\min}} & \frac{\Delta t}{\tau_{\min}} \frac{w_3}{w_1 + w_3} \\ 0 & \frac{\Delta t}{\tau_{\min}} \frac{w_2}{w_2 + w_4} & 1 - \frac{\Delta t}{\tau_{\min}} \end{bmatrix} \tag{11}$$

Comparing L_{23} and L_{32}, if the interaction between particles 2 and 3 were pairwise (like Modified Curl's), then

$w_2L_{23} = w_3L_{32}$; however, the presence of w_1 in L_{23} and w_4 in L_{32} prevents pairwise matching. This approach is well-mixed (the sum of the rows is 1) because within a row the denominators involving w are identical. However, because within each column the denominators involving w are different, it is impossible for the terms involving Δt to cancel unless all of the w_i are equal. Therefore, without any correction, this approach is only conservative if each particle has an identical weight.

If a correction is to be applied, then it is necessary that such a correction produces an L_{ij} that is well-mixed. Any method which renormalises x_i^{k+1} by subtracting or dividing by $\left\langle x_i^{k+1} \right\rangle$ is not well-mixed because L_{ij} is no longer tridiagonal—every particle is involved in the computation of the mean which renormalises each particle. The renormalisation procedure should be embedded into the formulation of L_{ij} and not treated as a second step so it can be transparently assessed whether L_{ij} is well-mixed (or conservative!).

4. Proposed Conservation Method

To maintain the well-mixed property of L_{ij} while also making it conservative, it is proposed that the normalisation occurs to L_{ij} directly, which also means that it remains tridiagonal. A method for achieving this [25] is to iteratively normalise L_{ij} so that it alternately becomes conservative, then well-mixed. The errors in conservation and well-mixedness are respectively defined as:

$$\begin{aligned} \frac{1}{w_j}\sum_i w_i L_{ij} &= \left(1+\varepsilon_{c,j}\right)\times 1 \\ \sum_j L_{ij} &= \left(1+\varepsilon_{w,i}\right)\times 1 \end{aligned} \tag{12}$$

where the conservation and well-mixed criteria are only satisfied if all of the errors are zero. Let L_{ij} be well-mixed, but not conserved. The mth iteration of a conservative—but not well-mixed—array can be computed by using the conservation error to normalise L_{ij}:

$$\forall_{i,j}\hat{L}_{ij}^m = L_{ij}^m \div \left(1+\varepsilon_{c,j}^m\right) \tag{13}$$

It is necessary to compute the well-mixed error for the array computed by Eq. (13) and normalise to produce the next iteration of L_{ij}:

$$\forall_{i,j} L_{ij}^{m+1} = \hat{L}_{ij}^m \div \left(1+\hat{\varepsilon}_{w,i}^m\right) \tag{14}$$

Equation (14) ensures that the final L_{ij} is well-mixed, while Eq. (13) converges so that for increasing m, the conservation error monotonically converges to 0.

This procedure alters L_{ij} so that is no longer identical to Eqs. (7) and (10), but it does maintain the relative form that if $w_{i+1} > w_{i-1}$ then $L_{i,i+1} > L_{i,i-1}$. The impact of this alteration is assessed in the next section.

5. Evaluation of Method

The test case to evaluate the method is Direct Numerical Simulations (DNS) of homogeneous isotropic turbulence using a single-step irreversible chemical kinetics mechanism [26,27]. This DNS has previously been used to evaluate a number of turbulent combustion models [28,7,8]. A homogeneous case permits a direct comparison with the implicitly-conservative equal-weight method. Although the introduction of different weights is unnecessary and artificial here, the mixing process is numerically identical to an inhomogeneous case, so can be assessed fairly.

For the current simulations, 131 072 particles were used in an ensemble of 5 for each case. Because the streams have undergone some mixing prior to the initial conditions, it is necessary to initialise conditional fluctuations Z'' according to Eq. (9).

Table 1 reports the parameters that were used in the simulations. Case 1 uses equal weights for all particles; because this is inherently conservative, it can be used as a baseline for the other MMC-IEM simulations. Cases 2–5 assess the effect of relaxing the error tolerance to the extreme of Case 5, where no iterations were performed. Greater variation in w substantially increases the number of iterations required for convergence, so the wider range of Case 6 can be directly compared to Case 4 as having the same specified convergence error.

Table 1 also reports the 95% confidence intervals for the average cumulative error in the mean of Z per timestep, computed as the difference between the final mean and the initial mean divided by the total number of timesteps. Because Z is a passive scalar, this value should be zero, but Case 1 has errors of the order of numerical precision, which is to be expected for an algebraically-conservative scheme. For Cases 2–4 and 6, the conservation error per timestep is approximately 5 orders of magnitude smaller than the target maximum conservation error, which is because convergence occurs when all the particles have a conservation error less than ε_{max}; therefore, many particles' conservation error could be orders of magnitude less. By extrapolation of Case 5, no correction yields a conservation error of approximately 1%. The central limit theorem states that these errors decrease with increasing number of particles used, so in inhomogeneous simulations—where the number of particles is 3–4 orders of magnitude smaller—the conservation error will be approximately 2 orders of magnitude larger.

Figure 1 shows the mean temperature results. The MMC-IEM results for Cases 1–5 are indistinguishable, while Case 6 is slightly colder. MMC-IEM generally reproduces the trend of the DNS, with combustion phased slightly ahead of the MMC-Curl results [7].

Table 1: Parameters of different MMC-IEM cases. The weights were randomly sampled from a uniform distribution with the range specified, except for Constant with equal w; ε_{max} is the error tolerance used to define convergence of Eq. (13); and the conservation error reports the 95% confidence intervals for the average change to the mean of Z per timestep.

Case	*w* range	ε_{max}	Conservation error
1	Constant	0	$[-8.17\times^{-18}, -2.71\times10^{-19}]$
2	0.9–1.0	10^{-7}	$[-1.36\times^{-12}, 2.12\times10^{-12}]$
3	0.9–1.0	10^{-6}	$[-2.26\times^{-11}, 1.25\times10^{-11}]$
4	0.9–1.0	10^{-5}	$[-2.04\times^{-10}, 1.63\times10^{-10}]$
5	0.9–1.0	-	$[-4.08\times^{-7}, 2.71\times10^{-7}]$
6	0.1–1.0	10^{-5}	$[-7.19\times^{-11}, 1.09\times10^{-10}]$

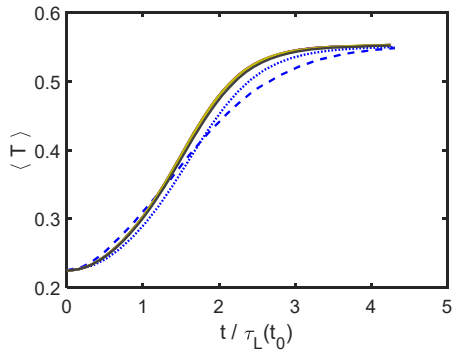

Figure 1: Mean temperature; time is normalized by the initial integral timescale. DNS [26] (blue dashed); MMC-Curl [7] (blue dotted); Cases 1–5 collapse onto each other (yellow); Case 6 (black) is marginally delayed.

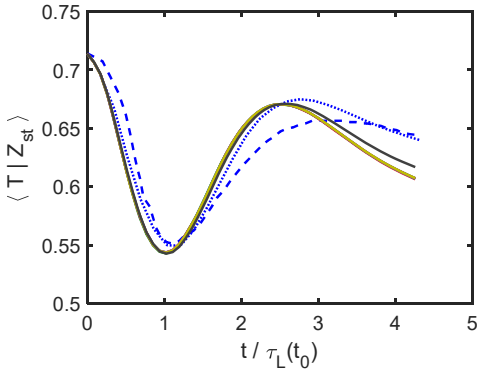

Figure 2: Conditional mean temperature in the vicinity of the stoichiometric mixture fraction. As per Figure 1.

The conditional mean temperature in the vicinity of the stoichiometric mixture fraction (Figure 2) behaves similarly to the mean temperature in that MMC-IEM is slightly advanced of MMC-Curl. Also, Case 6 is noticeably different to the remainder of the cases.

6. Conclusions

A method has been proposed to make the MMC-IEM mixing model conservative to a specified numerical precision for the case where particles have different weights. Without the correction, the conservation error per timestep is significant and would impact results. The method is proven to improve the conservation of the scheme, with decreasing error tolerance in the mixing method's conservation producing decreasing errors in the results' conservation. When the variation in weights is relatively small, the method produces almost identical results to the implicitly conservative approach when all particles have equal weights. However, the method produces somewhat different results when the variation in weights is large, and this can be attributed to a significant change in the transport equations that are solved due to conservation. However, the change in results caused by conservation is relatively small compared to the difference between MMC-IEM and other mixing methods. Therefore, there should be confidence that this approach is suitable for general application to turbulent combustion modelling.

Future work will assess the effect of $\Delta t/\tau_{min}$ on the convergence, apply the method to inhomogeneous flows, and extend to multi-dimensional reference spaces.

7. Acknowledgements

The author is grateful to Prof. A.Y. Klimenko for inspiration in devising this method and Prof. E.R. Hawkes for discussions that led to this application.

8. References

[1] A.Y. Klimenko and S.B. Pope, Phys. Fluids 15 (2003) 1907–1925.
[2] A.Y. Klimenko, in *Proceedings of Clean Air VII* (2003) 14.4.
[3] C. Dopazo, Phys. Fluids 22 (1979) 20–30.
[4] J. Janicka, W. Kolbe, and W. Kollmann, J. Non-Equilib. Thermodyn. 4 (1979) 47–66.
[5] J. Villermaux and J.C. Devillon, Chemical Reaction Engineering: Proceedings of the Fifth European/Second International Symposium on Chemical Reaction Engineering 1972 (B1-13)–(B1-24).
[6] C. Dopazo and E.E. O'Brien, Acta Astronaut. 1 (1974) 1239–1266.
[7] A.P. Wandel and A.Y. Klimenko, Phys. Fluids 17 (2005) 128105.
[8] A.P. Wandel, Combust. Theory Model. 17 (2013) 707–748.
[9] L. Valino and C. Dopazo, Phys. Fluids A 3 (1991) 3034.
[10] A.P. Wandel and R.P. Lindstedt, Phys. Fluids 21 (2009) 015103.
[11] A.P. Wandel and R.P. Lindstedt, Proc. Combust. Inst. 34 (2013) 1365–1372.
[12] A.P. Wandel and R.P. Lindstedt, Proc. Combust. Inst. 37 (2019) 2151–2158.
[13] M. du Preez, A.P. Wandel, D. Bontch-Osmolovskaia and R.P. Lindstedt, Phys. Fluids 33 (2021) 045109.
[14] Y. Ge, M.J. Cleary and A.Y. Klimenko, Proc. Combust. Inst. 33 (2011) 1401–1409.
[15] C. Straub, S. De, A. Kronenburg, and K. Vogiatzaki, Combust. Theory Modell. 20 (2016) 894–912.
[16] S.K. Ghai and S. De, Combust. Flame 203 (2019) 362–374.
[17] A. Varna, M.J. Cleary and E.R. Hawkes, Combust. Flame 181 (2017) 342–353.
[18] A. Varna, M.J. Cleary and E.R. Hawkes, Combust. Flame 181 (2017) 354–364.
[19] Z. Li, E.R. Hawkes, A. Wehrfritz and B. Savard, Combust. Flame 258 (2023) 113039.
[20] C. Yu, P. Breda, M. Pfitzner and U. Maas, Proc. Combust. Inst. 39 (2023) 2299–2308.
[21] F. Gao, Phys. Fluids A 3 (1991) 2438–2444.
[22] E.E. O'Brien and T.-L. Jiang, Phys. Fluids A 3 (1991) 3121–3123.
[23] R. Miller, S. Frankel, C. Madnia and P. Givi, Combust. Sci. Technol. 91 (1993) 21–52.
[24] A.P. Wandel, Phys. Fluids 35 (2023) 041703.
[25] A.P. Wandel, *Development of Multiple Mapping Conditioning (MMC) for Application to Turbulent Combustion*, Ph.D. thesis, UQ (2005).
[26] S. Mitarai, J.J. Riley and G. Kosály, Phys. Fluids 15 (2003) 3856–3866.
[27] P. Sripakagorn, G. Kosály and J.J. Riley, Combust. Flame 136 (2004) 351–363.
[28] S. Mitarai, J.J. Riley and G. Kosály, Phys. Fluids 17 (2005) 047101.

Fundamentals and New Concepts Paper 8

B. Z. Dlugogorski and A. R. Masri, Eds

Towards Clean Combustion and Decarbonisation
Proceedings of the Australian Combustion Symposium
26 – 29 November 2023, Darwin, Northern Territory, Australia

Instantaneous temperature field prediction of jet in hot coflow flames using machine learning

Jordan Kildare[1,*], Wai Tong Chung[2], Michael Evans[3], Zhao Tian[1], Paul Medwell[1] and Matthias Ihme[2]
[1]School of Electrical and Mechanical Engineering, The University of Adelaide, SA 5005 Australia
[2]Department of Mechanical Engineering, Stanford University, CA 94305 USA
[3]UniSA STEM, The University of South Australia, SA 5095 Australia

Abstract

A multi-scale U-Net machine learning model is developed to predict instantaneous temperature fields from OH- and CH_2O-PLIF measurements in ethylene and natural gas flames in a jet-in-hot-coflow burner. The objective is to provide a fast and accurate method of non-invasive temperature measurements which can be applied to a large range of jet in hot coflow (JHC) flames. The model was trained on data from 12 ethylene flames and 5 natural gas flames, over a range of jet Reynolds numbers (1k–30k), at coflow oxygen concentrations of 3–9% by volume. Images of the temperature fields and radial profiles are compared against the predicted fields in previously unseen cases, showing very good agreement with bulk flame features, mixing profiles, and peak temperature values across the described conditions. The results indicate that generalisation to a larger number of flame cases within the similar fuel and oxidant ranges is achievable with little to no further training, allowing for rapid temperature field prediction from OH- and CH_2O-PLIF measurements.

Keywords: artificial intelligence, temperature and radical fields, turbulent combustion, planar laser-induced fluorescence

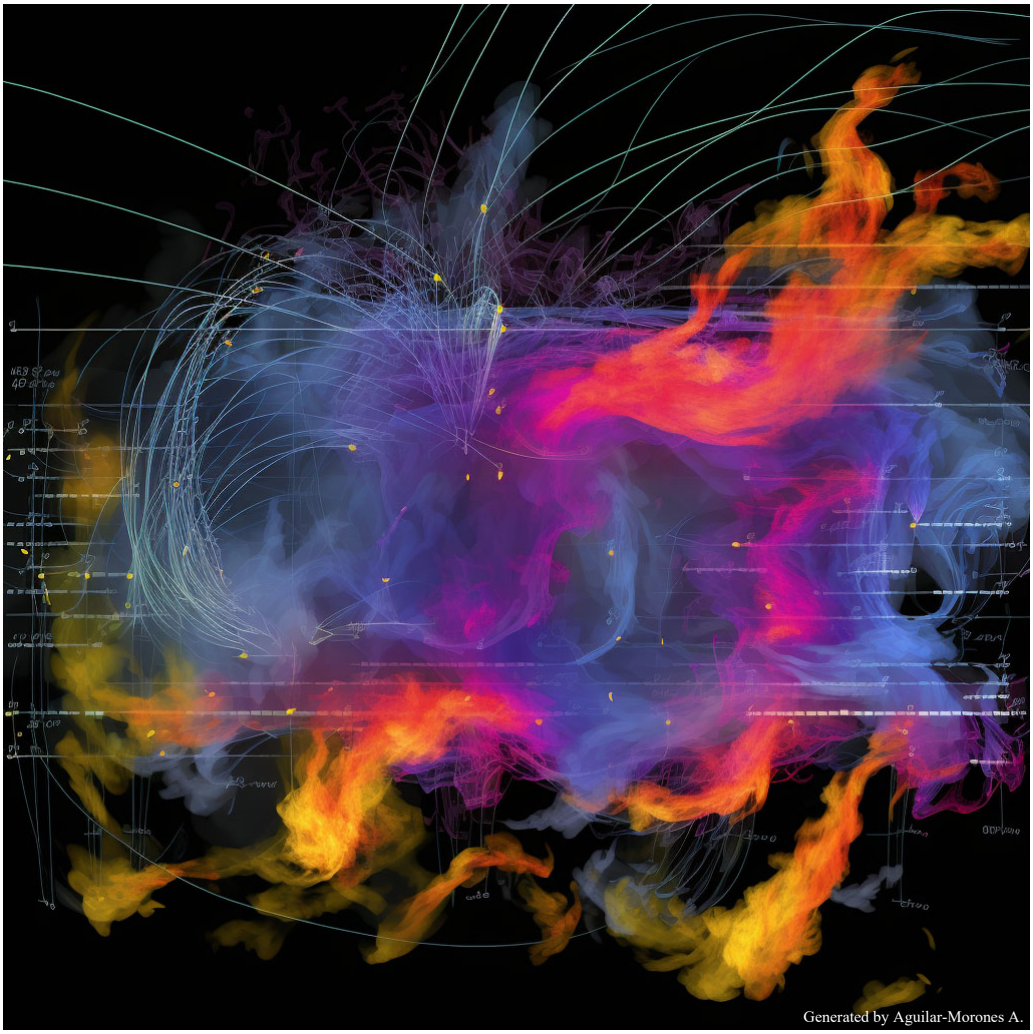

Artistic artificial intelligence images generated were based on the abstract content.

* Corresponding author:
Phone: (+61) 421 845 585
Email: jordan.kildare@adelaide.edu.au

Fundamentals and New Concepts Paper 9
B. Z. Dlugogorski and A. R. Masri, Eds

Towards Clean Combustion and Decarbonisation
Proceedings of the Australian Combustion Symposium
26 – 29 November 2023, Darwin, Northern Territory, Australia

Analysis of large-scale energy storage using Bilger's oxyfuel process

M. M. Kratzer[1] and A. Y. Klimenko[1, *]
[1]Centre for Multiscale Energy Systems, School of Mechanical and Mining Engineering, University of Queensland, QLD 4072 Australia

Abstract
This work investigates a model of large-scale chemical energy storage through a systems analysis. This analysis is aimed to provide insight into the looming energy storage problem which is caused by a shift towards energy grids supported by a significant proportion of energy generated via renewables. To suppress the large seasonal variations of energy production associated with such a grid, a long-term, large-scale energy storage system may be utilised, where here, we investigate the use of Bilger's oxyfuel process [1]. This process permits effective storage of renewable energy while allowing for carbon-control. This analysis is performed via a simple MATLAB model, allowing for fast and efficient modelling of the reservoir sizing required to support seasonal variations for different Australian states.

Keywords: energy storage, systems analysis, green hydrogen

1. Introduction

As the cost of green energy continues to decrease, the economic, along with societal, benefits of transitioning towards a renewable energy-supported grid are becoming clear. While such a technological shift relies on many well-developed technologies, such as increasingly efficient techniques of wind and solar generation, there remain unresolved issues with this transition.

The fundamentally intermittent nature of renewable energy generation can cause strain on traditional base-load generators, potentially leading to instabilities in both power supply and electricity cost. Due to a combination of daily and seasonal variations in power usage and generation electricity prices may vary between order of magnitude increases to negative values. Hence, to prevent excess electrical and economic loading, the usage of such renewable energy-supported grids requires both large-scale and long-term energy storage to suppress such power variations.

Clearly the generation and consumption of electricity must always remain balanced due to the conservation of energy. Storage may be utilised to balance energy supply and demand, while preventing instabilities in the grid. A mixture of different renewable energy sources, such as solar, wind and pumped hydro, may lead to different modes of instabilities in the grid. This is due to the different characteristic times of different renewable energy sources.

Maintaining the required energy balance within an energy grid with variations in energy generation and consumption requires the introduction of energy storage facilities. Some examples of characteristic response times for different storage methods are shown in Table 1.

Table 1: Comparison of Characteristic Response Times for Different Methods of Energy Storage [5]

Type of Storage	Discharge time	Storage Capacity
Kinetic energy: Turbomachinery and flywheels	Near instant	1-100 kWh
Electrochemical: Batteries and fuel cells	Seconds to hours	0.1-10 MWh
Gravitational: Pumped hydro	Hours to days	0.1-100 GWh
Chemical: Hydrogen/Methane gas storage	Days to years	0.1-100 TWh

Daily variations, such as seen in the daily 'Duck curve' [3] which arises due to increased energy requirements in the late evening, may be accounted for by fast-responding, low-capacity storage methods. Examples of such systems include inertia-based stabilisation components, such as heavy turbomachinery (including both simple flywheels and mechanical generators).The excess hourly and daily energy are primarily purchased by commercial entities, which provide a service of energy storage, generating capital through the buying and selling of energy, dependant on the fluctuating energy prices.

2. Storage of Hydrogen and Its Derivatives

The previously outlined characteristics of both large-scale storage and transport outline issues with the utilisation of the current well-developed technologies, namely, the difficulty and cost of local transport and size restrictions.

The role of hydrogen within the concept of a "hydrogen economy" is often misunderstood, with some focusing primarily on its potential utility as an energy source in electric vehicles using hydrogen fuel cells.

* Corresponding author:
Email: a.klimenko@uq.edu.au

While this could, in principle, become an important application of hydrogen technology, it will need to compete with battery-powered cars which are already seeing large scale production. The major role which hydrogen and its derivatives (being methane and ammonia) appear to have an advantage over batteries is long-term energy storage and transport.

Due to these potential advantages, there has been recent interest in the underground storage of hydrogen, with investigations focusing on the usage of salt caverns [4] and depleted gas reservoirs [5]. While the practicality of the use of depleted gas reservoirs has not yet received sufficient analysis, we note that there are mostly depleted gas reserves in Australia which still contain on the order of 10% hydrogen [6], hence, may be suitable for long-term stable energy storage.

Australia shows promise in both the production and export of renewable energy. For this investigation we consider two separate cases, with either the export of the excess produced renewable energy or specifically generated energy for the purpose of export. To match current LNG export, Queensland would need to export H_2 in quantities of 1 or 10 Mt for the first and second scenarios. Similarly, Australia would need to export 5 to 33 Mt for the second scenario [7]. We note that to produce 20Mt of green hydrogen via electrolysis, the energy requirement would necessitate a dedication of 10 000 km^2 of land, assuming PV solar panels are utilised [8]. For electrolysers with efficiencies of around 70%, this would require approximately 200GL of water per annum.

Unlike the fossil fuels widely utilised in the current Australian energy grid, the combustion of hydrogen is particularly clean, due to the absence of carbon. Along with the benefit of carbon-free combustion products, hydrogen has some beneficial physical and chemical properties, such as the greatest specific chemical energy of any gas, with content on a mass basis, with lower heating value 2.4 and 6.4 times greater than methane or ammonia respectively. While these physical properties appear very beneficial, there still exist disadvantages which may affect its usefulness as the primary agent for long-term storage.

A primary benefit of the usage of methane is the development of the technology, with piping and transport being well understood and regulated. In comparison, at the time of writing, there exists only one ship designed for liquid H_2 transport, being the Suiso Frontier, which is still operating as an experimental vessel. Along with this, hydrogen is known to be more difficult to use in gas power systems due to issues of hydrogen embrittlement. Despite this, manufacturers have developed turbines which are suited for hydrogen both as a pure fuel and in mixtures.

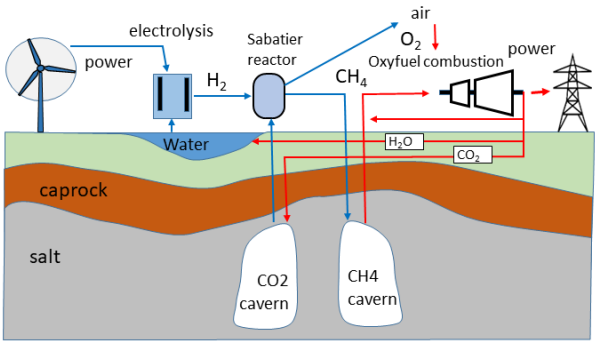

Fig 1: Storage with carbon control using Bilger's oxyfuel combustion process, reproduced from [8].

3. Carbon-Controlled Storage and Transport with Methane

Recently, power-to-gas systems have been investigated as storage systems capable of supporting seasonal variations in energy supply and demand. Power-to-gas systems convert electrical energy into chemical energy. In such an energy system, hydrogen is the primary product, which is produced through the electrolysis of water. The global reaction for this process is simply described by the reaction

$$H_2O(l) \Rightarrow H_2(g) + \frac{1}{2}O_2(g) \qquad (1)$$

After the electrolysis step the produced hydrogen may be transported either in its current form, converted into methane or ammonia then transported, or alternatively, stored on site for later use in energy generation. Such a model is sometimes referred to as a power-to-gas-to-power system, as it permits the storage and transmission of energy through the production of multiple species of gas [2,9]. Methane can be produced from hydrogen on industrial scales through the Sabatier reaction. This reaction involves the methanation of a H_2-CO_2 mixture. The global reaction is exothermic and reads,

$$4H_2(g) + CO_2(g) \Rightarrow CH_4(g) + 2H_2O(l) \qquad (2)$$

These processes may be undertaken by way of Bilger's oxyfuel process [4], which implies carbon control and storage. The produced methane may be stored in underground reservoirs, which is a well-developed technology, and later, when an energy output is required, the methane may be combusted to generate power. The combustion of methane in pure oxygen, which is produced in stoichiometric quantities by the electrolysis process (1) is given by

$$CH_4(g) + 2O_2(g) \Rightarrow CO_2(g) + 2H_2O(l) \qquad (3)$$

It is beneficial to capture the oxygen produced through the electrolysis for use in this combustion process, since the separation of oxygen from the surrounding air would lead to an energy penalty of 0.9MJ/kgO_2. Additionally, using oxygen in place of air excludes nitrogen from the reaction, hence producing no oxides of nitrogen.

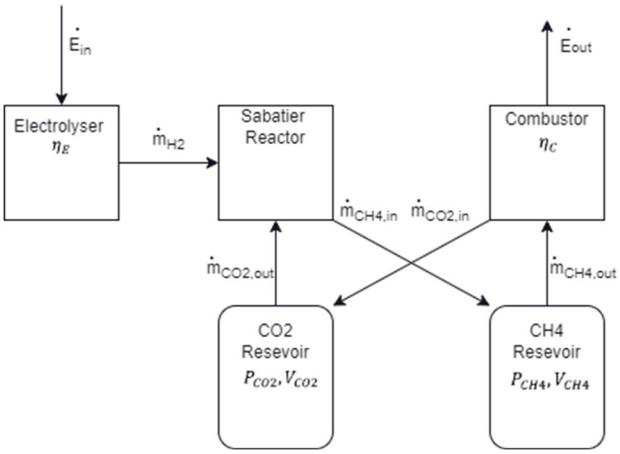

Fig 2: Simplified cycle schematic including relevant parameters

For a system operating in this manner, the facility may be designed to operate as a cycle. This would require two separate underground reservoirs, one for storing CH_4 as fuel for the combustor, and another for storing CO_2 acting as an input to the Sabatier reactor. The carbon dioxide acts as a working fluid of a thermodynamic cycle, and hence is not released into the atmosphere, leading to complete carbon control. The water used in the electrolysis can be recovered and, at least in principle, may be recycled from the combustor and reactor products. This cycle is shown in Figure 1.

A similar process was discussed in Jensen et al [10], where a cycle was proposed which utilises developing fuel technology. While such a model would work similarly to this one, due to the difficulty in scaling up fuel cell technology for large-scale energy storage, we propose this cycle as a stronger choice to cover seasonal variation in energy demand.

4. System Modelling

To investigate the practicality of this energy storage system, simulations were constructed in the MATLAB language. We construct a simplified model of the cycle shown in Figure 2. In this simplified model, 5 individual components are modelled. These components are the electrolyser, Sabatier reactor, combustion chamber and the CO_2 and CH_4 underground storage caverns.

We assume here that most of the stored energy takes the form of potential chemical energy and not total enthalpy such as in compressed air storage. With this assumption, we may ignore major and minor pressure losses in the system, and not model any compressors or expanders which would exist in a real system. Figure 2 shows a representation of the cycle including the important parameters, being the input and output power, $\dot{E}_{in}$ and $\dot{E}_{out}$, the gas mass flow rates, $\dot{m}_\iota$, cavern pressure, P_i, volumes, V_i, along with the electrolyser and combustor efficiencies, η_E and η_C. For a preliminary investigation we model both the electrolyser and combustor to have an efficiency of 65%, which may be an optimistic assumption, but leads to a total system efficiency of around 42%, which is near the 36% efficiency found by Bundy et al. in the analysis of a similar energy system [11]. The relevant equations for the components in the simplified model are the electrolyser output flow rate,

$$\dot{m}_{H2} = \eta_E C_E \dot{E}_{in} \tag{4}$$

mass flow through the reaction chamber,

$$\dot{m}_{CH4} = 2\dot{m}_{H2} \tag{5}$$

energy output from the combustor,

$$\dot{E}_{out} = \eta_C C_C \dot{m}_{CH4} \tag{6}$$

and reservoir pressure, approximated here as to be given by the ideal gas law,

$$P_i = \frac{R_i T}{V_i} m_i \tag{7}$$

for constant reservoir temperature T and specific gas constant R_i. For salt caverns, the minimum and maximum pressure limits have been reported to lie between approximately 7 and 17 MPa respectively [2]. These pressure limits, along with the total system efficiency, are used to size the caverns.

To find the required total cavern size to cover the seasonal variations, we compare the average daily energy demand to the average yearly demand and consider a system which buys energy when this difference is positive and sells when it is negative. Using energy data from the Australian Energy Market Operator (AEMO) we may find the minimum allowable cavern sizes for Queensland, a state with small seasonal variations and Victoria, a state with large seasonal variations.

The cavern pressure and yearly energy demand data for the respective states is shown in Figs. 3 and 4. These caverns were sized by utilising a simple bisection search, minimizing both cavern sizes until all excess power could be stored without exceeding the maximum or minimum cavern pressures. To support this simplified problem, the caverns must be sized at $1.24\times 10^7 \mathrm{m}^3$ and $9.10 \times 10^6 \mathrm{m}^3$ for Victoria and Queensland respectively.

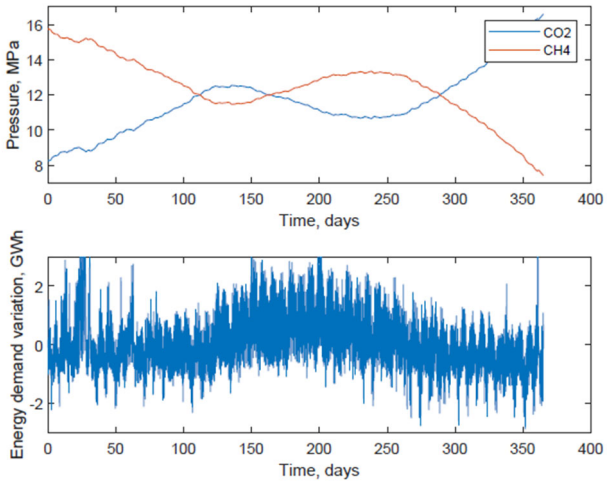

Figure 3: Cavern Pressure and energy demand variations in Victoria from 2022 AEMO data.

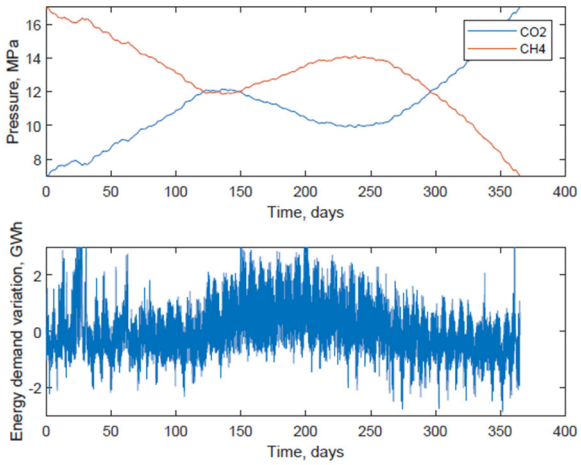

Figure 44: Cavern Pressure and energy demand variations in Queensland from 2022 AEMO data.

To account for the initial conditions of the demand data, the initial cavern pressures to support this minimal size were found as $P_{CO2} = 8.25$ MPa and $P_{CH4} = 15.75$ MPa for Queensland and $P_{CO2} = 7.05$ MPa and $P_{CH4} = 16.95$ MPa for Victoria.

The results of this analysis depend strongly on both the input data and the selected total system efficiency. The efficiency of both electrolysis and combustion likely will not be optimal in a system with significant power variations such as seen in Figure 3. Performing the same analysis while using a total system efficiency of 36% such as in Bundy et al. [11] leads to increased required cavern sizes of $1.09\times 10^7 m^3$ and $1.24\times 10^7 m^3$ respectively. Even at the reduced system efficiency, salt caverns of suitable volume exist, with the KING-1 and KING-2 caverns both having a usable gas volume of over $2\times 10^7 m^3$ [2]. While this implies that large caverns could be suitable for accounting for supporting an Australian energy grid, Australian salt deposits are still under investigation for their suitability in dynamic storage.

5. Conclusions

This work investigated the utility of Bilger's oxyfuel process as the basis of a power-to-gas system which could support seasonal variations in energy supply and demand within Australian states. This work found that both Queensland and Victoria would each require two separate caverns with a working gas volume of $1.24 \times 10^7 m^3$ and $9.10 \times 10^6 m^3$ respectively, both of which could be potentially constructed using naturally occurring salt caverns.

6. Acknowledgment

This work is supported by the ARC Discovery Scheme (DP220103352). The Authors wish to thank the reviewers for their valuable comments.

7. References

[1] R. W. Bilger, "Zero Release Combustion Technologies and the Oxygen Economy" Fifth Int. Conf. on Techn. Combust. Clean Environ., Lisbon, Portugal, p. 12–15, 1999

[2] T. Wang, J. Li, G. Jing, Q. Zhang, C. Yang, and J. J. K Daemen, "Determination of the maximum allowable gas pressure for an underground gas storage salt cavern – A case study of Jintan, China", J. Rock. Mech. Geotech. Engin., vol. 11, pp. 215-262, 2019.

[3] J. Kosowatz. "Energy storage smooths the duck curve." Mech. Engin. 140, vol. 6 , pp. 30-35, 2018.

[4] M. Kuhn, M. Streibel, N. Nakaten, and T. Kempka, "Integrated Underground Gas Storage of CO2 and CH4 to Decarbonise the 'Power-to-gas-to-gas-to-power' Technology", Energy Procedia, vol. 59, pp. 5-19, 2014.

[5] N. S. Muhammed, et al. "Hydrogen storage in depleted gas reservoirs: A comprehensive review." Fuel, vol. 337, pp. 127032, 2023.

[6] C. J. Boreham, D. S. Edwards, K. Czado, N. Rollet, L. Wang, S. van der Wielen, D. Champion, R. Blewett, A. Feitz. P. A. Henson. The APPEA Journal 61 (2021) 163–191.

[7] M. Kanaani, B. Sedaee, M. Asadian-Pakfar,. Journal of Energy Storage, 45 (2022) 103783.

[8] A. Y. Klimenko, "Bilger's Zero Carbon Release Combustion Technology as Energy Storage", 14th Asia-Pacific Conf. Comb., Kaohsiung, Taiwan, 2023.

[9] A. Litheko, B. Oboirien, and B. Patel, "Analysis of the application of power-to-gas (P2G) technology in the road transport system of South Africa", Sustain. Energy. Tech. Assess., vol. 52, pp. 2213, 2022.

[10] S. H. Jensen, C. Graves, M. Mogensen, C. Wendel, R. Braun, G. Hughes, Z. Gao, S. A. Barnett, Energy Environ. Sci., vol. 8, pp. 2471, 2015.

[11] C. Budny, R. Madlener, and C. Hilgers, "Economic feasibility of pipe storage and underground reservoir storage options for power-to-gas load balancing", Energy Conversion and Management, vol. 102, 2015.

Author Index